CHARACTERISATION AND MODELLING OF PRECIPITATION DURING THE EARLY STAGES OF TEMPERING FOR LOW CARBON LOW ALLOY Q&T STEELS

by

YULIN JU

A thesis submitted to the University of Birmingham for the degree of

DOCTOR OF PHILOSOPHY

School of Metallurgy and Materials

College of Engineering and Physical Sciences

University of Birmingham

September 2018

Preface

This project was carried out by Yulin Ju in School of Metallurgy and Materials, University of Birmingham (from September 2014 to September 2018), under the supervision of Dr. Martin Strangwood and Prof. Claire Davis.

The present work is original and no part of this work has been submitted for a degree at any other university. Wherever other researchers' work has been cited, it is acknowledged in the text with references listed at the end of this thesis.

Parts of the work have been published or accepted by journals as followed:

[1] Yulin. Ju, Aimee Goodall, Martin Strangwood, Claire Davis. Characterisation of precipitation and carbide coarsening in low carbon low alloy Q&T steels during the early stages of tempering. Materials Science and Engineering: A, 738 (2018) 174 - 189.

[2] Yulin. Ju, Aimee Goodall, Claire Davis, Martin Strangwood. Characterisation of precipitation and coarsening of carbides during tempering in a low alloyed quenched and tempered steel. THERMEC International Conference on Processing & Manufacturing of Advanced Materials Processing, Fabrication, Properties, Applications. Materials Science Forum, 2018, accepted.

[3] Aimee Goodall, Yulin. Ju, Claire Davis, Martin Strangwood. Effect of tempering on hardness of Q & T steel plate. THERMEC International Conference on Processing & Manufacturing of Advanced Materials Processing, Fabrication, Properties, Applications. Materials Science Forum, 2018, accepted.

Abstract

Low carbon low alloy quench and tempered (Q&T) steel plates up to 100 mm thick are used in applications such as cranes and earth movers due to their combination of high strength and toughness. In terms of ensuring that appropriate tempering conditions are used to give optimum properties through thickness in thick plate Q&T steels it is desirable to be able to predict the effect of composition and tempering conditions (time and temperature) on the microstructure and hence the hardness evolution. In this project, carbide precipitation and coarsening behaviour in three S690-based steels (Base, Base-Mo-V and Base-Cr-Mo-V-Si steels) have been investigated during tempering at 600 °C up to 16 hours to determine the role of alloying additions of Mo, V, Cr and Si. Kinetic modelling (DICTRA model and mathematical model) for carbide coarsening has been carried out and compared with experimental observations.

Auto-tempering occurs during water quenching with ε'-carbide and cementite being present within the martensite laths for all three steels. Cementite is the predominant as-quenched carbide in the Base and Base-Mo-V steels, whereas ε'-carbide constitutes a larger number percentage in the Base-Cr-Mo-V-Si steel consistent with the effect of the Si addition in retarding the transformation from ε'-carbide to cementite during auto-tempering. In the Base steel, cementite (predicted equilibrium carbide), located within the laths and on the lath/grain boundary, becomes the stable second phase after 2 hours tempering and has an elliptical shape, which coarsens with time on tempering from 2 hrs to 16 hrs. However, in the Base-Mo-V and Base-Cr-Mo-V-Si steels, elliptical cementite (in the laths and on the lath/grain boundaries) and needle-shaped cementite (within the laths) both exist during tempering; furthermore, finer elliptical secondary Mo-V-rich

carbides are observed within the laths after tempering for 4 hrs. In the three steels, the inter- and intra-lath cementite coarsen independently with time during tempering from 2 hrs to 16 hrs. Substitutional elements, i.e. Mn, Mo, Cr, and V, enrich cementite in the three steels, and it is their diffusion that dominates the coarsening of cementite. Therefore, the rates of coarsening of cementite in the three steels rank as Base> Base-Mo-V> Base-Cr-Mo-V-Si due to different diffusivities of the substitutional elements that are partitioning into cementite during tempering as well as any effects of Si in the matrix. The coarsening of cementite contributes to the softening process in the three steels on tempering with the presence of the fine needle-shaped cementite within the laths in the Base-Mo-V and Base-Cr-Mo-V-Si steels contributing to their greater resistance to softening. The observation of fine secondary alloy carbides after 4 hours tempering does not appear to result in any secondary hardening peak in the Base-Mo-V and Base-Cr-Mo-V-Si steels, which is considered to be due to the low alloy contents and hence low amount of secondary alloy carbides.

The inter-lath cementite constitutes most of the cementite volume fraction and its coarsening contributes most to the decrease of hardness during tempering, hence, it is important to predict the coarsening behaviour for inter-lath cementite. DICTRA modelling was carried out to predict inter-lath cementite coarsening in the Base and Base-Mo-V steels and compared with experimental observations. The simulation results show that the DICTRA model gives coarsening rates that are too slow and significantly deviate from the experimental data. Rather than setting parameters to fit the experimental data, a new mathematical model, based on the finite difference method, was established for coupled inter-lath cementite particles, where dissolution of the smaller particle and coarsening of the larger one were treated as a continuous and simultaneous process. The

rate-controlling step for the model is the dissolution of the smaller particle driven by diffusion of Mn (as the predominant substitutional element in the Base steel that enriches cementite). The mathematical model then predicts the shortest dissolution times for smaller particles in different coupled inter-lath cementite systems. It is also found that the predicted size increase for the larger particle due to dissolution of a single smaller one is much less than the experimentally observed size increase for the larger particles, suggesting that different particle arrangements which include more than two particles should be considered. It appears that the simulated simplest particle arrangement with only the largest and smallest particles included does appear in the SEM images, and the simulation for coarsening is in a rough agreement with the observed results. For a complete analysis of tempering in the Base steel the observed multi-particles in different size ranges along the lath boundary also need to be considered, where a multi-sized inter-lath cementite model is required in the future.

Acknowledgements

I would like to express my enormous gratitude to my supervisors Dr. Martin Strangwood and Prof. Claire Davis for their guidance and encouragement through my Ph.D study. I am so proud to be their student, and I really appreciate this opportunity to work with them and learn how to do research sensibly from them. I overcame loads of difficulties with their help and patience during my Ph.D study. The memory of their support will never fade in my life, and their spirit of exploration in science will be inherited for my future.

I sincerely thank to the School of Metallurgy and Materials for provision of research equipment during my Ph.D study. I also gratefully thank to TATA Steel (UK) and British Steel Ltd for provision materials and technique support. Massive thanks are also given to China Scholarship Council (CSC) to provide financial support during my Ph.D study in University of Birmingham.

I gratefully acknowledge to the following people who helped me to overcome my experimental difficulties: Siben Jiang, Shanshan Si and Jinsen Tian in Universitry of Birmingham, and Ishwar Kapoor, Dr. Geoff West and Dr. Lei Zhou in WMG University of Warwick. I also thank to all my friends in UK for their help: Qi Wei, Aimee Goodall, Jiaxin Wen, Jiejie Wu and so on.

I sincerely thank my husband Dr. Fei Wang for his encourage and support during my Ph.D study.

Finally, I would like to give me enormous gratitude to my parents who encouraged me to study overseas four years ago. Their selfless love and constant support encourage me to be a better person in my life. I am so proud to be their daughter and I would dedicate my thesis as a gift to them.

Contents

List of Figures

List of Tables

Chapter 1 Introduction

High Strength Low Alloy (HSLA) steel is a type of low alloyed steel which provides better mechanical property mixes, such as strength, toughness, weldability and formability, than conventional carbon steels [1]. Hence, this grade of steel has been the subject of considerable research and development work investigating composition, processing, structure and mechanical properties with widespread industrial application. Quenched and tempered (Q&T) steels, which can be considered as a type of HSLA steel, normally have a relatively low carbon content and also contain alloying elements such as Mn, Mo and Cr, Table 1-1 [2]. Q&T plates have desirable mechanical properties combining high strength and good toughness; and with thickness varying from 8 mm up to 130 mm; the minimum yield stress can reach 630 MPa and tensile strength ranges from 690 MPa to 930 MPa based on composition and thickness [3]. In addition, Q&T plates also have excellent weldability, but they need to be treated cautiously during welding and fabrication, because of their high yield stress and tensile strength, to ensure that the desirable properties are maintained. Q&T plates have been developed for widespread use in applications such as mining and quarrying equipment, material handling, construction and earth moving industries giving a reduction of weight compared to other steel grades [4].

Table 1-1. Typical Q&T steel chemical composition [2]

Composition	C	Si	Mn	S	P	Cr	Mo	Nb	V	Ni	Cu
Mass percentage/%	0.20	0.50	1.60	0.010	0.025	1.00	0.70	0.060	0.08	1.50	0.40

The manufacturing process for RQT (hot rolled-quenched-tempered) plate grades involves, at least, two stages: Stage 1 is reheating the plates, which are hot rolled from slab, to a re-austenisation temperature (about 900 °C) and then roller pressure quenching to room temperature to obtain hard martensitic microstructure; Stage 2 is tempering the hardened steels to improve the toughness at the desired strength level. Although the strength of Q&T plates decreases with the improvement of toughness and ductility during tempering, the addition of different alloying elements can slow and reduce the softening process with secondary hardening occurring with time to obtain a beneficial balance between strength and toughness. For example, the presence of Si can delay and stabilise the formation of transition iron carbides (ε-carbides or ε'-carbides), and retard the nucleation and coarsening process of cementite in the temperature ranges between 400 and 700 °C [5]. Molybdenum slows down the coarsening process of cementite and promotes the formation of M_2C, which achieves a secondary hardening effect. Chromium can take the place of iron atoms in cementite if there is a sufficient content in solution [6], and tends to form $M_{23}C_6$ and M_7C_3 affecting the softening process. The precipitation sequences vary with different contents of Cr and Mo, as shown in Figure 1-1; higher contents of Cr give earlier precipitation of M_7C_3 compared with M_2C [7].

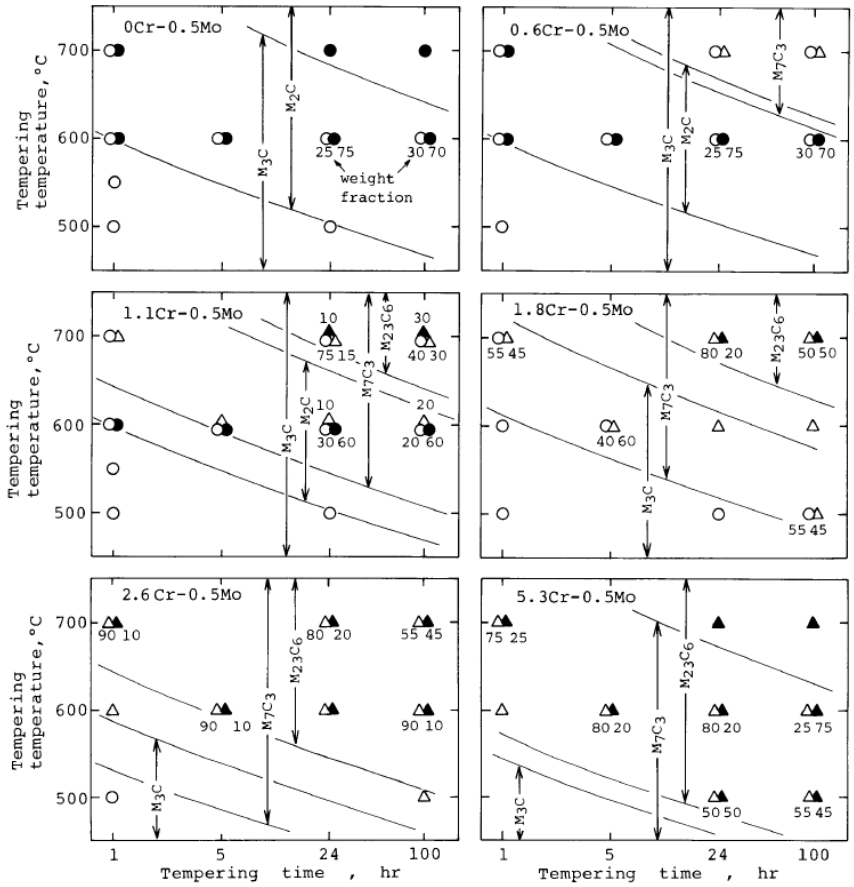

Fig.5 Carbide phase diagrams of Cr-0.5%Mo steels during tempering
Note; ○ M3C ● M2C △ M7C3 ▲ M23C6

Figure 1-1. The evolution of carbide phases for Cr-0.5%Mo steels during tempering [7].

The production of Q&T plates in a range of thicknesses requires a range of tempering times (and temperatures) to be used, particularly with the development of increasingly heavier gauges. Full thickness tempering can vary from less than half an hour for the thin (around 8 mm) to several hours for the thick (up to 130 mm) plate. In addition, for thick plates a range of tempering times are experienced by the microstructure through thickness due to the time required to heat the material to the tempering temperature. In order to optimise tempering - property - thickness combinations for a range of Q&T plates, it is necessary to be able to predict the effect of composition and tempering

conditions (time and temperature) on the matrix and precipitate populations. Q&T steels need to develop a stable precipitate structure, and hardness, strength and toughness levels, at short (e.g. thin plate or thick plate surface) and long (thick plate centre) tempering times. In this project, the effects of composition and tempering conditions on the precipitation responses for low carbon low alloy Q&T steel plates (S690-based steels) have been investigated, and thermodynamic and kinetic modelling techniques have been used to simulate the coarsening process of precipitates.

There are 8 chapters included in this thesis:

Chapter 1 gives the description of the project background.

Chapter 2 reviews the tempering responses for low carbon (plain and alloyed) martensitic steels.

Chapter 3 reviews the reported analytical and numerical models used for coarsening of carbides in the matrix and along grain/subgrain boundaries in steels.

Chapter 4 describes the materials and methodology used for experimental observations.

Chapter 5 presents the characterisation results of carbide precipitation and coarsening for the three low carbon low alloy Q&T steels.

Chapter 6 presents the DICTRA simulation for coarsening of inter-lath cementite in the Base and Base-Mo-V steels which is further compared with the experimental data.

Chapter 7 describes the establishment of the mathematical model for coarsening and dissolution of coupled inter-lath cementite based on the experimental observation.

Chapter 8 summarises all the experimental and simulation results and suggests the future work.

Chapter 2 Tempering responses for low carbon alloyed martensitic steels

2.1 Martensite formation during quenching

Martensite, a hardened microstructure, forms from the transformation of austenite when quenching to room temperature in steels, where carbon formerly in the austenite remains in solid solution during the displacive transformation. The crystal structure changes from face-centred cubic (FCC) of austenite to body-centred tetragonal (BCT) of martensite, compared with the body-centred cubic (BCC) of ferrite because of the supersaturated carbon in solid solution, which results in higher hardness but lower toughness and ductility. Two major morphologies of martensite, named as lath martensite and plate martensite, form in alloyed steels based on the different contents of carbon. For low carbon steels (alloyed and plain carbon), such as Q&T plates (S690-based steels) studied here, the microstructures are generally lath-like martensite. The lath boundaries consist of a high density of dislocations arranged as low-angle grain boundaries (LAGBs) with misorientation angles less than 3° (mostly 1-2°) [8]. Whereas, the packet boundaries, where one packet contains several laths, and prior austenite grain boundaries are high-angle grain boundaries (HAGBs) with misorientations ≥ 15° [9]. The low/high angle-grain boundaries can be regarded as disordered two-dimensional regions with only few atomic size thickness (5-10 Å), where solute diffusion along boundaries is generally orders of magnitude faster than that in the bulk, depending on temperature [9, 10].

Martensite initially forms at the martensite start (Ms) temperature, and the formation of marensite proceeds until the temperature falls to reach the martensite finish (Mf)

temperature. The Mf temperature is normally about 100 - 200 °C lower than the Ms temperature in steels with carbon contents ≤ 0.4 wt % [11]. The Ms and Mf temperatures are influenced by the alloying elements present in steels. As shown in Figure 2-1, they both decrease with an increase in carbon contents [11-14]. The decrease of the Mf temperature results in an increasing volume fraction of retained austenite present after quenching. Normally, in plain carbon martensitic steels with carbon contents ≤ 0.5 wt %, the volume fraction of retained austenite is below 2 % [5]. Very low volume fractions of interlath retained austenite (thin film shape) have been detected after quenching in some low carbon alloyed steels [15, 16], such as Fe-0.2C-(2-4)Mo steels with less than 2% volume fraction of retained austenite detected after water quenching [16].

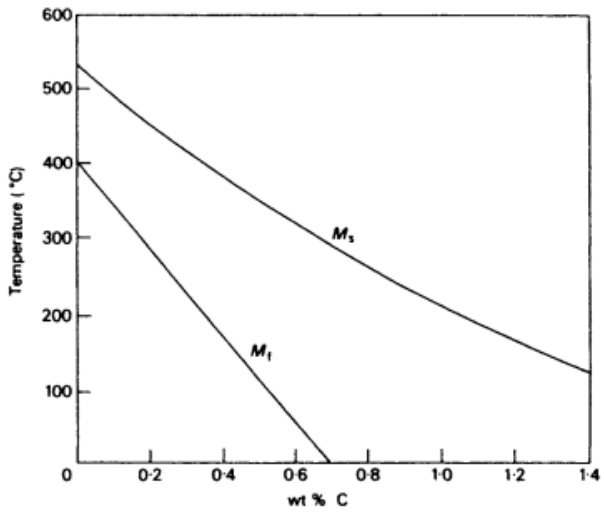

Figure 2-1. The carbon effect on the marteniste start (Ms) and finish (Mf) temperatures [11-14].

As for other alloying compositions in the parent phase, the influence on Ms is obviously different, where the addition of Cr, Mn, Ni, Mo, V, Si, Nb and B decreases Ms temperature, whereas Al, Ti, V, Co can increase Ms temperature in a certain concentration range [17, 18]. Generally, at a smaller carbon content, there is a weaker

influence of alloying elements. There are several empirical Ms equations related with particular composition ranges, with the assumption that all the alloying elements should be in solid solution [19]. For low carbon alloyed steels, Andrews' linear equation [20] and Steven and Haynes equation [21] have both shown reasonably good estimates of Ms temperatures with small deviations (Andrews' linear equation shows a deviation for high Cr-alloys, and Steven and Haynes equation for high-Mo alloys [19]) from measured Ms temperatures; the composition ranges for both formulae are indicated in Table 2-1 and Table 2-2 [22].

Andrews linear equation [20]:

Ms (°C)=539.0 - 423.0 (wt % C) - 30.4 (wt % Mn) - 12.1 (wt % Cr) Equation 2-1

- 17.7 (wt % Ni) - 7.5 (wt % Mo) + 10.0 (wt % Co) - 7.5 (wt % Si)

Steven and Haynes equation [21]:

Ms (°C)=561.0 - 476.0 (wt % C) - 33.0 (wt % Mn) - 17.0 (wt % Cr) Equation 2-2

-17.0 (wt % Ni) - 21.0 (wt % Mo) + (10.0(wt % Co) - 7.5(wt % Si))

Table 2-1. Composition (wt %) ranges of Andrews linear martensite start temperature equation [22]

	C	Mn	Si	S	P	Ni	Cr	Mo
Minimum composition	0.11	0.04	0.11	0	0	0.00	0.00	0.0
Maximum composition	0.60	4.87	1.89	0.046	0.046	5.04	4.61	5.4

Table 2-2. Composition (wt %) ranges of Steven and Haynes martensite start temperature equation [22]

	C	Mn	Si	S	P	Ni	Cr	Mo
Minimum composition	0.11	0.2	0.11	0.004	0.005	0.00	0.00	0.0
Maximum composition	0.55	1.67	1.74	0.014	0.038	5.04	3.34	1.0

Generally, Ms temperature is relatively high (normally well above room temperature) in low carbon alloyed steels, which means the steels can become tempered during cooling below Ms (termed auto-tempering). During this process, carbon atoms can diffuse and redistribute themselves after martensite formation, resulting in carbide precipitation during quenching. Selected area diffraction pattern (SADP) analysis in the transmission electron microscope (TEM) has been used to identify the auto-tempered carbides in the as-quenched martensite, where ε-carbides (or ε'-carbides) and cementite have both been confirmed for steels with different Ms temperatures due to various alloying compositions and different quenching processes [23-30], Figure 2-2. Different cooling rates result in different extents of auto-tempering: the slower the cooling rate, the greater the amount of auto-tempering.

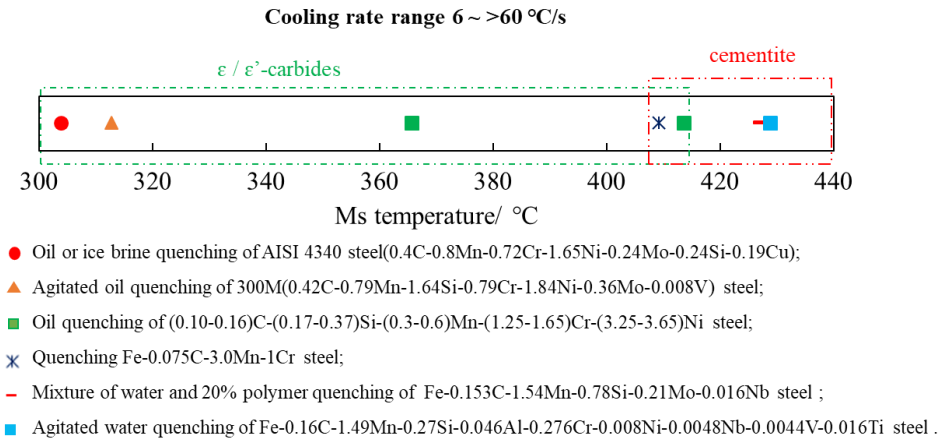

Figure 2-2. ε-carbide (or ε'-carbide) and cementite precipitate during auto-tempering in steels with different Ms temperatures and different quenching processes (based on the reported literature) [23-30].

ε-carbides, proposed by Jack [31] with a close-packed hexagonal crystal structure (chemical composition $Fe_{2.4}C$), or ε'-carbides with orthorhombic symmetry (chemical composition between Fe_2C and Fe_3C), named by Taylor [32] with the carbide being partially ordered, have been identified within as-quenched martensite laths for steels with a relatively low Ms temperature [23-26, 29], Figure 2-2. The orientation relationship (OR) reported between ε'-carbides and the tempered martensitic matrix is $(001)_{\varepsilon'}$ // $(011)_{\alpha}$, $[100]_{\varepsilon'}$ // $[100]_{\alpha}$ [29, 32-34], which is analogous to the Jack OR [31] ($(011)_{\alpha}$ // $(0001)_{\varepsilon}$, $(101)_{\alpha}$ // $(10\bar{1}1)_{\varepsilon}$,$[11\bar{1}]_{\alpha}$ // $[1\bar{2}10]_{\varepsilon}$) for hexagonal ε-carbides in alloyed steels with carbon content lower than 0.5 wt % [23, 35-38]. The habit plane for ε'-carbide was identified as {012}α by Taylor using trace analysis in Fe-C-Ni steels [32], Figure 2-3. However, the habit plane for the transition iron carbides (ε'-carbides or ε-carbides) can migrate to {001}α when they are well beyond any early stage of "spinodal" clustering [23, 29, 35-38]. Furthermore, the needle-axis for ε/ε'-carbide is parallel to <100>α when the electron beam is along <001>α [23, 38, 39].

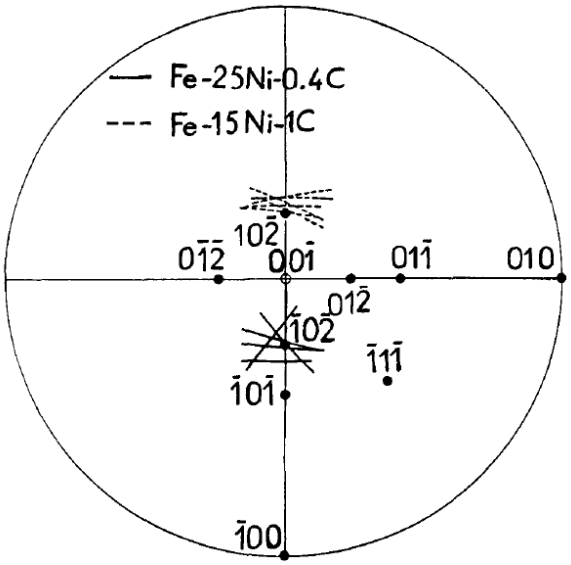

Figure 2-3. Stereogram of the ε'-carbide habit plane normals as measured from a number of TEM micrographs. The habit plane is close to the four variants of the {012}α plane [32].

Cementite, with an orthorhombic structure, has been observed within as-quenched martensite laths for steels with a relatively high Ms temperature (≥410 °C) due to auto-tempering [27, 28, 30], Figure 2-2. Cementite is preferentially precipitated at the interface of any pre-existing transition iron carbides within the laths, or on the subgrain boundaries (e.g. lath boundaries in low carbon alloyed steels) and high-angle grain boundaries (such as packet boundaries and prior austenite grain boundaries) [40, 41]. Bagaryatski OR and Isaichev OR are the reported orientation relationships (OR) between cementite and the tempered martensitic matrix in different steels, Table 2-3, which are measured using SADP and Kikuchi line diffraction patterns [28-30, 35, 36, 38, 42-44].

Bagaryatski OR: $(211)_{\alpha}$ // $(001)_{Fe3C}$, $[01\bar{1}]_{\alpha}$ // $[100]_{Fe3C}$, $[\bar{1}11]_{\alpha}$ // $[010]_{Fe3C}$ [45];

Isaichev OR: $(110)_{\alpha}$ // $(\bar{1}03)_{Fe3C}$, $[1\bar{1}\bar{1}]_{\alpha}$ // $[010]_{Fe3C}$, $[311]_{Fe3C}$ 0.91° from$[1\bar{1}1]_{\alpha}$ [46];

Bagaryatski OR is normally confirmed by the conventional SADP technique, whereas Isaichev OR is more convincingly shown by the Kikuchi line diffraction pattern technique [28-30, 35, 36, 38, 42-44]. Actually, Isaichev OR and Bagaryatski OR are related with each other by rotating by approximately 3.5° about $[010]_{Fe3C}$ and [111]α axis [44], which are within the error of the conventional SADP technique (±5°) [43]. Hence, Wells [36] has concluded that the accuracy of conventional SADP is not sufficient to preclude the Isaichev OR. The habit plane for cementite has been observed as {011}α in tempered lath martensite [35, 36, 38, 47]. In addition, cementite aligns along <110>α when the electron beam is along <001>α in tempered low carbon alloyed steels [38, 39].

ε-carbides and cementite can co-exist, for example both have been observed in a 0.36C-0.40Si-0.77Mn-2.66Cr-2.26Mo-0.82V steel within martensite laths during quenching using a very slow cooling rate (10 minutes cooling from 400 to 100 °C in the furnace) when significant auto-tempering occurs, although the Ms temperature is relatively low (Ms approximately 305 °C) [48].

Table 2-3. Summary of orientation relationship (OR) and habit plane information for cementite in alloyed steels from the reported literature [28-30, 35, 36, 38, 42-44]

Steel	OR with matrix (measuring method)	Habit plane
Fe-0.153C-1.54Mn-0.78Si-0.21Mo-0.016Nb	Bagaryatski (SADP)	-
Fe-0.16C-1.49Mn-0.27Si-0.046Al-0.276Cr-0.008Ni-0.0048Nb-0.0044V-0.016Ti	Bagaryatski (SADP)	-
Fe-0.023C -(0.43-5.7)Al	-	{110}α
Fe-0.014C / Fe-0.017C-0.45Mn	-	{110}α
Fe-24Ni-0.57C	Bagaryatski (SADP)	In untwinned region: {110}α; twinned region{112}α.
AISI 4340	Bagaryatski (SADP)	-
Fe-1.22C-0.26Si-0.6Mn	Bagaryatski (SADP)	{112}α (twinned martensite)
Fe-0.29C-0.13Mn-0.005Si-0.007S	Isaichev at the twin boundary before the occurrence of recrystallization (CBKLDP-convergent beam Kikuchi line diffraction patterns)	-
Fe-1Mn-0.5Si-0.2C	Bagaryatski and Isaichev (TKD-transmission Kikuchi diffraction)	-

2.2 Physical metallurgy of tempered martensitic steels

Martensite tends to have high strength but, in the as-quenched condition, can be brittle so it is necessary to modify the mechanical properties by tempering in the range 150 - 700 °C [5]. In this tempering temperature range, the softening process occurs progressively accompanied by an increase in ductility as the structure changes from as-quenched martensite to tempered martensite.

2.2.1 Tempering responses of plain carbon martensitic steels

The tempering of plain carbon martensitic steels takes place in the following distinguishable stages, where the temperature ranges are dependent on tempering time and carbon contents [49, 50]. The assumption is that tempering starts from an as-quenched structure with carbon in solid solution, which is slightly different from the auto-tempered martensite (discussed in section 2.1) where carbon has already partially diffused out of solid solution to form ε/ε'-carbide or cementite.

(1) Stage 1 (typically temperatures are up to 250 °C, and soaking time is commonly about 1 - 3 hours): Carbon atoms firstly diffuse to form transition iron carbides, either close-packed hexagonal ε-carbides [35-38, 51] or orthorhombic ε'-carbides [32-34, 52], within the laths when the tempering temperature is as low as 80 °C [51]. The tetragonality of martensite is partially lost as the matrix carbon content is reduced [5], which removes the associated strain in the lattice. The formation of ε/ε'-carbides, which reduces the matrix carbon level, results in the moderate hardness decrease in the first tempering stage in the martensitic steels, Figure 2-4 [40].

(2) Stage 2 (typically temperatures are between 200 and 350 °C, and soaking time varies from 2 to 8 hours): The pre-existing ε/ε'-carbides are replaced by cementite gradually [41], where cementite can start precipitating at temperatures as low as 100 °C [5]. Any retained austenite present decomposes into ferrite and cementite in this tempering stage. Cementite can nucleate not only on the pre-existing carbides within the lath but also on low/high-angle grain boundaries [40]. The initial morphology of cementite in this very early tempering stage is normally plate-shape with chemical composition Fe_3C [41]. The matrix loses its tetragonality to become ferrite with a reduction of dislocation density and the formation of cementite [5], leading to a continuous hardness decrease, Figure 2-4 [40].

(3) Stage 3 (temperatures from 300 °C and up to 700 °C): In this tempering temperature range, the spheroidisation and coarsening of cementite within the lath and on the boundaries is one of the microstructural changes for tempered lath martensite, which contributes to a further hardness drop, Figure 2-4 [40]. When tempering at 400 - 700 °C, cementite gradually spheroidises, changing to rod-shape and finally near spherical shape (aspect ratio around 1.5) with larger sizes [53]. In this temperature range, cementite particles also coarsen by Ostwald ripening, where larger particles grow at the expense of smaller ones to minimise the surface to volume ratio [54, 55], losing their crystallographic-based morphology and decreasing overall interfacial energy. The cementite particles located at low/high-angle boundaries preferentially coarsen faster due to the greater solute diffusivity in these regions, whereas particles remaining in the lath coarsen slower [56, 57] with a slower solute diffusivity (a more quantified discussion for cementite coarsening given in section 2.2.2).

In addition, the rearrangement of dislocations within the lath and at the lath boundary continues to occur in this temperature range, resulting in a further decrease in dislocation densities [5, 41, 58]. For example, there is negligible dislocation content observed within martensitic lath in a 4130 steel tempered at 650 °C for 1 hr [41]. However, the original lath structure is preserved during the early stage of tempering, such as in a Fe-0.2C steel tempered at 600 °C for 12 hrs [56].

With an increase in the tempering temperatures between 600 °C and 700 °C, equi-axed ferrite grains with spherical cementite particles, located in the grain or on the grain boundaries, form to minimise the grain boundary area [59], leading to a sharp decrease of hardness. Actually, two mechanisms for the formation of equi-axed ferrite grains have been reported:

I. One mechanism is due to the occurrence of recovery and grain growth, because the residual high-angle grain boundaries rearrange to minimise the grain boundary area where the dislocation density has been removed during the previous tempering stages (recovery process), leading to there being insufficient strain energy to drive recrystallisation [41, 56]. This process normally takes place when tempering at high temperatures for a relatively long time (dozens of hours), such as in a Fe-0.2C steel tempered at 700 °C for 12 hrs [56].

II. The other mechanism is because of the occurrence of recrystallisation. In this case, recovery of dislocations appears to be retarded, leaving enough dislocation strain energy to drive recrystallisation [41]. It has been observed that the cold deformed as-quenched martensite can be recrystallised readily

during tempering due to the introduction of sufficient dislocation strain energy and inhomogeneous deformed regions [60], such as in the cold deformed Fe-0.12C-1.4Mn-0.29Mo steel tempered at 675 °C for 2 hrs [61].

Actually, the formation of equi-axed ferrite grains with spherical cementite particles is not desirable, as it replaces the fine lath microstructures that retain good combinations of high strength and toughness [41].

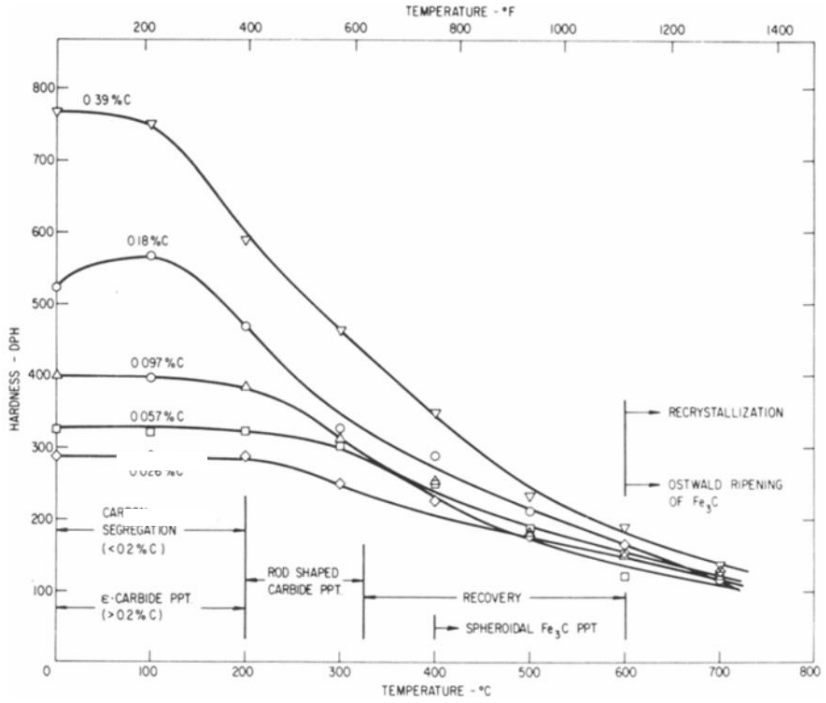

Figure 2-4. Hardness of Fe-C martensitic steel tempered for 1 hr from 100 °C to 700 °C [40].

2.2.2 Tempering responses of alloying martensitic steels

The tempering process for alloyed martensitic steels is more complicated than that for plain carbon steels:

Firstly, ε-carbides or ε'-carbides form as needle-like carbides with the rapid diffusion of carbon, where the initial temperature for their formation can be as low as 80 °C [51].

The firstly formed intra-lath ε-carbides grow with slightly higher tempering temperature or longer time in different alloyed steels, Table 2-4; meanwhile, a few finer inter-lath ε-carbides start to form at a relatively higher tempering temperature, Table 2-4 [62, 63]. Throughout the temperature range of transition iron carbide formation, excess retained carbon has still been found in solid solution in the matrix [41], which is similar to observations for plain carbon martensitic steels.

Table 2-4. The sizes for intra-/ inter-lath ε-carbides in different alloyed steels under different tempering conditions from the reported literature [62, 63]

	Tempering temperature/ time	Sizes for intra-lath ε- carbides	Sizes for inter-lath ε-carbides
Fe-0.32C-0.26Si-1.05Mn-0.72Cr-0.28Mo	190 °C / 36 mins	50 - 150 nm long and 5 - 30 nm wide	-
	230 °C / 36 mins	50 - 200 nm long and - 50 wide	30 - 100 nm long and - 30 nm wide
Fe-0.39C-0.65Mn-1.67Si-0.34Mo-0.72Cr-1.75Ni-0.1Al-0.06V-0.002Ti-0.007Nb	120 °C / 1 hr	Carbide diameter 3.2 ± 1.3 nm	-
	120 °C / 3 hrs	Carbide diameter 4.5 ± 1.3 nm	-
	120 °C / 5 hrs	Carbide diameter 5.6 ± 2.0 nm	-
	120 °C / 8 hrs	Carbide diameter 7.6 ± 2.0 nm	-
	150 °C / 1 hr	Carbide diameter 9.3 ± 2.4 nm	A few finer carbides on the lath boundary (no sizes reported)

Secondly, with an increase of tempering temperature (over a wide range of temperatures from 200 °C to 350 °C [64]) and time, the transformation from ε/ε'-carbides to cementite occurs, where cementite initially has a high aspect ratio (length/width, up to 8) [53, 64]. For example, in a Fe-0.55C-2.2Si steel, ε-carbides and cementite have been both detected after tempering for 20 mins at 250 °C; however, with the temperature increasing

to 450 °C, ε-carbides can persist after tempering for 30 s, but they are totally replaced by cementite after tempering for 5 mins [64]. In this stage, only carbon diffuses without any redistribution of alloying elements [65], for example, no detectable alloying element redistribution in the cementite and ferritic matrix in ASIS 4340 steel was measured by atomic probe tomography after tempering at 325 °C for 2 hrs [29].

When the tempering temperature increases between 400 °C and 700 °C, cementite spherodises and coarsens with time [5], similar to the observation in plain carbon martensitic steels, where the aspect ratio for cementite can decrease from near 8 to approximately 1.5 combined with size increases [53]. The reported cementite coarsening rates in different steels (including plain carbon and alloyed steels) are shown in Figure 2-5:

1) The rates of coarsening for cementite in alloyed steels are much slower than those in plain carbon steels, Figure 2-5 (b), as the carbide forming substitutional elements with low diffusivities, like Mn, Cr and Mo, can partition into cementite when the equilibrium condition is approached [29, 41, 66-68], which retards the coarsening of cementite compared to that in plain carbon steels [68]. For example, Mn, Cr and Mo have all been detected to partition into elliptical cementite in a AISI 4340 steel tempered at 575 °C for 2 hrs [29]. Therefore, the partitioning and diffusion of alloying elements, such as Mn, Cr, Mo and Si, dominates the coarsening of cementite [68, 69].

2) The coarsening for inter-lath cementite is quicker than that for intra-lath cementite tempered at high temperatures, for example Figure 2-5 (a) for the Fe-0.45C-0.22Si-0.62Mn-0.004P-0.0038S steel, due to the faster solute boundary diffusion. The diffusivities for substitutional elements (i.e. Mn, Mo and Cr, which enrich cementite

during tempering) differ by orders of magnitude in different regions (i.e. matrix / volume(V) diffusion), low-angle grain boundary (LAGB) and high-angle grain boundary (HAGB)), ranking as $D_{HAGB} > D_{LAGB} > Dv$, where the diffusivity spectrum for substitutional elements in metals is shown in Figure 2-6.

3) The intra-lath cementite normally dissolves first when the secondary carbides start precipitating, whereas the inter-lath cementite still persists, such as that in a Fe-0.1C-1.99Mn-1.60Mo steel where cementite within the lath has dissolved after 100 hrs tempering at 600 °C when secondary Mo_2C precipitates, but it still persists along the lath/grain boundary [57].

4) The coarsening of cementite can also be influenced by tempering temperature and time, Figure 2-5 (a). The higher the temperature, the faster the rate of coarsening for cementite, due to the quicker solute diffusion at higher temperatures [67, 70].

The dislocation recovery continues in this tempering stage [5, 41, 58], e.g. in a 12% Cr steel tempered at 750 °C where the dislocation density decreases from 0.86×10^{-14} m^{-2} after 1 hour tempering to 0.09×10^{-14} m^{-2} after 100 hours tempering [58]. In addition, the matrix lath structure is retained for low carbon alloyed steels in this tempering stage [1, 71], which is quite similar to that observed in plain carbon steels. The morphology of the typical lath structure can even remain quite fine when tempering for several hours, as the alloying elements enriched cementite particles pin the lath boundaries and contribute to the preservation of lath microstructures [41], i.e. in a Fe-0.19C-1.41Mn-0.29Mo-0.61V-0.0019B-0.033Ti tempered at 625 °C for 1 hr, or in a RQT-701 based steel tempered at 580 °C for 27 hrs or 600 °C for 4 hrs [1, 71].

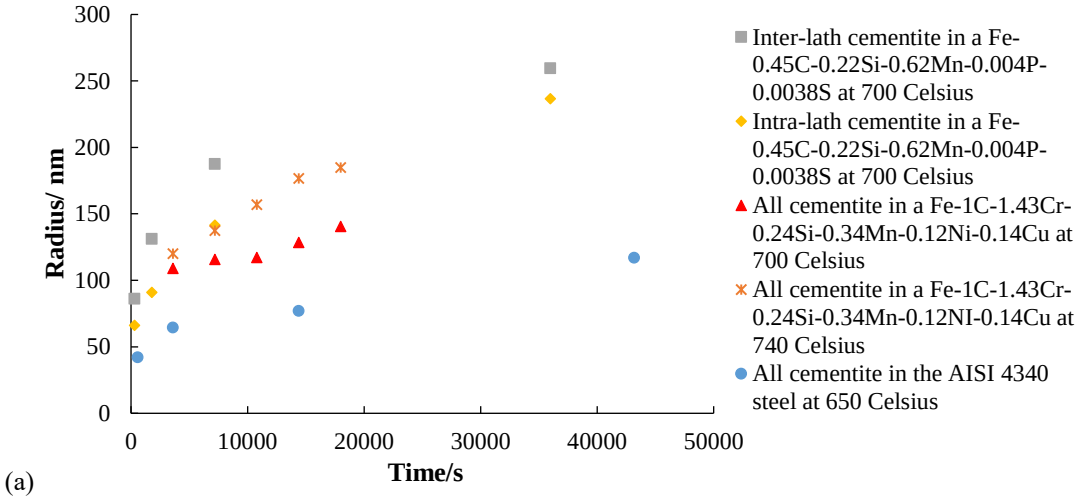

(a)

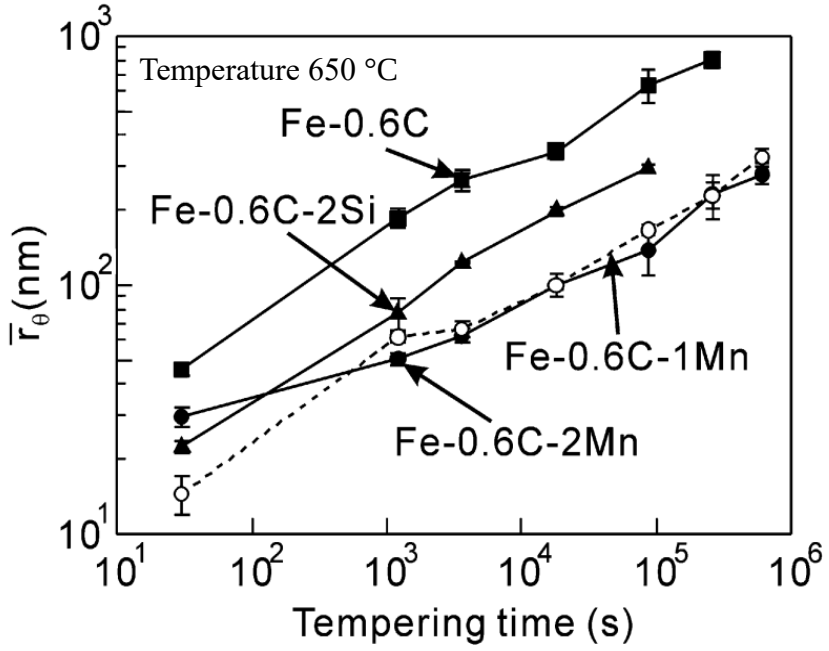

(b)

Figure 2-5. The cementite coarsening rates in different steels (plain carbon and alloyed steels) under different tempering conditions [59, 67, 68, 70, 72].

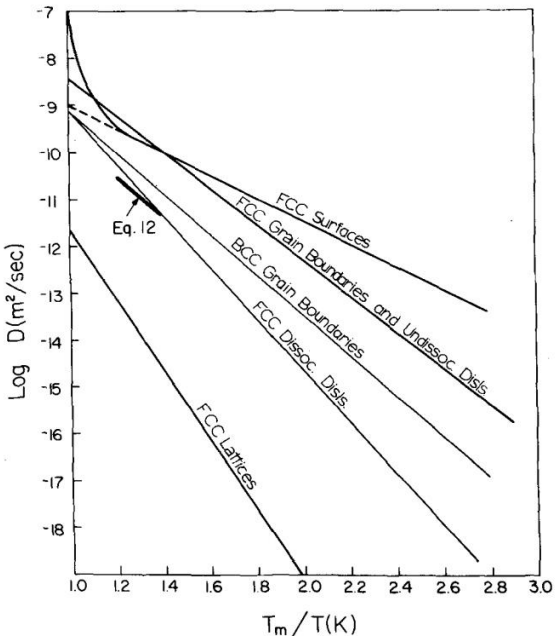

Figure 2-6. Diffusivity spectrum for substitutional elements in metals (derived by Gjostein curves [73]) represent the average data with a reduced reciprocal temperature scale used [74].

Finally, with strong carbide-forming alloying elements (e.g. Mo, Cr, V) in the steels, stable alloy carbides with substantially higher enthalpies of formation are promoted, which retain a smaller size than the iron carbides even during prolonged tempering; these are discussed fully below. The diffusivities for substitutional elements are several orders of magnitude lower than those for interstitial elements (such as carbon), hence, the required temperature range is approximately 500 - 700 °C and the tempering time is up to 4 hours for the precipitation of alloy carbides [5]. For instance, Cr-carbides (M_7C_3 and $M_{23}C_6$) combined with cementite were observed for the Fe-0.1C-2.55Cr-0.73Mo steel after tempering for 4 hrs at 617 °C [75].

Generally, there are two different categories of alloying elements added in the martensitic steels, non/weak carbide-forming alloying elements, such as Si and Mn, and

strong carbide-forming elements, like Cr, Mo and V. Hence, different alloying elements have different effects on tempering response and softening process.

1. Non/weak carbide-forming alloying elements

1) The effect of silicon on tempering response

The effect of Si on carbide precipitation during the tempering process in low carbon alloyed steels was first investigated by Owen [76]. Higher content of Si can stabilise the existence of ε/ε'-carbides, delay the transformation from ε/ε'-carbides to cementite [5, 77, 78] and retard the coarsening of cementite at relatively high tempering temperatures [5, 68]. For example, 2 wt % Si can lead to approximately 33% reduction on the average cementite radius increase in Fe-0.6C-2Si steel compared with plain carbon Fe-0.6C steel tempered at 650 °C for 1000 s, Figure 2-5 (b) [68]. Silicon normally partitions during tempering [68, 77, 79-81], where the rejection of silicon atoms from cementite into the ferrite matrix occurs during the initial coarsening of cementite [68, 77, 81]. A Si-enriched layer in the matrix (1 - 2 nm wide region) at the cementite/ferrite interface forms with Si concentration up to 12 wt % [81], which is regarded as the kinetic barrier for carbon to diffuse in/out of cementite retarding the cementite coarsening or dissolution processes.

Actually, Si can increase the hardness of tempered martensite at all tempering temperatures due to its contribution to solid solution strengthening, the inhibition of the transformation from ε/ε'-carbides to cementite and cementite coarsening, and the promotion of secondary alloy carbides [82]. Si partitions into solid solution in the matrix [68, 77, 79-81], contributing to the solid solution strengthening, as the solid solution strengthening coefficient for Si (about 83 MPa per 1 wt %) is much higher than that for

some of the substitutional alloying elements in steels, such as Mn, Mo and Cr [83]. In addition, the retardation of coarsening of cementite in high Si-containing steels results in a higher hardness being observed, i.e. 0.05% - 2% Si steels (Fe-0.35C-0.35Mn-(0.05-2)Si-5Cr-1.3Mo-0.4V steels) tempered at 450 and 500 °C [84, 85], Figure 2-7. As the coarsening of cementite is inhibited in high Si-containing steels, carbon is available for secondary alloy carbides to precipitate at relatively lower temperatures, resulting in a shift of the secondary hardening peak to slightly lower temperatures [77, 85]. For example, the secondary hardening peak for the 2% Si steel appears at around 550 °C compared with that in a 0.05% Si steel located at approximately 570 °C, Figure 2-7. However, the level of precipitation hardening does not change significantly in the 0.05% - 2% Si steels tempered at 600 °C, Figure 2-7 [85].

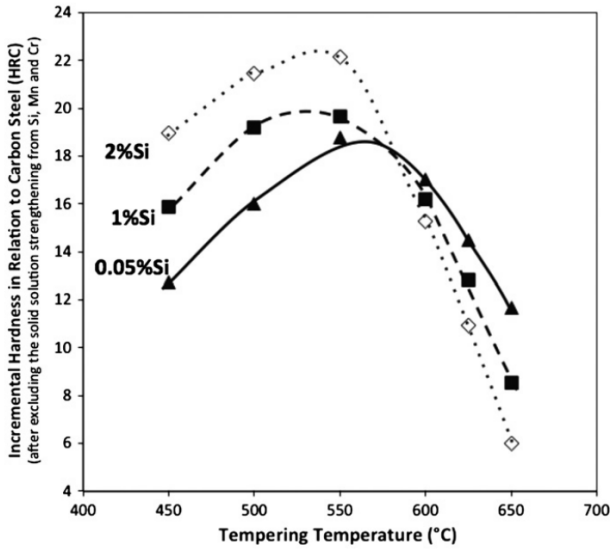

Figure 2-7. Precipitation hardening curves for 0.35C-(0.05-2)Si-0.35Mn-5Cr-1.3Mo-0.4V steels after a 2×2 hrs tempering [85].

2) The effect of manganese on tempering response

Manganese is a weak carbide-forming element, and it is normally dissolved in the matrix at lower temperatures, however, it gradually enriches cementite at higher temperatures [17, 68, 79, 86]. For example, in Fe-0.6C-1Mn and Fe-0.6C-2Mn steels tempered at 650 °C, the measured Mn concentration in cementite eventually remains constant after 2.8 hrs, indicating that the Mn concentration in cementite achieves the equilibrium condition, although the measured values are slightly lower than the equilibrium values from Thermo-Calc, Figure 2-8 [68]. Figure 2-5 (b) indicates that the coarsening of cementite has been greatly retarded in Mn or Si containing Fe-0.6C steels during tempering at 650 °C for the same time. The inhibition of coarsening of cementite by Mn is even more effective than that by Si at this temperature as the partitioning effect of Mn from the matrix to cementite plays a significant role in slowing down the cementite coarsening process [68]. The effect of Mn on the resistance of softening in Mn-containing Fe-0.2C steels during tempering at different temperatures is shown in Figure 2-9. The softening retardation by Mn is very small at low temperatures such as 204 °C, as the temperatures are too low for Mn to be incorporated into the cementite. However, the retardation increases as the temperature increases, such as 592 °C or 649 °C, principally due to the fact that Mn can diffuse and partition into cementite particles at the higher temperatures, which retards the coarsening of cementite, resulting in a finer and more numerous carbide population, finally leading to a higher hardness [82].

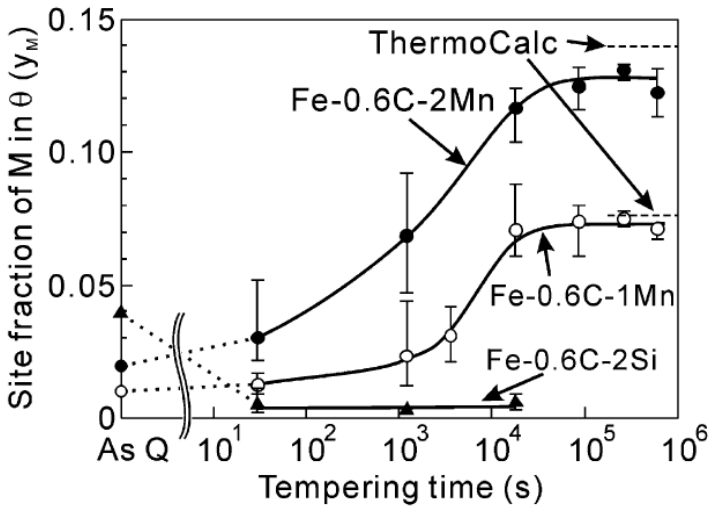

Figure 2-8. The concentrations of Mn and Si in cementite for Fe-0.6C steels with different contents of Mn and Si tempered at 650 °C, where site fraction M in cementite $Y_M=X_M/(X_M+X_{Fe})$, X_M and X_{Fe} are the atomic fractions of an alloying element and iron respectively [68].

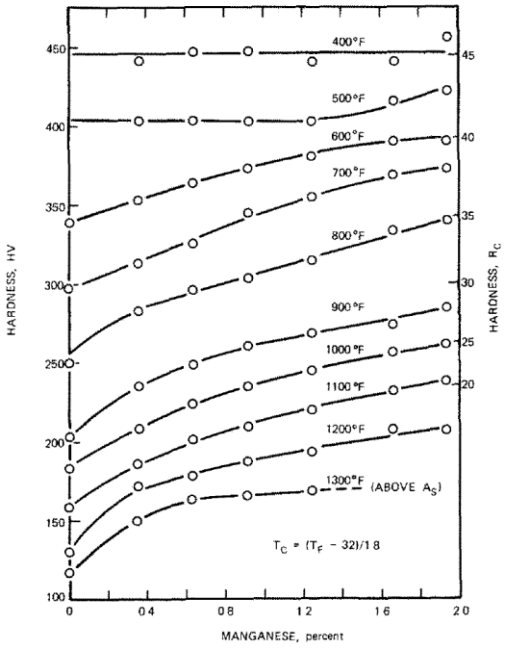

Figure 2-9. Hardness of tempered martensite in 0.2 wt % carbon steels containing different amounts of manganese [82].

2. Strong carbide-forming alloying elements

As discussed previously, cementite can be enriched with alloying elements, such as Cr and Mo, which retard the cementite coarsening behaviour. Also, the presence of the strong carbide-forming elements (Cr, Mo and V) can promote the formation of stable and fine alloy carbides, where a relatively coarser cementite dispersion is replaced by a much finer alloyed carbide dispersion, resulting in retardation of the loss of hardness from coarsening and promoting secondary hardening [17]. The greater the amount of alloying elements present in the steel, the higher hardness of the steel compared with a plain Fe-C steel, as seen in Figure 2-10.

Table 2-5. Five stable alloy carbides observed during tempering processes [5, 7, 87-90]

(The underlined elements are the predominant elements in the alloy carbides)

Types of alloying carbides	Possible alloying elements contained in the carbides	Shape	Crystal structure
MC (M_4C_3)	<u>V</u>, Mo, Fe, Cr	Disk/plate-like	FCC
M_2C	<u>Mo</u>, V, Fe, Cr	Fine needles	HCP
M_6C	<u>Mo</u>, V, Fe, Cr	Foil-shape	FCC
$M_{23}C_6$	<u>Cr</u>, Fe, V, Mo	Rod-like	Cubic(complex)
M_7C_3	<u>Cr</u>, Fe, V, Mo	Fine rod-like	HCP

Five stable alloy carbides related with Cr, Mo and V can form during tempering, listed in Table 2-5. MC (M_4C_3) and M_2C precipitates are typically the next types of carbides

to form after cementite and primarily contribute to secondary hardening. MC is promoted in V-containing steels with as little as 0.1 wt % V, and it often becomes substoichiometric composition due to the carbon deficiency in the carbide, being frequently nearer M_4C_3 [5, 91, 92]; hence, M_4C_3 is also denoted by MC in the literature [93]. The actual chemical compositions of MC (M_4C_3) and M_2C vary for different steels depending on the alloying elements present, Table 2-5.

MC is more stable and thermodynamically determined to be the equilibrium carbide in multicomponent steels, i.e. Cr-Mo-V steels with ≥ 0. 1 wt % V [94, 95], Figure 2-14 and Figure 2-15. The morphology of MC carbides is normally reported to be disk/plate-like [57, 93, 96, 97]. The crystallographic orientation relationship between MC and the ferritic matrix obeys the Baker and Nutting OR [98].

Baker and Nutting OR [98]: $(100)_{MC}$ // (100)α, $[010]_{MC}$ // [011]α, $[001]_{MC}$ // $[01\bar{1}]$α.

MC carbides normally precipitate on the {001}α habit plane in tempered martensitic steels [57, 93, 96], and preferentially form on dislocations, grain/subgrain boundaries and in-situ cementite/matrix interfaces [93, 96, 99, 100]. The coarsening of MC carbides is quite slow, thus, these finer MC particles remain even during a prolonged tempering process [101], resulting in the strongest effect on the resistance to softening and highest hardness increase compared to other strong-carbide forming elements, i.e. Mo and Cr, with the same content, Figure 2-10 [82].

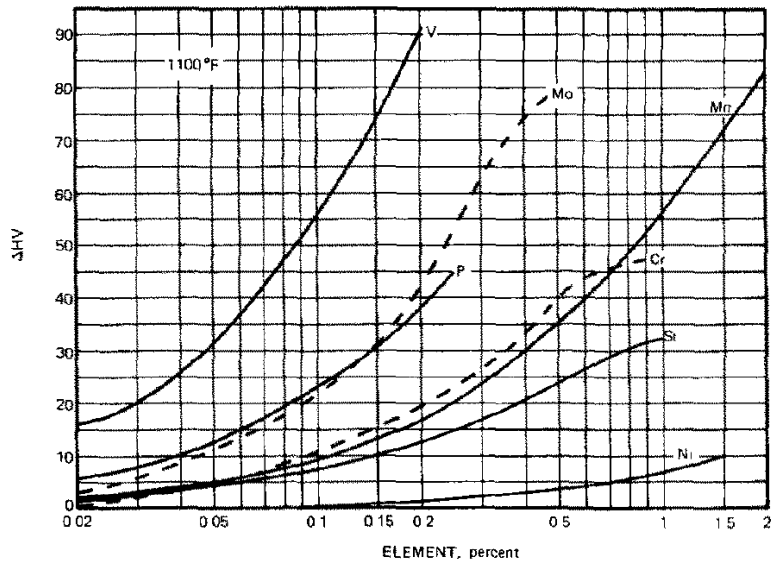

Figure 2-10. Effect of alloying elements on the hardness of martensite tempered at 592°C for 1 hr in 0.15-0.19)C-(0.3-0.5)Mn steels with different additions of alloying elements [82].

M_2C carbides (Mo-enriched carbides) are stable carbides formed in ternary Fe-C-Mo steels with lower Mo-to-C content ratio (such as Fe-0.33C-0.65Mo-0.93Cr-0.20V steel [102]) at relatively lower temperatures (≤ 600 °C); however, higher Mo-to-C content ratio (such as Fe-0.38C-1.54Mo-1.23Cr-0.21V steel [102]) encourages the formation of another equilibrium Mo-enriched carbides M_6C at comparatively higher temperatures (i.e. 700 °C) after extended tempering [101, 103]. The precipitation sequence is normally cementite → M_2C → M_6C or cementite → M_6C [104, 105]. M_2C carbides generally precipitate as smooth fine needles (aspect ratio 9 - 10) and grow along the three equivalent <001>α directions of ferrite [96, 102, 106, 107]. Pitsch-Schrader OR [108], which has initially been observed for ε-carbides when tempered in twinned martensite [51], and Wang-Dunlop OR [106] have been identified between M_2C and the tempered martensitic matrix [96, 106].

Pitsch-Schrader OR [108]: $(0001)_{M2C}//(011)_{\alpha}$, $(1\bar{1}00)_{M2C}//(0\bar{1}1)_{\alpha}$, $[11\bar{2}0]_{M2C}//[100]_{\alpha}$; Wang-Dunlop OR [106]: $(0001)_{M2C}//(021)_{\alpha}$, $[11\bar{2}0]_{M2C}//[100]_{\alpha}$, $(\bar{1}100)_{M2C}//(01\bar{2})_{\alpha}$.

The Pitsch-Schrader OR has generally been observed after relatively long time tempering, e.g. in a Fe-0.23C-2.65Mo steel tempered at 550 °C for 200 hrs [96]. However, the Wang-Dunlop OR, which has a 2° deviation from the Pitsch-Schrader OR, has only been identified in steels with higher carbon contents after short tempering times at lower temperatures, such as a Fe-1.3C-0.62Si-0.28Mn-4Cr-4.8Mo-6.3W-0.41Co-3.1V steel tempered at 560 °C for 1 hour [106], due to the high tetragonality of the martensitic matrix, leading to small rotations from the Pitsch-Schrader OR [106]. M_2C can not only precipitate at the pre-existing cementite/matrix interfaces in the lath but also on the low/high-angle grain boundaries with dissolution of cementite supplying soluble Mo to constitute M_2C carbides as Mo can enrich cementite when tempering at high temperatures [57, 109]. As shown in Figure 2-11, M_2C also contributes to the resistance to softening and occurrence of secondary hardening: the higher the content of Mo, the more obvious the secondary hardening peak present due to the fine M_2C (Mo-enriched carbides) replacing the coarser cementite particles [110]. In addition, M_6C carbides appear after a very long time tempering at higher temperatures, such as in a Fe-0.12C-2.57Cr-0.95Mo-0.34V-0.71Mn-0.34Si steel tempered at 660 °C for 150 hrs [95]. The orientation relationship between M_6C and the matrix is reported as $(100)_{M6C}//(100)_{\alpha}$, $(011)_{M6C}//(011)_{\alpha}$, $(0\bar{1}1)_{M6C}//(0\bar{1}1)_{\alpha}$ in different steels [93, 100, 111]. The precipitation of M_6C carbides can occur either on the existing carbides, such as M_2C carbides or cementite, or sometimes they form as individual particles on low/high-angle grain boundaries (i.e. lath boundaries and prior austenite grain boundaries) [95, 100].

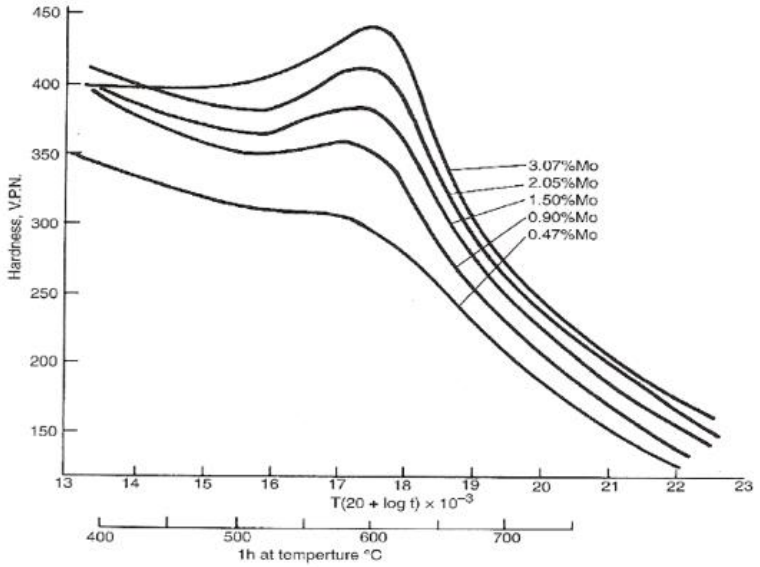

Figure 2-11. Effect of molybdenum content on the secondary hardness as a function of tempering temperature in a 0.1 wt % carbon steel tempered for 1 hr [110].

In Cr-containing steels, $M_{23}C_6$ and M_7C_3 can either directly transform from cementite as Cr can take the place of iron atoms in cementite if there is sufficient soluble Cr in solid solution or precipitate after M_2C carbides in Cr-Mo-containing steels [6]. The precipitation sites for $M_{23}C_6$ and M_7C_3 are similar to those for M_2C carbides (at the cementite/matrix interface and on the low/high-angle grain boundaries) [100, 101, 112-114]. The actual chemical compositions of $M_{23}C_6$ and M_7C_3 depend on the bulk chemical composition for different alloyed steels, Table 2-5. The free energy of formation of M_7C_3 and $M_{23}C_6$ are similar [101], therefore, comparatively small bulk chemical composition changes can significantly influence the stability of these two Cr-enriched carbides, finally leading to different precipitation sequence. There are two precipitation sequences reported in Cr-containing steels after long time tempering [7, 75, 88, 95, 101, 105, 113, 114]:

(a) Cementite $(FeCr)_3C \rightarrow M_7C_3 \rightarrow M_{23}C_6$ or Cementite $(FeCr)_3C \rightarrow M_{23}C_6$

(b) Cementite $(FeCr)_3C \rightarrow M_{23}C_6 \rightarrow M_7C_3$ or Cementite $(FeCr)_3C \rightarrow M_7C_3$

The first situation, (a), normally occurs in steels with higher Cr contents [113, 114], such as 12Cr1MoV steel where $M_{23}C_6$ is the most stable carbide [114]. However, the second precipitation sequence, (b), takes place in Cr-Mo-V steels with lower Cr contents [7, 75, 88, 95, 101, 105], such as 1Cr-Mo-V or 2.5Cr-(0.7-0.95)Mo-(0-0.35)V steels where M_7C_3 carbides finally form as the equilibrium carbides during long-term tempering (thousands hours) [75, 95, 105]. The orientation relationship between $M_{23}C_6$ and the ferritic matrix has been reported as $(011)_{M23C6}$ // $(001)\alpha$, $(\bar{1}1\bar{1})_{M23C6}$ // $(110)\alpha$, $(\bar{2}\bar{1}1)_{M23C6}$ // $(\bar{1}10)\alpha$ [100, 101]; whereas, the orientation relationship between M_7C_3 and the ferritic matrix obeys: $(0001)_{M7C3}$ // $(011)\alpha$, $(1\bar{1}00)_{M7C3}$ // $(100)\alpha$, $(11\bar{2}0)_{M7C3}$ // $(01\bar{1})\alpha$ [112, 113]. Due to the formation of the above two Cr-enriched carbides in Cr-containing steels, the softening process varies in steels with different Cr contents during tempering. Figure 2-12 shows the hardness changes in Fe-0.35C steels with different Cr contents during tempering [115]. In low Cr steels (<0.5% Cr), continuous softening apparently occurs in the temperature range of 400 - 700 °C, whereas secondary hardening peaks show up in the steels with Cr contents 2 - 4% due to the formation of Cr-carbides (reported to be M_7C_3). However, there exists a plateau of hardness for 12% Cr steel, which suggests that secondary hardening starts earlier, but coarsening of the Cr-carbides proceeds at a similar rate to that in the steels with lower Cr contents.

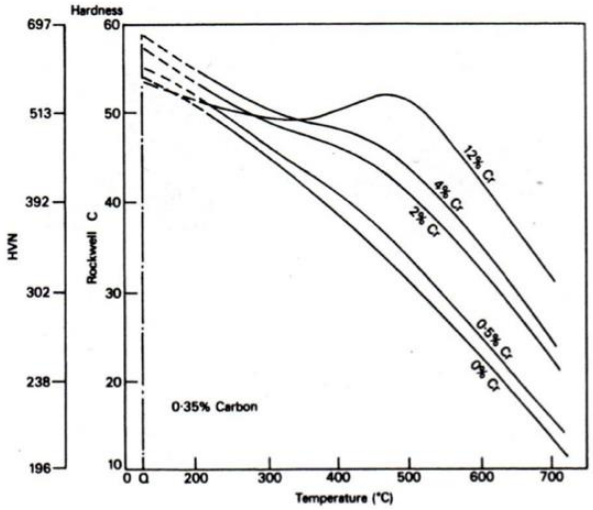

Figure 2-12. Effect of chromium on the secondary hardening as a function of tempering temperature in a 0.35 wt % carbon steel tempered for 1 hr [115].

In Cr-Mo-containing steels, the carbide evolution sequence is different from that in ternary Fe-C-Mo or Fe-C-Cr steels. As shown in Figure 1-1 (Baker-Nutting diagram for Cr-0.5Mo steels), in low Cr-containing steels, such as 0.6Cr-0.5Mo steel, M_2C is the only carbide precipitated even after long time tempering at 600 °C, and it starts to form after tempering for only 1 hour [7]. In the 1.1Cr-0.5Mo steel, the carbide evolution sequence is $M_3C \rightarrow M_3C + M_2C \rightarrow M_3C + M_2C + M_7C_3$ when tempered at 600 °C for 100 hrs [7], which is the same as that in a 2.25Cr-1Mo steel tempered at 600 °C for up to 1000 hours, Figure 2-13 [116]. Higher contents of chromium give an earlier precipitation of M_7C_3 compared to M_2C [7].

In addition, in Cr-Mo-V-containing steels [75, 94, 95, 117], the carbide evolution sequence is affected not only by the individual alloying elements but also by the synergistic action of these elements as a function of tempering time and temperatures, Figure 2-14 and Figure 2-15:

[1] In Figure 2-14, the bulk V/Mo ratio influences the formation of M_2C: the higher the bulk V/Mo ratio, the lower the probability of M_2C precipitation. For example, the precipitation sequence in steel 1 with very low V/Mo ratio is $M_3C \rightarrow M_3C + M_2C + M_{23}C_6 + M_7C_3 \rightarrow M_2C + M_{23}C_6 + M_7C_3 \rightarrow M_7C_3$ tempered at 600 °C. However, the carbide evolution sequence for steel 3 with higher V content is varied to $M_3C \rightarrow M_3C + M_7C_3 + M_{23}C_6 \rightarrow M_7C_3 + MC \rightarrow M_6C + M_7C_3 + MC$ tempered at the same temperature where MC forms as one of the equilibrium carbides without M_2C precipitation [75, 95], which remains consistent with the stable carbides (MC, M_7C_3 and $M_{23}C_6$) present in the Fe-0.12C-1.0Cr-0.3Mo-0.25V-0.2Ni-0.3Si-0.4Mn steel (higher V/Mo ratio) tempered at 560 °C for 200 hrs [117].

[2] M_7C_3 is stable in steels with lower Cr contents, whereas $M_{23}C_6$ is stable in steels with relatively higher Cr contents [94], Figure 2-15, which remains consistent with the two precipitation sequences for Cr-containing steel (discussed in previous paragraph).

[3] The equilibrium carbide M_6C forms in steels with relatively higher Mo contents, such as in the Fe-0.15C-1.5Cr-1.05Mo-0.3V-0.4Ni-0.3Si-0.5Mn steel tempered at 560 °C for over 120 hrs [117]. Higher bulk V contents contribute to the earlier formation of M_6C [75, 95], Figure 2-14.

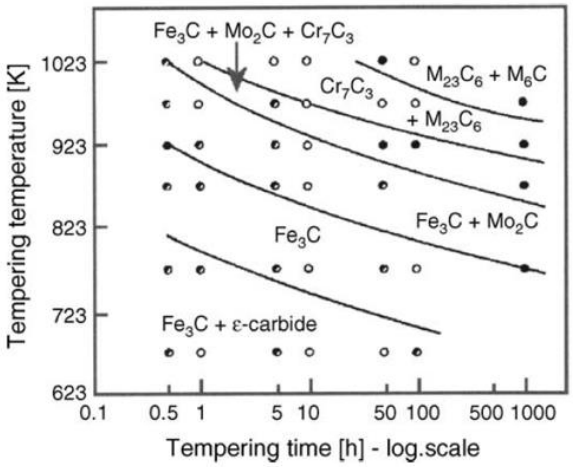

Figure 2-13. Baker-Nutting diagram showing evolution of carbides during tempering in 2.25Cr-1Mo steel [116].

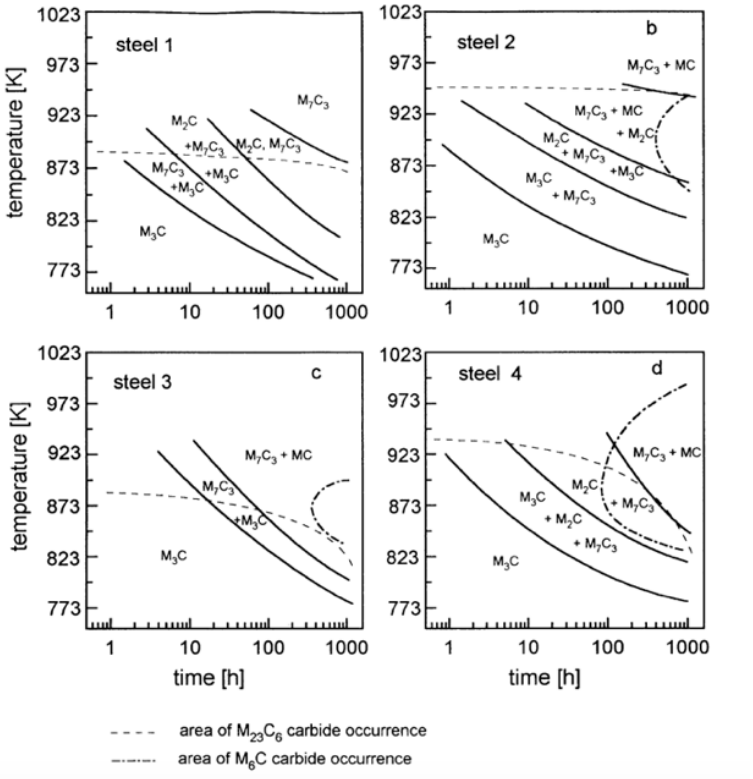

Figure 2-14. Time-temperature-precipitation diagram showing the evolution of carbides during tempering; steel 1: 0.09C-0.66Mn-0.32Si-**2.4Cr-0.02V-0.70Mo**; steel 2: 0.10C-0.66Mn-0.35Si-**2.55Cr-0.73Mo-0.12V**; steel 3: 0.10C-0.67Mn-0.27Si-**2.62Cr-0.32V-0.70Mo**; steel 4: 0.12C-0.71Mn-0.34Si-**2.57Cr-0.95Mo-0.34V** [95].

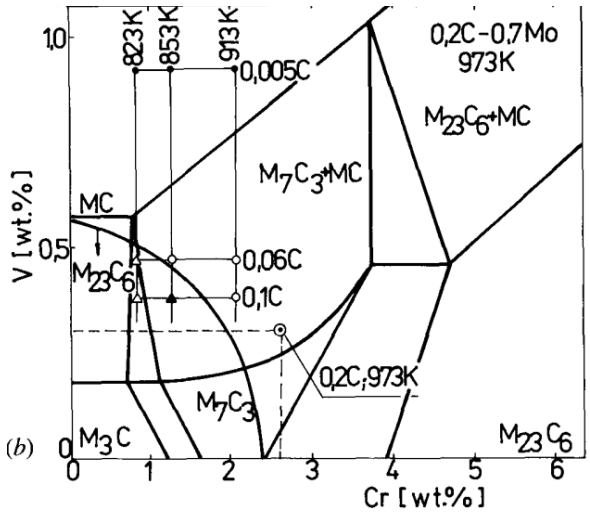

Figure 2-15. Carbide constitution diagram for 0.2C-0.7Mo-xCr-yV steels tempered at 700 °C [94].

2.3 Summary

In summary, auto-tempering occurs during quenching in low carbon alloyed steels, and either transition iron carbides (ε-carbides or ε'-carbides) or cementite have been observed due to different Ms temperatures and cooling rates. Cementite firstly forms at the expense of the pre-existing transition iron carbides and the retained carbon in solid solution. With an increase of tempering temperatures and times, cementite starts to undergo coarsening, where inter-lath cementite normally coarsens faster than intra-lath cementite due to more rapid solute boundary diffusion. Alloying elements play a significant role in determining the carbide precipitation and coarsening rates during tempering. Silicon can stabilise the presence of transition iron carbides (ε-carbides or ε'-carbides), delay the formation and coarsening of cementite, and promote the precipitation of secondary alloy carbides, resulting in a shift in the secondary hardening peak to the lower temperatures. Manganese, molybdenum and chromium can enrich cementite particles and slow down the rate of coarsening for cementite to maintain good mechanical properties when tempering at high temperatures. In addition, molybdenum and vanadium have a larger tendency to form fine M_2C (Mo-carbides) and MC (V-carbides) depending on the bulk V/Mo ratio, which contribute to secondary hardening. The precipitation sequences for Cr-Mo-V steels with lower bulk V/Mo ratio are expected to be $M_3C \rightarrow M_3C + M_2C \rightarrow M_3C + M_2C + M_{23}C_6 + M_7C_3 \rightarrow M_2C + M_{23}C_6 + M_7C_3 \rightarrow M_7C_3$. In Q&T steels, such as S690-based steels containing approximately 0.8 wt % Cr, 0.5 wt % Mo and 0.05 wt % V, the coarsening of cementite is expected to be retarded and secondary carbides are reported to precipitate. Figure 2-16 shows that the secondary hardening peak is present after tempering for around 2 - 3 hours at 600 °C in

a S690 steel, which is slightly different from the widely reported 2 wt % Cr-steel or 0.5 wt % Mo-steel, Figure 2-11 and Figure 2-12, where secondary hardening occurs after tempering for 1 hr in the temperature range 400 - 600 °C. In S690-based steels, secondary MC (V-carbides) may be inhibited as the bulk V/Mo ratio (V content) is relatively low and M_7C_3 (Cr-precipitates) might also be hindered with less than 1% chromium content in the matrix during the early stages of tempering; whereas finer, smooth and needle-like M_2C may be promoted, leading to the retardation of softening. However, no detailed investigation has been systematically carried out to explain the carbide evolution and coarsening behaviours in S690-based steels during tempering to establish the precipitation - property relationship.

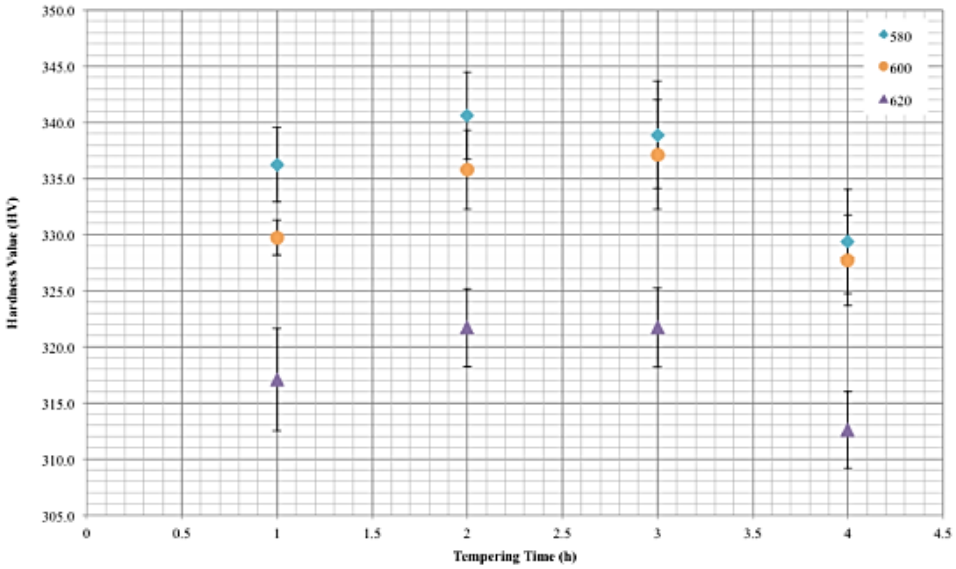

Figure 2-16. Vickers Hardness with standard deviation tempered at 580 °C, 600 °C and 620 °C between 1 and 4 hours for a S690 (Fe-0.17C-0.29Cr-0.53Mo-0.034V) steel [1].

Chapter 3 Carbide development and kinetic models for coarsening of carbides during tempering

3.1 Carbide development during tempering

Carbide development during tempering normally involves nucleation, growth and coarsening (Ostwald ripening) processes. Heterogeneities, such as vacancies, dislocations and grain/sub-grain boundaries with higher free energy, are present in the as-quenched lath-martensite. Due to the high Ms temperatures in low carbon alloyed steels, heterogeneous nucleation of auto-tempered carbides on dislocations or grain/ sub-grain boundaries occurs during quenching. As reviewed in Chapter 2, transition iron carbides (ε-carbides or ε'-carbides) form during auto-tempering or in the first stage of tempering due to the structural similarity between the transition iron carbides and matrix with lowest lattice misfit [118], which indicates a smaller driving force (lower interfacial energy and strain energy) for nucleation compared to other competing pseudo-equilibrium or equilibrium phases. Cementite has also been found as auto-tempered carbides in low carbon alloyed steels with very high Ms temperatures (well above 400 °C) [27, 28, 30]. Cementite can be fully developed with the disappearance of transition iron carbides when tempering at approximately 300 °C for different times under para-equilibrium condition, where only carbon from solid solution has been detected to diffuse [5, 29, 65]. The growth of cementite in this stage is controlled by the diffusion of carbon from solid solution, which is regarded as a non-equilibrium process, where Fick's second law is applied to mathematically predict the growth rate [119]. The growth of precipitates leaves a dispersion of precipitates embedded in the matrix with varied sizes,

finally resulting in the excess surface energy present in the system. With the tempering temperature increasing to 400 - 700 °C, cementite undergoes spheroidisation and coarsening processes, where cementite changes to elliptical/spherical shape with increasing sizes. In the coarsening or Ostwald ripening process, the larger particles coarsen at the expense of the smaller ones [54, 55] with the overall interfacial energy decreasing as low as possible by eliminating interfaces to achieve thermodynamic equilibrium for the system; this leads to an increase in the average particle size and decrease in number density [57]. Substitutional elements (e.g. Mn, Mo and Cr) have been detected to partition into cementite during coarsening (e.g. AISI 4340 steel tempered at 575 °C for 2 hrs) [29, 68] in low carbon alloyed steels when equilibrium is approached [41], where the diffusion of substitutional elements is the rate-controlling step for cementite coarsening. The diffusion coefficient for substitutional elements along the lath boundaries is a few orders of magnitude higher than that in the laths [74], therefore, the coarsening of inter-lath cementite occurs faster than that for intra-lath cementite. The direct driving force for coarsening is the different solubility at the precipitate/matrix interfaces under local equilibrium condition based on the Gibbs-Thomson equation [120, 121], as given in Equation 3-1. The concentration at the large particle/matrix interface is lower than that at the small particle/matrix interface, which leads to diffusional mass transfer from small particle region to large particle region.

$$C_\rho = C_0\left(1+\frac{2\lambda V_m}{\rho RT}\right) \qquad \text{Equation 3-1}$$

Where C_ρ is the solubility at the interface with the radius of curvature ρ; C_0 is the equilibrium solubility at a planar interface in the matrix, λ is the precipitates/matrix

interfacial energy; V_m is the molar volume of the precipitates; R is the ideal gas constant, and T is the absolute temperature.

The dislocation number density decreases during tempering in the lath martensite [5, 41, 58], whereas the martensite lath can still remain with inter-lath cementite pinning the lath boundary. In low carbon alloyed steels containing Mo, Cr and V, the coarsening of cementite can be accompanied by the precipitation of secondary alloy carbides, e.g. in a Fe-0.1C-1.99Mn-1.60Mo steel, the inter-lath cementite coarsens with the precipitation of secondary Mo_2C carbides within the laths from 10 hrs tempering at 600 °C [57]. Generally, the coarsening of intra- and inter-lath carbides results in a decrease in hardness in tempered martensite. Therefore, it is important to carry out cementite coarsening predictions during tempering in low carbon alloyed steels to determine the precipitation hardening contribution to hardness changes. The reported kinetic models for coarsening of carbides in the matrix and on the low/high-angle grain boundaries during tempering are reviewed in the following sections.

3.2 Kinetic models for the coarsening of carbides during tempering

3.2.1 Theoretical models for coarsening of carbides in a matrix through volume solute diffusion

1. LSW theory for spherical/ near spherical carbide coarsening in a matrix

The LSW theory, established by Lifshitz and Slyozov [122], and Wagner [123], has been used to theoretically analyse the coarsening of fixed spherical particles dominated by volume diffusion in the matrix. There are several assumptions for the model [121-124]:

1) The coarsening of fixed spherical particles in the matrix is controlled by the long range diffusion of solute atoms under steady-state conditions;

2) The volume fraction of particles is negligible and the inter-particle separations are infinitely large compared to the particle radius to ensure that no elastic interactions exist between particles, Figure 3-1 (a).

3) The particle size distribution should achieve the steady-state LSW distribution where the largest radius is 1.5 times the average radius, to mathematically maintain the stationary and self-similar coarsening process.

The LSW model is a “mean-field” description of a particle’s growth [121], in which the coarsening rate is independent of the surroundings with an ignorance of neighbouring particle sizes. The solute concentration profile around any of the spherical precipitates is shown in Figure 3-1 (b). The radial solute concentration inside the spherical particle ($R<r$) is constant and assumed to be N_β; at the particle/matrix interface ($R=r$), the solute concentration is based on the particular particle radius r; the solute concentration in the matrix is associated with the average particle radius $\bar{r}$ ($R>>r$). The quantitative LSW

equation for the coarsening of spherical particles after achieving the steady size distribution is

$$\bar{r}_t^{\,3}-\bar{r}_0^{\,3}=Kt$$

$$K=\frac{8D\lambda N_e V_m}{9RT} \qquad \text{Equation 3-2}$$

Where $\bar{r}_0$ is the initial average radius for particles; D is the atom diffusion coefficient in the matrix; λ is the particle/matrix interfacial energy; N_e is the atom solubility in solid solution for a plane interface; V_m is the molar volume of the particles; R is the ideal gas constant, and T is the absolute temperature. The LSW equation shows a growth law $r \sim t^{1/3}$ for spherical particles in a solid solution.

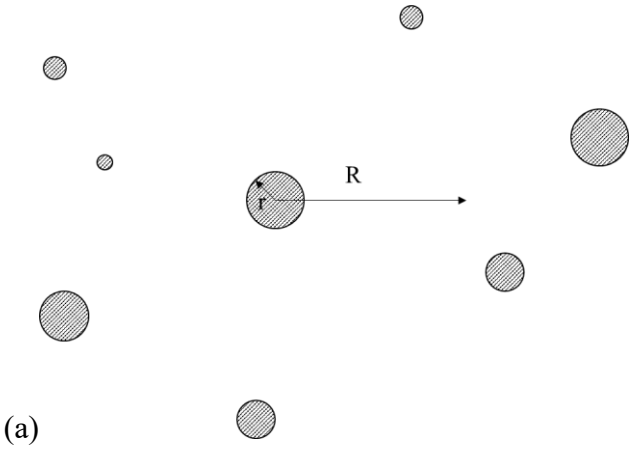

(a)

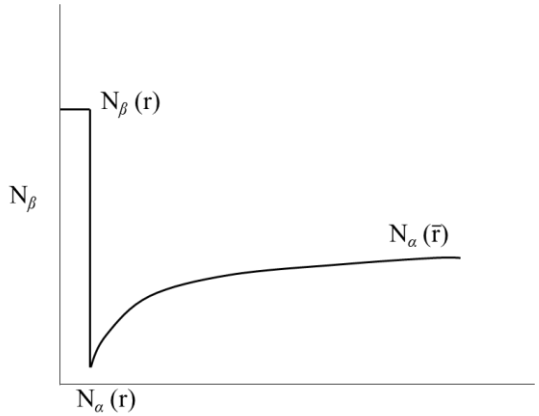

(b)

Figure 3-1. (a) An array of precipitates around a particular precipitate of radius r, and the separation between particles infinitely large compared with particles radius; (b) The concentration profile around the particular precipitate r [120].

In different tempered martensitic steels [68-70, 125, 126], the average radius of cementite in the matrix is proportional to the cube root of tempering time, where the exponents for the coarsening of cementite in these steels are in the range 0.30 - 0.34, which shows a qualitative agreement with LSW theory. However, the experimental rate constants (K) deviate from the theoretical values calculated by Equation 3-2 in different steels. There are several reasons for this:

I. Different solute atom diffusion for cementite coarsening. In Fe-C binary systems, the carbon diffusion coefficient has been reported to give a larger coarsening rate prediction for cementite by one to two orders of magnitude compared to experimental data [127]. Therefore, the coarsening of cementite is considered to be controlled by a coupled diffusion mechanism, where the carbon diffusion coefficient was replaced by a coupled diffusion coefficient. The local volume varies around the cementite particles during coarsening in Fe-C systems due to the molar volume differences for ferrite and cementite, resulting in the occurrence of volume constraint based on the

Kirkendall principle. Assuming the volume constraint is totally compensated by the diffusion of iron, Oriani [55] has proposed an effective coupled diffusion coefficient, Equation 3-3. Similarly, the local composition ratio should also be sustained during diffusional-controlled coarsening, which is referred as composition constraint. Li et al. [128] have developed a coupled diffusion analysis due to the composition constraint, Equation 3-4.

$$D_V=\frac{2V_C D_C D_{Fe}}{V_C D_{Fe}+n_C V_C^2 D_{Fe}+V_{Fe} D_C-V_{Fe}^2 n_{Fe} D_C} \quad \text{Equation 3-3}$$

$$D_{com}=\frac{n_{Fe} D_c D_{Fe} V_{Fe}}{n_{Fe} D_{Fe} (V_{Fe})^2+n_c D_c (V_c)^2}\left(V_{Fe}+\left(\frac{n_c}{n_{Fe}}\right) V_c\right) \quad \text{Equation 3-4}$$

Where n_{Fe}, n_C are the concentrations of iron and carbon in ferrite, respectively; D_{Fe}, D_C are the diffusion coefficients of iron and carbon in ferrite, respectively; V_{Fe} is the atomic volume in ferrite; and V_C is the difference in molar volume of Fe between ferrite and cementite.

In Fe-0.24/ 0.42/ 0.79 C binary steels [125], the coupled diffusion coefficients (D_v or D_{com}) have been used to calculate the cementite coarsening rates, however, the non-steady state size distribution can still lead to deviations from experimental data. In addition, in the Fe-C-M (M stands for the substitutional elements, e.g. Mn, Mo, Cr) systems, if the alloying elements can be strongly partitioned into cementite, the diffusion of alloying elements is regarded as the rate-controlling step during cementite coarsening. Hence, Björklund et al. [129] have established the cementite coarsening rate equation in Fe-C-M systems based on the cubic growth law:

$$\bar{r}^3 - \bar{r}_0^3 = \frac{8\lambda V_m^{cem} D_M^{\alpha}}{27RT(1-K_M)^2 u_M^{\alpha}} t$$ Equation 3-5

Where D_M^{α} is the diffusion coefficient of the alloying element M in ferrite; V_m^{cem} is molar volume of the cementite particles; λ is the particle/matrix interfacial energy; u_M^{α} is the solubility of M in ferrite matrix; K_M is the distribution coefficient for the element between cementite and ferrite, and can be defined as $K_M=(u_M^{cem}u_{Fe}^{\alpha})/(u_M^{\alpha}u_{Fe}^{cem})$, where u_{Fe}^{cem} is the solubility of Fe in cementite, u_M^{cem} is the solubility of M in cementite, u_{Fe}^{α} is the solubility of Fe in ferrite matrix; R is the ideal gas constant, and T is the absolute temperature.

This model has been checked for the coarsening of cementite in a Fe-C-Cr steel, where Cr partitions into cementite, Figure 3-2 [126]. The experimental cementite coarsening rate shows a very good agreement with the calculation tempered at 700 °C, where the equlibrium partitioning of chromium between ferrite and cementite is achieved. However, the observed coarsening rates at 500 and 600 °C are much faster than the calculated ones probably due to the chromium-diffusion and carbon-diffusion mixed-controlled coarsening at that temperature [126].

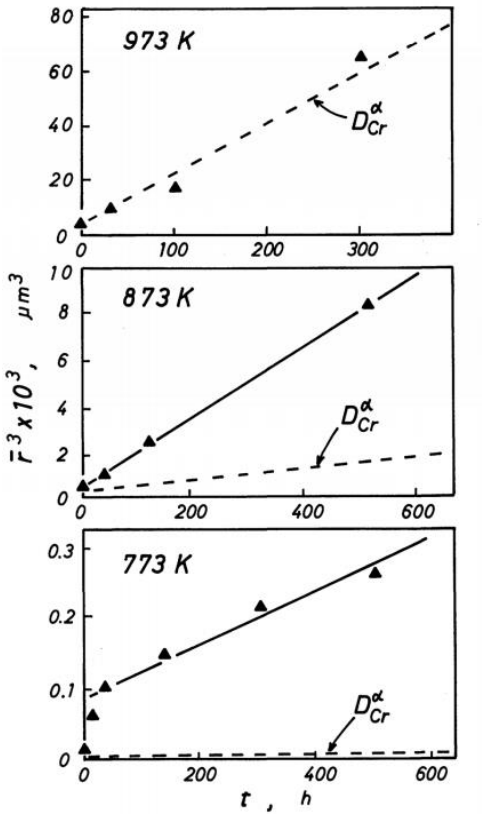

Figure 3-2. The coarsening of cementite in a Fe-C-Cr steel. The solid line represents the experimental relationship between $\bar{r}^3$ and tempering time t; the broken line is the calculated coarsening rate for cementite using Equation 3-5 with D_{Cr} [126].

II. Particle volume fraction. The coarsening rate constant increases with an increasing volume fraction, even at very small values, although the qualitative growth law that the mean radius linearly changes with $r \sim t^{1/3}$ has been maintained [130]. A higher particle volume fraction can result in the occurance of diffusional interaction between particles, finally leading to the disagreement of coarsening rate constant between LSW theory and the experimental data. Actually, modifications of LSW theory with the consideration of non-zero volume fraction for multiparticle coarsening systems have been made; however, these modifications can still not predict the coarsening of spherical particles sensibly in different systems compared with expeimental data

[130-135], such as giving an inconsisitent prediction compared with experimental observation for the coarsening of Ni_3Al precipitates in Ni-Al system using the modified LSW models [131, 132].

III. The time-independent size distribution. Experimental cementite particle size distributions during coarsening in different steels (i.e. binary Fe-C steels and Fe-0.33C-1.03Mn-0.27Si-0.0005B steel) [69, 125] have been reported to be broader and skewed at smaller size ranges with a cut-off size $2\bar{r}$ ($\bar{r}$ is the average radius), compared to the assumed asymptotic steady-state size distribution $1.5\bar{r}$. Normally, a narrow size distribution coarsens slowly, whereas a wide distribution coarsens quickly [120]. In Fe-C binary steels, the smaller the departure from the steady-state size distribution, the lower the errors in the predicted coarsening rates tempered at 600 - 700 °C with coupled diffusion coefficient [125].

In summary, a qualitative growth law $r \sim t^{1/3}$ for coarsening of spherical or near spherical particles in the matrix has been proposed in the LSW theory, however, the theoretical quantitative rate constant cannot match the experimental observation due to the following reasons - different solute diffusion between particles, particle volume fraction and size distribution. Although modifications of LSW theory have been proposed, the prediction still deviates from the experimental data. Therefore, it is inappropriate to use the LSW theory and reported modifications to quantitatively predict the coarsening of carbides (i.e. elliptical cementite) in the matrx in steels during tempering.

2. Models for the coarsening of non-spherical (needle/plate/rod-shaped) carbides in a matrix

In some alloyed martensitic steels, non-spherical (needle/plate/rod-shaped) carbides with high aspect ratio (up to 10) form within the martensite laths and coarsen with time during tempering, such as cementite and M_2C (Mo-rich carbide). These non-spherical carbides can lead to a resistance to softening during tempering due to the increased interfacial area producing more barriers for dislocation motion. Two different situations have been observed to occur for these carbides during coarsening: one is carbide coarsening accompanied with spheroidisation; the other is carbide coarsening with the preservation of carbide shape. Based on the two observed conditions, different analytical models have been developed: Lee et al. [136, 137] model for coarsening of shape-preserving carbides within the laths in multicomponent steels with two or more kinds of substitutional element diffusing and Yamasaki and Bhadeshia's [57, 107, 138] model for the above two situations with constant composition in ternary steels with the volume diffusion of one sort of substitutional elements.

A. Lee, Allen and Grujicic model [136, 137]

Rod-like multicomponent secondary M_2C (M=Mo, V, Cr, W) carbides with very low volume fraction have been observed to precipitate and coarsen in the matrix in different steels (listed in Table 3-1) during tempering [136]. Due to its very low volume fraction (the maximum reported is less than 2.5 %), the qualitative growth law of the LSW theory, $\bar{r}^3-\bar{r_0}^3=Kt$ for volume diffusion (K is the rate constant), is assumed to be obeyed, which is similar to the Björklund, Donaghey and Hillert model for cementite in the Fe-C-Cr system [129]. The rate constant K should differ significantly from that in the LSW theory for spherical particles. Based on the following assumptions:

1) The M_2C carbides are shape-preserving during coarsening where the shape of the rod is assumed to be represented by a cylinder of length l and radius r with two hemispherical caps of the same radius, where $l/r=2A_s$ (A_s is the aspect ratio, which does not significantly vary with time);

2) The coherency stresses around carbides are insignificant and the surface free energy is equal to surface stress, both of which are isotropic;

Lee, Allen and Grujicic [137] have theoretically derived coarsening rate constant equations (K_r and K_l) for the radius and length of rod-like M_2C carbides respectively and compared the prediction with experimental measurements [136].

$$K_r=\frac{2\sigma_s V_m^{\beta}}{RT\ln(\frac{l}{r})}\left[\sum_M (k_M-k_{Fe})(k_M-1)\frac{X_{M,\infty}^{\alpha}}{D_M^{\alpha}}\right]^{-1}$$

$$K_l=\frac{16As^3\sigma_s V_m^{\beta}}{RT\ln(\frac{l}{r})}\left[\sum_M (k_M-k_{Fe})(k_M-1)\frac{X_{M,\infty}^{\alpha}}{D_M^{\alpha}}\right]^{-1}$$

Equation 3-6

Where $K_l= 8\ A_s^3\ K_r$; σ_s is the interfacial energy of the side of the rod-like particle; V_m^{β} is the volume per gram atom of M_2C carbide; A_s is the average particle aspect ratio; R is the gas constant; T is the absolute temperature; l is the length; r is the radius; k_i (i=M,Fe) is the partitioning coefficient of elements M and Fe and defined as X_i^{β}/X_i^{α}, where X_i^{β} and X_i^{α} are the mole fractions of element i in M_2C carbides and ferrite matrix; D_M^{α} is the diffusion coefficient for element M in the matrix; $X_{M\infty}^{\alpha}$ is the equilibrium mole fraction of M in the matrix with particles of infinite radius [137].

Table 3-1 shows the comparison between the measured and predicted coarsening rate constant in terms of length for the rod-like M_2C carbides in different steels tempered at

510 °C. Only in the AF1410 steel, the prediction shows a good agreement with the experimental data; however, for SRG samples, the predicted values deviate greatly from experimental observations. However, there is no detailed explanation for this given in the literature [136]. In addition, the justification for the selection of values used in Equation 3-6 to obtain the predicted values in Table 3-1 remains vague, i.e. the choice of interfacial energy values and the solute diffusivities, potentially limiting applicability to other steel systems. Furthermore, the model is based on the qualitative growth law $\bar{r}^3-\bar{r}_0^3=Kt$, however, the observed sized distribution is not in agreement with the original asymptotic LSW size distribution. Possible reasons for this include: the rod-like particle shape; the nonzero volume fraction (although it is very small) and presence of other coexisting phases.

Table 3-1. Comparison of measured and predicted length coarsening rate constant K_l for M_2C carbides in different steels tempered at 510 °C [136]

Steels	Measured K_l (m^3/s)	Predicted K_l (m^3/s) (Fe database) (σ_s=0.7 J/m^2)	Ratio of measured K_l to predicted K_l
Fe-0.16C-2.1Cr-1.05Mo-10.15Ni-14.25Co (AF1410)	1.364×10^{-29}	1.448×10^{-29}	0.942
Fe-0.23C-0.06Cr-3.96Mo-10.24Ni-14.17Co (SRG1)	1.632×10^{-29}	3.510×10^{-29}	0.465
Fe-0.24C-0.02Cr-1.03Mo-4.96Ni-15.99Co (SRG2)	1.243×10^{-29}	3.041×10^{-30}	4.087
Fe-0.24C-0.71Cr-2.82Mo-4.97Ni-16.08Co (SRG3)	3.629×10^{-30}	2.344×10^{-30}	1.548
FE-0.24C-1.40Cr-1.52Mo-4.98NI-16.06Co (SRG4)	2.404×10^{-30}	3.692×10^{-30}	0.651

B. Yamasaki and Bhadeshia model [57, 107, 138]

Based on experimental observations for coarsening of Mo_2C or V_4C_3 carbides in Fe-C-Mo or Fe-C-V ternary steel systems during tempering respectively, this model was specifically established for the coarsening of intragranular needle/plate-shaped secondary Mo_2C or V_4C_3 carbides with constant composition. There are several assumptions adopted in the model:

1) Ostwald ripening occurs after the completion of precipitation of the needle/plate-shaped carbides (i.e. Mo_2C or V_4C_3);

2) The specific shape for the needle/plate-shaped particles in the model is assumed as a cylinder with hemispherical tips;

3) The interfacial energy for the carbides is isotropic.

Furthermore, Zener's theory for diffusional growth has been used in this one-dimensional coarsening model with the following assumptions [139, 140]:

a) The growth is isothermal and diffusion-controlled;

b) The diffusion coefficient is independent of composition and concentration;

c) The interface composition is under local equilibrium;

d) The tip of a needle is hemispherical with the composition at the interface remaining constant over the curved surface.

e) The growth takes place in a semi-infinite medium.

The concentration profile at the particle/matrix interface for a single needle-shaped particle in Zener's theory is shown in Figure 3-3. The growth rate for the needle-shaped particle is defined as

$$v=\frac{D}{L}\frac{\bar{c}-c_r^{\alpha\beta}}{c_r^{\beta\alpha}-c_r^{\alpha\beta}}$$ Equation 3-7

Where D is the solute diffusion coefficient; L is the diffusion distance; $\bar{c}$ is the solute concentration in the matrix; $c_r^{\alpha\beta}$ is the solute concentration in α phase at the interface of curvature r; $c_r^{\beta\alpha}$ is the solute concentration in β phase at the interface of curvature r.

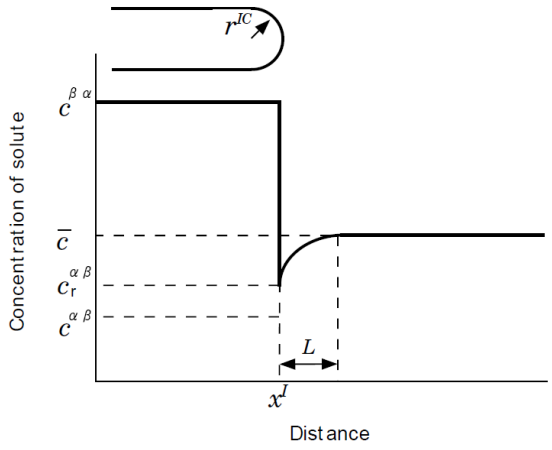

Figure 3-3. The schematic diagram showing the concentration profile at the interface between the matrix α and a single growing needle-shaped precipitate β with a curved interface. r^{IC} is the radius of the curvature at the needle tip; L is the diffusion distance; x^I is the position of interface [57].

In the Fe-C-Mo steel [57, 107], the intra-lath Mo_2C carbides have been observed to be needle-like and carbide coarsening occurs accompanied with spheroidisation due to the different solubility and Gibbs energy at the needle-tip compared to the needle length (cylindrical edge), Figure 3-4 (a). The equilibrium concentrations $c_{Mo,r}^{\alpha\,Mo_2C}$ at the hemispherical tip and cylindrical edge are given as:

$$c_{Mo,r}^{\alpha\ Mo_2C}=(1+\frac{2\Gamma}{r^{IC}})c_{Mo}^{\alpha\ Mo_2C}\ \text{(tip)} \qquad \text{Equation 3-8}$$

$$c_{Mo,r}^{\alpha\ Mo_2C}=(1+\frac{\Gamma}{r^{IC}})c_{Mo}^{\alpha\ Mo_2C}\ \text{(cylindrical edge)} \qquad \text{Equation 3-9}$$

Where Γ is the capillarity coefficient; r^{IC} is the particle crvature at the interface; $c_{Mo}^{\alpha\ Mo_2C}$ is the equilibrium concentration of Mo inside Mo_2C carbides. The coarsening or dissolution rates at the needle tip and cylindrical edge should be calculated separately for each particle (spheroidisation included) based on Equation 3-7:

$$v=-\frac{D}{\bar{d}}\frac{\overline{c_{Mo}}-c_{Mo,r}^{\alpha\ Mo_2C}}{c_{Mo}^{Mo_2C\ \alpha}-c_{Mo,r}^{\alpha\ Mo_2C}} \qquad \text{Equation 3-10}$$

$$\bar{d}=\left(N^{\beta}\right)^{-1/3} \qquad \text{Equation 3-11}$$

Where D is the volume diffusion coefficient for molybdenum; $c_{Mo,r}^{\alpha\ Mo_2C}$ is the equilibrium concentration of molybdenum at the tip / cylindrical edge interface of Mo_2C particles in ferrite matrix; $c_{Mo}^{Mo_2C\ \alpha}$ is the equilibrium concentration of molybdenum inside the Mo_2C particles; $\overline{c_{Mo}}$ is the average molybdenum concentration in the matrix; $\bar{d}$ is the mean diffusion distance between particles; N^{β} is the number density of Mo_2C particles.

However, in the Fe-C-V steel [57, 138], the plate-like V_4C_3 carbides are shape-preserving within the laths during coarsening due to the excellent coherency between V_4C_3 carbides and the matrix, as shown in the schematic diagram in Figure 3-4 (b). Therefore, the coarsening rate is only calculated at the plate tip for each intra-lath V_4C_3 carbide:

$$v = -\frac{D_V}{\bar{d}} \frac{\overline{c_V} - c_{V,r}^{\alpha V_4C_3}}{c_V^{V_4C_3 \alpha} - c_{V,r}^{\alpha V_4C_3}}$$ Equation 3-12

Where the parameters are similar as those in Equation 3-10 and Equation 3-11.

Coarsening simulations have been carried out for a single needle (Mo_2C) / plate (V_4C_3)-shaped carbide with average size in the two steels considered. In the Fe-C-Mo system, spheroidisation is included in the simulation where the growth rates at the needle tip and cylindrical edge are both calculated. Thus, the calculated average length decreases with time due to the combination of the two growth rates, Figure 3-5(a), which gives deviations from the experimental observation, especially after long time tempering (i.e. 1000 hrs). However, in the Fe-C-V system, the intra-lath V_4C_3 carbides remain plate-like, therefore, the calculation has only been carried out at the plate tip, which generally agrees well with the observations. However, a small deviation in Figure 3-5(b) still exists due to carbide size measurements for both intra- and inter-lath V_4C_3 carbides, where V_4C_3 carbides on the lath/grain boundaries spheroidise during coarsening. In general, the model is a mean field model using the average carbide size and spacing to work out the overall carbide coarsening behaviour, where Zener's theory is the basis for the model. It gives a relatively accurate prediction for coarsening of shape-preserving plate-like carbides in the matrix during tempering. However, there is a very large discrepancy between observation and the simulation when carbide spheroidisation occurs during tempering, such as the coarsening of Mo_2C in the Fe-C-Mo steel.

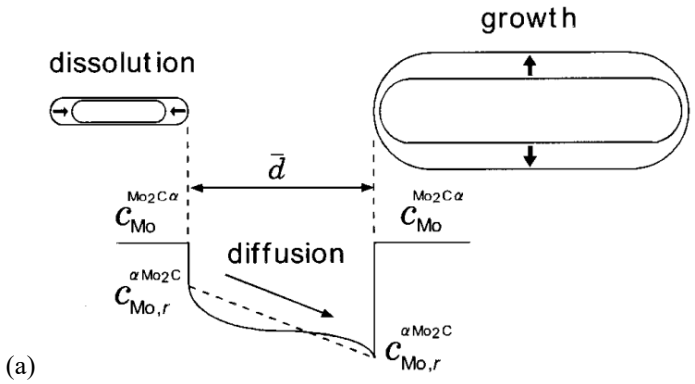

(a)

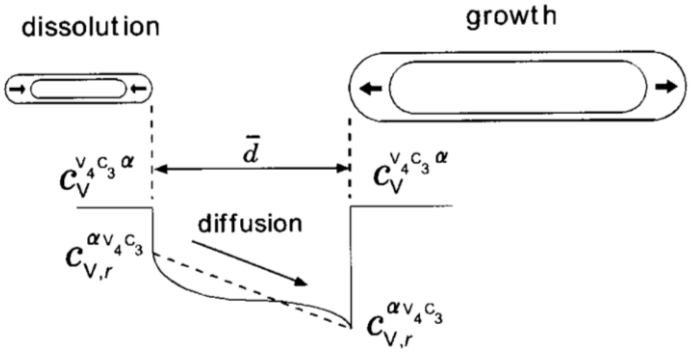

(b)

Figure 3-4. Schematic diagram showing the Ostwald ripening for (a) the needle-like Mo_2C carbides and (b) plate-like V_4C_3 carbides [57, 107, 138].

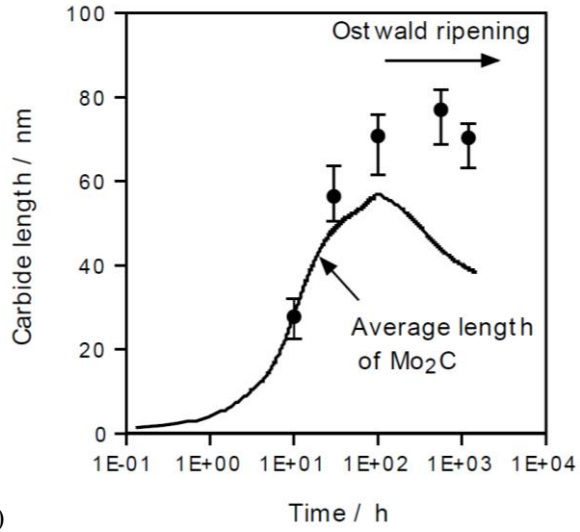

(a)

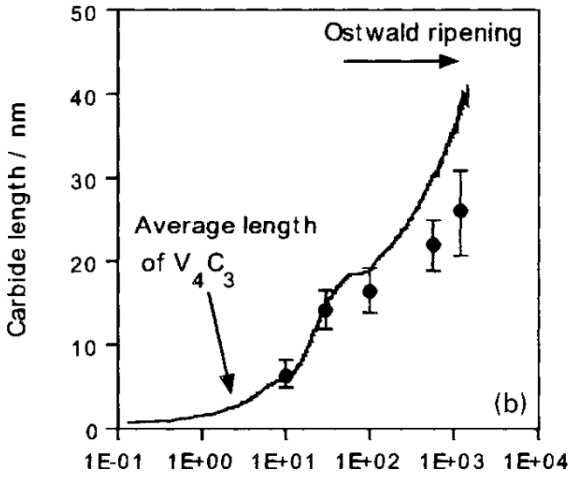

(b)

Figure 3-5. The calculation results compared with the observation (carbides in the lath and on the lath/grain boundaries) for the coarsening of (a) needle-shaped Mo_2C and (b) plate-shaped V_4C_3 carbides [57, 107, 138].

3.2.2 Theoretical models for coarsening of carbides on low/high-angle grain boundaries with solute boundary diffusion

When precipitates are situated on low/high-angle grain boundaries, the solute diffusion is along the high diffusion path (i.e. the dislocation network for low-angle grain boundaries or the high-angle grain boundary) with faster solute diffusivities (especially for substitutional elements). Therefore, the theoretical growth law for precipitates on a low/high-angle grain boundary should differ from that for intragranular precipitates in the matrix (r^3~Kt). The theoretical growth law for particles on the high-angle grain boundary has firstly been addressed by Speight [141] and Kirchner [142] based on the following assumptions:

1) The equilibrium shape of particles is assumed to be two symmetrical hemispherical caps along the boundary [141-146], which is determined by the minimisation of particle

surface free energy and equilibrium with grain-boundary tension, Figure 3-6. However, the particles are circular in the boundary plane [141, 142, 145];

2) The mass transfer for particles is assumed to occur in the boundary plane that is actually a two-dimensional medium. The precipitates should only receive or lose solute at the surface intersected by the boundary; however, the original shape keeps constant during coarsening with sufficiently fast precipitate/matrix interface diffusion to allow solute transfer around precipitates;

3) The solute diffusion is under steady-state condition, and the diffusion flux is isotropic.

The theoretical growth law for precipitates located on high-angle grain boundaries is then [120, 142]:

$$r_t^4 - r_0^4 = \frac{9\lambda V_m \omega D_{g.b} N_{g.b}}{32ABRT} t$$

$$A = 2/3 + (\lambda_{g.b}/2\lambda) + (1/3)(\lambda_{g.b}/2\lambda)^3 \quad \text{(constant)} \qquad \text{Equation 3-13}$$

$$B = (1/2)\ln(1/f_b) \text{ (constant)}$$

Where, $D_{g.b}$ is the solute grain boundary diffusivity; ω is the grain boundary thickness; λ is the interfacial energy between particle and matrix; V_m is the molar volume of the precipitates; $N_{g.b}$ is the equilibrium solubility at the grain boundary; $\lambda_{g.b}$ is the grain boundary energy; f_b is the fraction of the grain boundary covered by particles; R is the ideal gas constant; T is the absolute temperature. Finally, the radius for the equilibrium shape (Figure 3-6) is comparatively larger than that for a spherical particle with the same

volume, and the size distribution for particles on the grain boundary is much narrower (cut-off size $1.33\bar{r}$ [142]) than that in the matrix [120].

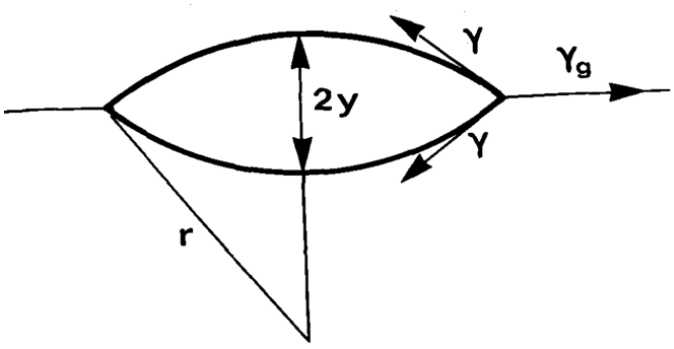

Figure 3-6. Equilibrium shape of precipitate at a grain boundary. γ is the particle/matrix interfacial energy, γ_g is the grain-boundary energy and r is radius for the spherical cap [141-146].

In addition, Ardell [145] has derived a theoretical growth law for precipitates located on low-angle grain boundaries where the solute diffusion is along the dislocation network with the assumptions of:

1) The precipitates are distributed uniformly on a dislocation network, where pipe diffusion along dislocations is assumed to be the only diffusion mechanism for mass transfer of a given precipitate to receive or lose solute;

2) The dislocation network contains spherical particles located on dislocation nodes in the 2D sub-grain boundary plane, where the spherical particle is shape-preserving during coarsening due to the relatively rapid diffusion around the precipitate-matrix interface, Figure 3-7 (a);

3) A precipitate of radius r is in the centre of a constructed spherical matrix cell of radius r', and the diffusion direction is confined into x and y dislocation lines instead of radial direction, Figure 3-7 (b);

4) Solute diffusion is under steady-state condition, and the diffusion flux is isotropic.

Based on the relationship between precipitate radius r and dislocation spacing h, the growth law can be divided into two conditions:

(a) r>>h

$$r^4-r_0^4=\frac{64qD_dN_d\lambda\eta V_m}{27\pi hRT}t \qquad \text{Equation 3-14}$$

(b) r≈h

$$r^5-r_0^5=\frac{0.311qD_dN_d\lambda NV_m}{\pi RT}t \qquad \text{Equation 3-15}$$

Where q is the cross-sectional area of the dislocation that transports the flux of solute atoms; D_d is the dislocation pipe diffusion coefficient; N_d is the solubility of atoms in dislocations in equilibrium with a precipitate of infinite radius; λ is particle interfacial energy; η is a function of the precipitate volume fraction; V_m is the molar volume of the precipitates; h is the dislocation spacing, which is associated with the misorientation angle θ; N is the total number of dislocations intersected by a precipitate; R is the ideal gas constant; T is the absolute temperature. Actually, it is quite difficult to precisely ascertain the dislocation spacing h. When the precipiates radius r is of the same order of magnitude as the dislocation spacing h, the coarsening kinetics can vary between $t^{1/4}$ and $t^{1/5}$. The shift from $r\sim t^{1/5}$ growth law to $r\sim t^{1/4}$ growth law should occur at shorter times with an increase of misorientation angle θ (the decrease of dislocation spacing h). The $r\sim t^{1/4}$ growth law should always be observed at the very beginning of coarsening with relatively large θ values where the boundary is regarded as having become the high-angle grain boundary.

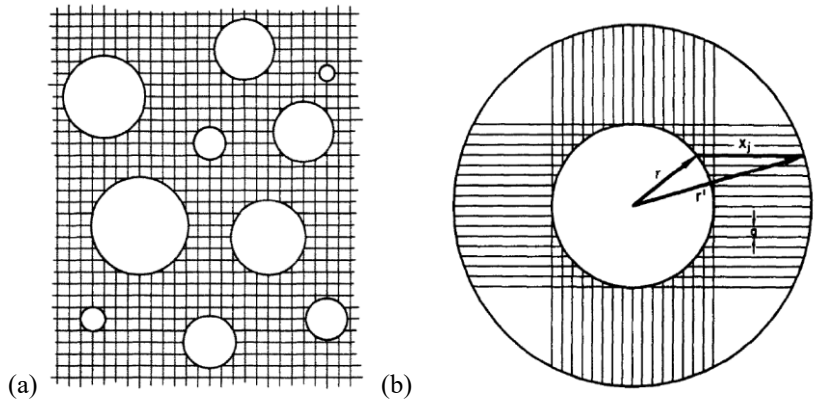

Figure 3-7. (a) A schematic view of spherical precipitates located on a low-angle grain boundary consisting of a square net-work of dislocation; (b) The diffusion geometry for an individual particle located on the sub-grain boundary associated with pipe diffusion, and the dislocation lines capable to transport solute atoms are displayed [145].

The above theoretical growth laws for particles on low/high-angle grain boundaries are also mean field models where the particle volume fraction is ignored. However, with an increase in the volume fraction, the particle diffusion field changes, which leads to an increase of coarsening rate constant (even at very small volume fractions), although the qualitative growth law $r=Kt^{1/4}$ or $r=Kt^{1/5}$ is still obeyed, consistent with the LSW theory [147]. In plain carbon and alloyed martensitic steels [59, 72, 148], the coarsening kinetics for carbides on low/high-angle grain boundaries has been checked using above theoretical and qualitative growth laws during tempering. In plain carbon martensitic steels with carbon contents varying from 0.2 wt % to 1.0 wt %, almost all the cementite particles have been observed on low/high-angle grain boundaries, where the experimental observation of coarsening of cementite is shown in Figure 3-8 [148]. The coarsening exponent for cementite ranged from 0.200 to 0.223, which agrees well with the qualitative growth laws $r\sim t^{1/4}$ / $t^{1/5}$ for particles on low/high-angle grain boundaries [141, 142, 145], indicating that the coarsening of cementite is controlled by solute

diffusion along the grain or sub-grain boundaries. Similarly, in a medium carbon alloyed steel (Fe-0.45%C-0.22%Si-0.62%Mn-0.004%P-0.0038%S) [59, 72], the coarsening exponent is 0.220 for cementite on the boundaries, which also demonstrates a combination of grain boundary diffusion and dislocation diffusion controlled coarsening, being similar to the cementite coarsening in plain carbon martensitic steels [148]. However, the exact coarsening rate constant K values are not reported in these steels to compare with the theoretical analysis used in Equation 3-13, Equation 3-14 and Equation 3-15.

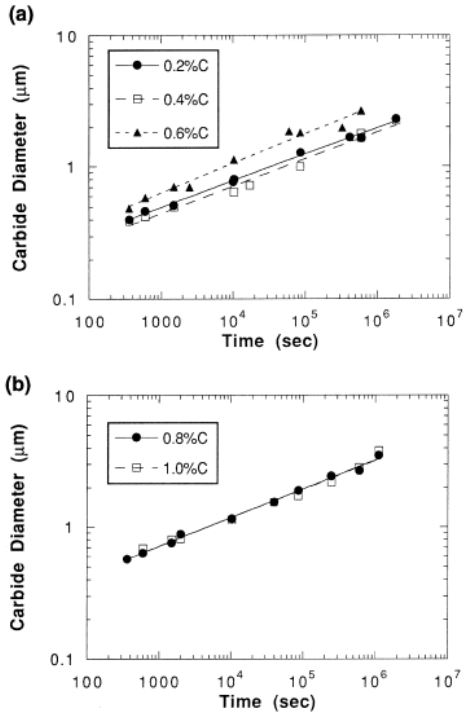

Figure 3-8. The coarsening of cementite on the low/high-angle boundaries in plain carbon steels (carbon contents 0.2 - 1.0 wt %) tempered at 600 °C for different times [148].

The theoretical solutions for coarsening of precipitates on low/high-angle grain boundaries mentioned above solely take grain boundary diffusion or dislocation pipe

diffusion for solute transfer into consideration. However, when solute transfer occurs not only along the boundary but also from matrix to a boundary, the above theoretical growth laws cannot be applied. Aaron and Aaronson [143, 144] have established an analytical model, which considers all the diffusion mechanisms, in Al-4%Cu alloy where larger intergranular Cu-precipitates coarsen at the expense of the smaller intragranular ones. The volume diffusion of Cu from matrix to the grain boundary to supply Cu atoms for large particles, grain boundary diffusion of Cu contributing to particle lengthening and interface diffusion and deposition over the particle surface for the thickening process have all been taken into account. The following assumptions are used in the model:

1) The particle shape is assumed to be the same as that in Figure 3-6, where the broad face of the precipitates is flat;

2) Each grain boundary has been filled with a set of square 'collector plates' with area A_v>>area of boundary occupied by a single precipitate, Figure 3-9, hence, the transport of Cu atoms from matrix to a boundary is dominated by the high solute diffusivity in the boundary region;

3) The composition in the grain boundary region is independent of time;

4) The diffusion is under steady-state condition, and local equilibrium is maintained at the grain boundary and interphase boundary.

The precipitate coarsening in this model is divided into lengthening and thickening processes. As the lengthening process is controlled by rapid Cu diffusion along the boundary, therefore, the qualitative growth law for precipitate half-length L in this model is treated to be similar as $L \sim t^{1/4}$ [141, 142], Equation 3-16. Meanwhile, the faster interphase boundary diffusion due to the disordered structure of precipitates/boundary interface enables the Cu atoms to be redistributed over the particle surface, hence, the

qualitative growth law for precipitate half-width S is assumed to be similar as $r \sim t^{1/2}$ [120], Equation 3-16. The theoretical coarsening law for precipitate half-length L and half-width S is given as

$$L=kt^{1/4} \qquad S=2\varphi t^{1/2}$$

$$k=\left[\frac{2\left[x_\alpha - x_\alpha^{\alpha\theta}\exp\left(\frac{\lambda_{\alpha\theta}V_{Cu}^{\alpha}}{RTR_2}\right)\right]A_V D_V^{1/2}}{\pi^{3/2}\left[x_\theta - x_\alpha^{\alpha\theta}\exp\left(\frac{\lambda_{\alpha\theta}V_{Cu}^{\alpha}}{RTR_2}\right)\right]R_2}\right]^{1/2} \qquad \text{Equation 3-16}$$

$$\varphi=\frac{2\delta D_{\alpha\theta}\left[\exp\left(\frac{\lambda_{\alpha\theta}V_{Cu}^{\alpha}}{RTR_2}\right)-1\right]x_\alpha^{\alpha\theta}}{\beta k^2\left(x_\theta - x_\alpha^{\alpha\theta}\right)}$$

Where x_α is the Cu solubility in the matrix; $x_\alpha^{\alpha\theta}$ is the Cu solubility on the grain boundary; x_θ is the Cu solubility in the precipitates; $\lambda_{\alpha\theta}$ is the interfacial energy at the precipitate/grain boundary interface; V_{Cu}^{α} is the molar volume of Cu-precipitates in the matrix; R_2 is the radius of the edge for given precipitates; A_v is the area of the 'collector plates'; D_V is the volume diffusion coefficient for Cu; δ is the thickness for interface boundary; β is the average fraction of half-length which a Cu atom diffuses along the interface boundary before it joins the precipitates.

In the Al-4% Cu system, the theoretical lengthening results show a good agreement with experimental observations, however, the thickening kinetics were much larger than the experimental data - this was attributed to growth inhibition due to faceting of the interface. Although this mean field model has not been reported for tempered martensitic steels, the assumptions and the analytical treatment in the model can be used for

reference for the simulation of coarsening of large intergranular carbides at the expense of small intragranular carbides during long time tempering (e.g. over hundreds of hours).

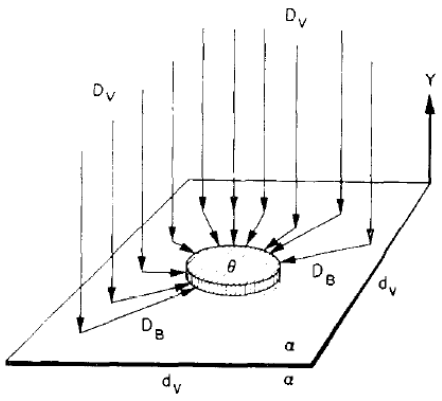

Figure 3-9. Schematic diagram of the "collector plate" model [143].

3.2.3 DICTRA model for coarsening of spherical or near spherical carbides in the matrix and on low/high-angle grain boundaries

DICTRA is widely used in simulating and solving numerical diffusion problems in multicomponent alloys, assuming that thermodynamic equilibrium holds locally at all phase interfaces, which also means that there is no difference in the chemical potential across the phase interfaces, and the concentration of components can be acquired from the phase diagram [149]. Thermodynamic and mobility databases are both used in DICTRA simulation, and the diffusion-controlled phase transformation in DICTRA is treated in one space variable (one-dimensional diffusion) with three different geometries in planar, cylindrical and spherical cells of one or more various phases. DICTRA simulation is also regarded as the simplest method in obtaining quantitative kinetic information in numerous material systems without the consideration of many other possible effects during phase transformation process [150-152], such as the finite

mobility of the interface and any elastic stress, but still has been proven to be accurate enough. The accuracy of DICTRA simulation not only depends strongly on the accuracy of the thermodynamic and kinetic data but also relies on the different assumptions in the models. Hence, the best way to check the accuracy of the DICTRA model is to compare the predicted results with experimental data [153].

In a binary alloy system under isothermal conditions, the flux, J, of a species k in one direction z is defined using Fick's first law:

$$J_k=-D_k\frac{\partial c_k}{\partial z} \qquad \text{Equation 3-17}$$

Where, J_k is the diffusion flux of k: the amount of substance k diffusing per unit time and per unit area perpendicular to the diffusion direction z, in mol/(s·m^2); D_k is the diffusivity coefficient of species k, which depends on the temperature and concentrations, m^2/s; c_k is the concentration of species k in the matrix, mol/m^3.

When combined with the continuity equation, Equation 3-17 is described as

$$\frac{\partial c_k}{\partial t}=\frac{\partial}{\partial z}(D_k\frac{\partial c_k}{\partial z}) \qquad \text{Equation 3-18}$$

However, in a multi-component system, the flux J_k depends on the concentration gradients of all independent elements in the system. The multicomponent equation extension to Fick's first law proposed by Onsager [154, 155] under isothermal and isobaric condition in direction z is expressed as

$$J_k = -\sum_{j=1}^{n} D_{kj}^{n} \frac{\partial c_j}{\partial z} \qquad \text{Equation 3-19}$$

Where component n is regarded as the dependent component; c_j is the concentration of species j in the matrix, mol/m^3; D_{kj}^{n} is the (n-1)(n-1) diffusivity matrix [149], and in a volume-fixed frame where only substitutional species contribute to the volume, D_{kj}^{n} can be expressed as $D_{kj}^{n}=D_{kj}-D_{kn}$ (when j refers to the substitutional elements), or $D_{kj}^{n}=D_{kj}$ (when j is the interstitial elements) with the elimination of concentration gradient. Basically, the concentration gradient of one element results in the diffusion of another elements. In a multi-component system, it is necessary to work out the true driving forces (chemical potential gradients) for diffusion, and the kinetic parameter related with the flux and driving force is the mobility M_k of a component k. Hence, the diffusion coefficient becomes

$$D_{kj} = c_k M_k \frac{\partial u_k}{\partial c_j} \qquad \text{Equation 3-20}$$

Where the chemical potential u_k is available from the thermodynamic database and the mobility M_k is from mobility database which has been established based on the assessment of the experimental information [156].

The movement of the interface is controlled by the mass balance obtained from the fluxes of the diffusing elements from / to the interface. For the migration of the interface, the flux balance equation between phase α and β is defined as:

$$v^{\alpha}c_k^{\alpha}-v^{\beta}c_k^{\beta}=J_k^{\alpha}-J_k^{\beta} \qquad k=1,2,\ldots,n \qquad \text{Equation 3-21}$$

Where v^{α}, v^{β} are the interface migration rates; c_k^{α}, c_k^{β} are the concentrations of species k in the two different phases near the interface; J_k^{α}, J_k^{β} are the diffusional fluxes of k in the two phases respectively.

The one-dimensional coarsening model in DICTRA has been developed in order to treat the Ostwald ripening process. The assumptions adopted in the coarsening model are

1) The coarsening of the system can be described by simulating a single spherical particle of initial maximum radius R_1 at the centre of a spherical cell of radius R_2 determined by the surrounding matrix;

2) The particle size distribution obeys the Lifshitz-Slyozov-Wagner size distribution: the maximum particle size is 1.5 times the average size [122, 123]. The ratio of particle maximum and average size remains constant at 1.5 throughout the modelling process;

3) The shape of the particle is supposed to maintain spherical during the whole calculation, and the matrix in the cell is in equilibrium with the particle.

Therefore, the relationship between the volume fraction of particles and the radius of the matrix is given below

$$Q_p=\frac{V_1}{V_2}=\frac{R_1^3}{R_2^3} \qquad \text{Equation 3-22}$$

Where Q_p is the volume fraction of the particles; V_1 and V_2 are the volume of particle and matrix respectively; R_1 is the radius of the particle; and R_2 is the radius of matrix

cell. At the outer boundary of the matrix cell, the equilibrium is defined by the average composition in the whole system. A schematic diagram of the coarsening model is shown in Figure 3-10, and in this coarsening model, the interfacial energy is added to the Gibbs energy function for the particle:

$$\Delta G = \frac{2\lambda V_m}{r} \qquad \text{Equation 3-23}$$

Where λ is the interfacial energy, J/m^2, V_m is the particle molar volume in $m^3/$ mol; r is taken as R_1 (largest particle) or R_0 (particle with average size) respectively, m. A particle of the maximum size has a smaller Gibbs energy addition compared to the particle of average size according to Equation 3-23, leading to the shift in equilibrium to cause the largest particles to grow at the expense of smaller ones [149]. There is one cell, which contains two regions (particle and matrix) in this coarsening model.

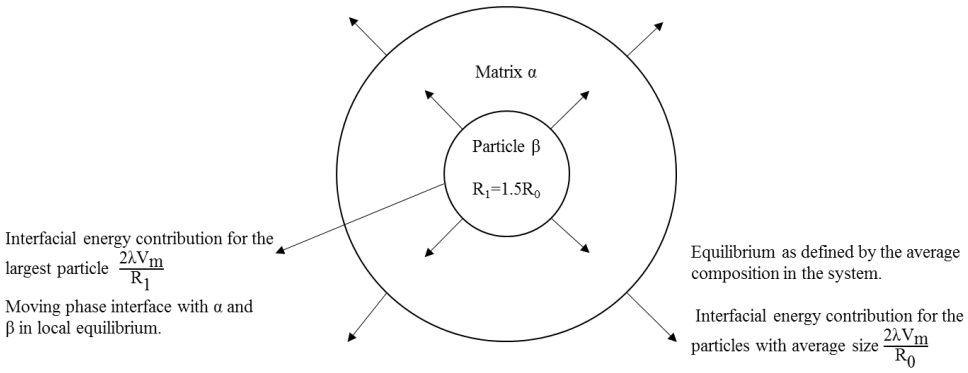

Figure 3-10. Schematic diagram of the DICTRA coarsening model. The moving interface between particle and matrix is in local equilibrium. At the matrix cell boundary, equilibrium is defined by the average composition in the system [157, 158].

As DICTRA solves a one-dimensional diffusion problem, the coarsening model can be used for the simulation of coarsening of carbides not only in the matrix but also on low/high-angle grain boundaries, which has been widely reported in different steels and compared with experimental observations during tempering [149, 152, 157, 159, 160].

In simple Fe-0.6C binary and Fe-0.6C-2Mn/2Si ternary steels, the DICTRA prediction for the coarsening of cementite during tempering is shown in Figure 3-11 [161]:

a) When tempering at 450 °C, the experimental data agree well qualitatively (i.e. correct trend-line shape) with the simulation for the coarsening of cementite in Fe-0.6C-2Mn/2Si ternary steels where the radius of cementite nearly remains constant due to the addition of Mn or Si with very low diffusivities. Whereas the simulated cementite radius is much larger than the measured one in binary Fe-0.6C steel tempered at the same temperature.

b) When tempering at 650 °C, the comparison between the experimental observation and simulation is quite similar to that at 450 °C in Fe-0.6C binary system, where the predicted radius is larger than the observed one. However, in Fe-0.6C-2Mn/2Si ternary systems, the predicted radius is much smaller than the experimental data, which indicates that the diffusivity of Mn or Si in the mobility database is too small to give a reasonable simulation at relatively higher temperatures (650 °C).

Two reasons for the discrepancies are considered in the literature; the uncertainty of the kinetic data available in the mobility database and the assumption of the particle shape [160], however, there is no detailed experimental examination reported. Furthermore, the simulation and the measurement in the two steels have not specified whether it is for

cementite in the matrix or on the boundary separately, which might also contribute to the disagreement.

In addition, the coarsening model has also been used to simulate the coarsening of alloy carbides within the laths, where the diffusion of substitutional elements is the rate-controlling step for coarsening, such as MX carbides in a Fe-0.11C-9Cr-0.47Mo-1.84W-0.20V-0.46Ni steel at 600 °C for thousands of hours, Figure 3-12 [159]. The simulation and experimental data both show a very slow coarsening rate for MX carbides within thousands of hours due to the slow diffusivity of substitutional alloying elements (such as W). However, a discrepancy still exists between the experimental observation and the prediction [160] with the predicted radius increasing linearly with time, whilst the experimental radius firstly increases from 0 hr to 5×10^3 hrs but then decreases from 5×10^3 hrs to 25×10^3 hrs at the same temperature; again no detailed explanations were reported for this phenomenon.

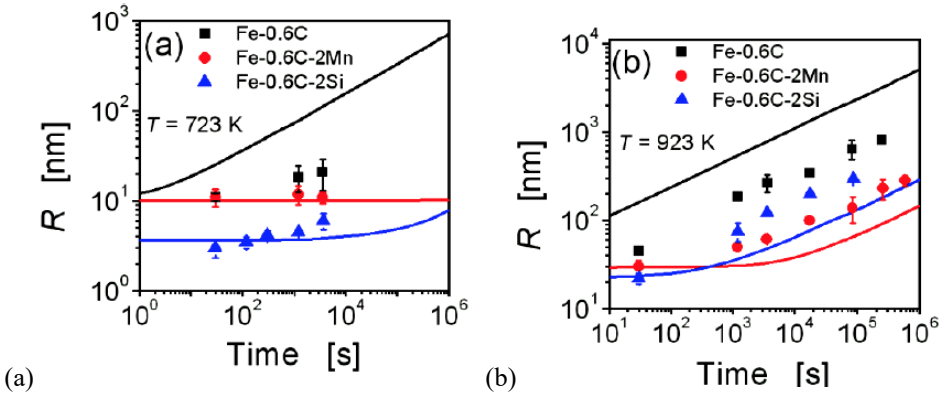

Figure 3-11. Time and composition dependent variation of cementite particle radius R at (a) 450 and (b) 650 °C where the symbols represent the experimental data and the lines represent the simulation results [161].

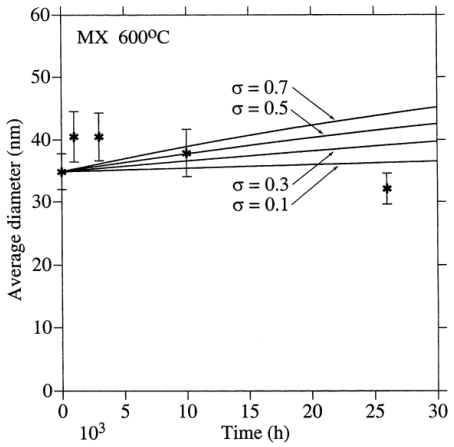

Figure 3-12. Comparison between the simulation results (the solid lines) and experimental results (the symbols) for the coarsening of MX carbides within the laths in a Fe-0.11C-9Cr-0.47Mo-1.84W-0.20V-0.46Ni steel at 600 °C for thousands of hours [159].

Solute diffusion along the low/high-angle grain boundary is also regarded as one-dimensional diffusion, therefore, the DICTRA coarsening model has also been employed to predict the coarsening of carbides on low/high-angle grain boundaries, such as the coarsening of $M_{23}C_6$ or Laves phase on low/high-angle grain boundaries in creep resistant steels during long time tempering (thousands of hours) [149, 157, 159]. Figure 3-13 shows the coarsening of intergranular $M_{23}C_6$ carbides in 12% Cr (a) and 9% Cr (b) creep resistant steels at different temperatures, where different interfacial energy values have been selected in the simulation [149, 157, 159], as it is very difficult to determine the interfacial energy values for alloy carbides on low/high-angle grain boundaries from experimental measurements. The results show that low interfacial energy values between 0.1 J/m^2 and 0.3 J/m^2 provide reasonable agreement compared to the experimental data (with experimental deviations) for the coarsening of $M_{23}C_6$ carbides tempered at 600 and 650 °C. However, the experimental diameter increase trend in the 9% Cr creep resistant steel at 600 °C, Figure 3-13(b), actually differs from the simulation.

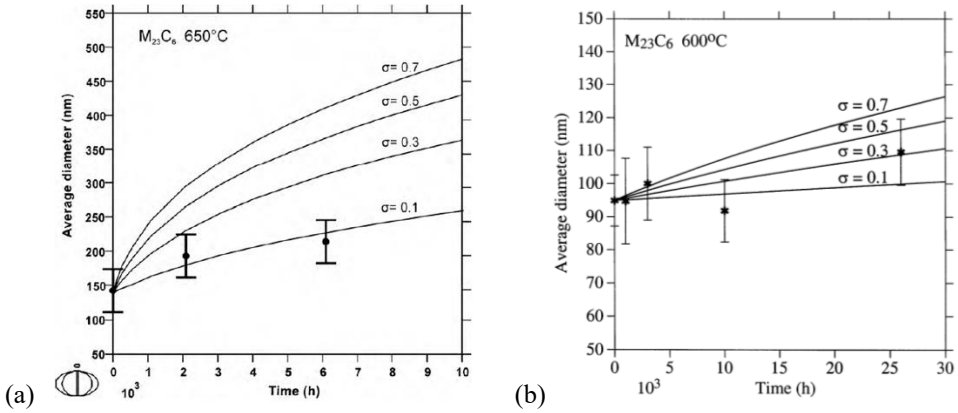

Figure 3-13. Simulation of coarsening of intergranular $M_{23}C_6$ in (a) Fe-12.6Cr-3.6W-0.15C-2.5Co-0.16Ta steel at 650 °C and (b) Fe-0.11C-9Cr-0.47Mo-1.84W-0.20V-0.46Ni steel at 600 °C compared with experimental measurements. The figure shows the average diameter as a function of time, and the solid lines are the simulations with different values of the interfacial energy: 0.1 - 0.7 J/m^2 [157, 159].

In summary, the DICTRA coarsening model (one-dimensional diffusion-controlled model) is a mean field model using a carbide with average size to represent the overall carbide coarsening behaviour, which has been used to simulate the coarsening of spherical or near spherical carbides in the matrix and on low/high-angle grain boundaries in martensitic steels during tempering. The average radius/diameter increase has been predicted, and the predicted radius/diameter increase has shown some agreement with the experimental data, although some discrepancies are still observed [149, 152, 157, 159, 160]. The possible reasons for the discrepancies are:

a. The assumptions in the model are not satisfied properly;

b. The kinetic data (e.g. diffusion coefficient for substitutional elements and any muti-component interaction effect) are uncertain in the mobility database;

c. The standard of choosing the input values for the model requiring for fitting remains vague, i.e. for interfacial energy values.

d. The separate inter- and intra-lath carbide coarsening behaviours have not been checked experimentally in all the reported steels before the model has been applied.

3.3 Summary

In plain carbon martensitic steels, transition iron carbides (ε-carbides or ε'-carbides) normally form first, then transform to cementite during tempering. As the tempering temperatures and times increase, cementite undergoes Ostwald ripening, where larger particles grow at the expense of smaller ones, occurring with a reduction in interfacial area to reach thermodynamic equilibria, which is the predominant microstructural change responsible for the decrease of hardness. Therefore, it is important to be able to predict the cementite coarsening behaviour to estimate the microstructural changes in this tempering stage. Most of cementite particles reside on the lath/grain boundaries (inter-lath), although there are still a few left in the matrix (intra-lath), where the rate-controlling steps for intra- and inter-lath cementite are solute volume diffusion and lath/grain boundary diffusion respectively. Therefore, the theoretical models and numerical models for the coarsening of carbides in the matrix and on the low/high-angle grain boundaries during tempering have been reviewed.

In recently reported literature, the coarsening kinetics of carbides in tempered martensite follows a qualitative growth law $r^n=Kt$ with the exponent n=3 for volume diffusion-controlled coarsening; or n=4/5 for grain/sub-grain boundary diffusion-controlled coarsening, where the carbides are spherical or near spherical in the matrix or in the 2D boundary plane. The theoretical rate constant equation K differs with various particle composition (i.e. the effect of substitutional elements) and volume fraction. For the coarsening of carbides on the grain/sub-grain boundaries, this theoretical model, $r^{4/5}=Kt$, has been used to give a qualitative analysis in different steels during tempering, where no rate constant K verification is available. In addition, for coarsening of needle/plate-

like carbides, an analytical mean field model based on Zener's theory has been established by Yamasaki and Bhadeshia. The prediction agrees well with the experimental data for shape-preserving carbides; however, with the occurrence of carbide spheroidisation, such as seen for Mo_2C, it deviates significantly from the observation during tempering.

In addition, computational DICTRA coarsening model (1D diffusion model) has been used to roughly predict the coarsening of spherical/ non-spherical carbides quantitatively not only in the matrix but also along low/high-angle boundaries in different steels, where some discrepancies exist between experimental observations and simulation results (reasons discussed in 3.2.3).

All the models discussed in this chapter are mean field model, which treat carbide coarsening and dissolution processes separately, and none of the models gives full quantitative predictions for cementite coarsening in low alloy martensitic steels.

3.4 Objectives of this project

The overall aim of this project is to investigate and model the effects of different tempering conditions (time and temperature) and compositions (e.g. Cr, Mo, Si and V additions) on the development of precipitation during tempering for S690-based steels (low carbon low alloy martensitic steels). To achieve this, the following objectives have been established:

(1) Investigating the size, type, distribution and chemical composition of carbides formed in auto-tempered martensite and during early stages of tempering in three S690-based steels with different additions of Cr, Mo, V and Si to provide input data on the precipitate sizes at the onset of coarsening.

(2) Thermodynamic prediction of possible carbides with chemical composition under equilibrium and pseudo-equilibrium conditions (suppression of equilibrium phases) to investigate the precipitation sequence during tempering in S690-based steels and provide the equilibrium carbide compositions for the simulation of carbide coarsening.

(3) Kinetic modelling (including DICTRA model and mathematical model) for the coarsening of inter-lath cementite quantitatively, where inter-lath cementite constitutes most of the volume fraction. In the mathematical model, coarsening of larger inter-lath cementite particle and dissolution of smaller one will be treated simultaneously, where the experimental observation is used to validate the model.

Chapter 4 Methodology and Materials

4.1 Materials

Three laboratory steel plates (based on a commercial grade S690 steel) were supplied by Tata Steel (UK) that were hot rolled to ~35 mm thickness and air cooled. The chemical compositions and thicknesses of the samples are given in Table 4-1. Commercial S690 steel has a composition close to that of Base-Cr-Mo-V. Samples measuring 15×20×20 mm taken from the centre position of the Base, Base-Mo-V, and Base-Cr-Mo-V-Si plates to investigate tempering responses in S690-based steels with different additions of alloying elements.

Table 4-1. Chemical compositions and thicknesses of S690-based steels (wt %)

Name	C	Si	Mn	P	S	Cr	Mo	Al	N	Nb	Ti	V	B	Thickness
Base	0.17	0.29	1.2	0.015	0.002	-	-	0.03	0.004	0.03	0.024	-	0.0025	40mm
Base-Mo-V	0.17	0.28	1.2	0.015	0.002	-	0.5	0.03	0.004	0.03	0.026	0.05	0.0025	36mm
Base-Cr-Mo-V-Si	0.17	1.24	1.2	0.016	0.002	0.8	0.5	0.04	0.006	0.03	0.027	0.05	0.0025	32mm

4.2 Heat treatment

Samples measuring 15×20×20 mm (15mm through thickness), taken from the Base, Base-Mo-V, and Base-Cr-Mo-V-Si plates, were re-austenitised at 925 °C for an hour and then quenched into room temperature water to produce a fully lath martensite structure. Quenched samples of the Base, Base-Mo-V, and Base-Cr-Mo-V-Si steels were tempered for 1 hr, 2 hrs, 4 hrs, 8 hrs and 16 hrs at 600 °C to investigate the carbide development with different alloying element additions (Mo, V, Cr and Si).

4.3 Microstructural characterisation

4.3.1 Sample preparation

4.3.1.1 SEM and XRD sample preparation

The quenched and tempered specimens (perpendicular to the rolling direction) from the Base, Base-Mo-V, and Base-Cr-Mo-V-Si steel plates were prepared for characterisation. Samples for furnace heat treatment were prepared with 3 mm machined from the plate surface to remove any influence of surface scale or decarburisation and after heat treatment cut through the mid position for characterisation. All samples were mounted in conducting Bakelite for optical and SEM analysis. The mounted samples were ground and polished using Metlog Method E [162]. An additional 3 μm step using MD-Dac disc was used. The polished samples were ready for XRD measurements, and for SEM observations, the polished samples were lightly etched in 2 % nital.

4.3.1.2 TEM sample preparation

1. Thin foil sample preparation: Thin slices (approximately 500 μm thick) were machined from the mid-position of the quenched and tempered specimens (15×20×20 mm) of the Base, Base-Mo-V, and Base-Cr-Mo-V-Si steels using a diamond blade and cooling lubricant. Electron discharge machining (EDM) was used to prepare 3 mm diameter discs from the slices; care was taken to ensure that the discs did not bend during preparation. After cutting, the discs were ground with silicon carbide papers (grit no. 400-800-1200) to approximately 70 - 80 μm thickness. Electro-polishing process was carried out using a twin jet eletro-polisher (Tenupol-3) with 5 vol.% perchloric acid and

95 vol.% acetic acid solution at room temperature at 50 - 60 V potential giving a 0.16 - 0.18 A polishing current [30, 163]. At least five thin foil samples were prepared for each condition.

2. Carbon extraction replicas: Carbon extraction replica specimens were also prepared for selected tempered samples in the Base-Mo-V and Base-Cr-Mo-V-Si steels in order to measure the chemical compositions for very fine carbides by eliminating matrix composition effects. A schematic diagram of the preparation for carbon extraction replica specimens is shown in Figure 4-1. Firstly, the etched (using 2% nital) SEM samples were used for carbon deposition. A carbon film around 20 - 30 nm (colour grey-brown) was deposited on the etched sample surface. A sharp razor blade was used to cut the carbon film into several small squares (approximately 2×2 mm^2). The squares of the carbon film were removed from the sample surface by electrochemical etching using a solution of 5 % HCl in methanol at 3 volts potential, and were then washed in methanol followed by distilled water. Finally, the carbon film squares were removed from the distilled water and mounted onto copper grids for TEM examination.

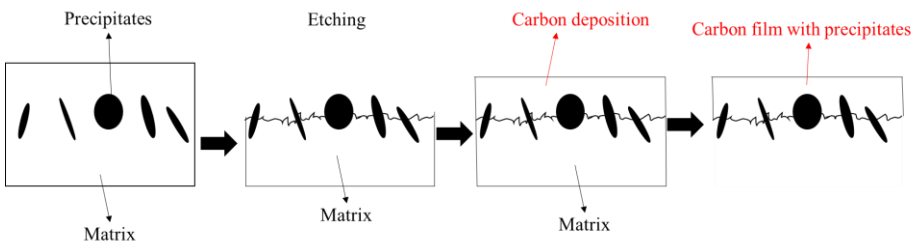

Figure 4-1. Schematic diagram showing the carbon extraction replica specimen preparation process.

4.3.2 Scanning electron microscopy

The precipitates in the quenched and tempered Base, Base-Mo-V, and Base-Cr-Mo-V-Si specimens were characterised using a JEOL 7000 scanning electron microscope (SEM) operating at 20 kV with a field emission gun (FEG). Generally, the magnification for the SEM images was X12000 to observe the development of precipitation for all conditions. However, in terms of characterising the precipitate size, volume fraction, number density and particle separation during tempering, the magnification of the SEM images was chosen differently in order to obtain a similar number of precipitates in each condition. At least five SEM images (including approximately 1000 particles) were selected, and Axiovision 4.6.3 image analysis software was used to obtain the particle sizes (length, width, and radius based on the equivalent circle diameter (ECD) method), distribution, number densities, volume fractions and separations between particles for tempered samples. Here, the number density and volume fraction measurements were based on the assumption that all the precipitates in the SEM images were from the surface of the specimens.

4.3.3 Transmission electron microscopy

A JEOL 2100 (200 kV) transmission electron microscope was used to acquire higher magnification images of carbides and confirm the carbide types present for the quenched and tempered samples of the three steels. Bright field (BF) imaging was used to characterise the morphology of precipitates, and compared with SEM results. Selected area diffraction patterns (SADP) and dark field (DF) images were used to determine the structure and type of the elliptical carbides in the laths and on the lath boundaries during

tempering, where three independent SAD patterns were included in each tempering condition for the three steels in this thesis (more than 20 particles were observed). FEI Tecnai F20 and FEI Talos F220X scanning transmission electron microscope (STEM) under high angle annular dark field (HAADF) imaging mode with energy dispersive X-ray spectroscopy (EDS) technique was used for the quantitative chemical analysis on individual particles in thin foil and carbon replica specimens; furthermore, elemental mapping was carried out to analyse chemical variations among different particles.

In order to accurately ascertain the auto-tempered carbide types within the laths for the three steels during quenching, the habit planes for the needle/plate-shaped carbides were indexed. Single surface trace analysis was carried out on 20 different areas from the TEM bright field images and SAD patterns. The needle/plate-like carbides existed normally in different orientations, and the interface planes were curved gently along its length, Figure 4-2 (a). However, the curved interface can be replaced by a single mean parallel plane to it, as shown in Figure 4-2 (a), and the plane normal **n**(hkl) to the interface trace should be marked on the TEM bright field images. The indexed SAD pattern was placed on the bright field image, and the angles θ_1 and θ_2 of the trace normal **n1**(hkl) from two **g** vectors in the SAD pattern were measured, as shown in Figure 4-2 (c). The needle was photographed at several beam directions. For each photograph, the true needle direction must lie in the plane defined by the cross product of the projected line and the zone axis. The needle direction was therefore the intersection of the great circles corresponding to these planes, which was produced by the CaRine crystallography software.

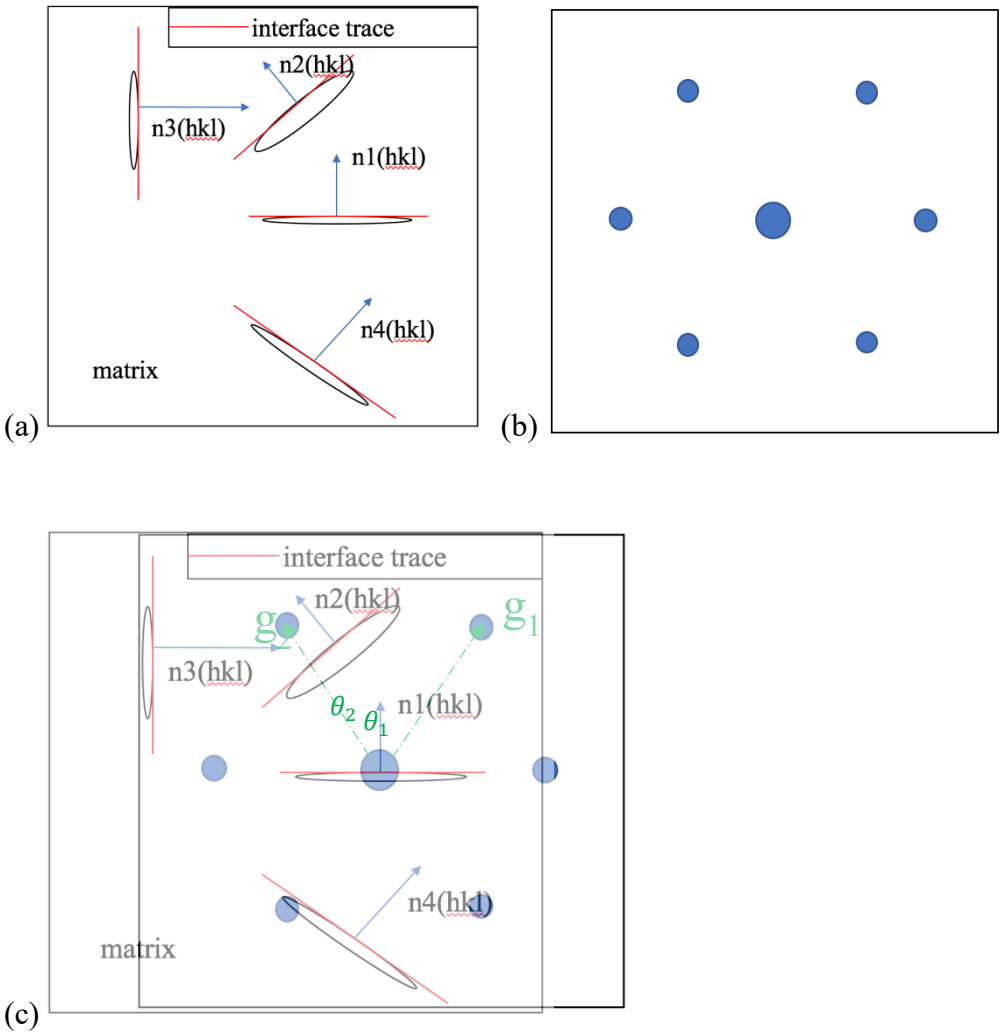

Figure 4-2. The schematic diagram showing the stages of determination of the interface planes.

In addition, the number percentages for different as-quenched carbides were confirmed using the bright field images from <100>α beam direction, where 10 different areas (around 1000 particles) were used.

Furthermore, in terms of understanding the development of precipitates during tempering, especially for the Base-Mo-V and Base-Cr-Mo-V-Si steels, it is necessary to measure the number density for very fine particles, which are not resolvable in SEM images. First of all, the TEM foil thickness is needed. Kossel-Möllenstedt (K-M) fringes

[164] in the convergent beam electron diffraction (CBED) pattern were used to work out the thickness of TEM samples, because the number of fringes increased by one as the thickness increased by one extinction distance. The measurements were carried out under two-beam condition with only one strong (hkl)-reflection [165].

Based on the two beam dynamic theory of electron diffraction, the equation used to determine the foil thickness t is

$$(\frac{S_i}{n_i})^2+(\frac{1}{n_i})^2(\frac{1}{\xi_g})^2=(\frac{1}{t})^2 \qquad \text{Equation 4-1}$$

Where S_i is the deviation for the i^{th}-fringe, ξ_g is the extinction distance and n_i is the number of fringes counted from the centre-line [166]. S_i can be calculated as

$$S_i=\frac{\lambda}{d^2}(\frac{\Delta\theta_i}{2\theta_B}) \qquad \text{Equation 4-2}$$

Where λ is the wavelength of the incident electrons, d is the inter-planar spacing for the operating reflection, $\Delta\theta_i$ is the separation between the chosen line to the centre-line, and θ_B is the separation between centre spot and diffracted spot, Figure 4-3. Plotting $(\frac{S_i}{n_i})^2$ against $(\frac{1}{n_i})^2$, and if the plot is a straight line, the foil thickness t is obtained by the intercept of the straight line with the $(\frac{S_i}{n_i})^2$ axis, Figure 4-4. Very low (hkl) values should be avoided due to the multiple scattering from systematic reflections.

In this project, the thickness measurements were carried out close to [113] zone axis using **g**=301. An example of the foil thickness measurement using CBED method for the as-quenched Base-Mo-V sample is shown in Figure 4-5 and Table 4-2. S_i was calculated based on Equation 4-2 with the inter-planar spacing input d_{301}=0.911 nm and the separation between different fringes, Table 4-2. All the $(S_i/n_i)^2$ data were plotted as a straight line against $(1/n_i)^2$ with the n_i value ranging 1 - 4, Figure 4-5 (b), and the intercept between the y-axis and the straight line was $1/t^2$=0.9961 nm^{-2}. Then the foil thickness, in this example, was estimated as t=155 nm.

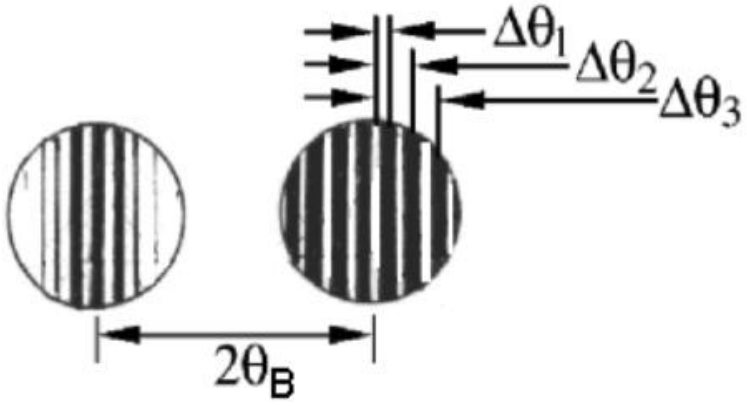

Figure 4-3. The separation 2 θ_B and $\Delta\theta_i$ under two-beam condition [165].

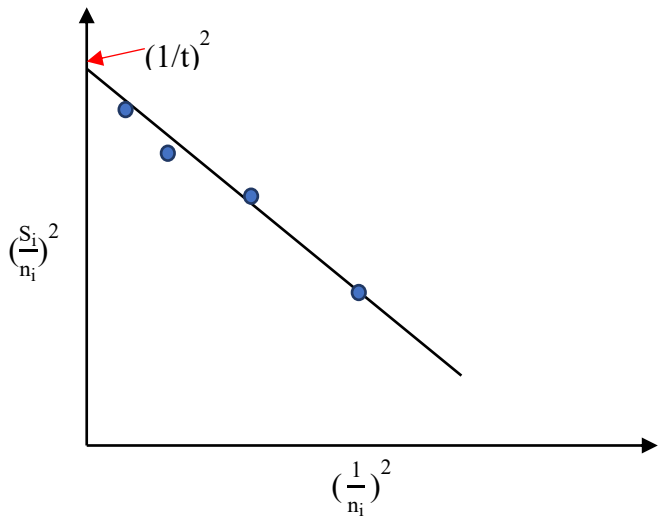

Figure 4-4. Schematic diagram of plotting $(S_i/n_i)^2$ against $(1/n_i)^2$. If the plot is a straight line, the intercept is $(1/t)^2$.

Table 4-2. The CBED data for TEM sample thickness measurement

S_i/nm^{-1}	n_i	$S_i^2/n_i^2/nm^{-2}$
0.0043	1	1.869×10^{-5}
0.0120	2	3.605×10^{-5}
0.0185	3	3.800×10^{-5}
0.0255	4	4.051×10^{-5}

(a)

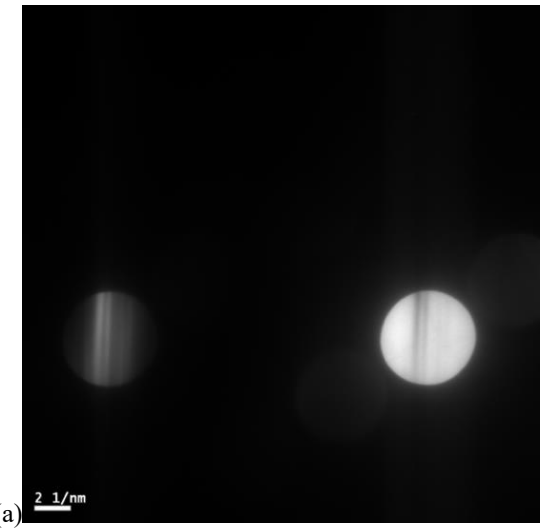

(b)

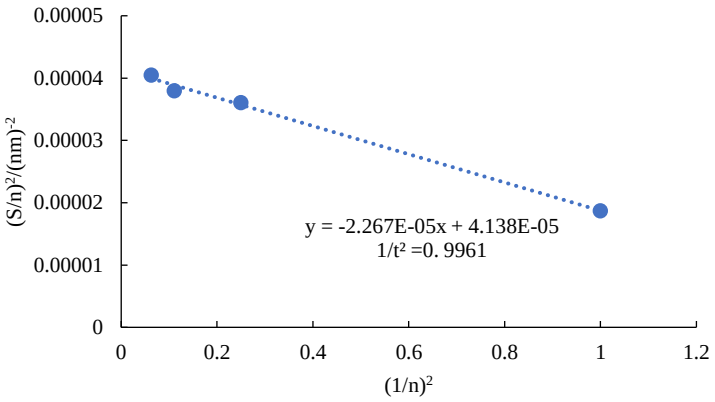

Figure 4-5. (a) A CBED pattern taken near [113] zone axis using **g**=301 for the as-quenched Base-Mo-V steel; (b) $(S_i/n_i)^2$ is plotted as a function of $(1/n_i)^2$ and the intercept of the straight line with the y-axis is $1/t^2$.

Approximately 1000 very fine particles (including needle-shape and elliptical shape with smaller size, i.e. red arrowed in Figure 5-16) were selected for the number density measurements in different tempered samples, and following equation was employed [167]:

$$N_V = \frac{N_A}{t} \qquad \text{Equation 4-3}$$

Where, Nv is the number density of particles per unit volume in a foil, N_A is the number density of particles per unit area and t is thickness of the specimens.

4.3.4 XRD measurements

XRD measurements were carried out to determine the matrix lattice parameter for the three steels in the as-quenched condition and after tempering in order to determine the amount of carbon retained in solid solution. In addition, XRD measurements were also used to check whether there was a significant volume fraction of retained austenite present after water quenching in the three steels, especially when it was greater than 1-2 % [15].

X-ray diffraction normally occurs with a parallel monochromatic beams of X-rays interacting with crystalline materials, and Figure 4-6 shows the diffraction of X-rays in a crystal where the atoms are arranged in four planes with inter-plane spacing d. For the

occurrence of diffraction, Bragg's Law should be satisfied, which is used to determine the inter-planar distance in the material.

$$\lambda=2d\sin\theta \qquad \text{Equation 4-4}$$

Where d is the inter-planar distance, θ is the half angle of the diffracted angle, and λ is the wavelength of the X-ray, depending on the type of the target.

A PANanlytical Empyrean XRD instrument was used with a cobalt target (wavelength λ=1.78901Å), and scanning time of 30 mins for a 2θ range from 45° to 128°. As discussed in Chapter 5, the martensite matrix was auto-tempered during quenching for the three steels, hence, the matrix would be expected to be body centred cubic ferrite. Four peaks ((011)α, (002)α, (211)α and (022)α) were detected and used to calculate the individual lattice parameter for the ferritic matrix in the three steels, Figure 4-7 (a); no austenite peak was found indicating no or an insignificant volume fraction of retained austenite present after quenching. The relationship between the calculated lattice parameters from the four peaks and $\cos^2\theta$ was obtained, as in Figure 4-7(b) for the as-quenched Base steel, where the relatively accurate lattice parameter was extrapolated from the intercept with the vertical axis.

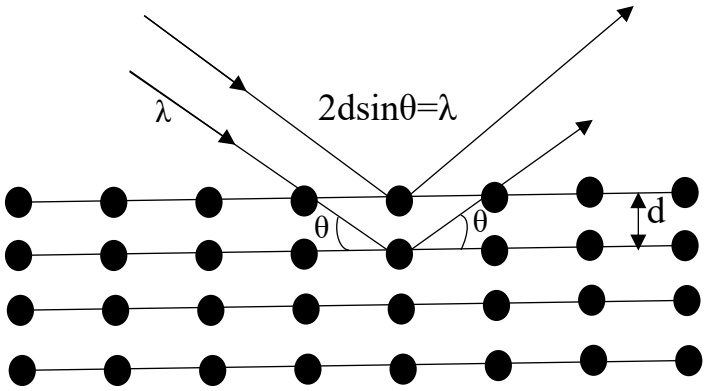

Figure 4-6. Diffraction of X-rays in a crystal where the spheres represent the atoms in the crystal structure.

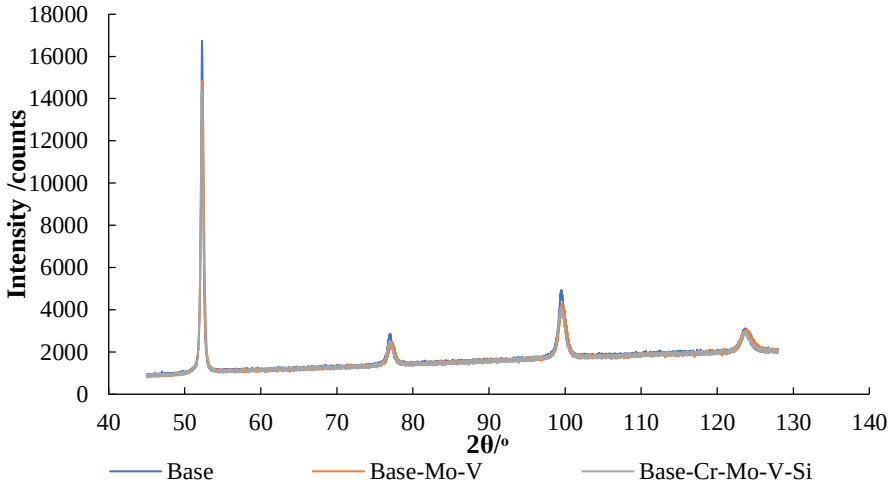

(a)

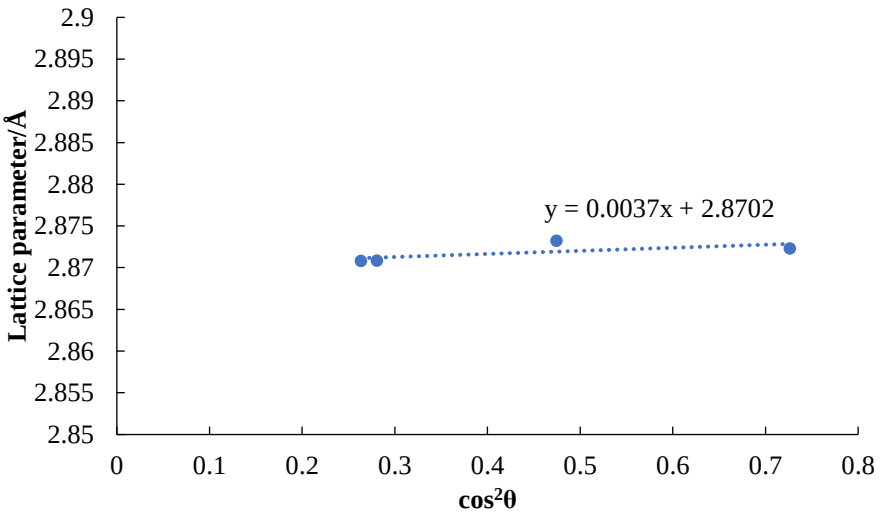

(b)

Figure 4-7. (a) The measured XRD spectra for the as-quenched three steels; (b) the relationship between the lattice parameters and $\cos^2\theta$ from (011)α, (002)α, (211)α and (022)α peaks for the as-quenched Base steel, where the comparatively accurate lattice parameter is the intercept of Y-axis as 2.8702 Å.

4.4 Thermodynamic prediction using Thermo-Calc software

Thermo-Calc version 4.1 and the TC-Fe7 database with graphical mode were used to predict equilibrium and pseudo-equilibrium phases and their compositions for the steels, as listed in Table 4-1. The specific phases (BCC iron, FCC iron, cementite, MC, M_2C, M_6C, M_7C_3 and $M_{23}C_6$), depending on the chemical compositions for the three steels, were selected to simulate equilibrium and pseudo-equilibrium carbides (pseudo-equilibrium due to the addition of Mo, Cr, and V) at 1 ºC intervals from 500 ºC to 650 ºC. The pseudo-equilibrium carbides were predicted with the alloy equilibrium precipitates suppressed: MC suppressed for Base-Mo-V steel, and $M_{23}C_6$, M_7C_3 and MC suppressed for Base-Cr-Mo-V-Si steel.

The predicted equilibrium and pseudo-equilibrium precipitates for the Base, Base-Mo-V and Base-Cr-Mo-V-Si steels at 600 ºC are listed in Table 4-3. The equilibrium precipitate for the Base steel (no alloying elements added) is predicted as cementite and the equilibrium volume percentage of cementite is predicted as 2.5 %. However, for the Base-Mo-V and Base-Cr-Mo-V-Si steels, the equilibrium precipitates are predicted as MC (Base-Mo-V), and M_7C_3, $M_{23}C_6$ and MC (Base-Cr-Mo-V-Si) respectively. In addition, the pseudo-equilibrium carbides are both predicted as cementite and M_2C for the Base-Mo-V and Base-Cr-Mo-V-Si steels at 600 ºC.

Table 4-3. Predicted equilibrium and pseudo-equilibrium carbides for three S690-based steels due to the addition of Cr, Mo and V (the elements in bold for the carbides are the predominant ones)

	Base	Base-Mo-V	Base-Cr-Mo-V-Si
equilibrium precipitates	Cementite((**Fe**Mn)$_3$C)	MC((**VMo**)C)	M_7C_3((**Cr**FeMoMnV)$_7$C$_3$) MC((**VMo**Cr)C) $M_{23}C_6$((**Cr**FeMn)$_{23}$C$_6$)
pseudo-equilibrium precipitates	-	Cementite((**Fe**MnMoV)$_3$C) M_2C((**Mo**VMn)$_2$C)	Cementite((**Fe**MnCrMoV)$_3$C) M_2C((**Mo**VMnCr)$_2$C)

Chapter 5 Characterisation of precipitation and carbide coarsening for S690-based steels during the early stages of tempering

In order to understand the influence of different alloying elements on the carbide evolution and coarsening during the early stages of tempering, characterisation of carbide precipitation and coarsening has been carried out by SEM, TEM, STEM and XRD techniques in three S690-based steels after different tempering conditions (time and temperature). The carbide type, size, volume fraction, number density, chemical composition and separations between particles have been studied for selected samples.

5.1 The occurrence of auto-tempering during water quenching in the three steels

As shown in Figure 5-1 and Figure 5-2, auto-tempering occurs in the three steels resulting in carbide precipitation within the martensite laths during water quenching, which is associated with high Ms temperatures (> 400 °C) predicted using the Steven and Haynes equation [21], Table 5-1. For the Base and Base-Mo-V steels, the Ms temperatures are both above 420 °C, thus, cementite is expected to precipitate based on the reported results in steels with similar compositions (Ms ≥ 410 °C) in Table 5-1[27, 28, 30]. However, auto-tempering might be inhibited in the Base-Cr-Mo-V-Si steel with a lower Ms temperature, Table 5-1, and the transformation from ε/ε'-carbides to cementite might be also retarded consistent with a higher content of Si (1.3 wt %) in this steel.

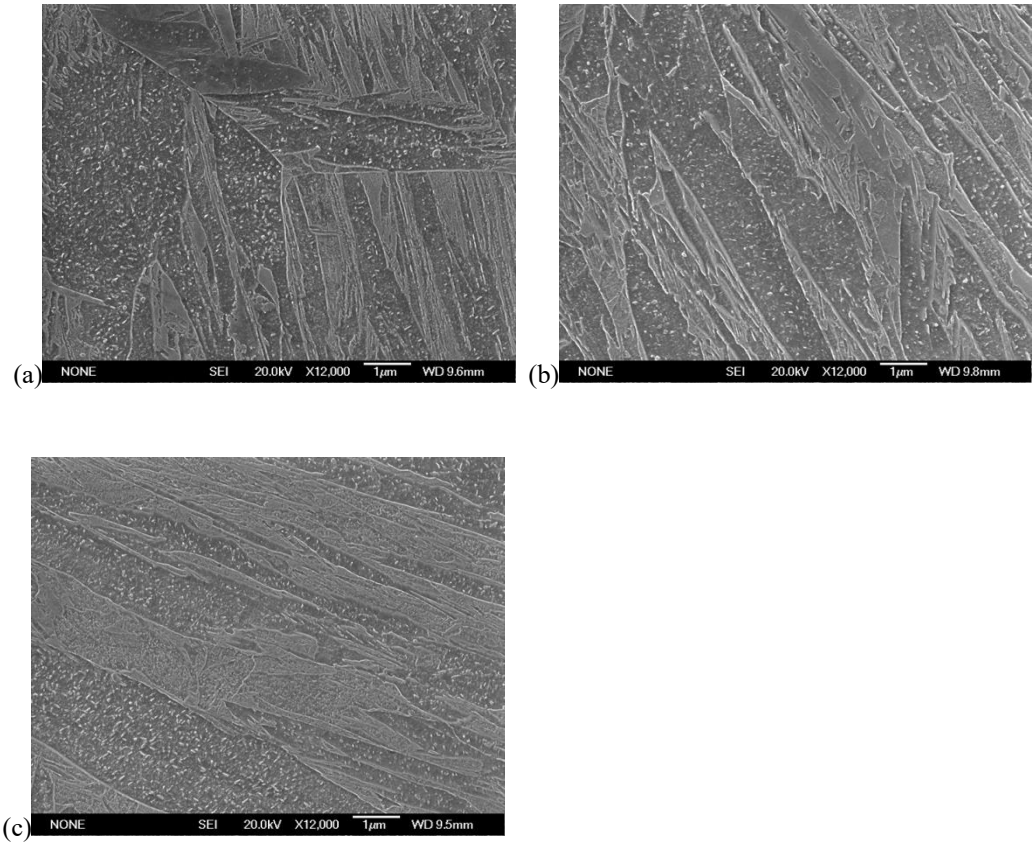

Figure 5-1. SEM images showing the as-quenched carbides present within the martensite laths: (a) Base steel; (b) Base-Mo-V steel; (c) Base-Cr-Si-Mo-V steel.

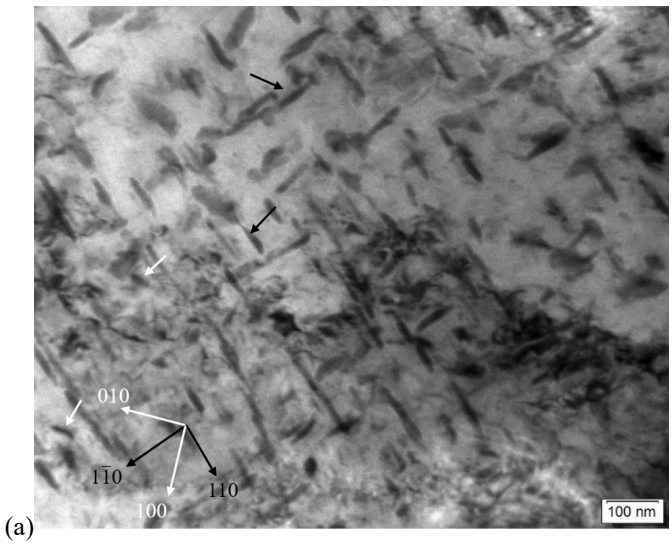

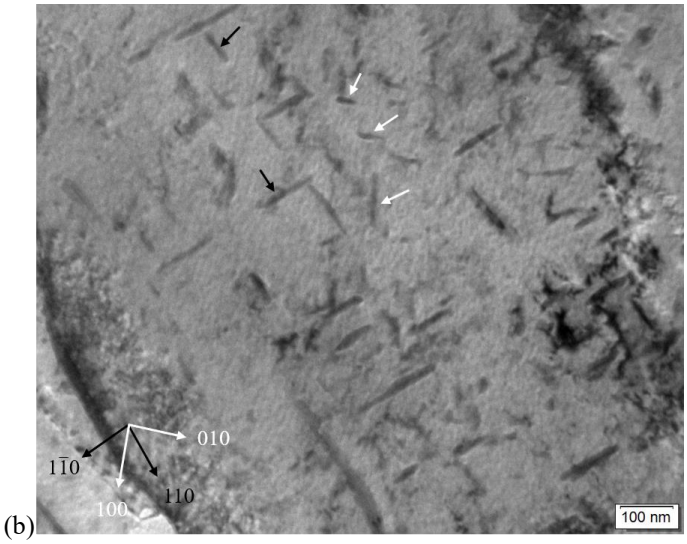

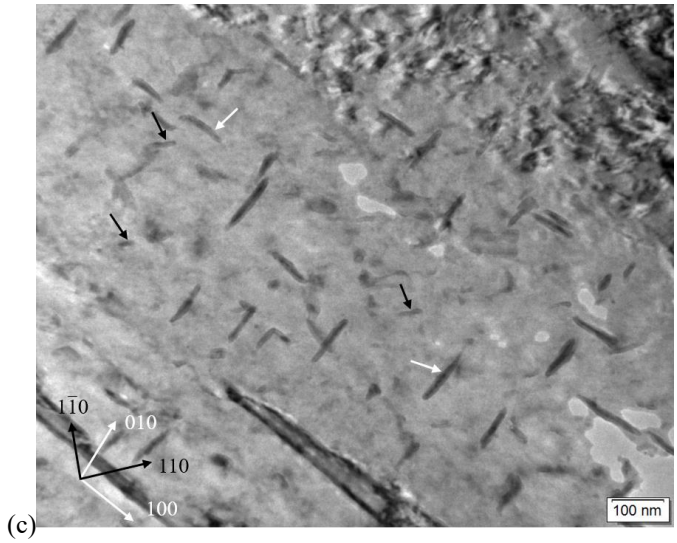

Figure 5-2. TEM images showing the as-quenched carbides present within the martensite laths from <001>α beam direction: (a) Base steel; (b) Base-Mo-V steel; (c) Base-Cr-Mo-V-Si steel. The black arrows indicate cementite, whereas the white arrows indicate ε'-carbide.

Table 5-1. Ms temperatures predicted using the Steven and Haynes equation [21] for the three steels

Alloy steels	Martensite start temperature (°C)
Base steel	426
Base-Mo-V steel	423
Base-Cr-Si-Mo-V steel	405

As the martensitic matrix has auto-tempered, the matrix would be expected to be body centred cubic rather than body centred tetragonal. In order to determine the amount of retained carbon in solid solution, the lattice parameters for the as-quenched and selected tempered samples in the three steels have been measured using XRD; and the lattice parameter-alloying composition equation, derived by Bhadeshia [168], has been applied:

$$a_{BCC} = 0.28664+(3a_{Fe}^2)^{-1} \times[(a_{Fe} -0.0279x_C^{\alpha})^2(a_{Fe}+0.2496x_C^{\alpha})-a_{Fe}^3]- 0.003x_{Si}^{\alpha}+0.006x_{Mn}^{\alpha} +0.007x_{Ni}^{\alpha} +0.031x_{Mo}^{\alpha}+0.005x_{Cr}^{\alpha}+0.0096x_V^{\alpha}$$ Equation 5-1

Where, a_{Fe} is the lattice parameter of pure ferrite (0.28664nm [169]); x_i^{α} represents the mole fraction of species i in the matrix: in the as-quenched condition, x_i^{α} is equivalent to the chemical composition in the steels; after tempering for 2 hrs in the Base steel (reaching equilibrium condition, discussed in section 5.2), x_i^{α} is the equilibrium substitutional alloying content of species i in the matrix from Thermo-Calc calculation; a_{BCC} is the measured lattice parameter (from Table 5-2). The amount of carbon trapped in solid solution after quenching in the Base and Base-Mo-V steels is similar, Table 5-2,

indicating a similar degree of auto-tempering. However, the retained carbon content in the as-quenched Base-Cr-Mo-V-Si steel is slightly higher than that in the Base and Base-Mo-V steels, which indicates that a little bit more carbon is trapped in solid solution in this steel due to the effect of Si slowing down carbon diffusion to form carbides during auto-tempering and the lower Ms temperature.

Table 5-2. Lattice parameters and retained carbon contents in the matrix for the three steels

	Lattice parameter/ nm	Retained carbon content in the matrix (/ wt %)
Base-AQ	0.28702	0.108
Base-Mo-V-AQ	0.28712	0.109
Base-Cr-Mo-V-Si-AQ	0.28717	0.130
Base-2 hrs	0.28679	0.037
Base-equilibrium (Thermo-Calc)	-	0.027

As-quenched carbides are present within the martensite laths for the three steels, Figure 5-2, due to the relatively high Ms temperatures (>400 °C) promoting carbide precipitation. Determination of the zone axis and indices of the in-plane normal to the long axis of the plate/needle-shaped carbides in the as-quenched condition has been used to construct the great circles of potential habit planes to confirm the type of as-quenched carbides present in the three steels. As shown in Figure 5-3, these great circles mainly form two groups; the first has a common intersection around {012}α pole, which would

be consistent with ε'-carbides [32, 170], whilst the second group intersects around the {011}α pole - a common habit plane for cementite [35, 36, 38, 47]. In addition, there are few great circles intersected around {001}α pole, being consistent with ε'/ε -carbides, due to their formation well beyond any early stage of "spinodal" clustering [23, 29, 35-38]. Therefore, cementite and ε'-carbides are coexisted within the laths after water quenching in the three steels. As reported in literature [23, 38, 39], cementite and ε'-carbide precipitates are aligned along <110>α and <100>α respectively when the electron-beam coincides with <001>α. Thus, the relative amounts of cementite and ε'-carbides can be determined, Figure 5-4. In the Base and Base-Mo-V steels, cementite particles are the predominant as-quenched carbides with few ε'-carbides retained after auto-tempering; however, in the Base-Cr-Mo-V-Si steel, it has been found that ε'-carbides constitute a larger number percentage compared to cementite.

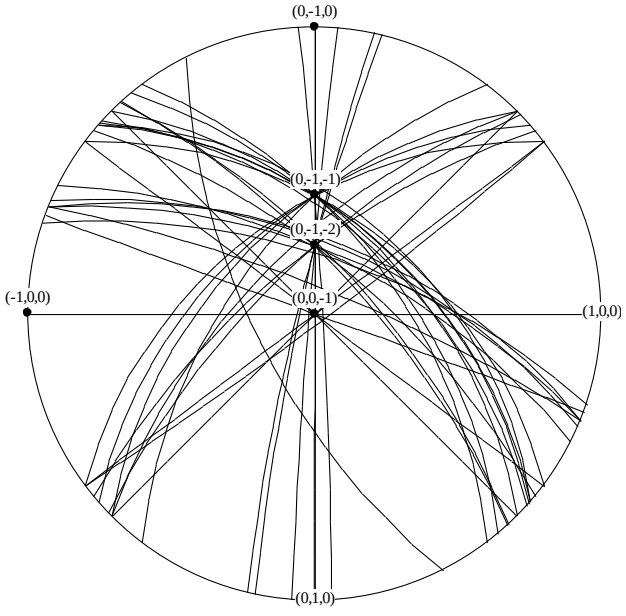

(a)

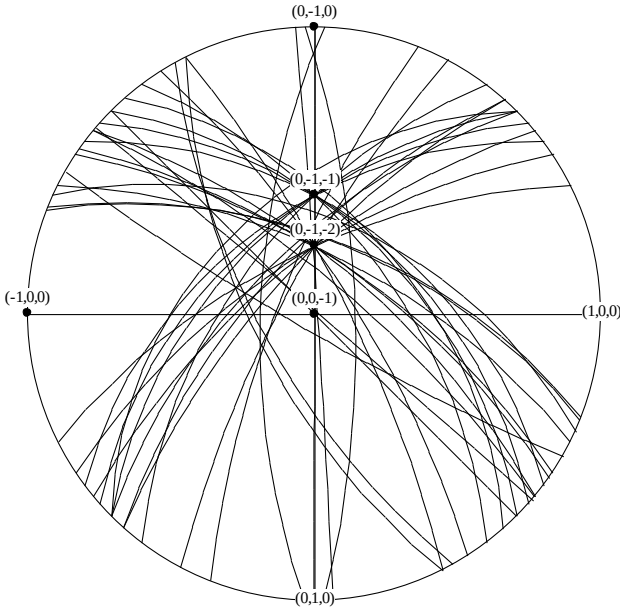

(b)

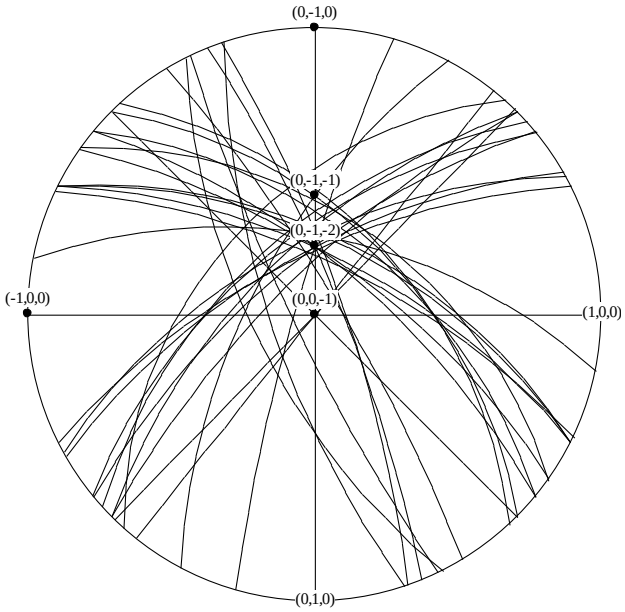

(c)

Figure 5-3. Stereograms indicating the habit planes for the auto-tempered carbides formed during water quenching for the three steels: (a) Base steel; (b) Base-Mo-V steel; (c) Base-Cr-Mo-V-Si steel.

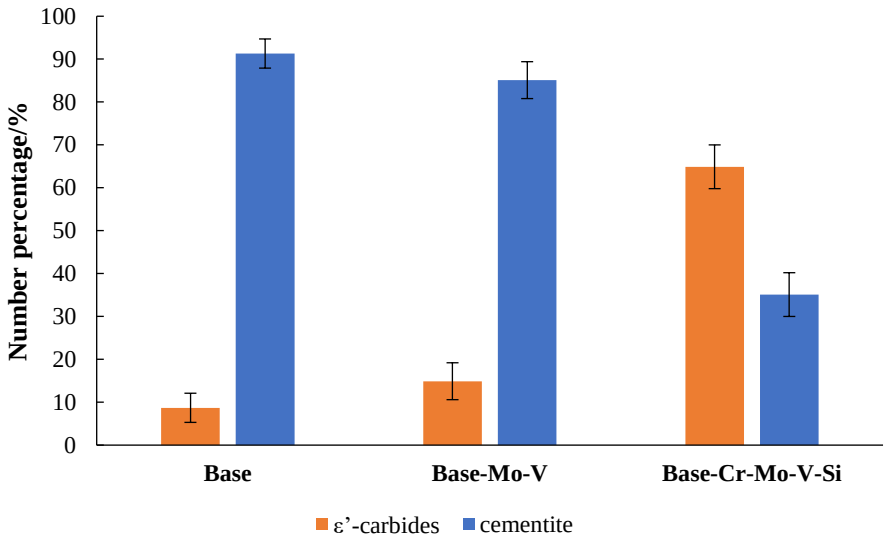

Figure 5-4. The number percentages of cementite and ε'-carbides in the as-quenched condition in the three steels.

5.2 Carbide precipitation and coarsening in the Base steel

As shown in Figure 5-5 (a) and Figure 5-6 (a), elliptical (sometimes spherical) carbides are observed in the laths and on lath boundaries with some fine needle-shaped carbides (arrowed in Figure 5-6(a)) remaining within the laths after tempering for 1 hour. The elliptical carbides are consistent with cementite, where the carbide type has been determined by selected area diffraction patterns (SADP) and dark field images for three independent particles in Figure 5-7, Figure 5-8 and Figure 5-9. The process for the identification of zone axis from cementite is described as followed:

Step 1. Comparing the measured d-spacing for the diffracted spots with the theoretical d-spacing of different poles from cementite to determine the corresponding poles for diffracted spots in the SAD pattern. For example, in Figure 5-7 (b), comparing the measured d-spacing of diffracted spots 1 - 4, Table 5-3, with the theoretical values in Table 5-4 to determine that the diffracted spots 1/3, 2 and 4 are from $\{111\}_{cementite}$, $\{011\}_{cementite}$ and $\{100\}_{cementite}$ respectively.

Step 2. Measuring the angles between the diffracted spots, and matching the measured angles with the theoretical ones between the determined poles in step 1. For instance, the angles between the diffracted spots 2 and 3, and between 2 and 4 are 41.7° and 90° respectively in Figure 5-7 (b), which is consistent with the theoretical angles of 41.93° between $\{011\}_{cementite}$ and $\{111\}_{cementite}$, and of 90° between $\{011\}_{cementite}$ and $\{100\}_{cementite}$ respectively.

Step 3. Confirming the zone axis for the SAD pattern. For example, the zone axis of the SAD pattern in Figure 5-7 (b) for the elliptical particle is the cross product of the two vectors: $[011]\otimes[100]=[01\bar{1}]$ of cementite.

The SAD patterns for another two individual particles in Figure 5-8 (b) and Figure 5-9 (b) are identified from $[00\bar{1}]$ and [312] zone axis of cementite respectively, all of which have confirmed that elliptical carbides precipitated within the laths and on lath boundaries after tempering for 1 hr at 600 °C are consistent with cementite.

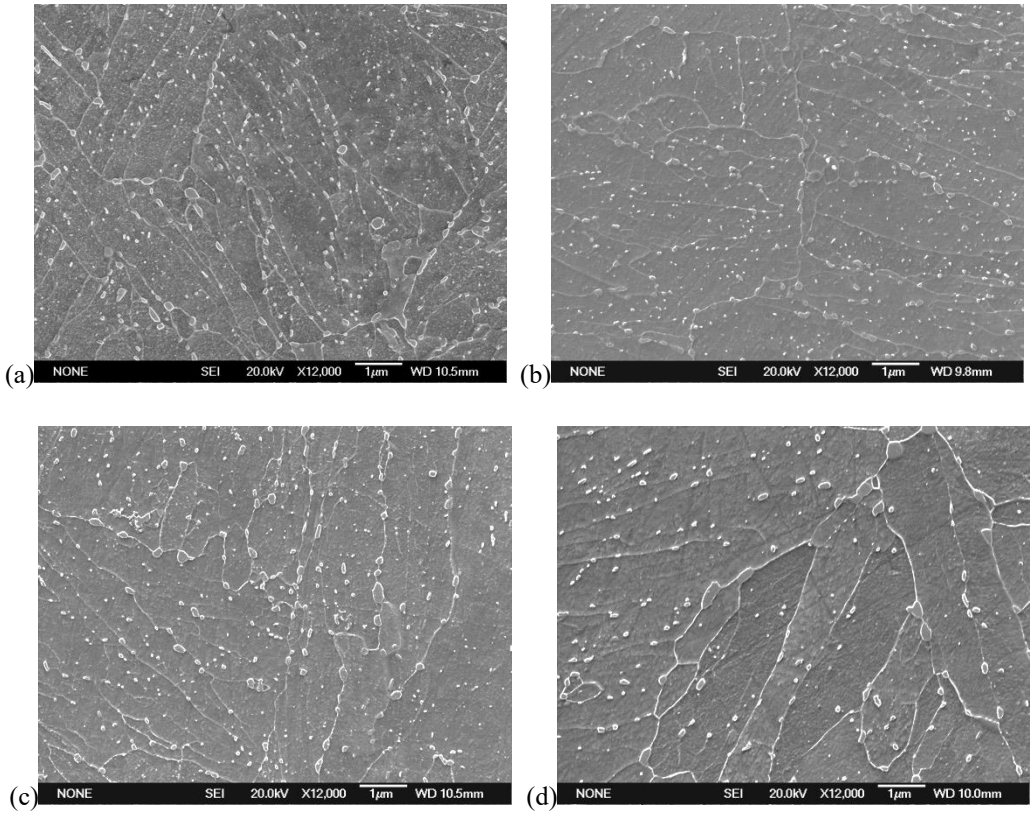

(e) 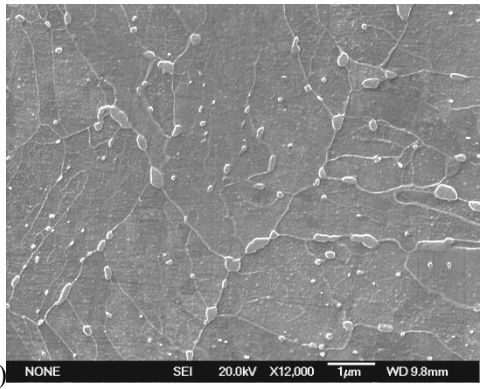

Figure 5-5. SEM images showing the precipitation and coarsening of carbides in the Base steel tempered at 600 °C for different times: (a) 1 hr; (b) 2 hrs; (c) 4 hrs; (d) 8 hrs; (e) 16 hrs.

(a) 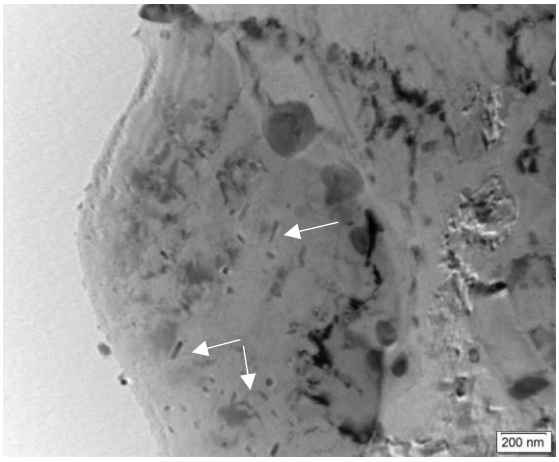

(b) 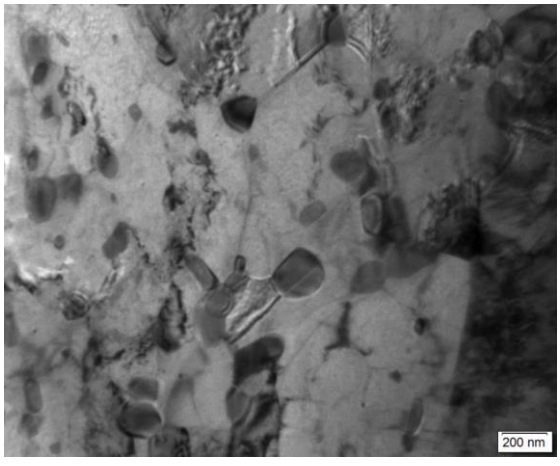

(c) 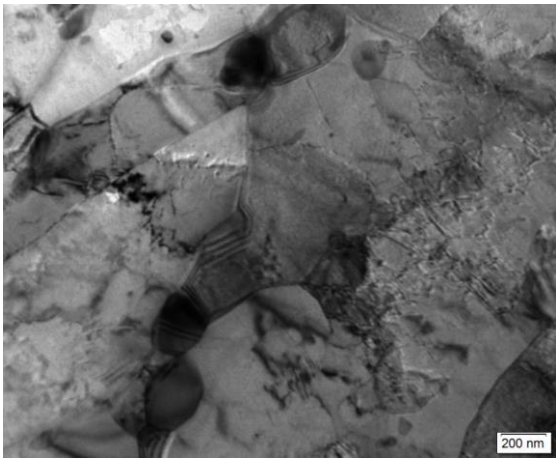

Figure 5-6. TEM bright field images showing the morphology of the carbides tempered at 600 °C for different times in the Base steel: (a) 1 hr; (b) 2 hrs; (c) 16 hrs. The white arrows indicates the needle-shaped carbides present after tempering for 1 hour at 600 °C in this steel.

(a) 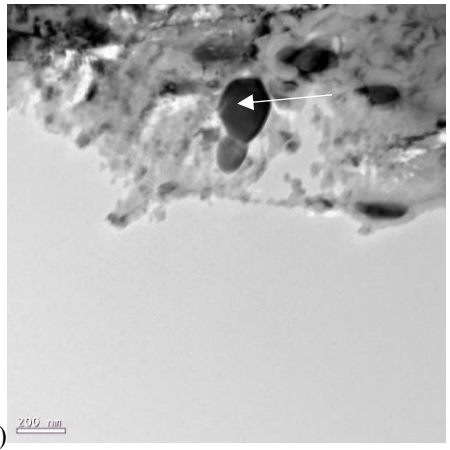

(b) 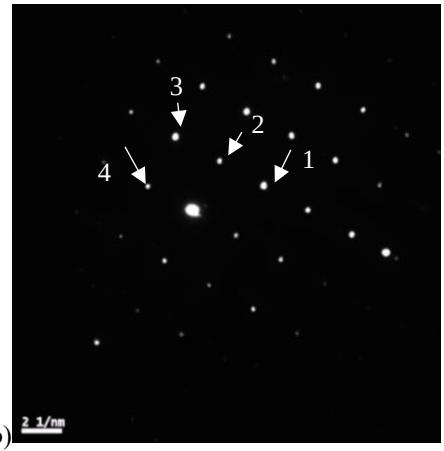

(c) 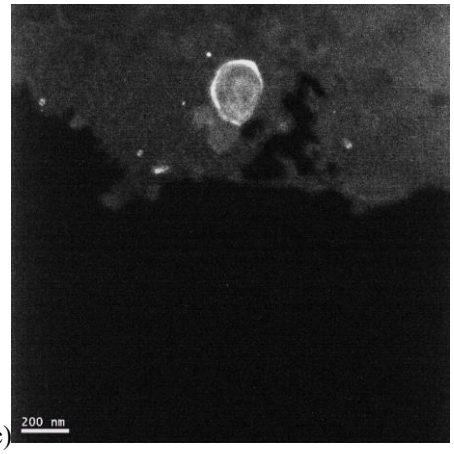

(d) 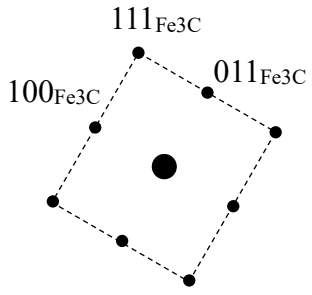

Figure 5-7. Characterisation of elliptical carbides after tempering for 1 hr at 600 °C in the Base steel: (a) Bright field image of a typical elliptical carbide; (b) SAD pattern for the particle consistent with the [01$\bar{1}$] zone axis of cementite as shown in (d); (c) Dark field image of the elliptical carbide with diffracted spot (111) selected.

Table 5-3. The measured d-spacing for the diffracted spots in the SAD pattern in Figure 5-7

	1	2	3	4
d-spacing/ nm	0.301	0.404	0.301	0.448

Table 5-4. The theoretical d-spacing of different poles for cementite

(using lattice parameter a=0.452 nm, b=0.508 nm, c=0.673 nm [171])

h	k	l	d-spacing/ nm
1	0	0	0.452
0	1	1	0.406
1	1	1	0.302

(a) 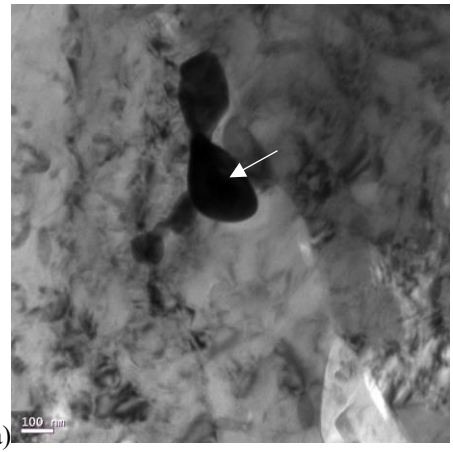

(b) 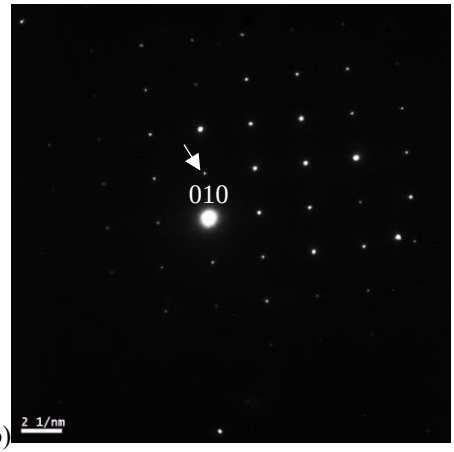

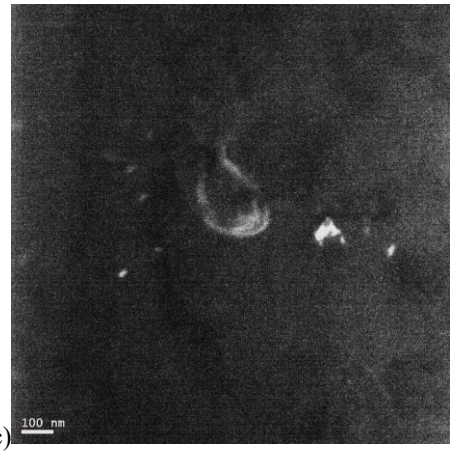

(c)

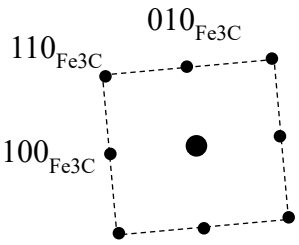

(d)

Figure 5-8. Characterisation of elliptical carbides after tempering for 1 hr at 600 °C in the Base steel: (a) Bright field image of a typical elliptical carbide; (b) SAD pattern for the particle consistent with the [00$\bar{1}$] zone axis of cementite as shown in (d); (c) Dark field image of the elliptical carbide with the diffracted spot (010) selected.

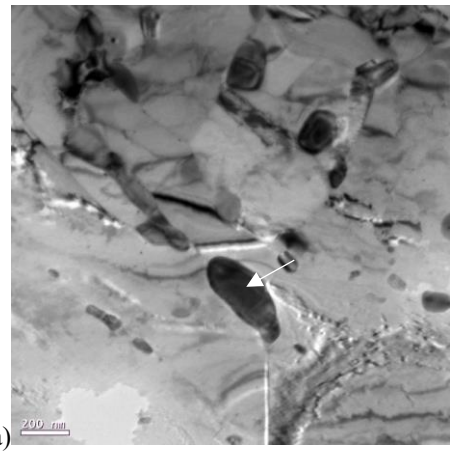

(a)

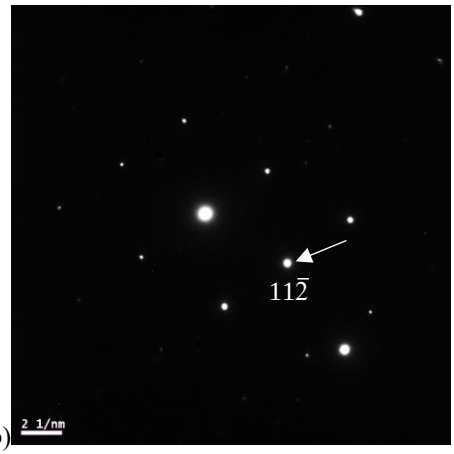

(b)

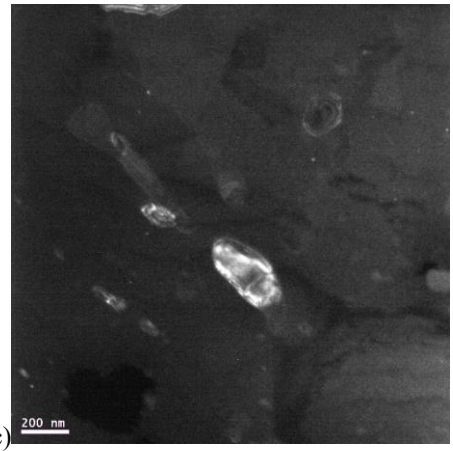

(c)

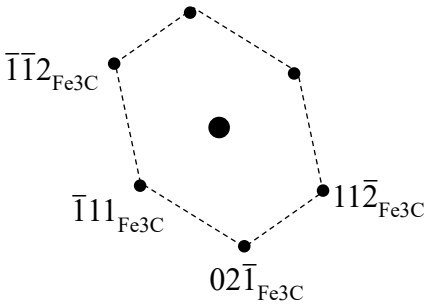

(d)

Figure 5-9. Characterisation of elliptical carbides after tempering for 1 hr at 600 °C in the Base steel: (a) Bright field image of a typical elliptical carbide; (b) SAD pattern for the particle consistent with the [312] zone axis of cementite as shown in (d); (c) Dark field image of the elliptical carbide with the diffracted spot ($11\bar{2}$) selected.

Cementite has been reported to gradually spheroidise, changing shape from needle/plate-shape to rod-shape and finally spherical shape with larger sizes, when tempering at 400 - 700 °C [53]. During tempering from 2 hrs to 16 hrs at 600 °C , all the intra- and inter-lath carbides become elliptical (even spherical) in shape and gradually coarsen with time, Figure 5-5 (b) - (e) and Figure 5-6 (b) (c). These elliptical carbides are consistent with cementite as well, as shown by the SAD patterns and dark field images for three independent particles after tempering for 2 hrs in Figure 5-10, Figure 5-11 and Figure 5-12, where [$00\bar{1}$], [$01\bar{1}$] and [210] zone axis of cementite have been identified from SAD patterns. The measured volume fraction for the elliptical cementite on tempering from 2 hrs onwards is listed in Table 5-5, which remains approximately constant with time and is consistent with the equilibrium volume fraction for cementite (predicted from Thermo-Calc) of 2.5%, allowing for experimental overestimation due to the etching effect. As there are no extra significant alloying elements in this steel that are expected

to affect the nature of the carbides, i.e. little potential for alloy carbides, once the equilibrium cementite volume fraction is established, Ostwald ripening occurs as cementite size increases, where large particles grow at the expense of the smaller ones [54, 55].

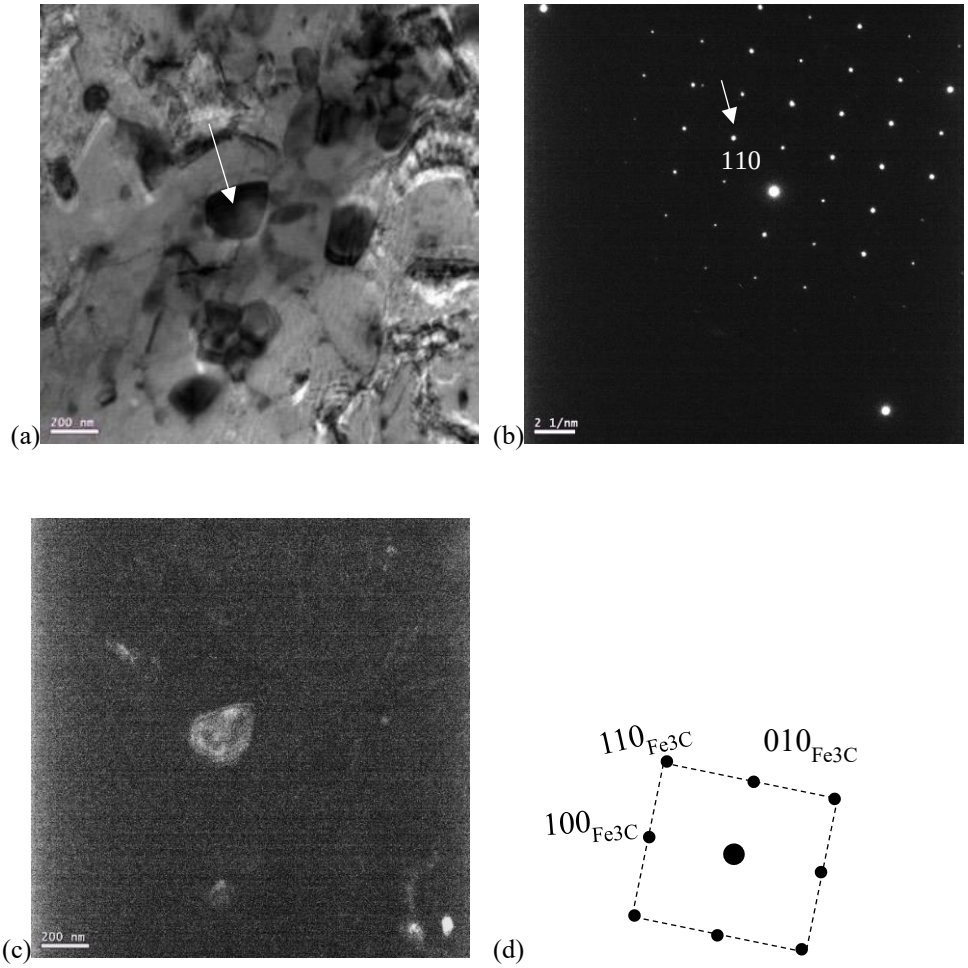

Figure 5-10. Characterisation of elliptical carbides after tempering for 2 hrs at 600 °C in the Base steel: (a) Bright field image of a typical elliptical carbide; (b) SAD pattern for the particle consistent with the $[00\bar{1}]$ zone axis of cementite as shown in (d); (c) Dark field image of the elliptical carbide with the diffracted spot (110) selected.

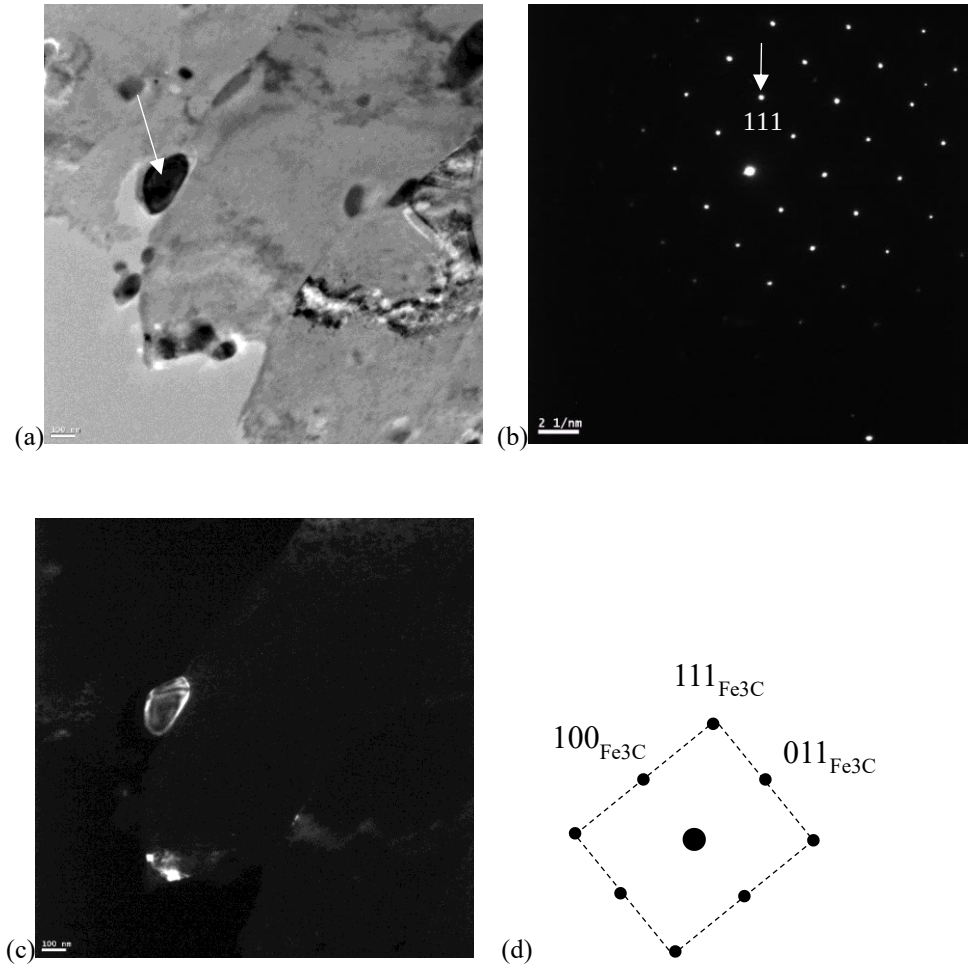

Figure 5-11. Characterisation of elliptical carbides after tempering for 2 hrs at 600 °C in the Base steel: (a) Bright field image of a typical elliptical carbide; (b) SAD pattern for the particle consistent with the $[01\bar{1}]$ zone axis of cementite as shown in (d); (c) Dark field image of the elliptical carbide with the diffracted spot (111) selected.

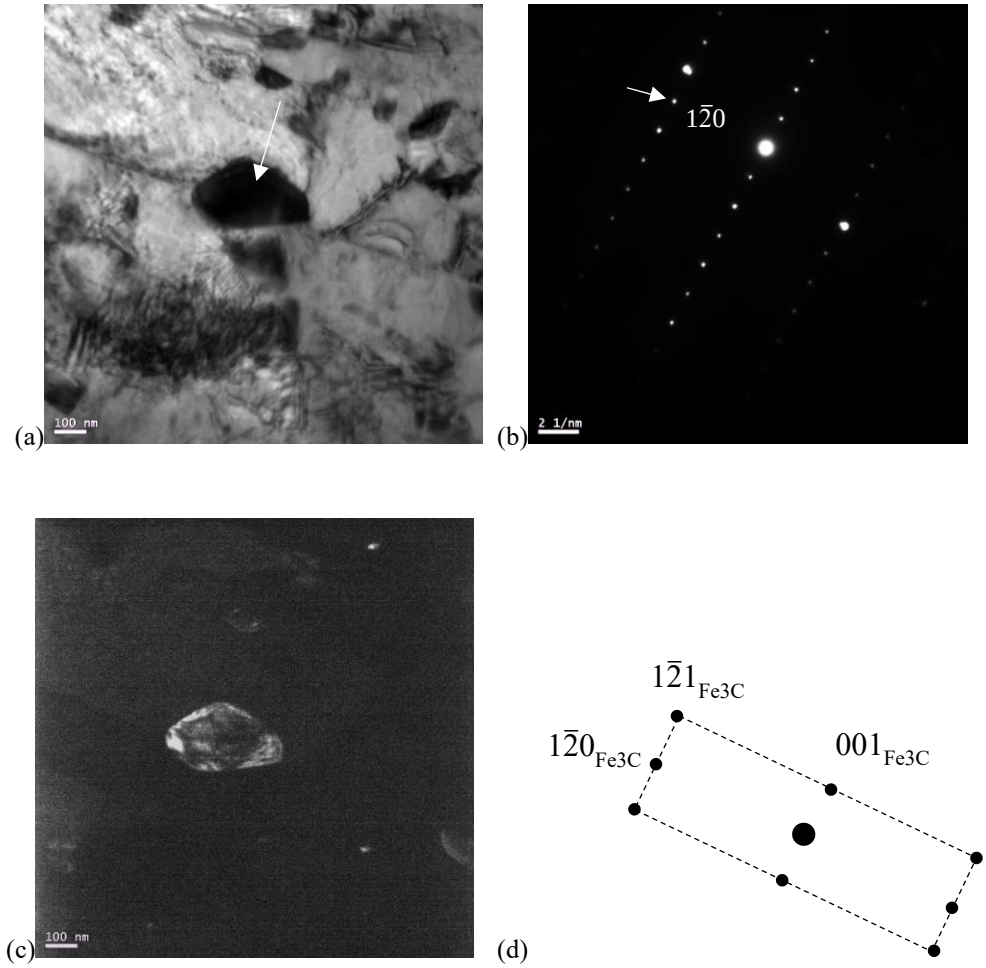

Figure 5-12. Characterisation of elliptical carbides after tempering for 2 hrs at 600 °C in the Base steel: (a) Bright field image of a typical elliptical carbide; (b) SAD pattern for the particle consistent with the [210] zone axis of cementite as shown in (d); (c) Dark field image of the elliptical carbide with the diffracted spot ($1\bar{2}0$) selected.

Table 5-5. Cementite volume percentages in the Base steel during tempering from 2 hrs to 16 hrs at 600 °C from SEM measurements

	2 hrs	4 hrs	8 hrs	16 hrs
Volume percentage (%)	2.9±0.3	3.0±0.5	3.0±0.5	2.8±0.4

As shown in Figure 5-13 and Figure 5-14, the coarsening process for inter- and intra-lath cementite occurs independently, as the volume fractions for each remain constant with time although the number densities vary due to different rates of coarsening. Generally, the inter-lath cementite constitutes the majority of the overall volume fraction for tempering from 2 hrs to 16 hrs compared to the intra-lath cementite. The number density for inter-lath cementite precipitates has decreased faster than that for intra-lath ones, whereas the sizes for inter-lath cementite are comparatively larger due to the faster solute boundary diffusion. A sharp decrease in cementite precipitate number density and increase in size occurs during tempering from 2 hrs to 4 hrs because of the existence of cementite particles with larger size differences and smaller separations after tempering for 2hrs, which accelerates the dissolution of the smaller cementite particles and the coarsening of larger ones. The number density and size changes become less with relatively longer tempering times, from 4 hrs to 16 hrs, indicating that the rate of coarsening slows as the cementite particles have smaller size differences reducing the driving force for coarsening. SEM measurements on carbide sizes are consistent with TEM measurements although the sizes for intra-lath carbides are slightly smaller from TEM results with higher resolution for slightly smaller particles.

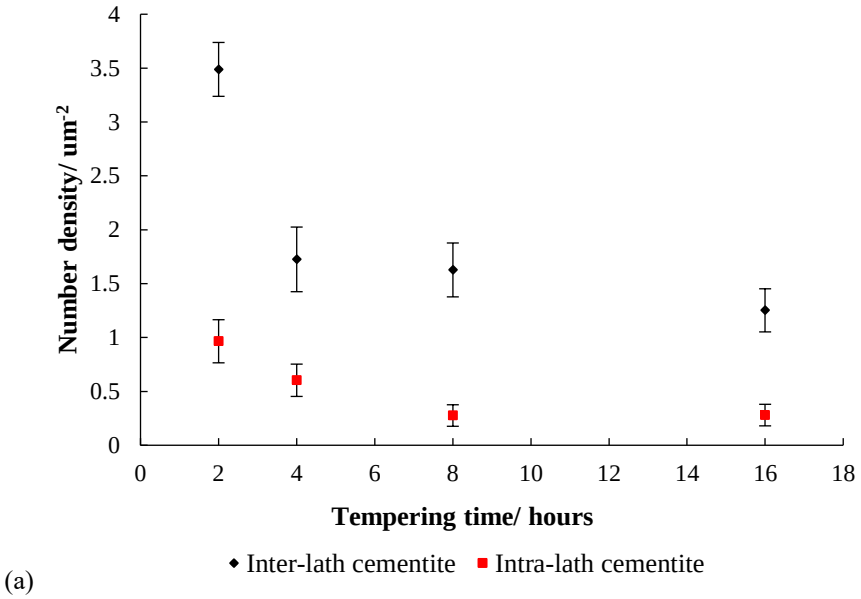

(a)

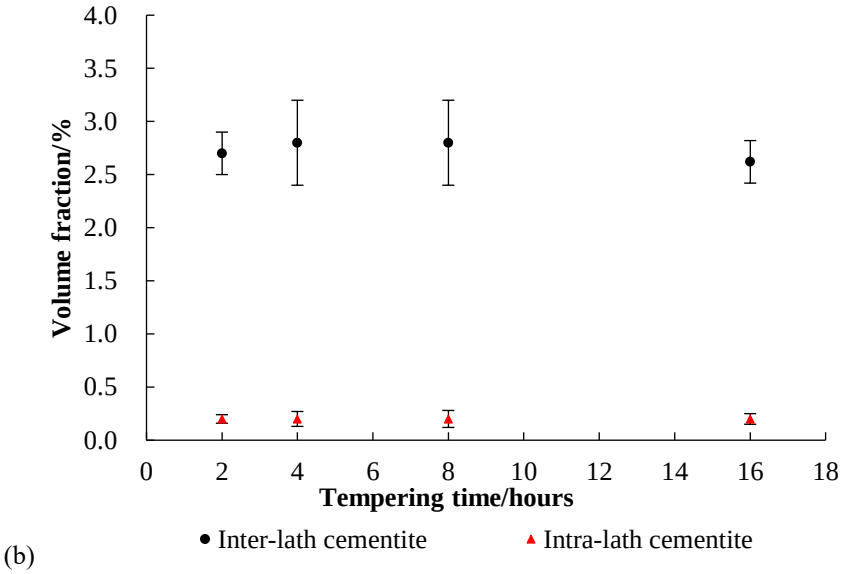

(b)

Figure 5-13. Number density (a) and volume fraction (b) for the elliptical intra- and inter-lath cementite respectively during tempering from 2 hrs to 16 hrs at 600 °C in the Base steel (SEM measurements).

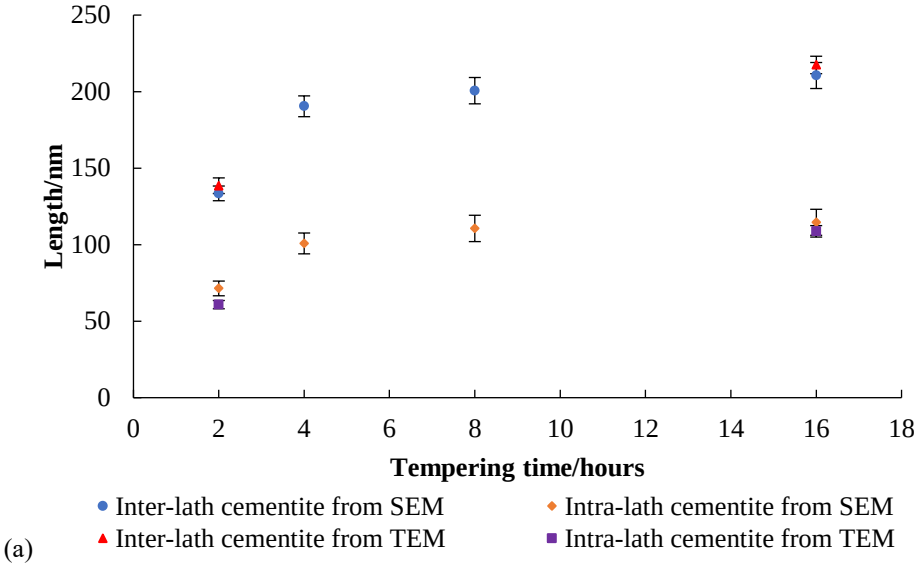

(a)

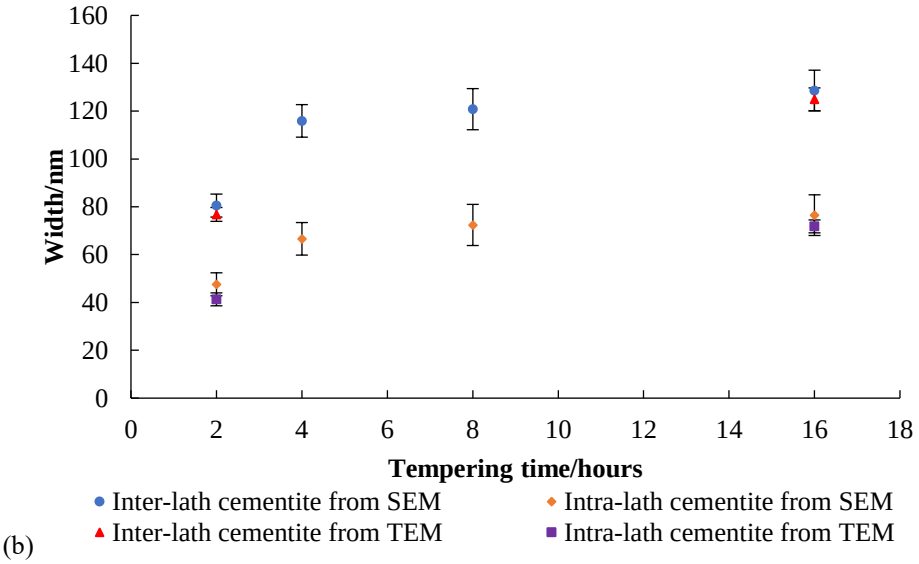

(b)

Figure 5-14. Average sizes of cementite during tempering from 2 hrs to 16 hrs at 600 °C in the Base steel: (a) average length; (b) average width.

5.3 Carbide precipitation and coarsening in the Base-Mo-V steel

Being similar to the Base steel, retained carbon is trapped in solid solution after water quenching in the Base-Mo-V steel, which is expected to diffuse out from solid solution to pre-existing carbides to make them grow during tempering. However, in this steel, not only the comparatively large elliptical inter- and intra-lath carbides, Figure 5-15 and Figure 5-16 (yellow arrowed), but also fine needle-shaped and even finer elliptical carbides (red arrowed in Figure 5-16) are present within the laths during tempering from 2 hrs to 16 hrs at 600 °C.

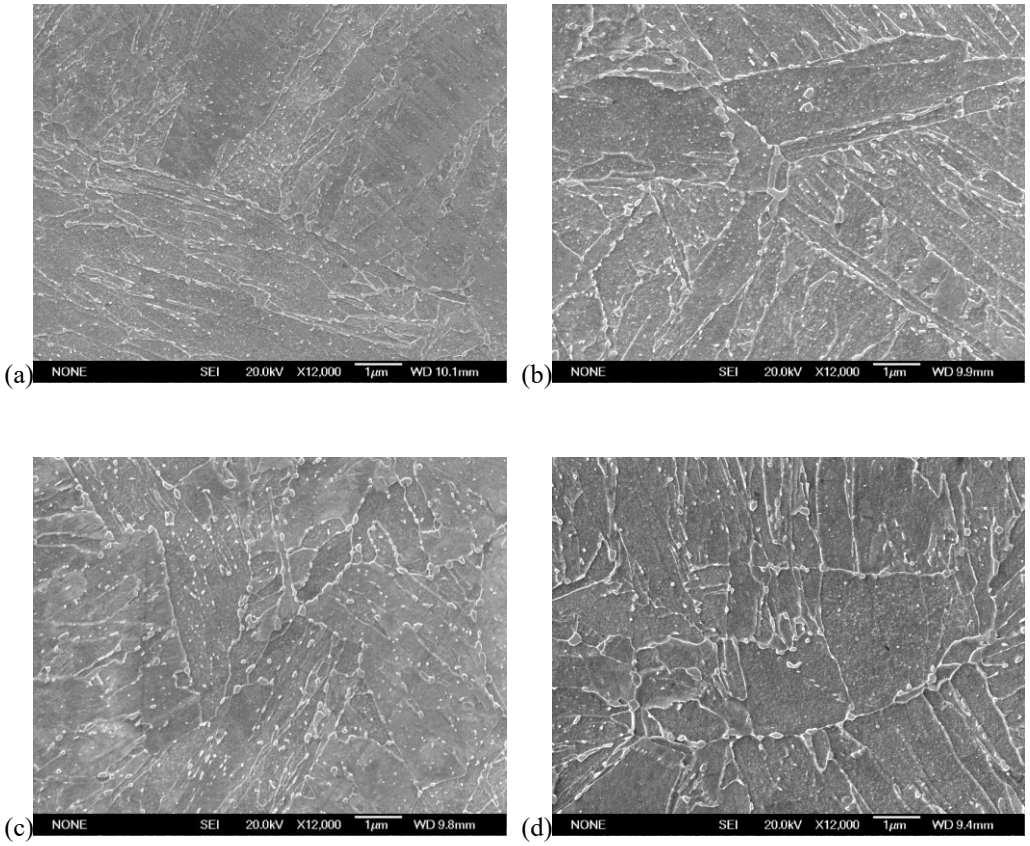

Figure 5-15. SEM images showing the precipitation and coarsening of carbides in the Base-Mo-V steel tempered at 600 °C for different times: (a) 2 hrs; (b) 4 hrs; (c) 8 hrs; (d) 16 hrs.

(a)

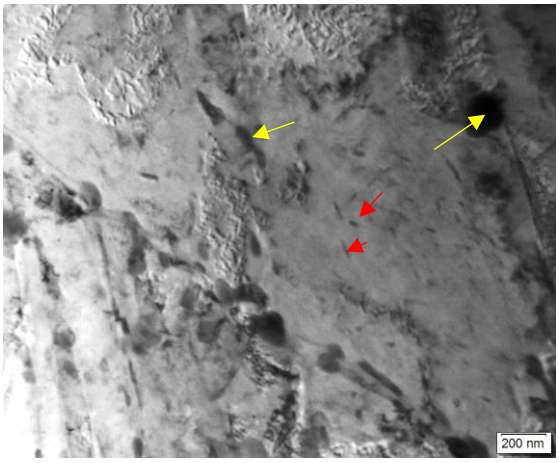

(b)

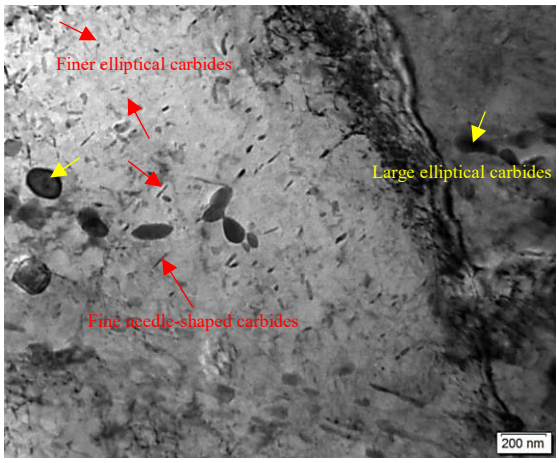

(c)

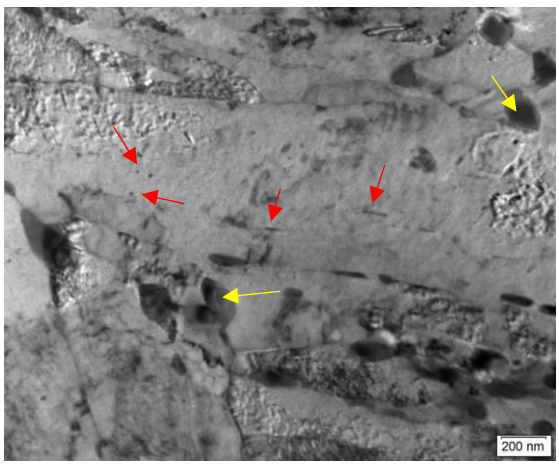

Figure 5-16. TEM bright field images showing the morphology of the carbides tempered at 600 °C in the Base-Mo-V steel after different tempering times: (a) 2 hrs; (b) 4 hrs; (c) 16 hrs. The yellow arrows refer

to the large inter- and intra-lath cementite; the red arrows indicate the needle-shape carbides and even finer elliptical carbides within the laths.

The large elliptical inter- and intra-lath carbides are confirmed as cementite when tempering from 2 hrs to 16 hrs at 600 °C, based on SAD patterns that are acquired from [5$\bar{3}$1], [101], and [212] zone axis of cementite for three independent particles after tempering for 2 hrs, Figure 5-17 to Figure 5-19, and from [010], [021], and [311] zone axis of cementite for another three particles after tempering for 16 hrs, Figure 5-20 to Figure 5-22. The large elliptical cementite particles account for nearly all the carbide volume fraction, where the elliptical cementite volume fraction remains nearly constant with time, Table 5-6, which is quite similar to the case for the Base steel during tempering from 2 hrs to 16 hrs. The inter-lath cementite constitutes most of the elliptical cementite volume fraction, Figure 5-23 (b), and remains approximately constant with time, while the number density gradually decreases with time (approximately by half), Figure 5-23 (a), indicating that coarsening for inter-lath cementite takes place independently from that for intra-lath cementite. The sizes for the elliptical inter-lath cementite are fairly larger with a greater number density decrease compared to intra-lath cementite due to the faster boundary solute (i.e. Mn, Mo and V) diffusion, Figure 5-24. In the Base-Mo-V steel, substitutional elements, Mn, Mo and V, are partitioning into cementite during tempering, as show in Table 5-7, Table 5-8 and Table 6-3 (section 6.1), and it is their diffusion which dominates the coarsening of the elliptical inter- and intra-lath cementite in this steel.

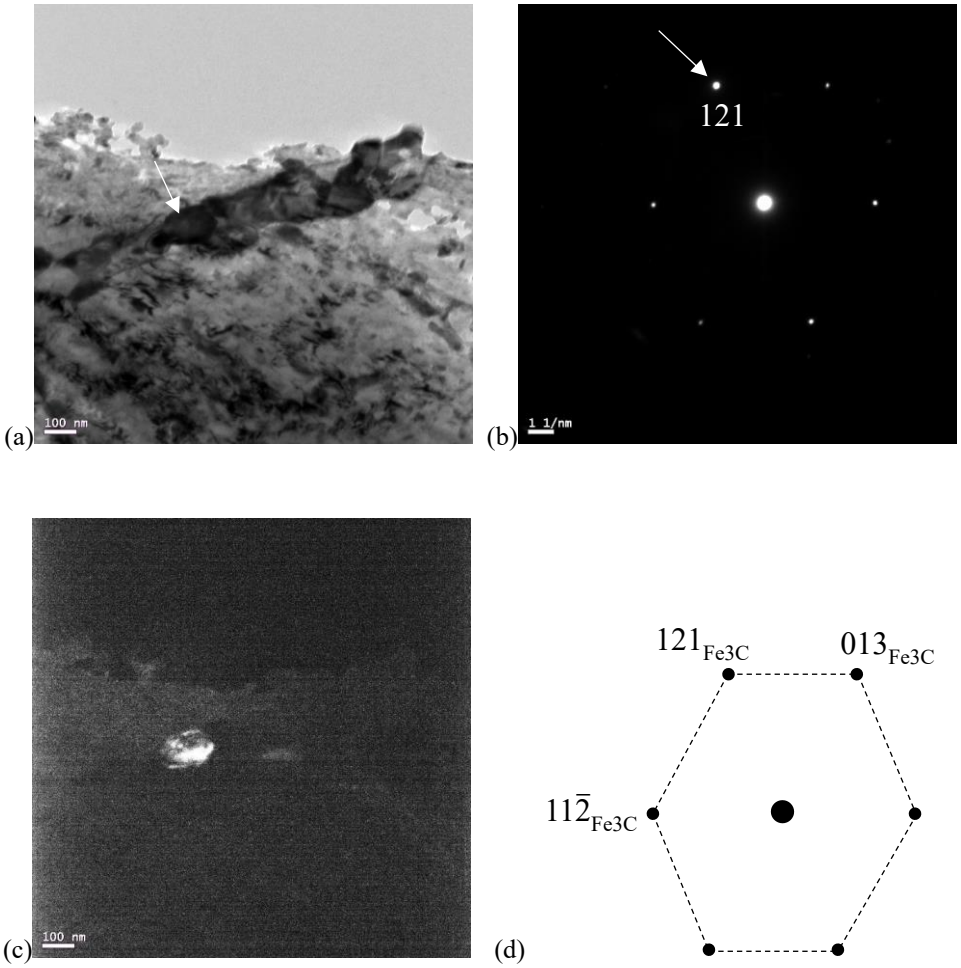

Figure 5-17. Characterisation of elliptical carbides after tempering for 2 hrs at 600 °C in the Base-Mo-V steel: (a) Bright field image of a typical elliptical carbide; (b) SAD pattern for the particle consistent with the $[5\bar{3}1]$ zone axis of cementite as shown in (d); (c) Dark field image with the diffracted spot (121) selected.

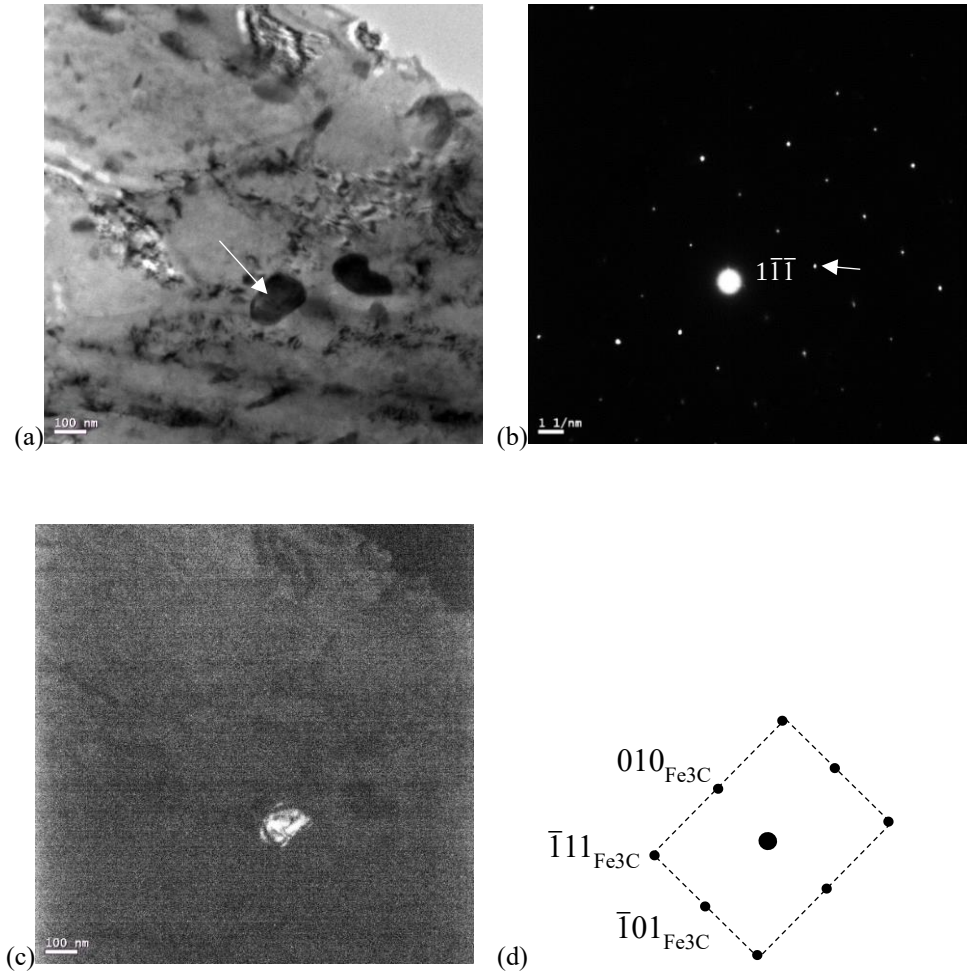

Figure 5-18. Characterisation of elliptical carbides after tempering for 2 hrs at 600 °C in the Base-Mo-V steel: (a) Bright field image of a typical elliptical carbide; (b) SAD pattern for the particle consistent with the [101] zone axis of cementite as shown in (d); (c) Dark field image with the diffracted spot ($1\bar{1}\bar{1}$) selected.

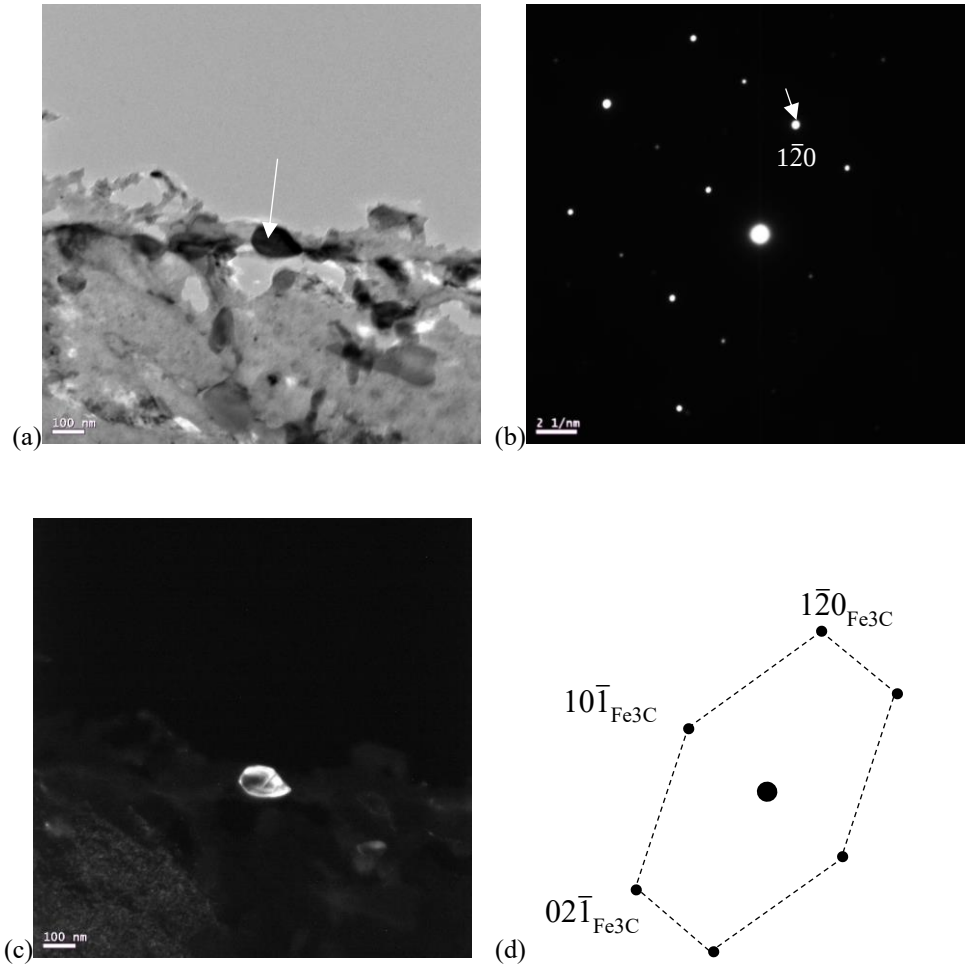

Figure 5-19. Characterisation of elliptical carbides after tempering for 2 hrs at 600 °C in the Base-Mo-V steel: (a) Bright field image of a typical elliptical carbide; (b) SAD pattern for the particle consistent with the [212] zone axis of cementite as shown in (d); (c) Dark field image with the diffracted spot ($1\bar{2}0$) selected.

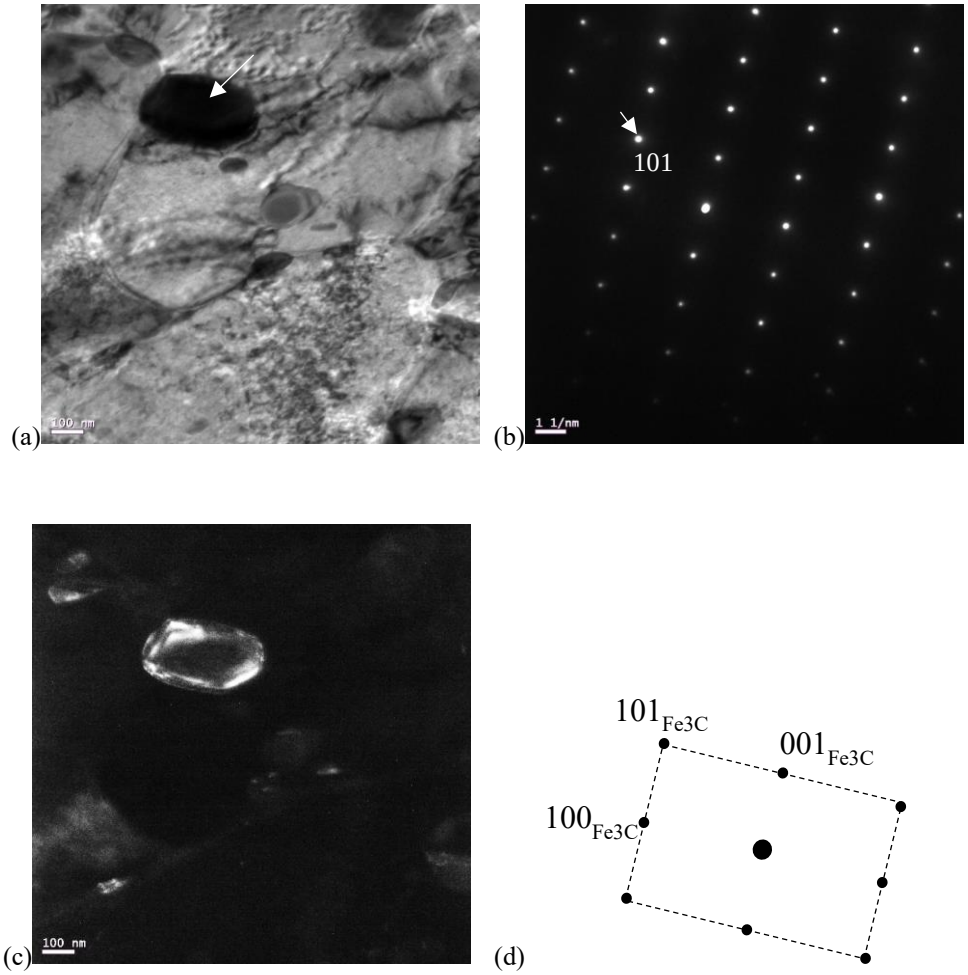

Figure 5-20. Characterisation of elliptical carbides after tempering for 16 hrs at 600 °C in the Base-Mo-V steel: (a) Bright field image of a typical elliptical carbide; (b) SAD pattern for the particle consistent with the [010] zone axis of cementite as shown in (d); (c) Dark field image with the diffracted spot (101) selected.

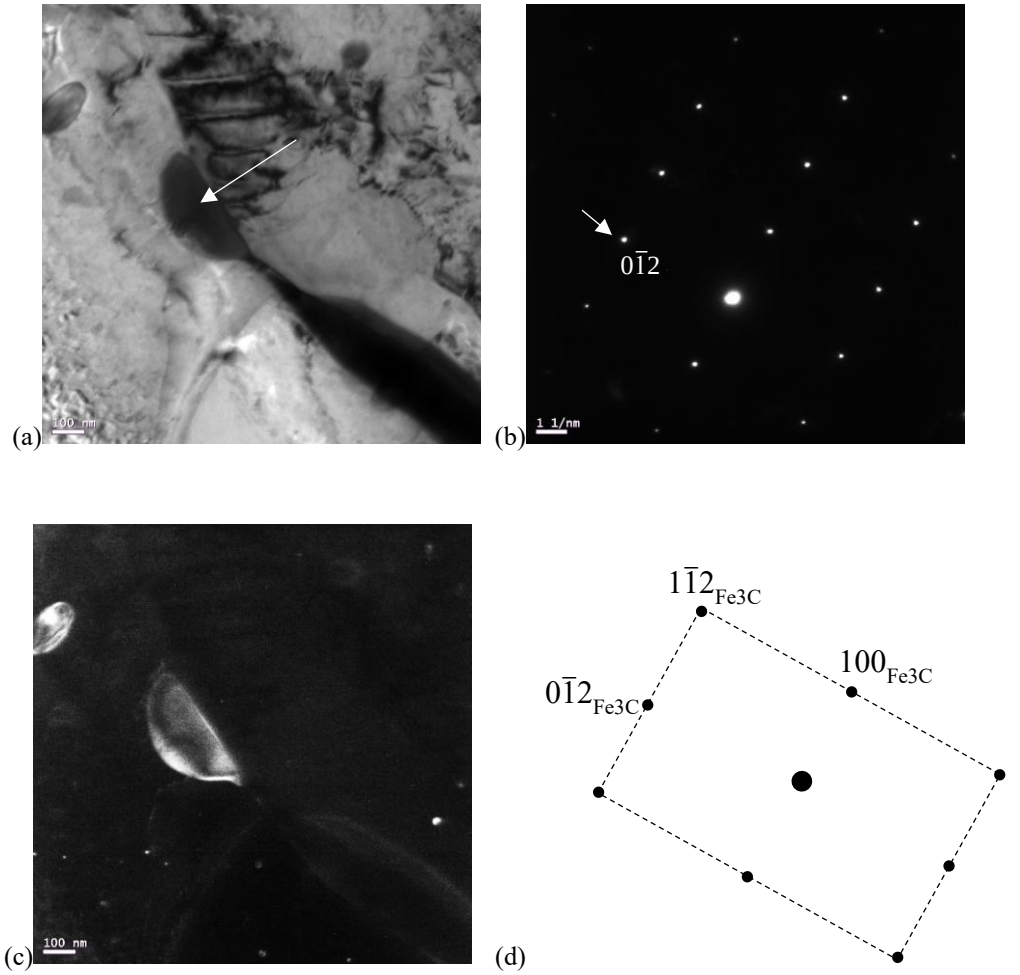

Figure 5-21. Characterisation of elliptical carbides after tempering for 16 hrs at 600 °C in the Base-Mo-V steel: (a) Bright field image of a typical elliptical carbide; (b) SAD pattern for the particle consistent with the [021] zone axis of cementite as shown in (d); (c) Dark field image with the diffracted spot (0$\bar{1}$2) selected.

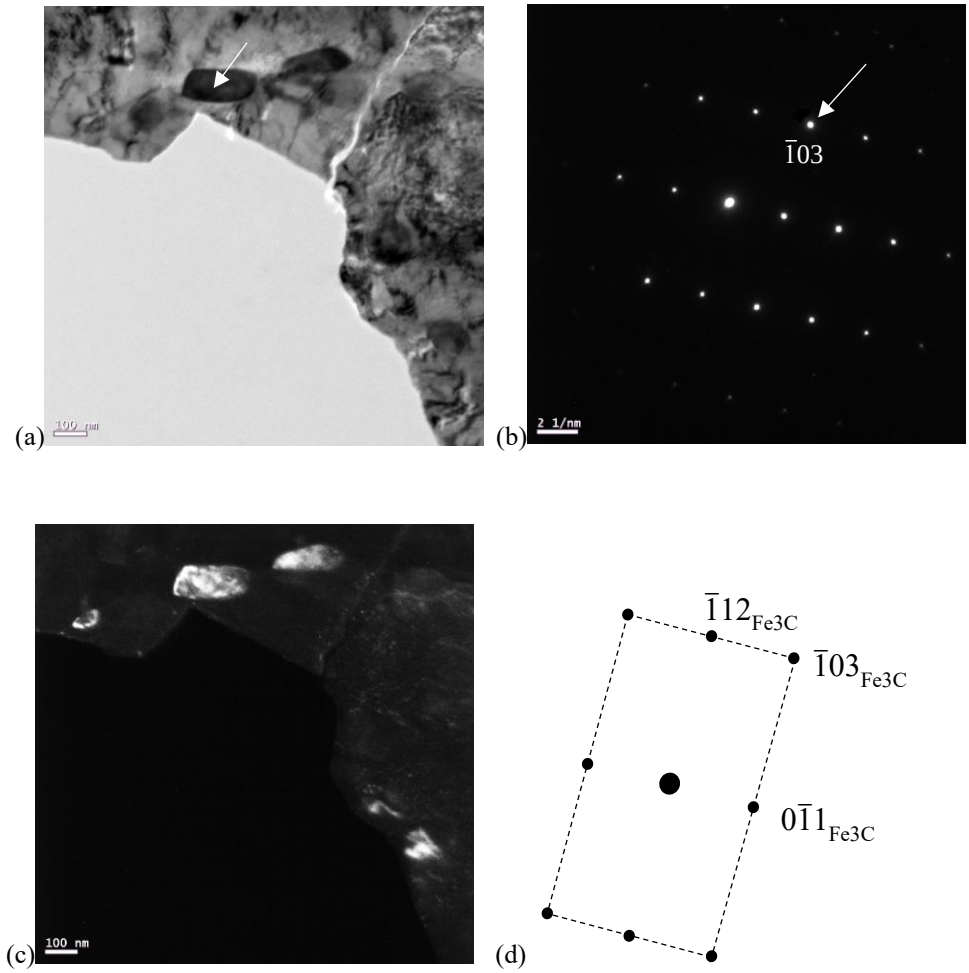

Figure 5-22. Characterisation of elliptical carbides after tempering for 16 hrs at 600 °C in the Base-Mo-V steel: (a) Bright field image of a typical elliptical carbide; (b) SAD pattern for the particle consistent with the [311] zone axis of cementite as shown in (d); (c) Dark field image with the diffracted spot ($\bar{1}03$) selected.

Table 5-6. The elliptical cementite volume percentages in the Base-Mo-V steel during tempering from 2 hrs to 16 hrs at 600°C from SEM measurements

	2 hrs	4 hrs	8 hrs	16 hrs
Volume percentage (%)	2.9±0.4	2.9±0.3	2.8±0.3	3.1±0.5

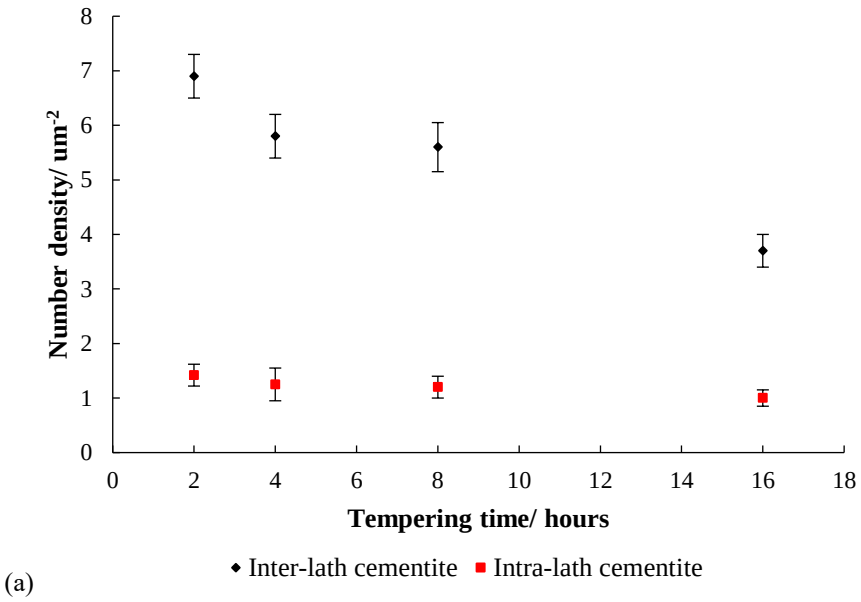

(a)

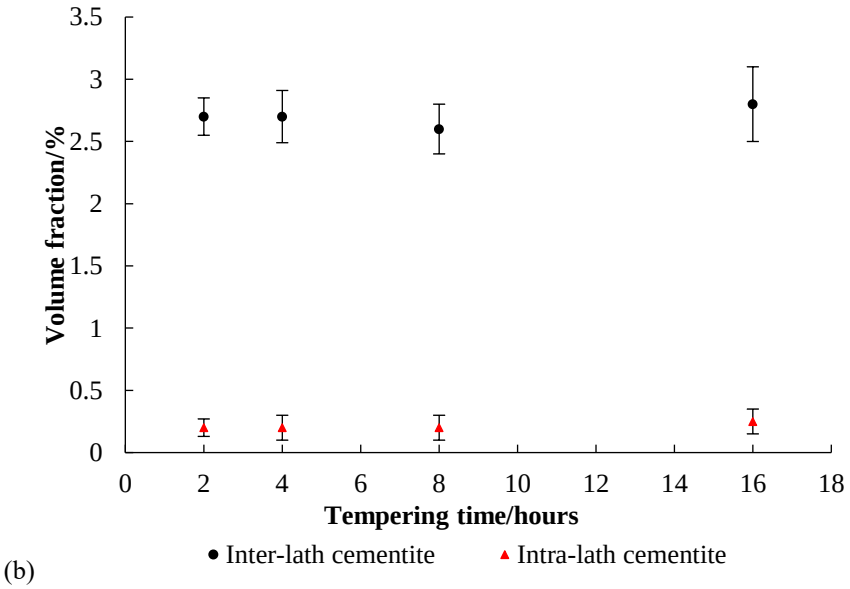

(b)

Figure 5-23. Number density (a) and volume fraction (b) for the elliptical intra- and inter-lath cementite respectively during tempering from 2 hrs to 16 hrs at 600 °C in the Base-Mo-V steel (SEM measurements).

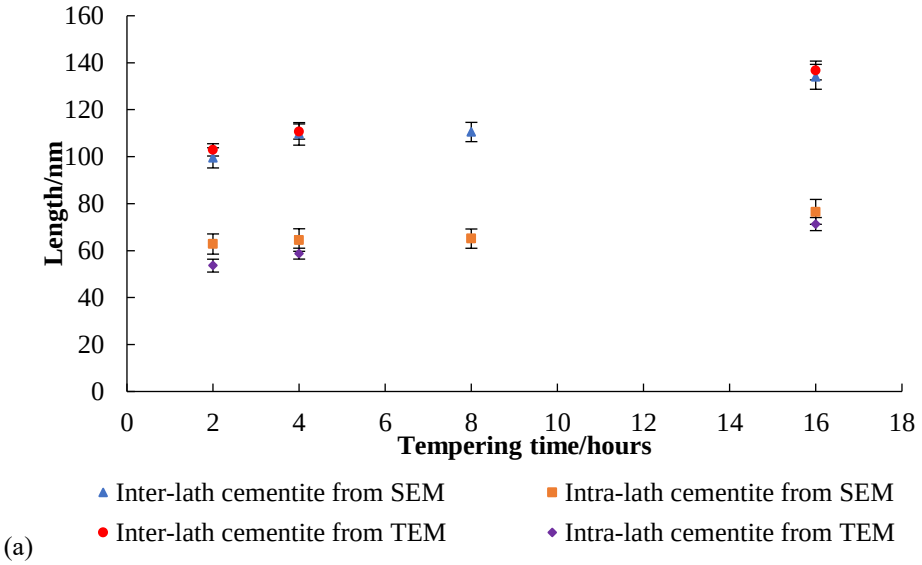

(a)

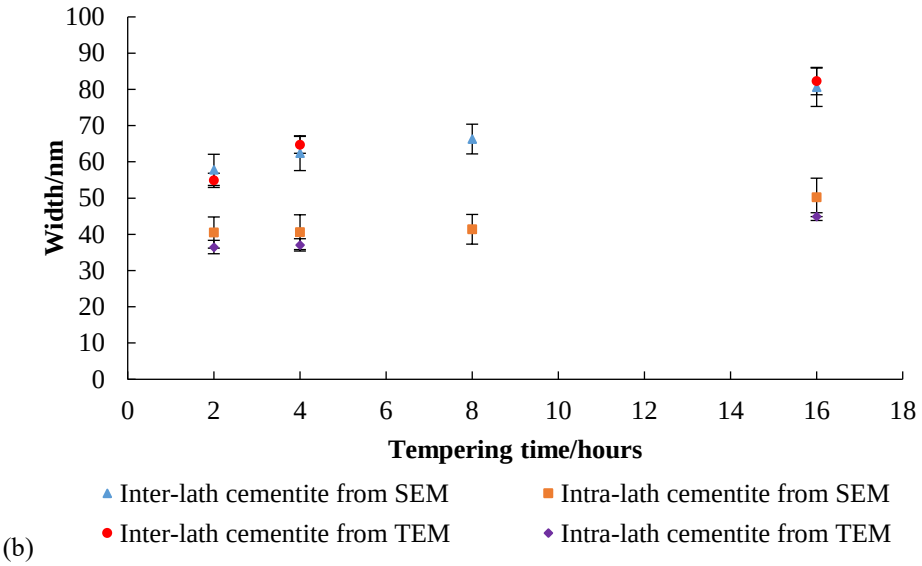

(b)

Figure 5-24. Average sizes for the elliptical cementite during tempering from 2 hrs to 16 hrs at 600 °C in the Base-Mo-V steel: (a) average length; (b) average width.

In addition, very fine carbides, including needle-shaped and elliptical shape carbides (red arrowed in Figure 5-16) are present within the marteniste laths during tempering from 2 hrs to 16 hrs at 600 °C in this steel, although they are not seen in the Base steel in the same tempering condition. The number density for these fine carbides changes with time,

Figure 5-25. It initially decreases when tempering from 0 hr to 2 hrs at 600 °C. The fine needle-shaped carbides existing after tempering for 2 hrs at 600 °C are consistent with cementite by the elemental mapping (Fe-rich carbides) in Figure 5-26 and EDS spectra in Figure 5-27. The substitutional element M, where M stands for Mn, Mo, V and Cr, to Fe ratio is defined as Y_M in order to consistently check the substitutional element content in carbides.

$$Y_M=\frac{wt(\mathrm{M})}{wt(\mathrm{Fe})} \qquad \text{Equation 5-2}$$

Where wt(M) is the weight percentage of M (M= Mn, Mo, V, Cr); wt(Fe) is the weight percentage of Fe from the EDS measurements. Based on the measured EDS spectra in Figure 5-27 (b), the measured contents of Mn, Mo and V in the needle-shaped carbides are similar to those in the elliptical cementite after tempering for 2 hrs (the matrix contribution should be considered), Table 5-7, illustrating the existence of the needle-shaped cementite after tempering for 2 hrs at 600 °C. In addition, there are no alloy carbides (such as M_2C type Mo-rich carbides) detected in the 2 hour tempered condition in this steel. However, with tempering time extending from 2 hrs to 4 hrs, the number density of fine carbides increases noticeably, indicating the precipitation of secondary hardening alloy carbides, as the number density attributed to fine needle-shaped cementite should decrease with time as coarsening progresses. The large elliptical and fine needle-shaped carbides are still present, Figure 5-28 (a), and the chemical compositions for these particles are consistent with cementite, Figure 5-29 and Table 5-8. An additional distribution of finer elliptical alloy carbides is observed in TEM samples, Figure 5-28 (b). The chemical compositions for these finer elliptical carbides obviously

differ from cementite, where the Mo peak is the predominant peak in the EDS spectrum in Figure 5-30 (b) compared to the dominant Fe peak in cementite in Figure 5-27 (b) and Figure 5-29 (b). The Y_{Mo} and Y_V values in these finer elliptical carbides are several hundreds of times larger than those in cementite, Table 5-8 and Table 6-3, indicating the precipitation of Mo-V-rich secondary alloy carbides. Actually, the measured Y_{Mo}, Y_V and Y_{Mn} in these finer elliptical alloy carbides are quite different from the predicted composition for the pseudo-equilibrium M_2C carbides (Thermo-Calc), Table 5-8, predominantly due to the precipitation of these finer elliptical alloy carbides not achieving the pseudo-equilibrium condition after tempering for 4 hrs. This additional set of carbides explains the increase in number density observed for fine carbides for tempering from 2 hrs to 4 hrs and are expected to be Mo-V-rich M_2C carbides in this steel with V/Mo ratio=0.1 and V=0.05 wt % based on the reported literature that M_2C carbides have precipitated after cementite in a 0.6Cr-0.5Mo steel [7], Figure 1-1, or Cr-Mo-V steels with low V/Mo ratio (< 0.17) and V< 0.1 wt % [75, 95], Figure 2-14. In addition, the time for the formation of secondary Mo-V-rich carbides also agrees with the reported formation time of M_2C in Cr-Mo-V steels with low bulk V/Mo ratio, e.g. less than 10 hrs tempering at 600 °C [95]. As the tempering time increases from 4 hrs to 16 hrs, the number density for fine carbides decreases, indicating the continuous dissolution of fine needle-shaped cementite as coarsening of cementite proceeds and the gradual growth of secondary alloy carbides. Finally, the needle-shaped cementite and secondary Mo-V-rich alloy carbides both persist within the laths after tempering for 16 hrs at 600 °C, indicated by the red arrows in Figure 5-16 (c), which remains consistent with the Fe-0.1C-1.6Mo steel [57] where the needle-shaped cementite and Mo_2C are both observed within the laths after tempering for 100 hrs at 600 °C.

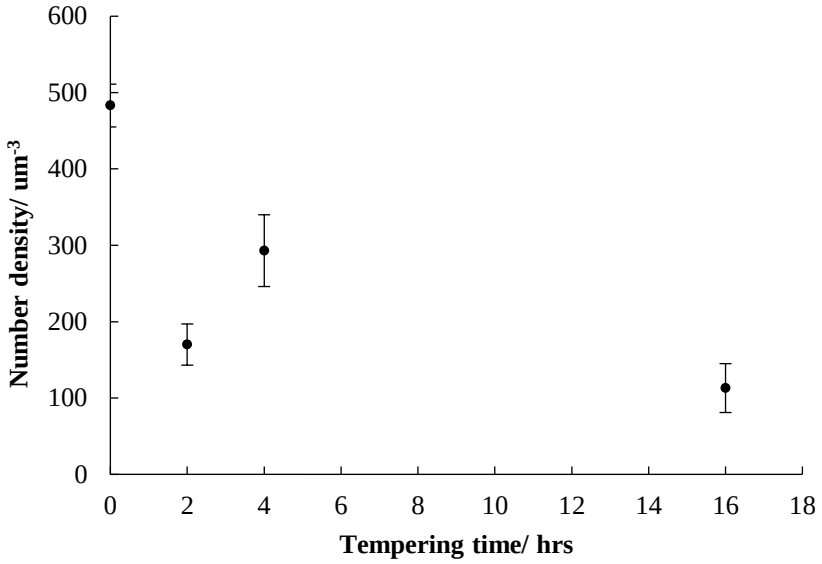

Figure 5-25. The number density variation for the fine carbides in the Base-Mo-V steel tempered from 0 hr to 16 hrs from TEM measurements.

(a) 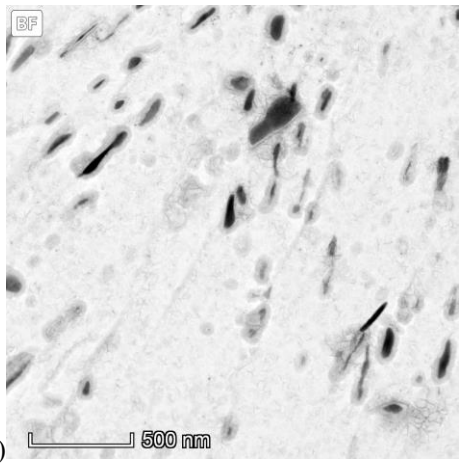

(b) 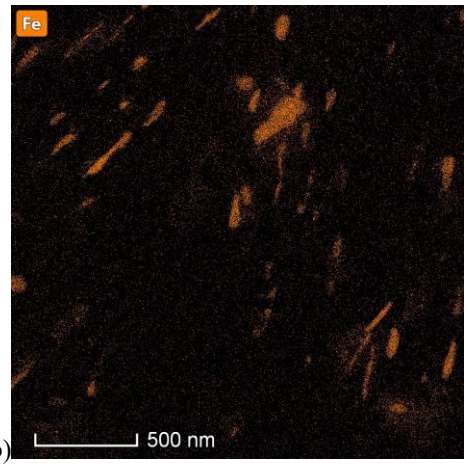

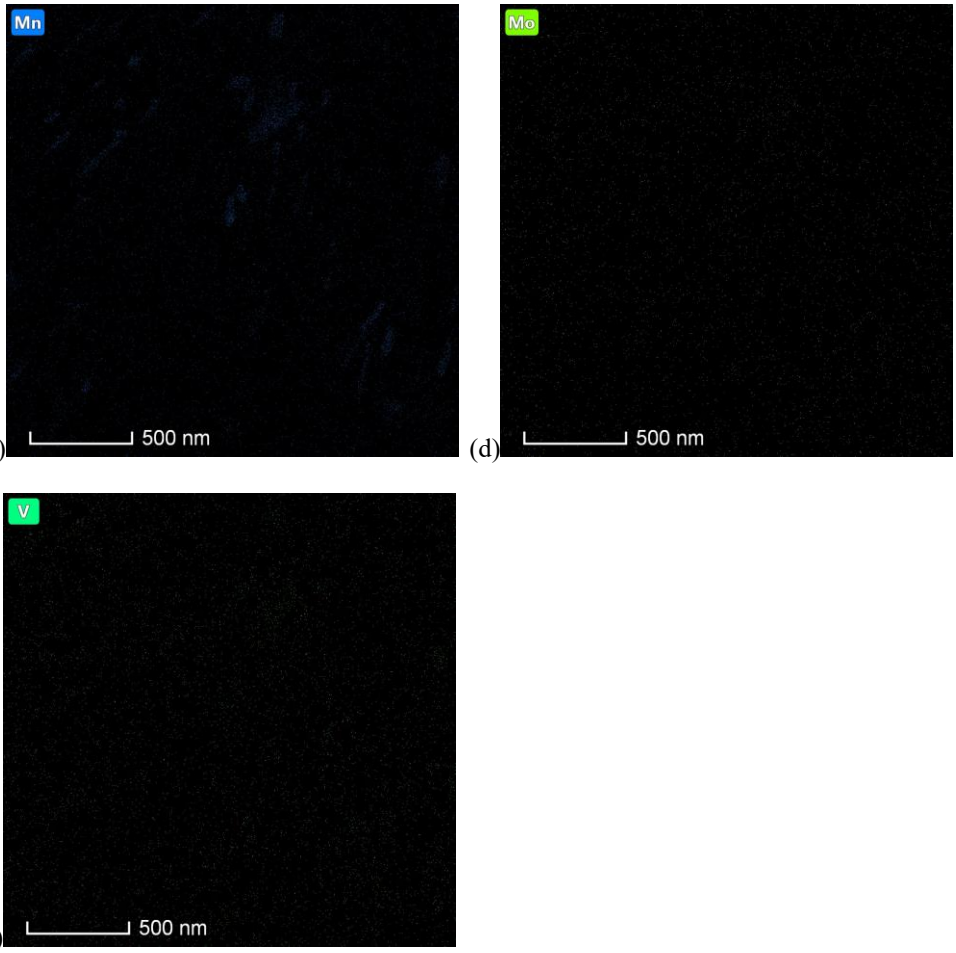

Figure 5-26. STEM observation of the large elliptical cementite and fine needle-shaped carbides in the Base-Mo-V steel after tempering for 2 hrs at 600 °C using a carbon replica specimen: (a) bright field image; (b)-(e) elemental mapping.

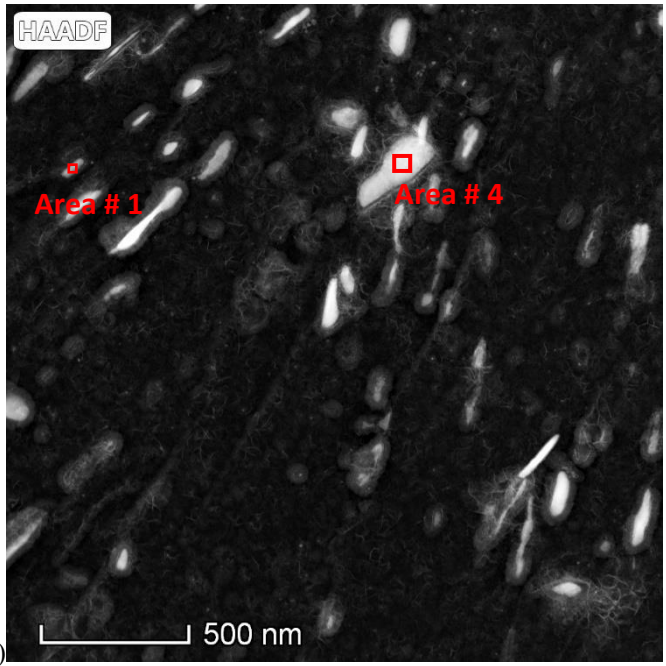

(a)

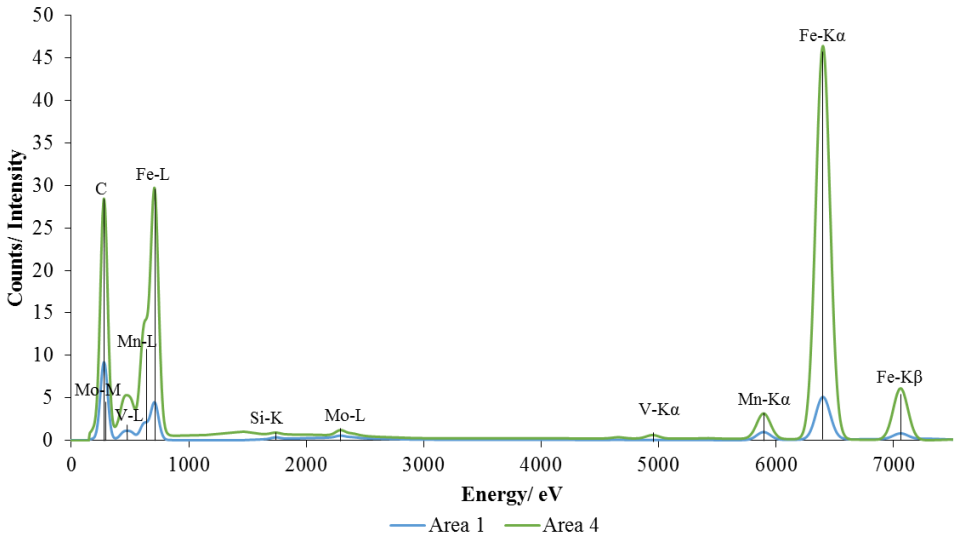

(b)

Figure 5-27. (a) HAADF image of the same area in Figure 5-26; (b) EDS spectra for the fine needle-shaped (Area 1) and large elliptical (Area 4) carbides respectively.

Table 5-7. The M to Fe ratio Y_M (M stands for Mn, Mo and V) for different particles using carbon replica specimens from EDS measurements for the Base-Mo-V steel tempered for 2 hrs at 600 °C

	Y_{Mn}	Y_{Mo}	Y_V
Needle-shaped cementite	0.114±0.019	0.024±0.007	0.010±0.004
Large elliptical cementite	0.088±0.014	0.016±0.003	0.012±0.003

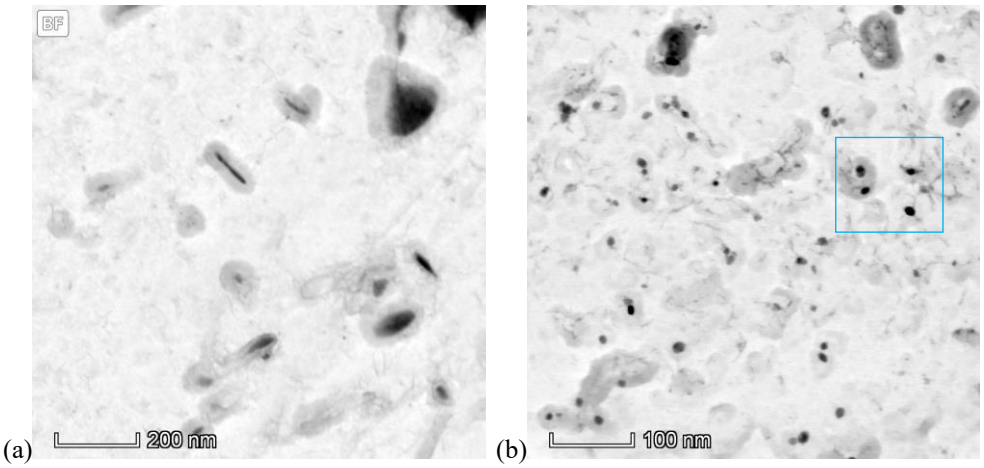

(a) (b)

Figure 5-28. STEM observation (bright field images) for the Base-Mo-V steel after tempering for 4 hrs at 600 °C using a carbon replica specimen: (a) area containing large elliptical and fine needle-shaped carbides; (b) area containing finer elliptical carbides.

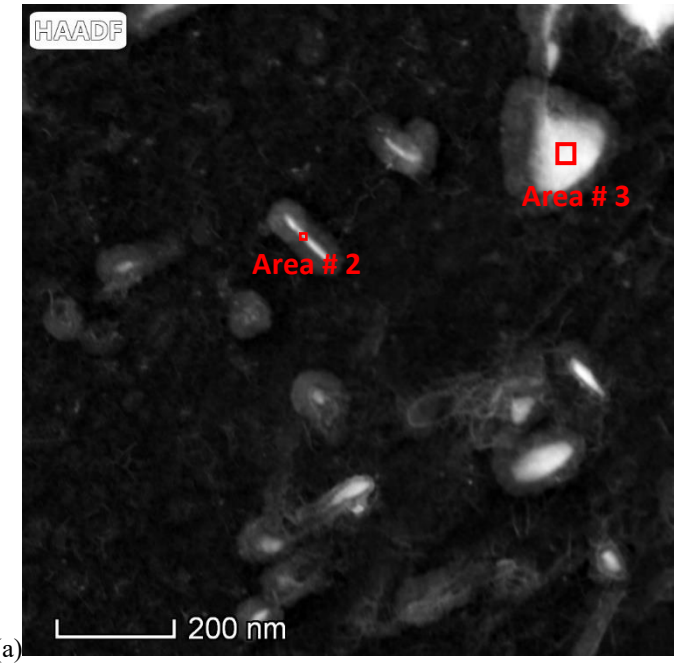

(a)

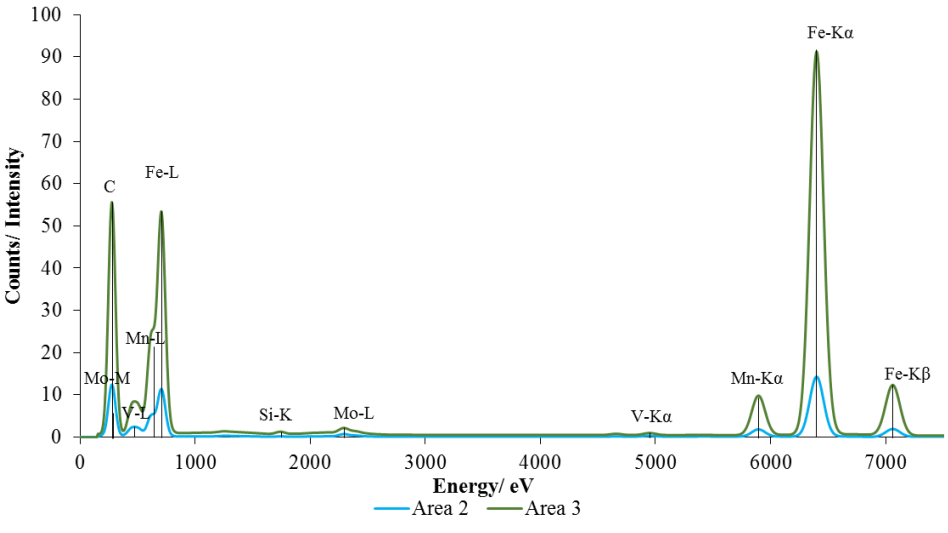

(b)

Figure 5-29. (a) HAADF image of the same area in Figure 5-28(a); (b) EDS spectra for fine needle-shaped (Area 2) and large elliptical (Area 3) carbides respectively.

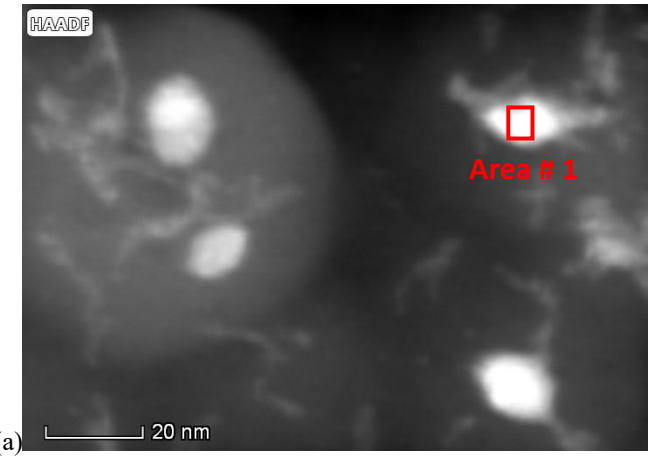

(a)

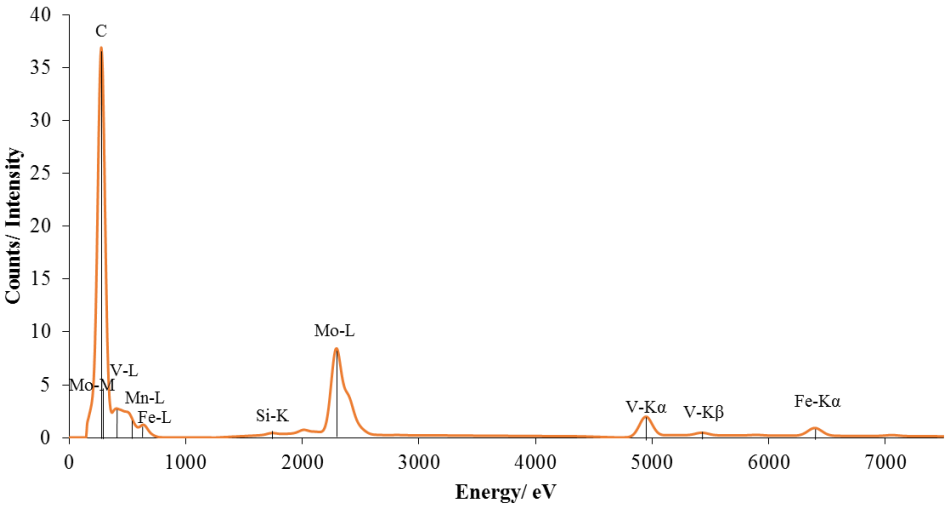

(b)

Figure 5-30. (a) HAADF image of the magnified area in Figure 5-28 (b); (b) the EDS spectrum for the finer elliptical carbide (Area 1).

Table 5-8. The M to Fe ratio Y_M (M represents Mn, Mo and V) for different particles using carbon replica specimens from EDS measurements for the Base-Mo-V steel tempered for 4 hrs at 600 °C

	Y_{Mn}	Y_{Mo}	Y_V
Needle-shaped cementite	0.114±0.018	0.021±0.006	0.013±0.004
Large elliptical cementite	0.092±0.012	0.019±0.002	0.012±0.003
Finer elliptical secondary carbides	0.077±0.011	14.750±1.279	2.132±0.304
Pseudo-equilibrium M_2C carbide (Thermo-Calc)	7.070	55.963	3.042

5.4 Carbide precipitation and coarsening in the Base-Cr-Mo-V-Si steel

In the Base-Cr-Mo-V-Si steel, a finer dispersion of carbides is observed compared to the Base and Base-Mo-V steels during tempering, Figure 5-31. The relatively large elliptical carbides are located within the laths and on the lath boundary, whereas some finer carbides with needle-shape and/or elliptical shape are distributed within the laths, arrowed in Figure 5-32.

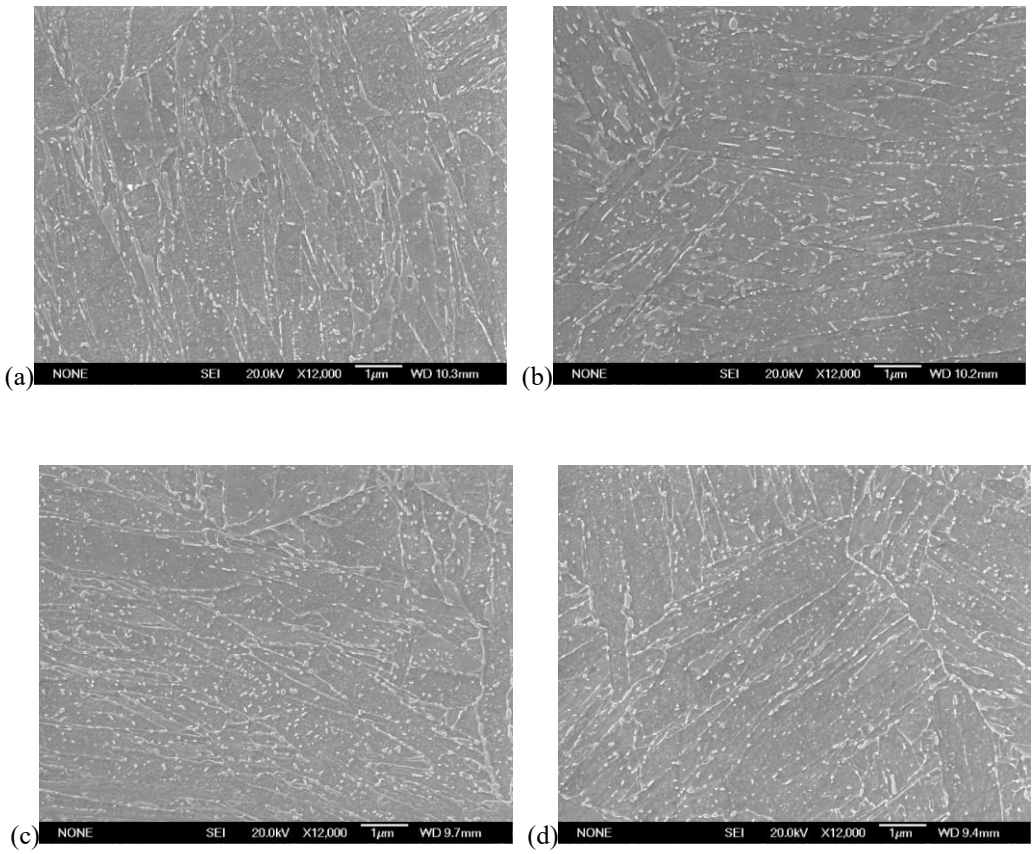

Figure 5-31. SEM images showing the precipitation and coarsening of carbides in the Base-Cr-Mo-V-Si steel tempered at 600 °C for different times: (a) 2 hrs; (b) 4 hrs; (c) 8 hrs; (d) 16 hrs.

(a)

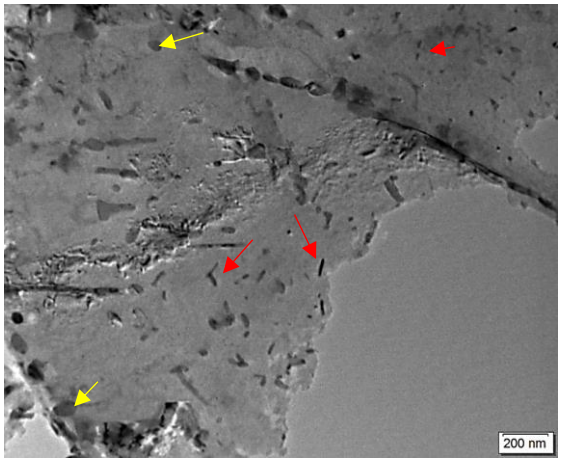

(b)

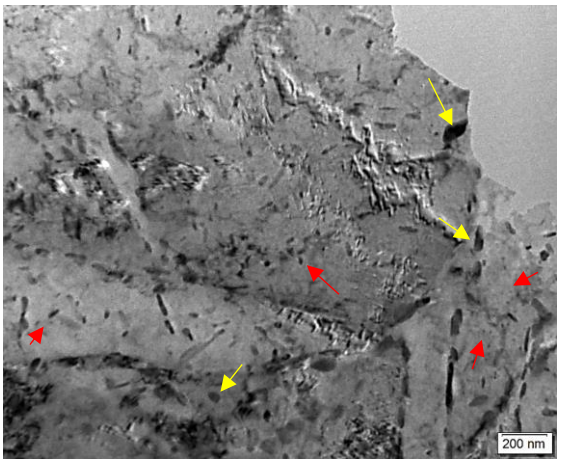

(c)

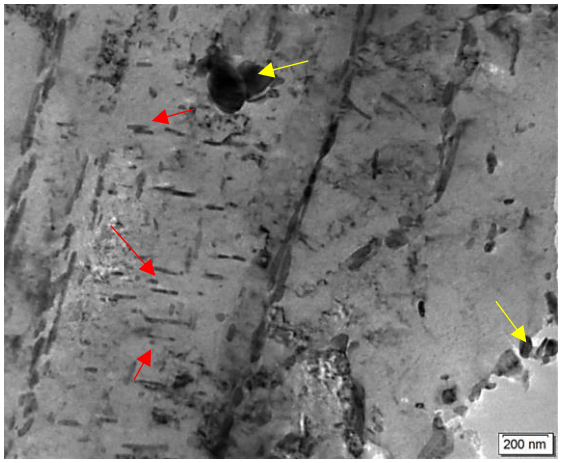

Figure 5-32. TEM bright field images showing the morphology of carbides tempered at 600 °C in the Base-Cr-Mo-V-Si steel after different tempering times: (a) 2 hrs; (b) 4 hrs; (c) 16 hrs. The yellow arrows refer to the comparatively large elliptical carbides on lath boundaries and within the laths; the red arrows refer to the fine carbides with needle-shape and elliptical shape within the laths.

These large elliptical carbides are consistent with cementite, as the SAD patterns have been acquired from [00$\bar{1}$], [631], and [110] zone axes of cementite for three individual particles after tempering for 2 hrs, and from [00$\bar{1}$], [101], and [111] zone axes of cementite for another three particles after tempering for 16 hrs at 600 °C, Figure 5-33 to Figure 5-38. Similarly to the Base and Base-Mo-V steels, the elliptical cementite volume fraction, obtained by SEM measurements, keeps approximately constant at 2.5%, with an overestimation due to the etching effect, on tempering from 2 hrs to 16 hrs, Table 5-9, where the inter-lath cementite constitutes the majority of the overall elliptical cementite volume fraction, Figure 5-39 (b). The volume fraction for inter-lath cementite remains approximately constant with time, whereas the number density decreases with time during tempering from 2 hrs to 16 hrs, demonstrating that coarsening for inter-lath cementite takes place independently from that for intra-lath cementite as their size increases, Figure 5-40. However, the coarsening rates are much slower than those in the Base and Base-Mo-V steels, consistent with the extra addition of Si inhibiting the coarsening/dissolution of cementite, as previously reported for Fe-0.6C and Fe-0.6C-2Si steels [68]. In this steel, the substitutional elements, Mn, Cr, Mo and V, are also partitioned into cementite, Figure 5-42 and Table 5-10, which remains consistent with the Base and Base-Mo-V steels. Due to the diffusivity for substitutional elements (i.e. Mn, Cr, Mo) along the lath/grain boundary being higher than that in the matrix, the coarsening for inter-lath cementite is quicker than that for intra-lath cementite, Figure 5-40, agreeing well with the Base and Base-Mo-V steels.

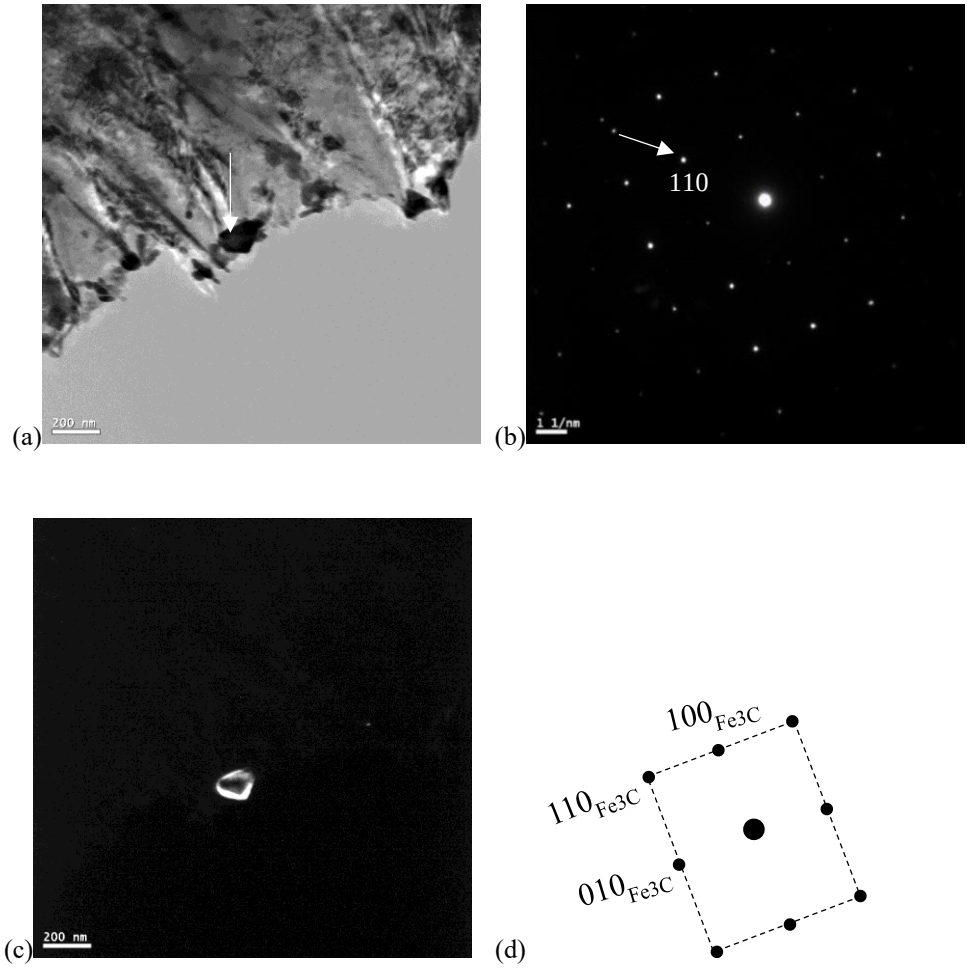

Figure 5-33. Characterisation of elliptical carbides after tempering for 2 hrs at 600 °C in the Base-Cr-Mo-V-Si steel: (a) Bright field image of a typical elliptical carbide; (b) SAD pattern for the particle consistent with the [00$\bar{1}$] zone axis of cementite as shown in (d); (c) Dark field image of the elliptical carbide with the diffracted spot (110) selected.

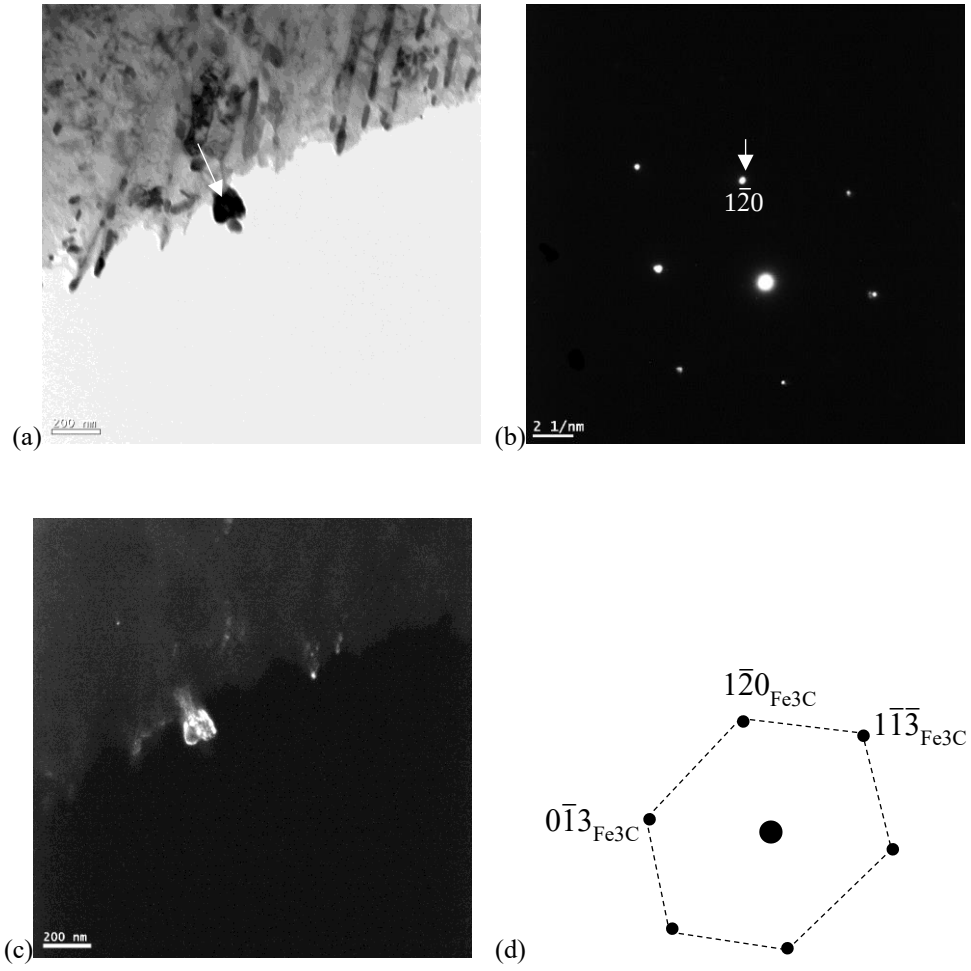

Figure 5-34. Characterisation of elliptical carbides after tempering for 2 hrs at 600 °C in the Base-Cr-Mo-V-Si steel: (a) Bright field image of a typical elliptical carbide; (b) SAD pattern for the particle consistent with the [631] zone axis of cementite as shown in (d); (c) Dark field image with the diffracted spot ($1\bar{2}0$) selected.

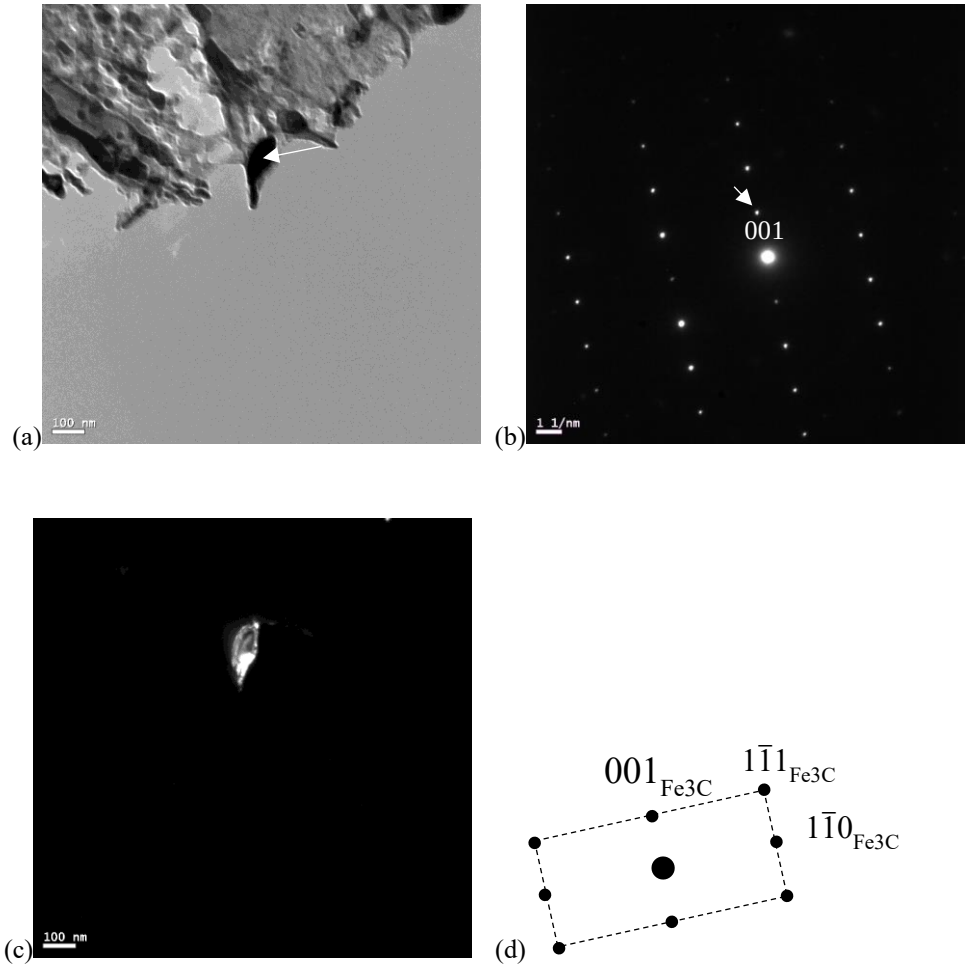

Figure 5-35. Characterisation of elliptical carbides after tempering for 2 hrs at 600 °C in the Base-Cr-Mo-V-Si steel: (a) Bright field image of a typical elliptical carbide; (b) SAD pattern for the particle consistent with the [110] zone axis of cementite as shown in (d); (c) Dark field image with the diffracted spot (001) selected.

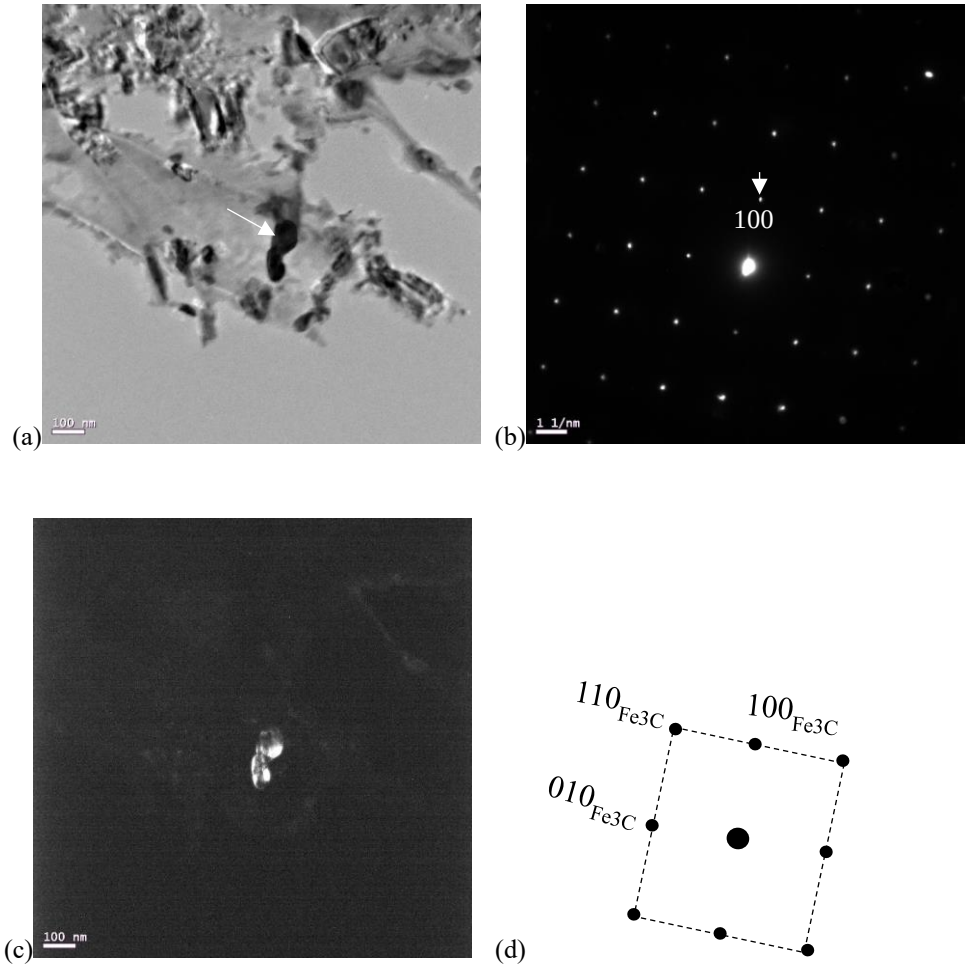

Figure 5-36. Characterisation of elliptical carbides after tempering for 16 hrs at 600 °C in the Base-Cr-Mo-V-Si steel: (a) Bright field image of a typical elliptical carbide; (b) SAD pattern for the particle consistent with the $[00\bar{1}]$ zone axis of cementite as shown in (d); (c) Dark field image with the diffracted spot (100) selected.

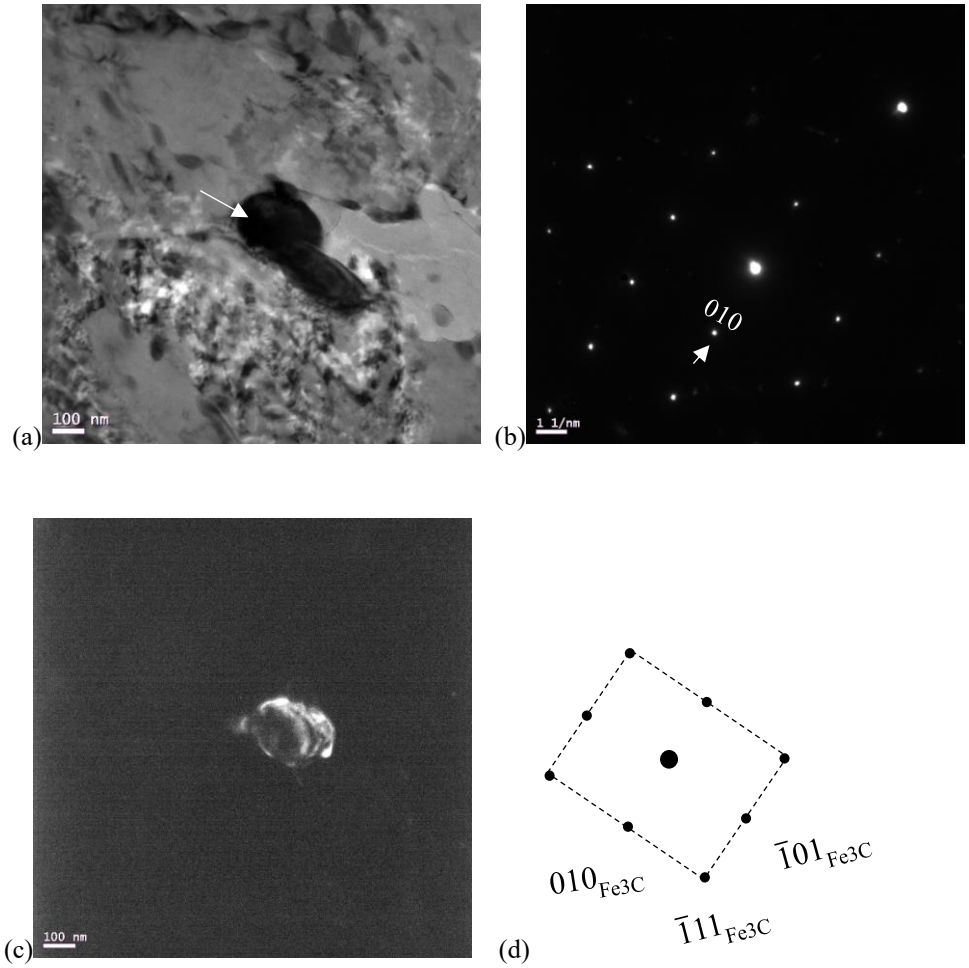

Figure 5-37. Characterisation of elliptical carbides after tempering for 16 hrs at 600 °C in the Base-Cr-Mo-V-Si steel: (a) Bright field image of a typical elliptical carbide; (b) SAD pattern for the particle consistent with the [101] zone axis of cementite as shown in (d); (c) Dark field image with the diffracted spot (010) selected.

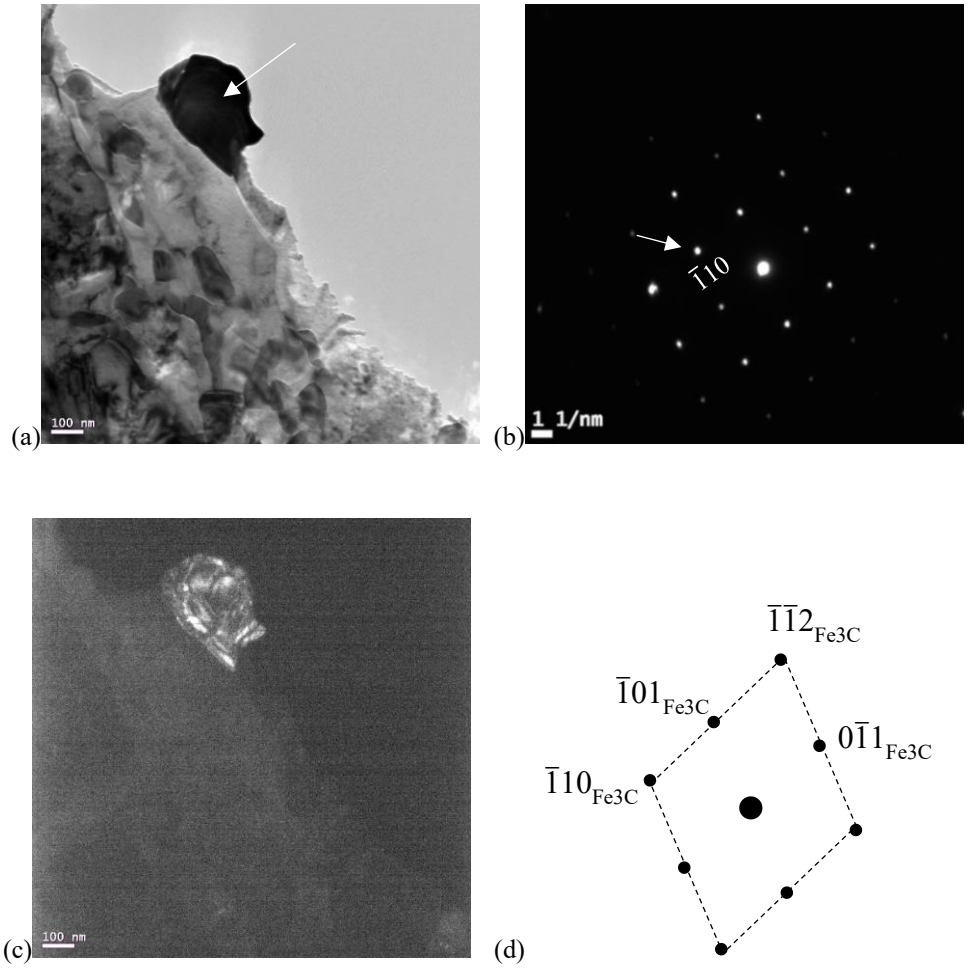

Figure 5-38. Characterisation of elliptical carbides after tempering for 16 hrs at 600 °C in the Base-Cr-Mo-V-Si steel: (a) Bright field image of a typical elliptical carbide; (b) SAD pattern for the particle consistent with the [111] zone axis of cementite as shown in (d); (c) Dark field image with the diffracted spot ($\bar{1}10$) selected.

Table 5-9. The elliptical cementite volume percentages in the Base-Cr-Mo-V-Si steel during tempering from 2 hrs to 16 hrs at 600 °C from SEM measurements

	2 hrs	4 hrs	8 hrs	16 hrs
Volume percentage (%)	3.0±0.6	3.1±0.4	2.8±0.2	3.0±0.3

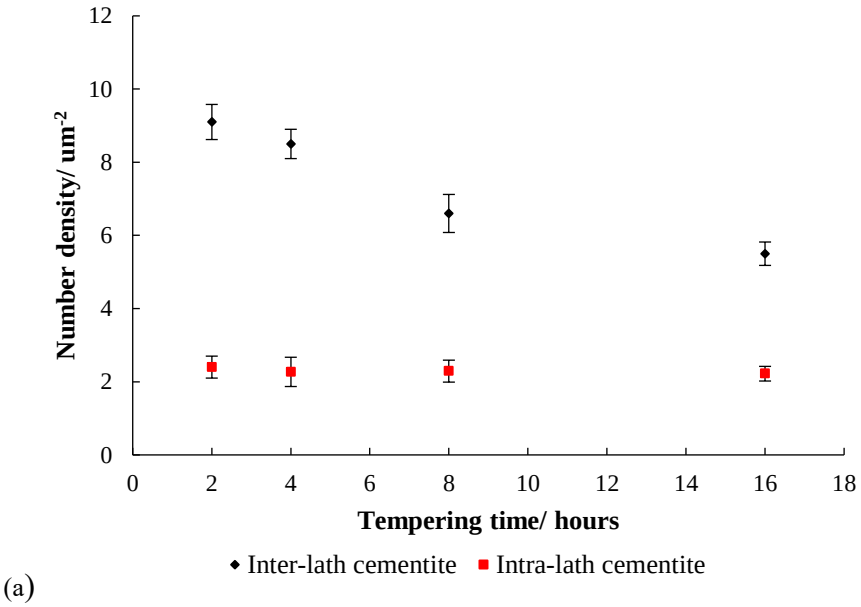

(a)

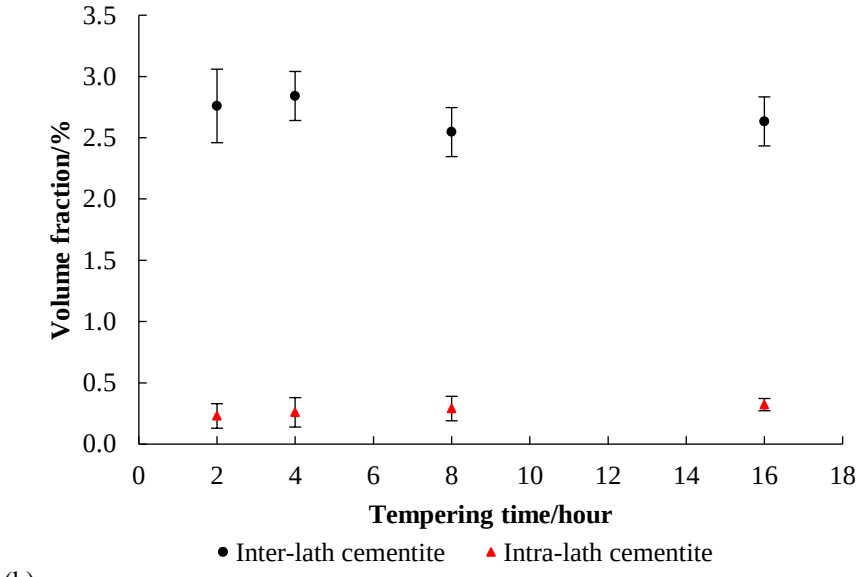

(b)

Figure 5-39. Number density (a) and volume fraction (b) for the elliptical intra- and inter-lath cementite respectively during tempering from 2 hrs to 16 hrs at 600 °C in the Base-Cr-Mo-V-Si steel (SEM measurements).

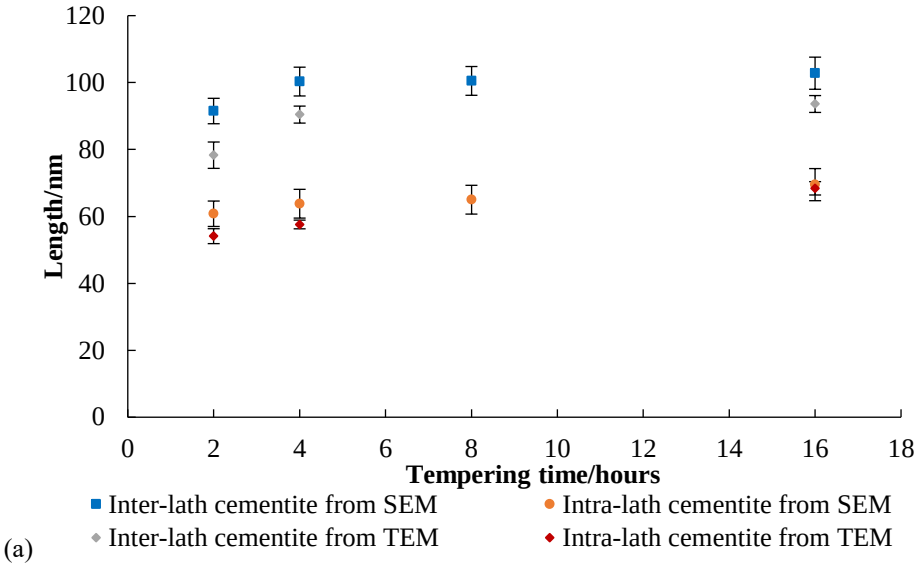

(a)

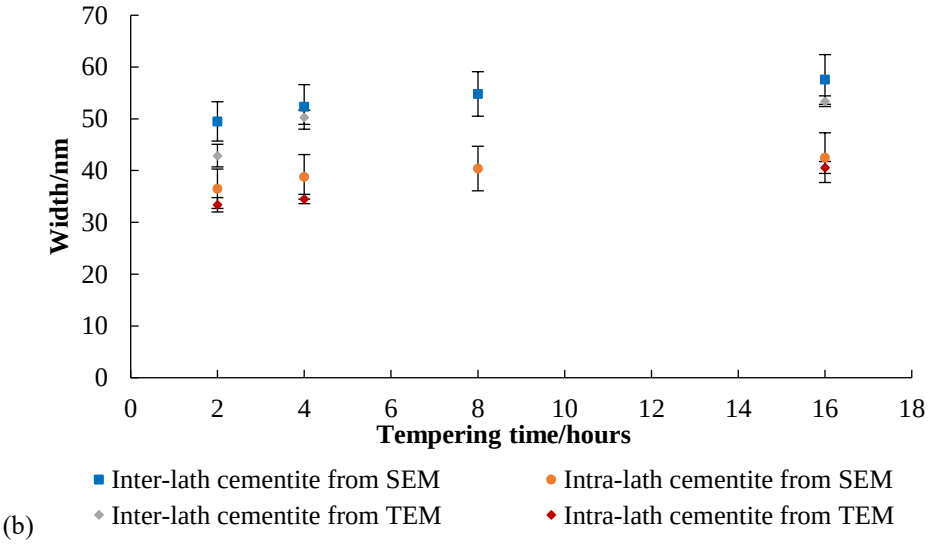

(b)

Figure 5-40. Average sizes of the elliptical cementite during tempering from 2 hrs to 16 hrs at 600 °C in the Base-Cr-Mo-V-Si steel: (a) average length; (b) average width.

In addition to the elliptical cementite particles, some fine carbides with needle-shape or elliptical shape (red arrowed in Figure 5-32) also exist within the laths during tempering from 2 hrs to 16 hrs at 600 °C, which is also observed in the Base-Mo-V steel. The number density variation for these fine carbides in this steel is quite similar to that in the

Base-Mo-V steel, Figure 5-41. Firstly, the number density decreases during tempering from 0 hr to 2 hrs, illustrating the dissolution of as-quenched carbides. The fine needle-shaped carbides present after tempering for 2 hrs are cementite, confirmed by the EDS spectra in Figure 5-42 and elemental mapping (Fe-rich carbides) in Figure 5-43. The chemical composition for fine needle-shaped carbides remain constant at that for the elliptical cementite, Table 5-10. In addition, no alloy carbides have been detected after tempering for 2 hrs. Then the number density for these fine carbides increases with tempering time increasing from 2 hrs to 4 hrs, indicating the precipitation of secondary hardening alloy carbides after tempering for 4 hrs, which agrees well with the Base-Mo-V steel. Mo-V-rich M_2C (one of the predicted pseudo-equilibrium carbides in this steel, Table 4-3) is also expected to be the secondary alloy carbide after cementite in this steel based on the Baker-Nutting diagrams for a 0.6Cr-0.5Mo steel [7], Figure 1-1, and Cr-Mo-V steels with low V/Mo ratio (< 0.17) and V< 0.1 wt % [75, 95], Figure 2-14. In the 0.6Cr-0.5Mo steel, M_2C carbides form after tempering for 1 hr at 600 °C and persist after 100 hours tempering at 600 °C; and only when the Cr content is larger than 1 wt %, do Cr-carbides (M_7C_3 and $M_{23}C_6$) precipitate, such as a small amount of M_7C_3 detected after tempering for 24 hrs at 600 °C in 1.1Cr-0.5Mo steel [7]. Finally, the number density for fine carbides gradually decreases during tempering from 4 hrs to 16 hrs, however, the number density for fine carbides in this steel is slightly higher than that in the Base-Mo-V steel after tempering for 16 hrs due to the higher content of Si retarding the dissolution of the needle-shaped cementite.

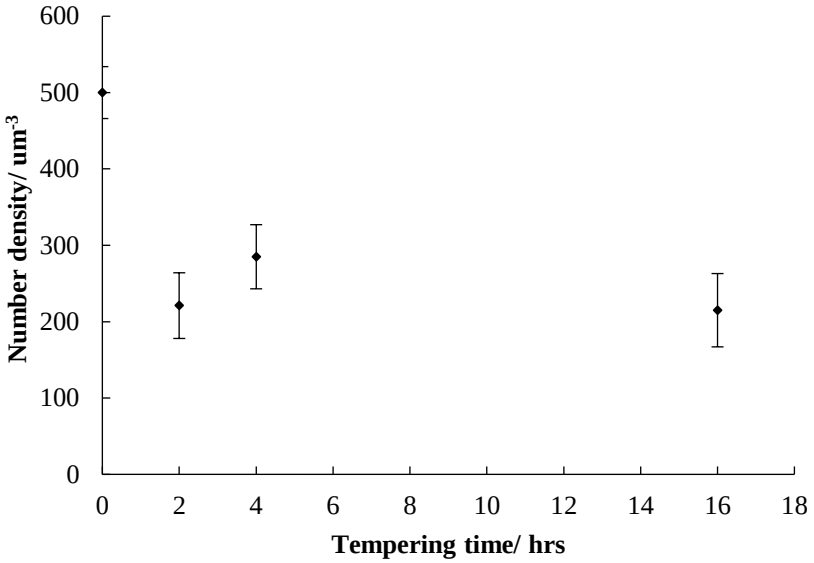

Figure 5-41. The number density variation for the fine carbides in the Base-Cr-Mo-V-Si steel tempered from 0 hr to 16 hrs at 600 °C from TEM measurements.

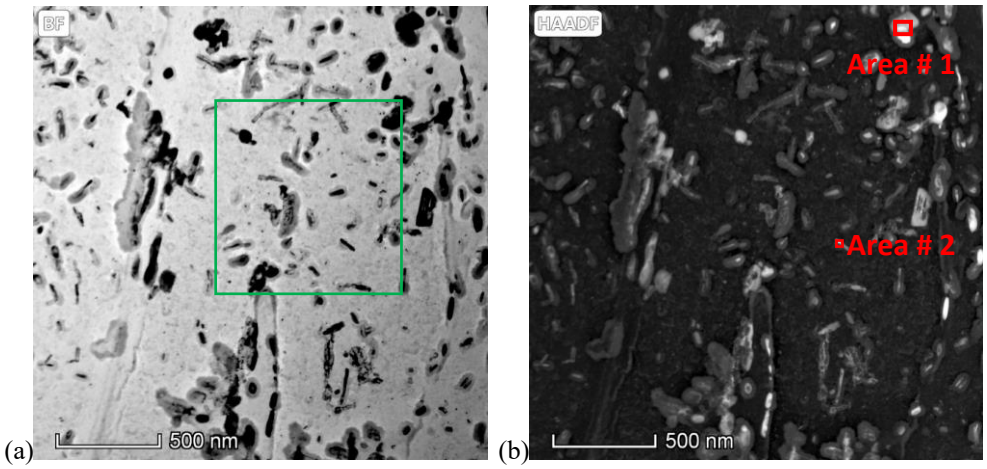

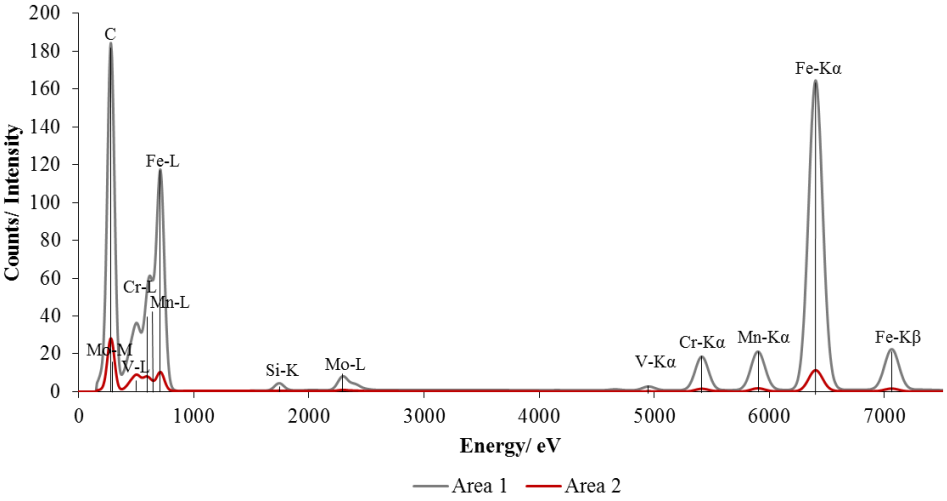

(c)

Figure 5-42. STEM observation of the comparatively large elliptical cementite and fine needle-shaped carbides in the Base-Cr-Mo-V-Si steel after tempering for 2 hrs at 600 °C using a carbon replica specimen: (a) bright field image; (b) HAADF image; (c) EDS spectra for the large elliptical cementite particle (Area 1) and fine needle-shaped cementite (Area 2).

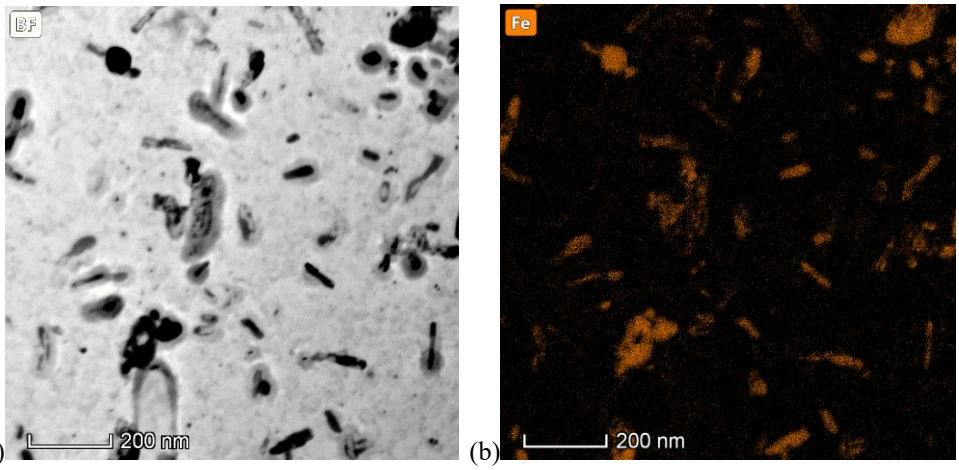

(a) (b)

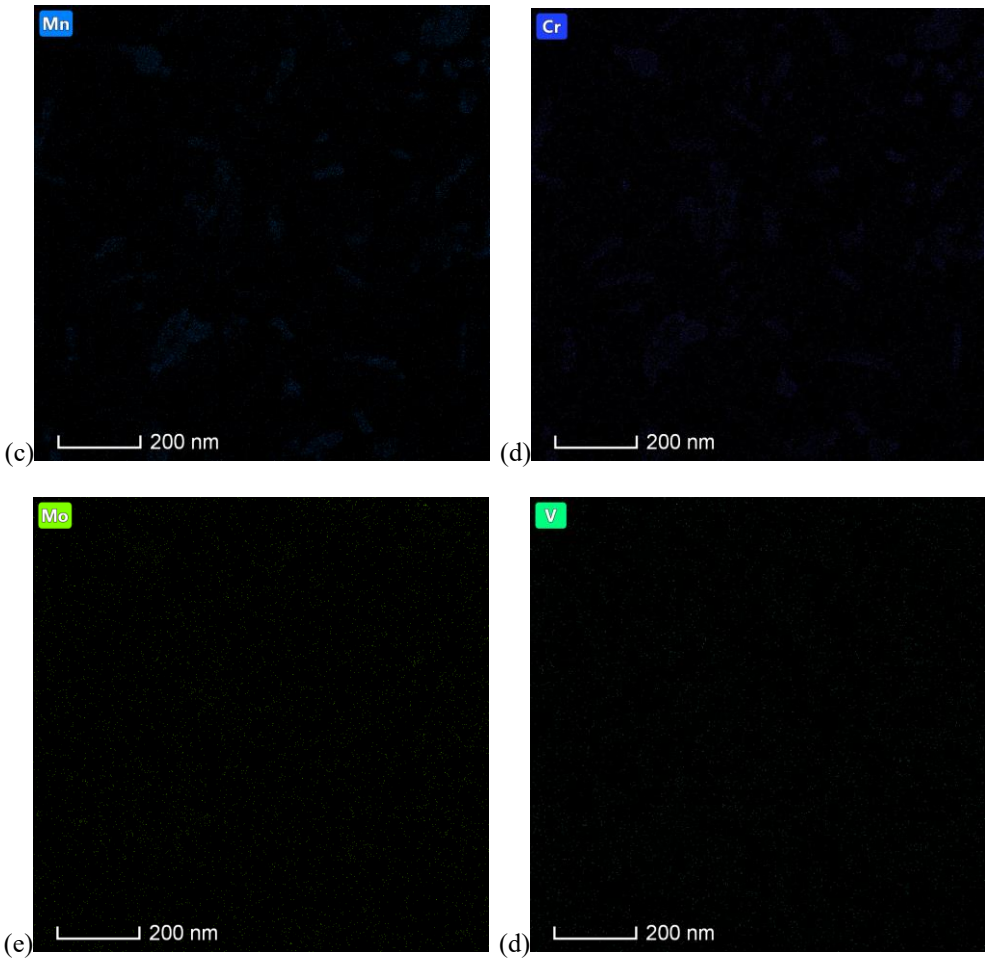

(c) (d) (e) (d)

Figure 5-43. (a) Bright field image of the area circled in Figure 5-42(a) in the Base-Cr-Mo-V-Si steel after tempering for 2 hrs at 600 °C; (b)-(d) elemental mapping.

Table 5-10. M to Fe ratio values, Y_M (M represents Mn, Cr, Mo and V), for different particles using carbon replica specimens from EDS measurements for the Base-Cr-Mo-V-Si steel tempered for 2 hrs at 600 °C

	Y_{Mn}	Y_{Cr}	Y_{Mo}	Y_V
Elliptical cementite	0.093±0.014	0.079±0.018	0.025±0.006	0.014±0.005
Needle-shaped cementite	0.113±0.017	0.108±0.019	0.039±0.008	0.012±0.005
Pseudo-equilibrium cementite (Thermo-Calc)	0.174	0.292	0.030	0.001

5.5 Discussion

5.5.1 The occurrence of auto-tempering in the three steels

Auto-tempering occurs during water quenching in all three steels, where carbon partially diffuses out from solid solution to form carbides within the martensite laths due to high Ms temperatures. Both ε'-carbides and cementite have been observed in the three steels based on the habit plane analysis. Based on the reported orientation relationship between the orthorhombic ε'-carbides and ferrite [29, 32-34] (discussed in section 2.1), the misfit is calculated as followed:

$$m_{\varepsilon}=\frac{|a_0-a_{\varepsilon'}|}{a_0}\times 100\% \qquad \text{Equation 5-3}$$

Similarly, the misfit between cementite and ferrite based on the Bagaryatski OR [45] (discussed in section 2.1) is in Equation 5-4.

$$m_{cem}=\frac{|\sqrt{2}a_0-a_{cem}|}{\sqrt{2}a_0}\times 100\% \qquad \text{Equation 5-4}$$

Where, a_0 is the lattice parameter for the ferritic matrix in the as-quenched condition obtained from XRD measurements, Table 5-2; $a_{\varepsilon'}$ is one of the lattice parameters for ε'-carbides and assumed to be 0.276 nm based on Taylor's results [32]; a_{cem} is one of the lattice parameters for cementite measured using interplanar spacing from SAD patterns in the three steels (0.4520 nm in the Base steel, 0.4521 nm in the Base-Mo-V steel, 0.4515 nm in the Base-Cr-Mo-V-Si steel). The misfit values between ε'-carbides and

ferrite for the three steels are obviously smaller than those between cementite and ferrite, Table 5-11 and Table 5-12, demonstrating that ε'-carbide can firstly precipitate as the transition iron carbide with lower nucleation barrier (lower interfacial energy) and then transform to cementite.

In the Base and Base-Mo-V steels, cementite is found to be the predominant as-quenched carbide. As the cooling process is only a few seconds (approximately 60 °C/s cooling rate [172]), the carbon diffusion distance in this time can be estimated (using equation $x=\sqrt{D_{VC}t}$) to be up to 90 nm using a step function for cooling from the ε'-carbide formation temperature with $D_{VC}=2.07\times10^{-6}\exp(-85048.3/RT)$ m^2/s used [173]. This would allow carbon to diffuse to the pre-existing carbides during quenching for a carbide spacing of approximately 100±50 nm (as measured in these samples). Therefore, it is feasible for cementite to form on the pre-existing ε'-carbides in the Base and Base-Mo-V steels. The formation of cementite is suppressed with Si contents exceeding 1.4 wt % [64], and it has been found that in the Base-Cr-Mo-V-Si steel, ε'-carbide becomes the predominant as-quenched carbide, which is consistent with the extra addition of Si in delaying the transformation from ε'-carbide to cementite during auto-tempering [5]. The retained carbon contents in the Base and Base-Mo-V steels remain constant after water quenching, Table 5-2, resulting in a similar hardness in the as-quenched condition for the two steels (458±12 HV for the Base steel, 454±11 HV for the Base-Mo-V steel). However, a slightly higher retained carbon content as well as alloying contents (such as Cr and Si) are present in the Base-Cr-Mo-V-Si steel, which leads to a little bit higher as-quenched hardness being observed (471±12 HV) in this steel.

A mixture of cementite and ε'-carbide is present as the auto-tempered carbides in the three S690-based steels, which is slightly different from literature reports where only cementite has been identified as the carbide in some as-quenched low carbon alloyed steels [27, 28, 30]. There are some possible reasons for this inconsistency:

(1) The quenching processes are different, e.g. polymer-water mixture quenching in the Fe-0.153C-1.54Mn-0.78Si-0.21Mo-0.016Nb steel [28] compared to water quenching in S690-based steels;

(2) The actual chemical composition slightly varies, e.g. a higher content of Si in the Base-Cr-Mo-V-Si steel;

(3) The techniques for the confirmation of carbide type are different between the reported steels [27, 28, 30] where SAD patterns were used, and S690-based steels where the trace analysis of habit plane measurement was used. Generally, the SADP technique is not sensitive enough to identify carbides with smaller sizes or smaller amounts due to their weak reflections especially when different types of carbides coexist.

Table 5-11. The misfit between ferrite and ε'-carbide based on the reported OR in the three steels

	Misfit/ %
Base	3.84
Base-Mo-V steel	3.87
Base-Cr-Mo-V-Si steel	3.89

Table 5-12. The misfit between ferrite and cementite based on Bagaryatski OR in the three steels

	Misfit/ %
Base steel	11.36
Base-Mo-V steel	11.34
Base-Cr-Mo-V-Si steel	11.17

5.5.2 Carbide precipitation and coarsening in the three steels during tempering at 600 °C

In the Base steel, the retained carbon content in solid solution decreases on tempering from 0 hr to 2 hrs, therefore, it is expected that carbon will continue to precipitate from solid solution in 2 hour's tempering time probably on the pre-existing carbides causing growth. The retained carbon content nearly achieves the equilibrium carbon content after tempering for 2 hrs, Table 5-2. The reduction of retained carbon content from the as-quenched state is predicted to lead to an approximately 200 HV hardness decrease based on the hardness - carbon content relationship [174], as carbon significantly contributes to solid solution strengthening. This is consistent with the significant hardness drop measured for the Base steel tempered from 0 hr to 2 hrs, where the hardness changes from 458±12 HV (as-quenched condition) to 263±3 HV (after tempering for 2 hrs). All the carbides present within the laths and on the lath/grain boundary are elliptical (even spherical) in shape and consistent with cementite after tempering for 2 hrs at 600 °C. The chemical composition for these elliptical cementite particles is confirmed as $(FeMn)_3C$ when tempering from 2 hrs to 16 hrs at 600 °C in the Base steel, discussed in

section 6.1, where Mn is partitioning into cementite to a constant content. As stated in section 5.2, the coarsening of cementite occurs as average size increases, which is the dominant microstructural change during tempering from 2 hrs to 16 hrs as the lath sizes remain approximately constant with time (0.6±0.3 um) in the Base steel [172]. Due to the coarsening of inter- and intra-lath cementite occurring independently, solute diffusion (i.e. Mn diffusion) between particles is either along the boundary or through the bulk between particles, but not through the bulk to a boundary in this steel. The precipitation sequence in this steel is cementite + ε'-carbide → cementite →independent coarsening of inter- / intra-lath cementite.

Coarsening of cementite occurs on tempering from 2 hrs to 16 hrs at 600 °C, resulting in a continuous hardness decrease in the Base steel, Figure 5-44. Based on the Hírsch and Humphreys precipitation hardening equation [175]

$$\sigma_p = \frac{6.26}{s} \ln \frac{D}{2.48\times10^{-4}} \qquad \text{Equation 5-5}$$

where D is the average particle diameter and s is the average separation between particles in um, strengthening from the elliptical inter- and intra-lath cementite is obtained, which can be converted to the Brinell hardness due to a useful engineering correlation - strength in MPa=3.4 (BHN) [176]. The hardness decrease originating from coarsening of inter- / intra-lath cementite in the Base steel is about 24 HB (≈24 HV), Figure 5-45, which is less than the actual hardness decrease (around 40 HV in Figure 5-44). The equation may be under predicting the effect of the change in size and number density of carbides on hardness, as the precipitation hardening equation was developed for a uniform

distribution of a single size distribution of precipitates, whereas the inter-lath and intra-lath elliptical cementite in the Base steel are different populations and not uniformly distributed (particularly for inter-lath cementite).

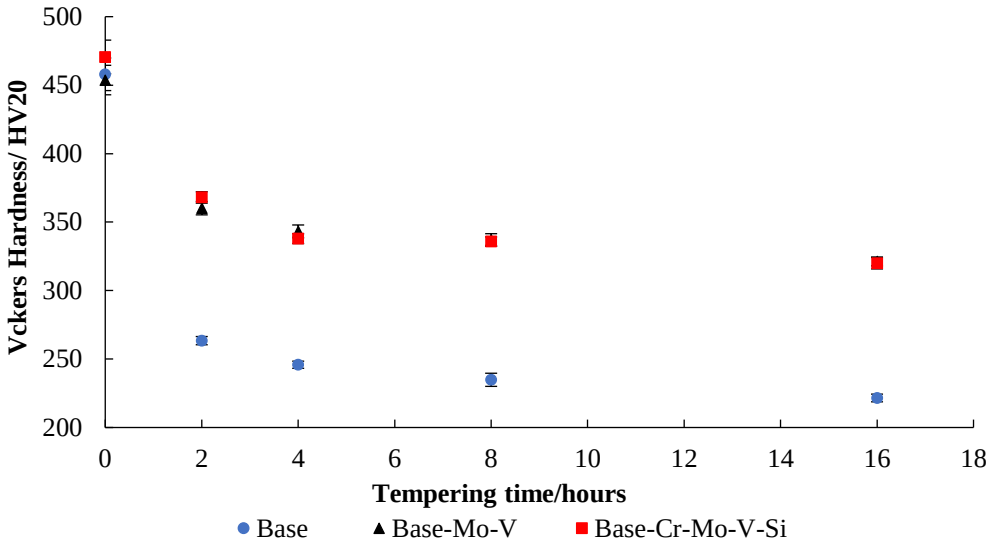

Figure 5-44. Hardness changes with time in the three steels tempered at 600 °C [172].

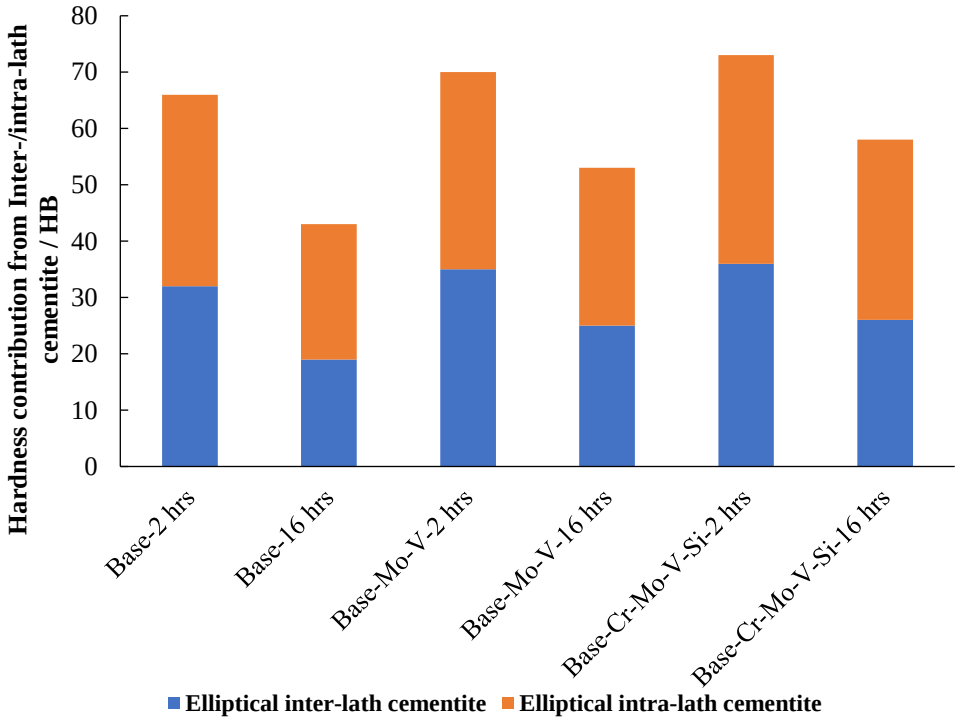

Figure 5-45. Predicted (using Hírsch and Humphreys precipitation hardening equation [175]) elliptical inter- / intra-lath cementite contribution to hardness in the three steels after tempering for 2 hrs and 16 hrs at 600 °C.

In the Base-Mo-V and Base-Cr-Mo-V-Si steels, a stable volume fraction for the large elliptical cementite also exists during tempering from 2 hrs to 16 hrs, Table 5-6 and Table 5-9, where the inter-lath cementite also constitutes the majority of the elliptical cementite volume fraction, Figure 5-23 and Figure 5-39, being consistent with the Base steel. Substitutional elements, such as Mn, Mo, Cr and V, also enrich the elliptical cementite particles in these two steels during tempering at 600 °C, agreeing well with the Base steel; this is approximately consistent with the Thermo-Calc prediction in that clear enrichment of Mn, Mo and Cr is seen. However, the alloying element content values are lower than predicted for the major elements of Mn and Cr which may be due to experimental errors (such as matrix effect) and/or insufficient time for the equilibrium levels to be reached. As discussed in the previous sections, the coarsening of cementite occurs during tempering from 2 hrs to 16 hrs, where again the coarsening of inter-lath cementite takes place independently from that of intra-lath cementite in the two steels. However, the rates of coarsening for the elliptical inter- / intra-lath cementite in the three steels differ and rank as Base> Base-Mo-V> Base-Cr-Mo-V-Si, Figure 5-46, due to the different diffusivities of substitutional elements that are partitioning into cementite during tempering as well as any effects of Si in the matrix. The rate of coarsening for the elliptical cementite in the Base-Mo-V steel is much lower than that in the Base steel due to its higher content of alloying elements (Mo and V). Normally, Mo has a smaller diffusivity compared to Mn in the ferrite matrix (D_{Mo} is about 1 order of magnitude lower than D_{Mn} in ferrite at 600 °C [177]), therefore, the cementite coarsening rate in the Base-

Mo-V steel is reduced compared to that in the Base steel. In the Base-Cr-Mo-V-Si steel, the spheroidisation and coarsening of cementite is slightly more inhibited with the extra addition of Si, where a finer dispersion of cementite is observed in Figure 5-31. Similarly to the Base steel, the sizes for the elliptical inter-lath cementite are obviously larger than those for intra-lath cementite in the two steels due to faster solute lath/grain boundary diffusion. In addition, fine carbides, including needle-shaped cementite and/or finer elliptical secondary Mo-V-rich carbides, are present on tempering in the Base-Mo-V and Base-Cr-Mo-V-Si steels. The secondary Mo-V-rich carbides, which are expected to be M_2C type carbides due to the low V and Cr contents in the two steels [7, 75, 95], are firstly observed after tempering for 4 hrs based on the fine carbide number density analysis, Figure 5-25 and Figure 5-41, and carbide composition measurements, Figure 5-30. Hence, the precipitation sequence for the two steels is cementite + ε'-carbide → cementite → secondary Mo-V-rich (expected to be M_2C) carbides + independent coarsening of inter- / intra-lath cementite at a lower coarsening rate than the Base steel. Solute diffusion in the Base-Mo-V and Base-Cr-Mo-V-Si steels is either along the lath boundary resulting in coarsening of inter-lath cementite, or through the bulk leading to coarsening of intra-lath cementite and formation of secondary Mo-V-rich carbides during the early stages of tempering.

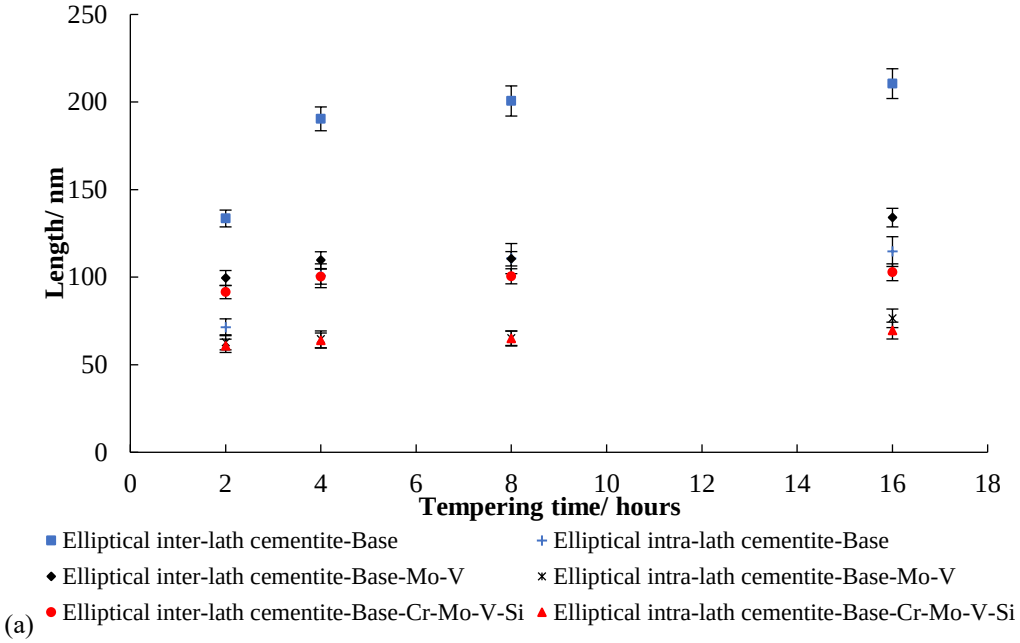

(a)

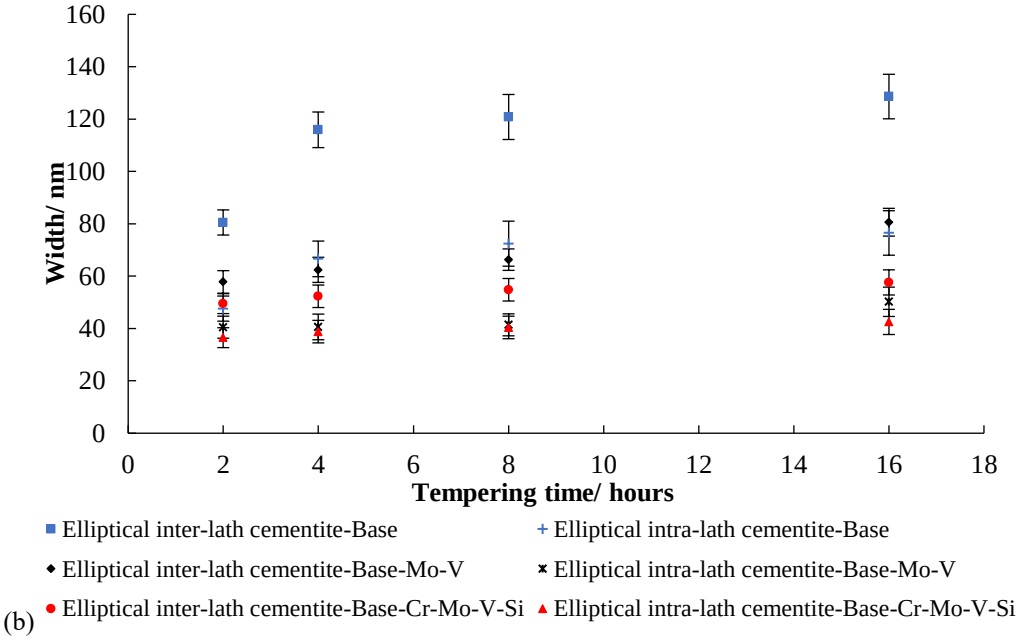

(b)

Figure 5-46. Average sizes of elliptical cementite particles during tempering from 2 hrs to 16 hrs at 600 °C in the three steels: (a) length; (b) width.

In the Base-Mo-V and Base-Cr-Mo-V-Si steels, the hardness results are approximately the same during tempering from 2 hrs to 16 hrs, and remain 100 HV higher than that in

the Base steel probably due to the existence of fine carbides (needle-shaped cementite or/and secondary alloy carbides) within the martensite laths, Figure 5-44. The hardness decrease in the two steels (around 40 HV) is similar to that in the Base steel on tempering from 2 hrs to 16 hrs, Figure 5-44. Actually, coarsening of the elliptical cementite in the two steels is estimated to contribute similarly to hardness decrease (Base-Mo-V: 17 HB (≈17 HV); Base-Cr-Mo-V-Si: 15 HB (≈15 HV)) using the Hírsch and Humphreys precipitation hardening equation [175], Figure 5-45. In addition, it is interesting to note that the observation of fine secondary alloy carbides (M_2C) after 4 hours tempering does not appear to result in any secondary hardening peak in the two steels, Figure 5-44, which is consistent with 0.1C-0.47Mo or 0.35C-0.5Cr steels [110, 115], where there is no significant secondary hardening peak present during tempering. This may be due to the low level of alloying content used (0.5 wt % Mo) resulting in only a small increase in overall number density of fine carbides.

5.6 Conclusions

1. Auto-tempering occurs in the three S690-based steels during water quenching, where cementite and ε'-carbide are both observed. In the Base and Base-Mo-V steels, cementite is the predominant as-quenched carbide; however, in the Base-Cr-Mo-V-Si steel, ε'-carbide constitutes a larger number percentage consistent with the extra addition of Si in slowing down the transformation from ε'-carbide to cementite during auto-tempering.

2. In the Base steel, only elliptical cementite is observed within the laths and on the lath/grain boundaries when tempering from 2 hrs to 16 hrs at 600 °C, during which time coarsening of cementite takes place. The coarsening of inter-lath cementite occurs independently from that of intra-lath cementite. The precipitation sequence for this steel during tempering from 0 hr to 16 hrs is cementite + ε'-carbide → cementite → independent coarsening of inter- / intra-lath cementite.

3. In the Base-Mo-V and Base-Cr-Mo-V-Si steels, relatively large elliptical inter- / intra-lath cementite and fine needle-shaped cementite within the laths are both present during tempering from 2 hrs to 16 hrs at 600 °C. The coarsening of inter-lath cementite takes place independently from that of intra-lath cementite. Secondary Mo-V-rich carbides have been firstly observed after tempering for 4 hrs at 600 °C. The precipitation sequence on tempering from 0 hr to 16 hrs for the two steels is cementite + ε'-carbide → cementite → secondary Mo-V-rich (expected to be M_2C carbide) carbide + independent coarsening of inter- / intra-lath cementite at a lower coarsening rate than the Base steel.

4. Substitutional elements, i.e. Cr, Mo, V and Mn, enrich cementite and secondary alloy carbides. Therefore, the diffusion of these elements is either along the lath/grain boundary resulting in the coarsening of inter-lath cementite, or through the bulk leading to the coarsening of intra-lath cementite (Base steel) and formation of secondary Mo-V-rich carbides (Base-Mo-V and Base-Cr-Mo-V-Si steels) when tempering from 2 hrs to 16 hrs at 600 °C. Solute diffusion does not occur significantly through the bulk to a boundary during tempering from 2 hrs to 16 hrs.

5. The as-quenched hardness for the Base and Base-Mo-V steels remain consistent, which is slightly lower than that in the Base-Cr-Mo-V steel due to a slightly higher retained carbon content as well as alloying contents (such as Cr and Si) being present in the Base-Cr-Mo-V-Si steel. However, the hardness decreases follow the same trend on tempering in the three steels, although the hardness results for the Base-Mo-V and Base-Cr-Mo-V-Si steels are similar and consistently about 100 HV higher than those for the Base steel during tempering from 2 hrs to 16 hrs. Coarsening of cementite contributes to the softening process in the three steels during tempering from 2 hrs to 16 hrs. In addition, the observation of fine secondary Mo-V-rich carbides after 4 hours tempering does not appear to result in any secondary hardening peak in the Base-Mo-V and Base-Cr-Mo-V-Si steels.

Chapter 6 DICTRA modelling for coarsening of inter-lath cementite in the Base and Base-Mo-V steels

As discussed in Chapter 5, the coarsening of inter-lath cementite in the Base, Base-Mo-V and Base-Cr-Mo-V steels tempered from 2 hrs to 16 hrs contributes to the decrease of hardness, Figure 5-45. As reported in the literature (section 3.2.3), DICTRA coarsening model (one-dimensional diffusion model) has been widely used in different steels to simulate the coarsening of carbides in a matrix and on the grain/sub-grain boundary, where the predicted average radius variations for carbides have shown some agreement with the experimental radius changes, although some discrepancies still have been observed [149, 152, 157, 159, 160]. However, it is still useful to carry out a simulation using the DICTRA coarsening model as a first step to predict how the average radius increases with time for inter-lath cementite in the Base and Base-Mo-V steels, and check the accuracy of the simulation compared with experimental observations.

6.1 The chemical compositions for inter-lath cementite and the ferritic matrix to choose proper systems in the coarsening model

It was found that the coarsening process took place for inter- and intra-lath cementite separately after tempering for 2 or more hours at 600°C under equilibrium (Base steel) or pseudo-equilibrium (Base-Mo-V steel) conditions (pseudo-equilibrium condition means a reaction step that the concentration of activated complexes at the transition state is approximately constant with time). Hence, the Ostwald ripening modelling for inter-lath cementite was carried out independently with the starting size of carbides used as input being the measured sizes from the 2 hrs tempered experimental data.

The chemical compositions for inter-lath cementite and the ferritic matrix in the Base steel after tempering for 2 hrs and 16 hrs have been measured. The selected inter-lath cementite particles are very close to the hole to obtain relatively accurate cementite chemical compositions. As shown in Figure 6-1 and Figure 6-2, the chemical composition for cementite is ascertained as $(FeMn)_3C$ in the Base steel during tempering. Y_M (M=Mn or Si in the Base steel), which is the M to Fe ratio, is defined using Equation 5-2 in order to consistently check the substitutional solute content (i.e. Mn or Si) in the inter-lath cementite and ferritic matrix. As shown in Table 6-1, Y_{Mn} in inter-lath cementite remains constant when tempering from 2 hrs to 16 hrs, which is much larger than that in the matrix. In addition, Y_{Si} in cementite is lower than that in the matrix, Table 6-1, indicating the depletion of Si in cementite. However, as reported in the literature (discussed in section 2.2.2), Si segregates in the cementite/ferrite interface in the matrix and significantly slows down the rate of coarsening for cementite [68, 77, 79-81], hence, the effect of Si on coarsening should not be ignored. Therefore, the systems chosen in the Base steel are simplified as Fe-C-Mn and Fe-C-Mn-Si where the diffusion of Mn is the rate-controlling step for coarsening of cementite.

(a)

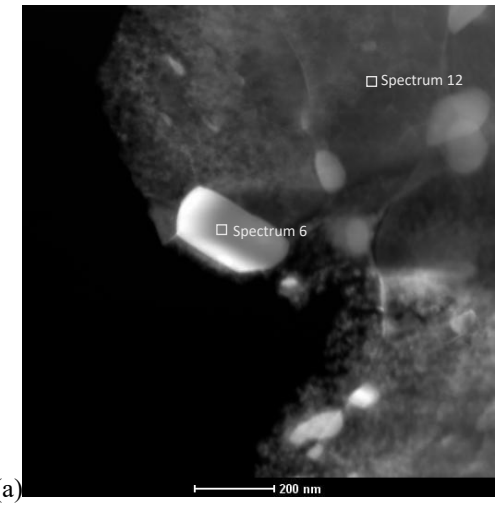

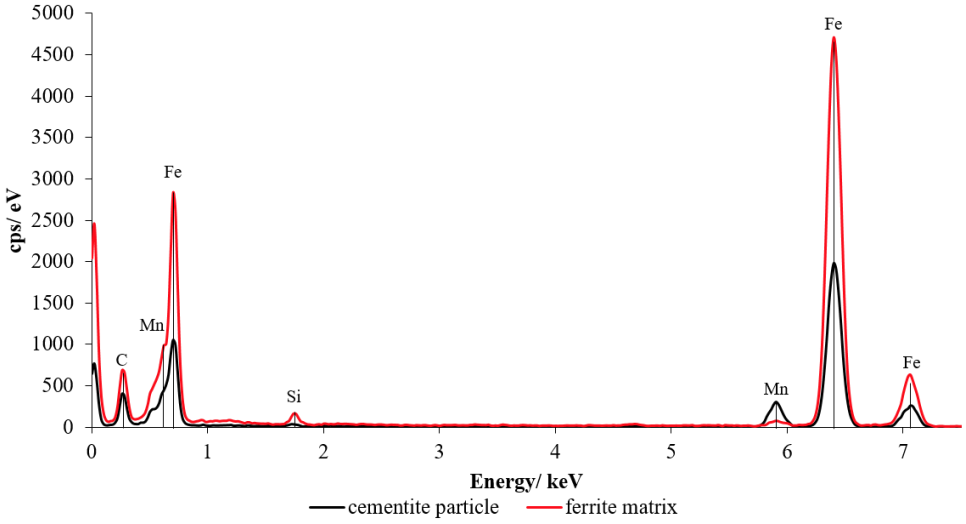

(b)

Figure 6-1. EDS measurements on the chemical composition for inter-lath cementite and the matrix in the Base steel after tempering for 2 hrs: (a) the morphology of the selected particle and matrix for EDS measurements; (b) EDS spectra for cementite and the ferrite matrix.

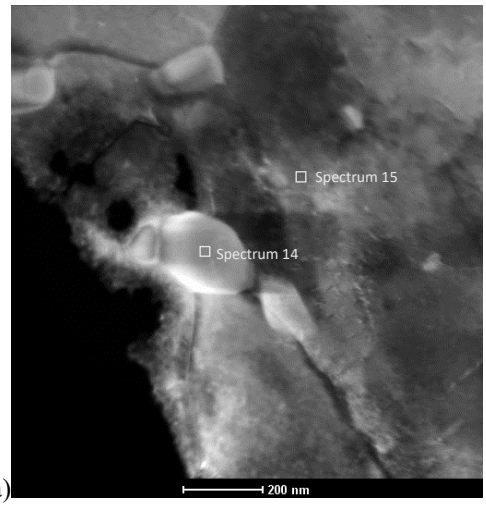

(a)

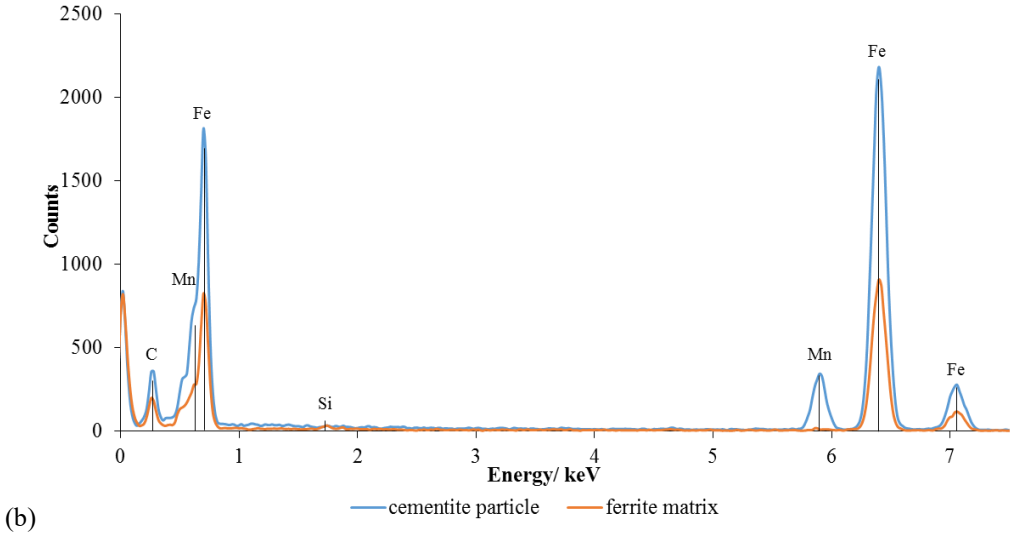

(b)

Figure 6-2. EDS measurements on the chemical composition for inter-lath cementite and the matrix in the Base steel after tempering for 16 hrs: (a) the morphology of the selected particle and matrix for EDS measurements; (b) EDS spectra for cementite and the ferrite matrix.

Table 6-1. Measured compositions (Y_{Mn} and Y_{Si}) for inter-lath cementite and the ferritic matrix in the Base steel tempered for 2 hrs and 16 hrs from EDS measurements

	2 hrs	16 hrs
Y_{Mn} for inter-lath cementite	0.140±0.016	0.146±0.014
Y_{Mn} for the ferritic matrix	0.012±0.002	0.012±0.003
Y_{Si} for inter-lath cementite	0.007±0.001	0.002±0
Y_{Si} for the ferritic matrix	0.013±0.002	0.010±0.002

Table 6-2. Thermo-Calc predicted equilibrium compositions (Y_{Mn} and Y_{Si}) for cementite and the ferritic matrix in the Base steel

	Equilibrium condition
Y_{Mn} for cementite	0.188
Y_{Mn} for the ferritic matrix	0.009
Y_{Si} for cementite	0.000
Y_{Si} for the ferritic matrix	0.003

The equilibrium chemical compositions in cementite and the ferrite matrix have been calculated using Thermo-Calc software in the Base steel, Table 6-2, which are further used in the coarsening model due to the inaccuracy and fluctuation of the alloying contents in cementite and the ferritic matrix measured from EDS measurements. Mn is partitioned into inter-lath cementite when tempering at 600 °C, and its diffusion along the lath boundary dominates coarsening of inter-lath cementite. The comparisons between the observed and calculated Y_{Mn} in cementite and ferrite are made:

(1) The measured Y_{Mn} in inter-lath cementite remains constant for tempering from 2 hrs to 16 hrs at 600 °C and is slightly lower than the predicted equilibrium Y_{Mn} in cementite, probably due to experimental errors, such as the matrix influence decreasing the apparent Mn content in cementite. This indicates that the equilibrium Mn content in inter-lath cementite is established after tempering for 2 hrs, and the observation here is approximately consistent with the observation of Mn contents in cementite in Fe-0.6C-1Mn and Fe-0.6C-2Mn steels tempered at 650 °C [68], Figure 2-8.

(2) The measured and predicted Y_{Mn} values in the matrix do not differ significantly.

Thus, a slightly higher coarsening rate might be expected if the predicted equilibrium Mn content in cementite is used in the coarsening model instead of the observed Mn content in inter-lath cementite due to a slightly larger Mn flux between cementite and the ferrite matrix.

As discussed in Chapters 4, cementite has been predicted as one of the pseudo-equilibrium carbides in the Base-Mo-V steel, Table 4-3, and the coarsening of inter-lath cementite occurs independently from that of intra-lath cementite during tempering from 2 hrs to 16 hrs at 600 °C (section 5.3). Therefore, the simulation of coarsening for inter-lath cementite is also carried out in isolation when tempering from 2 hrs to 16 hrs at 600 °C. As discussed in section 5.3, the chemical composition for cementite is confirmed as $(FeMnMoV)_3C$, where the measured Mn content in cementite is much larger than the Mo or V content, which agrees with EDS measurements for the inter-lath cementite in Figure 6-3, Figure 6-4 and Table 6-3. As shown in Table 6-3, Y_{Mn}, Y_{Mo} and Y_V in inter-lath cementite remain constant after tempering for 2 hrs and 16 hrs, which are all larger than those in the matrix, indicating the partition of substitutional elements (i.e. Mn, Mo and V) into cementite during tempering. The measured Y_{Mn}, Y_{Mo} and Y_V values in inter-lath cementite from thin foil specimens show some agreement with those in the large elliptical and fine needle-shaped cementite from carbon replica specimens in this steel tempered for 2 hrs and 4 hrs, Table 5-7 and Table 5-8, although a few discrepancies still exist, probably due to the influence from the matrix decreasing the measured Y_{Mn}, Y_{Mo} and Y_V values in inter-lath cementite for thin foil specimens.

The chemical compositions for the pseudo-equilibrium cementite and ferrite matrix in the Base-Mo-V steel are also calculated and listed in Table 6-4. Similarly to the Base

steel, the measured Y_{Mn} in inter-lath cementite in the Base-Mo-V steel is also lower than the predicted value, whereas the calculated and measured Y_{Mn} values in the ferrite matrix remain constant. The predicted Y_{Mo} and Y_V values in cementite and the ferrite matrix do not differ significantly from the observed values due to their low contents. Si is also depleted in cementite and partitioned into the matrix in this steel as the Y_{Si} in inter-lath cementite is lower than that in the matrix, which agrees with the Base steel; therefore, the influence of Si on cementite coarsening should not be neglected in the Base-Mo-V steel as well. Therefore, the systems used for coarsening of inter-lath cementite in the Base-Mo-V steel have been selected as Fe-C-Mn-Mo-V and Fe-C-Mn-Mo-V-Si, where the rate-controlling step for the coarsening of inter-lath cementite is the diffusion of substitutional elements such as Mn, Mo and V. The calculated chemical compositions for cementite and the ferrite matrix are also used in the coarsening model due to the inaccuracy and fluctuation of EDS measurements.

(a)

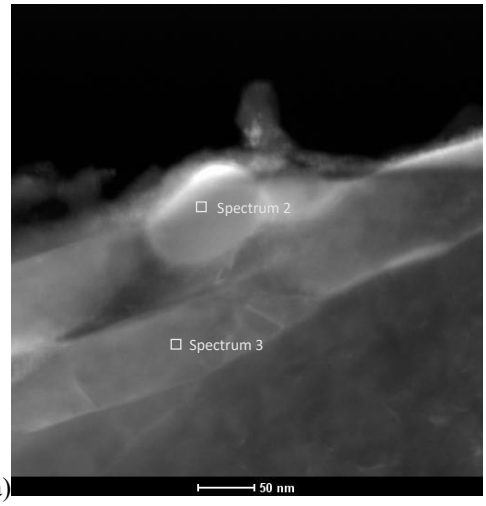

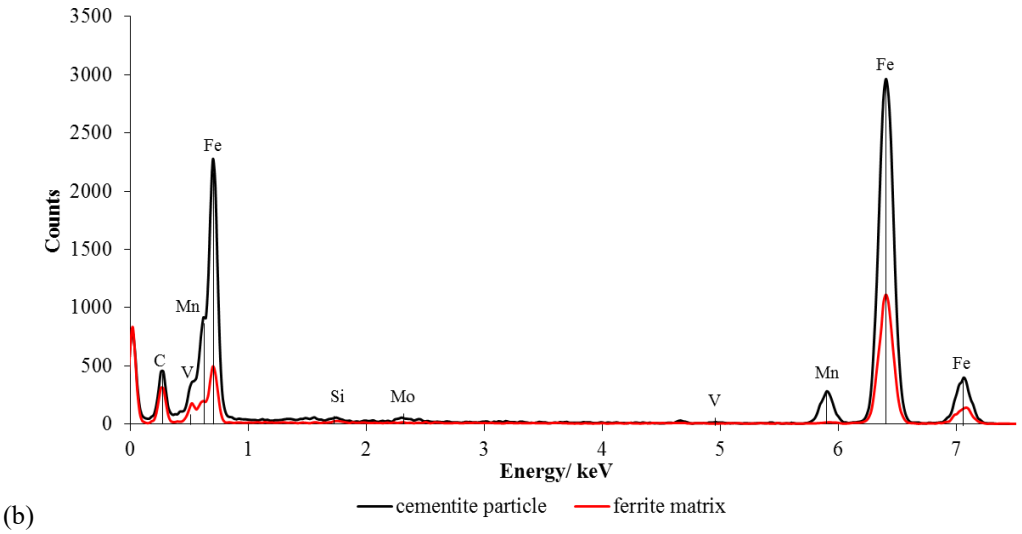

(b)

Figure 6-3. EDS measurements on the chemical composition for inter-lath cementite and the matrix in the Base-Mo-V steel after tempering for 2 hrs: (a) the morphology of the selected particle and matrix for EDS measurements; (b) EDS spectra for cementite and the ferrite matrix.

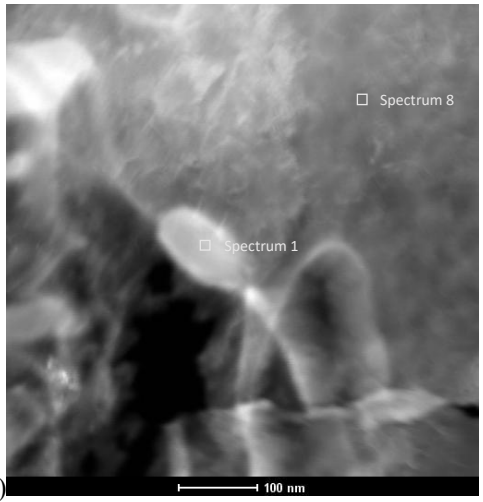

(a)

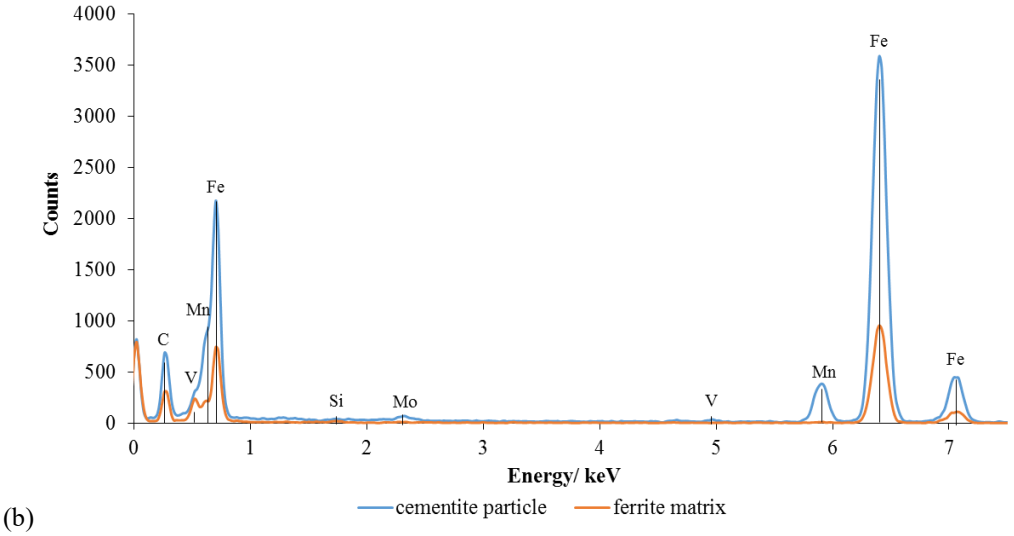

(b)

Figure 6-4. EDS measurements on the chemical composition for inter-lath cementite and the matrix in the Base-Mo-V steel after tempering for 16 hrs: (a) the morphology of the selected particle and matrix for EDS measurements; (b) EDS spectra for cementite and the ferrite matrix.

Table 6-3.Measured compositions (Y_{Mn}, Y_{Mo}, Y_V and Y_{Si}) for inter-lath cementite and the ferritic matrix in the Base-Mo-V steel tempered for 2 hrs and 16 hrs from EDS measurements

	2 hrs	16 hrs
Y_{Mn} for inter-lath cementite	0.086±0.021	0.089±0.018
Y_{Mn} for the ferritic matrix	0.010±0.003	0.010±0.004
Y_{Mo} for inter-lath cementite	0.016±0.004	0.015±0.003
Y_{Mo} for the ferritic matrix	0.004±0.001	0.003±0.001
Y_V for inter-lath cementite	0.005±0.001	0.004±0.001
Y_V for the ferritic matrix	0.000±0	0.001±0
Y_{Si} for inter-lath cementite	0.005±0.001	0.000±0
Y_{Si} for the ferritic matrix	0.007±0.001	0.008±0.001

Table 6-4. Thermo-Calc predicted compositions (Y_{Mn}, Y_{Mo}, Y_V and Y_{Si}) for cementite and the ferritic matrix in the Base-Mo-V steel

	Psuedo-equilibrium condition
Y_{Mn} for cementite	0.169
Y_{Mn} for the ferritic matrix	0.009
Y_{Mo} for cementite	0.010
Y_{Mo} for the ferritic matrix	0.001
Y_V for cementite	0.001
Y_V for the ferritic matrix	0.000
Y_{Si} for cementite	0.000
Y_{Si} for the ferritic matrix	0.003

6.2 The selection of parameters and simulation process in the DICTRA-coarsening model

A schematic diagram of the coarsening model in DICTRA software is shown in Figure 3-10, where the initial particle size and volume fraction were taken from 2 hours tempering experimental data, Table 6-5. The ferrite matrix cell radius was obtained based on Equation 3-22 where local equilibrium existed at the interface between the particles and ferrite matrix. The reported interfacial energy, λ, values between cementite and ferrite measured using different methods are listed in Table 6-6, among which λ= 0.5 J/m^2 measured from dihedral angle for lenticular-shaped cementite particles equilibrium with grain boundaries [178] is the most reasonable value for inter-lath cementite in the Base and Base-Mo-V steels. The molar volume of cementite is 0.6×10^{-5} m^3/mol from Thermo-Calc calculation, which is consistent with the reported value (0.78×10^{-5} m^3/mol) in Fe-0.6C steels [68, 160] and Thermo-Calc is further used to acquire the Gibbs free energy addition using Equation 3-23.

Table 6-5. The 2 hours experimental data for the DICTRA model in the Base and Base-Mo-V steels

	Base steel	Base-Mo-V steel
Average radius for inter-lath cementite /nm	47.8	34.3
Volume fraction for inter-lath cementite /%	2.7	2.7

Table 6-6. Selected literature values for the interfacial energy between cementite and ferrite

Reference	Cementite morphology and location	Temperature /K	Measuring method	Interfacial energy /J/m^2
[179]	Spherical shape (no location specified)	861	Coarsening rate and data fitting	0.56
[180]	Elongated spherical shape (no location specified)	903-963	Coarsening rate and data fitting	0.25-0.42
[178]	Lenticular shape (on the grain boundary)	973	Dihedral angle	0.52±0.13

Figure 6-5 shows the typical workflow when simulating diffusion problems in DICTRA, where the solid arrows represent the movement between different modules and the dashed arrows represent the data transferring within DICTRA [181]. All DICTRA diffusion simulations start from the SYS module, and then move to the DATA module, where the system can be defined by inputting the elements and phases, and both thermodynamic and kinetic data are retrieved. The retrieved data, which are used to describe the system, are sent to the GIBBS module, where DICTRA can access the data. Then, in the DICTRA module, the initial status of the system should be set with the definition of the geometry and boundary conditions. Generally, a system can contain multiple-cells, and each cell can include several regions. In each region the starting phases should be specified as well. In addition, various parameters, such as grid spacing and time step, for the numerical calculation should also be defined. Finally, the simulation starts to run within the DICTRA module. Figure 6-6 shows how the numerical procedure proceeds in DICTRA [182]. Thermodynamic and mobility data are both

applied to solve the diffusion equation at each grid point and time step at a given temperature. Interfacial equilibrium is used with the diffusion equation to work out the flux balance and obtain the elemental composition at each time step and grid point at a given temperature. After running the simulation, all the simulation results are stored in a dic format file, and the chosen information can be plotted in the POST module.

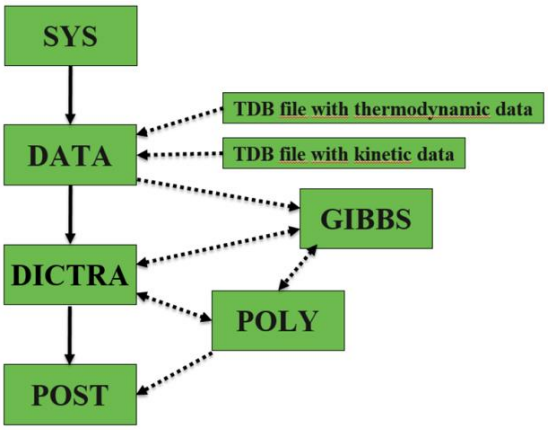

Figure 6-5. An example of DICTRA typical workflow [181].

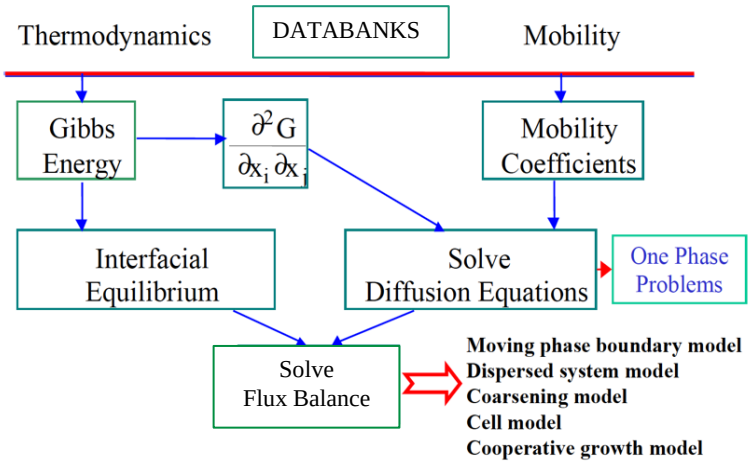

Figure 6-6. Numerical procedure in DICTRA [182].

DICTRA version 27 with the TCFe-7 thermodynamic database and the MOBFE-2 mobility database were used in this study. The systems for the coarsening model were simplified as Fe-C-Mn-M and Fe-C-Si-Mn-M (M represents the alloyed elements such as Mo and V) for the two steels. The active phases in this modelling process were selected as BCC (ferrite) and cementite, and the compositions of each active phase, obtained from Thermo-Calc calculations, were used as inputs in weight percent. A one-dimensional linear modelling method was used for the coarsening of cementite in the BCC phase. The temperature for the calculation was chosen to be the experimental tempering temperature of 600 °C. The simulation time was adjusted based on the experimental heat treatment time, and the smallest time step was input as 10^{-7} seconds as default to control the calculation. After the simulation process, the average particle radius against time was plotted and visualised in the POST module in DICTRA software.

6.3 The prediction results for coarsening of inter-lath cementite in the Base and Base-Mo-V steels using DICTRA model

In the Base steel, with an increase in tempering time from 2 hrs to 16 hrs, the predicted average radius for inter-lath cementite increases by less than 1 nm in the Fe-C-Mn and Fe-C-Mn-Si systems with interfacial energy λ=0.5 J/m^2, Figure 6-7. The predicted coarsening rate for inter-lath cementite is far slower compared to the experimental data on tempering from 2 hrs to 16 hrs at 600 °C. The addition of Si in the Fe-C-Mn-Si system can slightly decrease the coarsening rate compared to that in the Fe-C-Mn system, indicating the limited influence of Si on the activity of other alloying elements in the mobility database to further affect the coarsening rate in the simulation. In order to check the accuracy of the interfacial energy related governing equations used in DICTRA

simulations for particle coarsening within short tempering times, different interfacial energy values 0.4 - 0.6 J/m^2 between inter-lath cementite and the ferrite (based on the reported interfacial energy value 0.5±0.1 J/m^2 for lenticular-shaped cementite equilibrium with grain boundaries [178], Table 6-6) are used in the Fe-C-Mn-Si system in the Base steel. As shown in Figure 6-8, the coarsening rates remain constant with different interfacial energy values, resulting in a great discrepancy compared to the experimental observation.

Similarly, the predicted average radius for inter-lath cementite in Fe-C-Mn-Mo-V and Fe-C-Mn-Mo-V-Si systems in the Base-Mo-V steel also increases by less than 1 nm during tempering from 2 hrs to 16 hrs at 600 °C with interfacial energy λ=0.5 J/m^2, where the coarsening rate is too slow compared with the experimental observation. The effect of Si on the coarsening rate tends to be similar to that in the Base steel, although there are more alloying elements defined in the system. In addition, compared to the Base steel, Mo and V do not show much influence on changing the predicted rate of coarsening for inter-lath cementite, probably due to the similar diffusion coefficient for Mo and V as that for Mn defined in the mobility database in this software. However, the experimental data does demonstrate that the existence of Mo and V can significantly slow down the coarsening of inter-lath cementite, resulting in the inaccuracy of the simulation compared with the experimental observation.

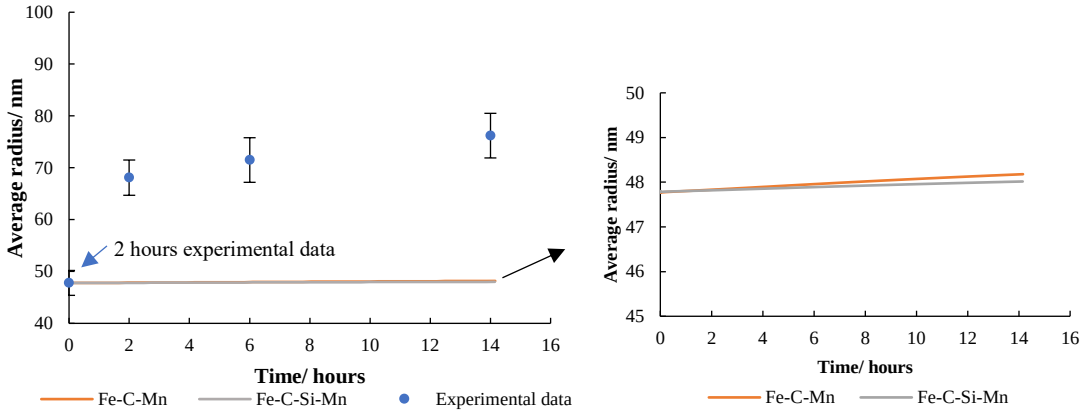

Figure 6-7. The coarsening of inter-lath cementite predicted by DICTRA model in Fe-C-Mn and Fe-C-Mn-Si systems with interfacial energy λ=0.5 J/m^2 compared with experimental data in the Base steel tempered at 600 °C.

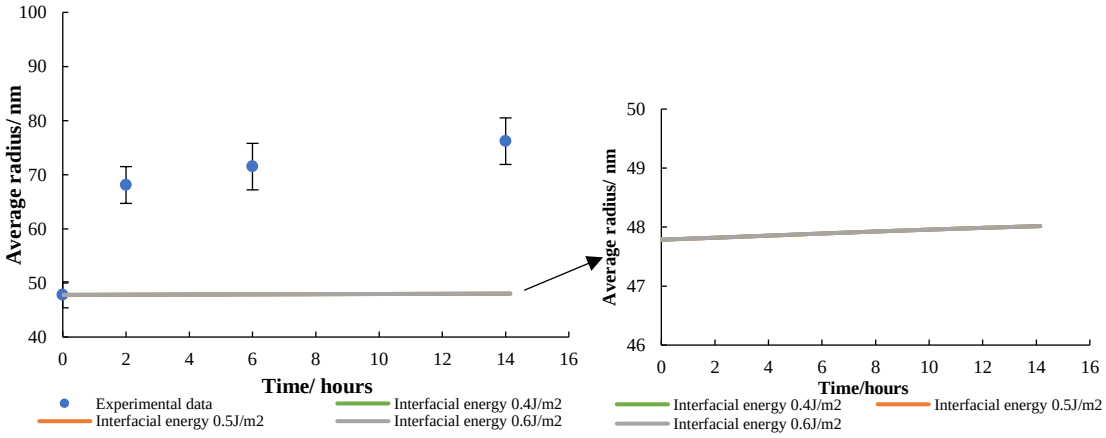

Figure 6-8. The coarsening of inter-lath cementite predicted by DICTRA model in the Fe-C-Mn-Si system with different interfacial energy values in 0.4 - 0.6 J/m^2 range compared with experimental data in the Base steel tempered at 600 °C.

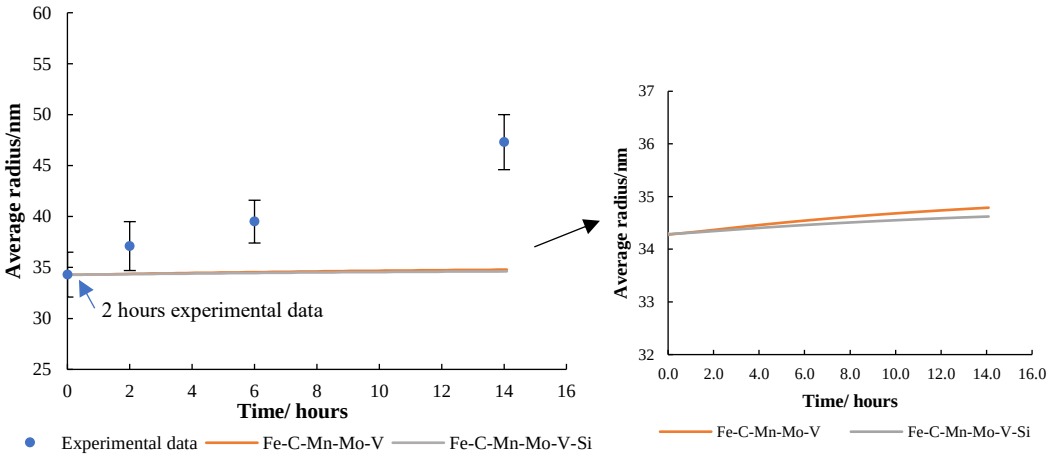

Figure 6-9. The coarsening of inter-lath cementite predicted by DICTRA in Fe-C-Mn-Mo-V and Fe-C-Mn-Mo-V-Si systems with interfacial energy λ=0.5 J/m^2 compared with experimental data in the Base-Mo-V steel tempered at 600 °C.

6.4 Discussion

Carbide forming elements, such as Mn, Cr, Mo and V, are expected to partition into cementite when the equilibrium condition is achieved [29, 41, 67, 68]. The cementite composition has been confirmed as $(FeMn)_3C$ in the Base steel or $(FeMnMoV)_3C$ in the Base-Mo-V steel. The partition of the substitutional elements, like Mn, Mo or V, into cementite in the Base and Base-Mo-V steels tempered at 600 °C shows agreement with the observation of partitioning of Mn into cementite in a Fe-C-Mn-Si steel tempered at 500°C for 0.83 hr [86] or Mn, Cr and Mo in cementite in AISI 4340 steel tempered at 575 °C for 2 hrs [30] (discussed in section 2.2.2). Mn is the predominant substitutional element partitioning into cementite in the Base and Base-Mo-V steels compared to Mo and V. The partitioning of substitutional elements, like Mn or Mo, in cementite can inhibit the rate of coarsening for cementite during tempering [68], as the diffusion of these substitutional elements between particles is very slow.

DICTRA 1D coarsening model has been used as a first step to simulate coarsening of inter-lath cementite in the ferrite matrix. As shown in Figure 6-7 and Figure 6-9, all the predicted rates of coarsening for inter-lath cementite are far slower than the experimental data in the two steels during tempering at 600 °C for 14 hours (from 2 hrs to 16 hrs), which are consistent with the predicted coarsening rate for cementite in a Fe-0.6C-2Mn steel [161] where the predicted radius remains constant with time tempered at 450 °C for 277.8 hrs or at 650 °C for 2.78 hrs, Figure 3-11. The predicted radii in the two steels increase linearly with very small slopes up to 14 hours, Figure 6-7 and Figure 6-9, which differ significantly from the experimental observation. In the Base steel, there is a sharp radius increase observed when tempering from 2 hrs to 4 hrs followed by a gentler one

for tempering from 4 hrs to 16 hrs; whereas in the Base-Mo-V steel, an approximately linear radius increase with relatively larger slope (compared to the simulation) has been observed. In addition, the predicted rate of coarsening for inter-lath cementite in the Base-Mo-V steel does not show any significant influence from the substitutional elements Mo and V compared to the Based steel.

In the literature, no detailed examinations of the accuracy of DICTRA 1D coarsening model for the simulation of coarsening of carbides in the matrix and along the grain/ sub-grain boundary have been carried out in different steels [149, 152, 157, 159, 160]. Actually, significant deviations have been found between the simulation and experimental observation for the coarsening of inter-lath cementite in the Base and Base-Mo-V steels during tempering from 2 hrs to 16 hrs. Possible reasons for these deviations are:

1. Uncertainties in the accuracy of the data available in the kinetic database in the software

(1) The diffusivities for substitutional elements might be reduced markedly in the kinetic database so that the predicted coarsening rates are too low compared to the experimental data for short tempering times.

(2) The reciprocal action of different substitutional elements (i.e. Mn, Mo or V) does not show any influence on the coarsening of cementite in the model, such as Figure 6-9 for the Base-Mo-V steel compared to Figure 6-7 for the Base steel, probably due to the very similar diffusivities defined in the kinetic database for these substitutional elements, which contradicts experimental data.

(3) The grain/sub-grain boundary diffusivity for substitutional elements is normally higher than the volume diffusivity [74]. However, there is no separate definition of solute grain/sub-grain boundary diffusivity in the software, which can be further used for the coarsening of carbides along the grain/sub-grain boundary.

2. Uncertainties about the interfacial energy effect in DICTRA governing equations

Interfacial energy determines the driving force for carbide coarsening: a higher interfacial energy value for an incoherent interface provides no particular crystallographic barrier for solute atom motion [120], resulting in a quicker coarsening rate. However, different interfacial energy values do not make any large contributions to changing the coarsening rates for tempering up to 14 hours at 600 °C in the simulation for the Base steel, Figure 6-8, which shows some agreements with Prat's [157] and Gustafson's [159] work where different interfacial energy values do not lead to significant radius increase in short times. Therefore, the simulation results call the DICTRA governing equations, which are associated with the interfacial energy such as Equation 3-23, into question when the coarsening time is relatively short.

3. The discrepancies between experimental observations and assumptions for the model

As discussed in the section 3.2.3, the discrepancies between the experimental data and assumptions in the DICTRA coarsening models might also result in inaccurate simulation results compared to the experimental observation [161]. Therefore, the assumptions used for DICTRA coarsening model have also been checked with experimental data in the two steels. One of the assumptions in the DICTRA coarsening

model is the definition of spherical particles existing in the system. Actually, the shape of inter-lath cementite deviates from the spherical shape, where most of inter-lath cementite particles in the two steels are slightly elongated with aspect ratios in the range 1 - 2, as shown in Figure 6-10. The change in particle shape can directly change the diffusion field around the particle, finally resulting in the variation of particle coarsening rates. Another assumption is that the particle radius ratio between maximum and average radii from size distribution is 1.5 and keeps stable during coarsening. However, the experimental ratio for inter-lath cementite in the two steels is higher than 1.5 (remaining around 2), Table 6-7, which are inconsistent with this assumption and might lead to the increase of coarsening rates [120].

In summary, the simulation of coarsening of inter-lath cementite in the Base and Base-Mo-V steels using DICTRA coarsening model is not accurate enough to match the experimental observations due to the above limitations. The deficiencies in the DICTRA model that could not be overcome by modifications to the substitutional element diffusivities or governing equations mean that an alternative modelling approach should be considered for simulating the coarsening of inter-lath cementite.

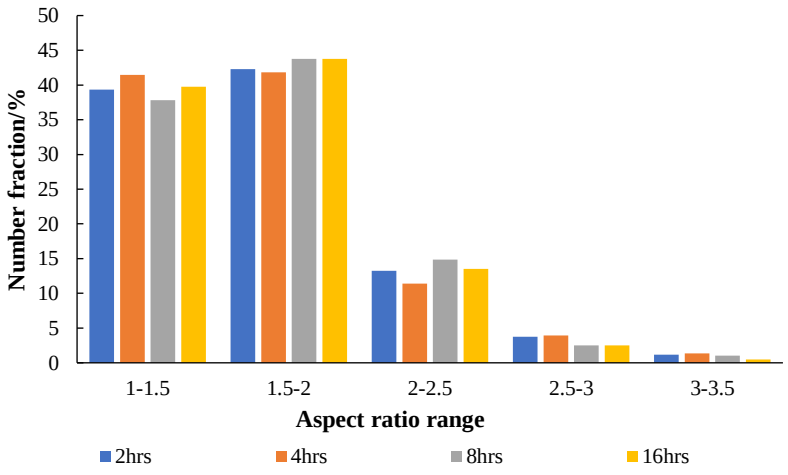

(a)

(b)

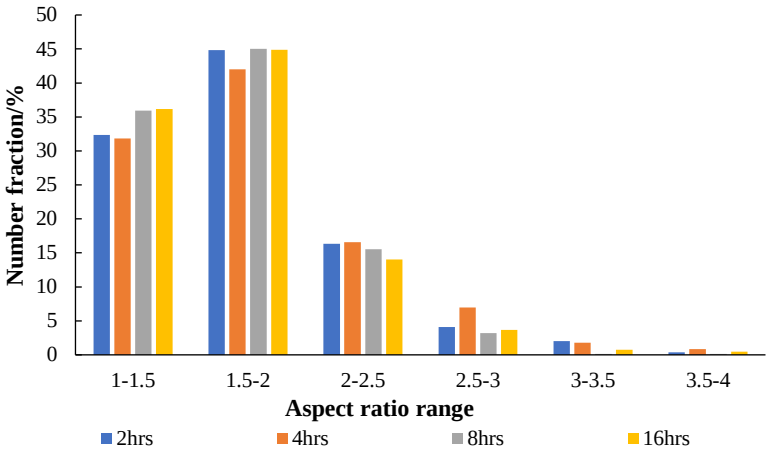

Figure 6-10. The aspect ratio - number fraction changes for inter-lath cementite during coarsening in the (a) Base and (b) Base-Mo-V steels after tempering from 2 hrs to 16 hrs from SEM measurements.

Table 6-7. The radius ratio between maximum and average radii for inter-lath cementite in the Base and Base-Mo-V steels tempered for 2 hrs and 16hrs respectively

	Ratio between maximum and average radii in Base steel	Ratio between maximum and average radii in Base-Mo-V steel
Inter-lath cementite for 2 hrs	2.0	1.9
Inter-lath cementite for 16 hrs	2.5	1.9

6.5 Conclusions

DICTRA 1D coarsening model predicts coarsening rates that are too slow for inter-lath cementite compared to the experimental data in the Base and Base-Mo-V steels during tempering from 2 hrs to 16 hrs at 600 °C. Different substitutional elements are taken into consideration in the model, however, the rates of coarsening for inter-lath cementite do not significantly change based on the simulation results. Possible reasons for these deviations have been discussed: uncertainties in the accuracy of the data available in the kinetic database in DICTRA, uncertainties about the interfacial energy effect in related DICTRA governing equations and the discrepancies between experimental observations and assumptions for the model.

Chapter 7 Mathematical modelling for coarsening and dissolution of coupled inter-lath cementite in the Base steel

In the Base steel, cementite is the equilibrium carbide precipitated during tempering from 2 hrs to 16 hrs where the inter-lath cementite constitutes most of the carbide volume fraction (section 5.2). The coarsening of inter-lath cementite occurs independently from that of intra-lath cementite during tempering from 2 hrs to 16 hrs at 600 °C. Figure 7-1 shows the arrangement of inter-lath cementite particles along the lath boundaries from SEM images, where the lath boundary is observed as a line connecting cementite particles. In terms of understanding dissolution and coarsening behaviours for inter-lath cementite with solute diffusion along the lath boundaries, it is very valuable and fundamental to build a mathematical model only for the coupled inter-lath cementite system, which treats the dissolution of smaller particle and coarsening of larger one as a simultaneous process.

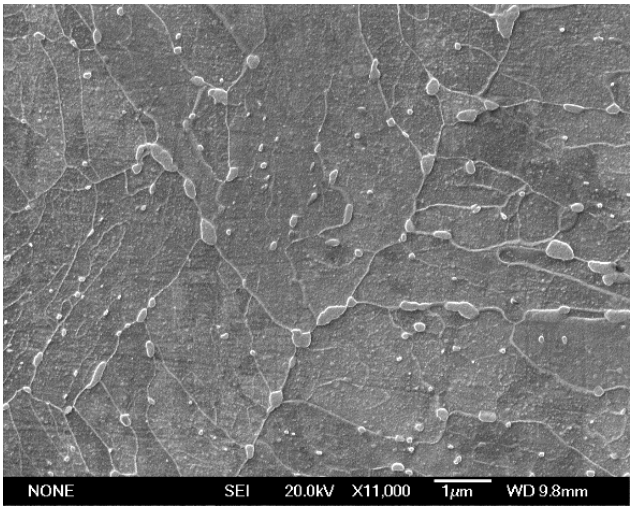

Figure 7-1. Example inter-lath cementite for the Base steel.

7.1 Analysis of experimental data to establish the model

As discussed in Chapter 5 and 6, the coarsening and dissolution of cementite along lath boundaries occurred under cementite volume fraction / composition equilibrium conditions during tempering from 2 hrs to 16 hrs at 600 °C in the Base steel. This indicates that the coarsening of inter-lath cementite took place with solute diffusion under steady-state condition, where Fick's first law was used to calculate the diffusional flux of solute atoms. A finite difference method was applied in the 1D mathematical diffusion model in this study and Matlab software was utilised to run the simulation.

As discussed in section 5.2, there is a faster coarsening rate for inter-lath cementite on tempering from 2 hrs to 4 hrs followed by a slower one from 4 hrs to 16 hrs. The inter-lath cementite number density - half-length distribution is shown in Figure 7-2. The number density significantly decreases for particles with half-length in 40 - 100 nm range and increases for particles with half-length in 130 - 200 nm range during tempering from 2 hrs to 4 hrs. The loss of particle volume from the smaller size range matches the increase of particle volume for the larger one (1.21×10^6 nm^3 when the area for the boundary plane is assumed to be 1 um^2 under the assumption that the particle number density measured from SEM images is the same as that in the boundary plane), therefore, the overall mass balance is obeyed. The smallest cementite particles with half-length in 40 - 50 nm range all dissolve for tempering from 2 hrs to 4 hrs, meanwhile, the largest cementite particles with half-length in 130 - 140 nm range have the maximum probability to coarsen to 190 - 200 nm range. In addition, during tempering from 4 hrs to 16 hrs, the overall particle mass balance is also obeyed where the increase of particle volume for the larger size range is consistent with the loss of particle volume from the

smaller one (1.48×10^6 nm^3 with the same assumptions as above). The smallest cementite particles with half-length in 50 - 60 nm range nearly all dissolve as the number density in this size range decreases significantly, while the largest cementite particles with half-length in 190 - 200 range nm have the maximum likelihood of coarsening to >260 nm (approximately 270 nm) during tempering from 4 hrs to 16 hrs.

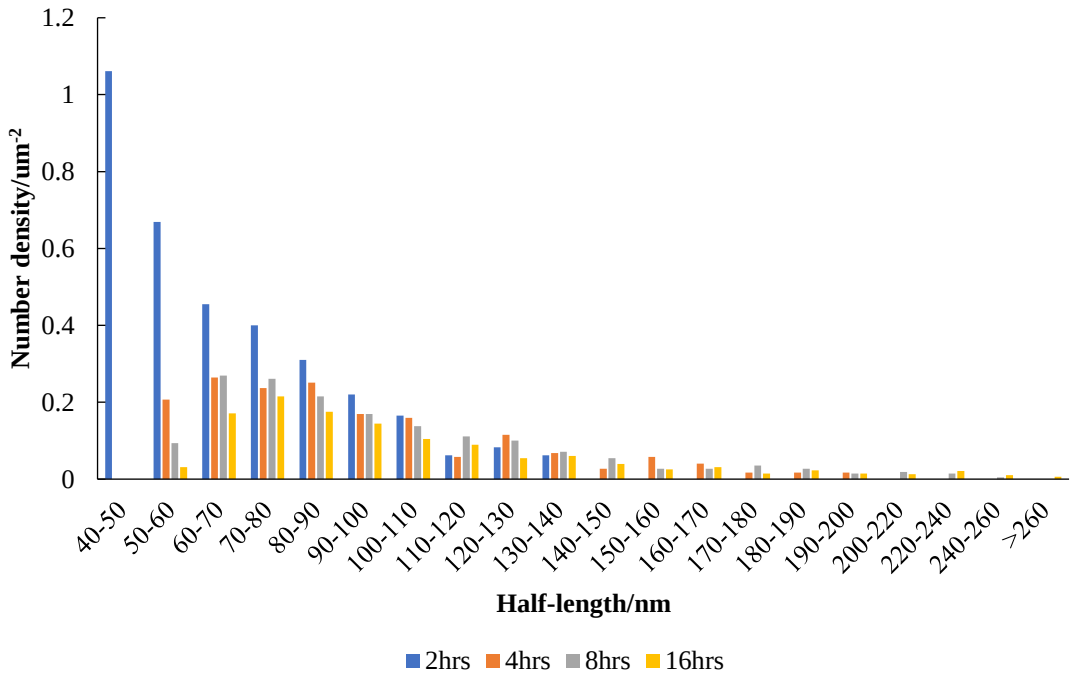

Figure 7-2. The number density - half-length distribution for cementite on the lath boundary in the Base steel tempered from 2 hrs to 16 hrs.

The coarsening direction for coupled inter-lath cementite particles with different separations and size (half-length) differences is from larger size difference with smaller separation to smaller size difference with larger separation (blue arrowed) in Figure 7-3. Therefore, particles with largest size difference and smallest separation are expected to coarsen first due to the highest driving force (highest solute concentration difference). The largest particle size difference is in the 90 - 100 nm range with a separation in the 0

- 200 nm range after tempering for 2 hrs, and in the 130 - 140 nm range with a separation of 0 - 400 nm after tempering for 4 hrs, indicated by the red rectangles in Figure 7-3.

A schematic diagram of the mathematical model for coarsening and dissolution of coupled inter-lath cementite particles is shown in Figure 7-4, where two particles with largest size difference (particles A and B) and the smallest separation between them are selected based on the experimental data in Figure 7-2 and Figure 7-3, as listed in Table 7-1. The simulation process covers the half-length of the largest particle A, the half-length of the smallest particle B and the smallest separation between particles A and B. Assuming that the particle in 2D was an ellipse, and in 3D was an ellipsoid with the width (2b), length (2a) and height (2a) shown in Figure 7-5. The length of the particle was along the lath boundary and the particle was circular with radius a in the 2D boundary plane. The equation for the radius of curvature ρ of the vertex along the length is

$$\rho=\frac{b^2}{a}=\left(\frac{1}{As}\right)^2 a \qquad \text{Equation 7-1}$$

Where, As is particle aspect ratio; a is the half-length of the particle.

This mathematical model is based on finite difference method, where the length step Δx and time step Δt are included. As discussed in Chapter 5, the matrix is expected to be ferrite as all the excess carbon precipitates from the martensitic matrix during the first two hours of tempering in the Base steel based on the calculated retained carbon contents in Table 5-2. As discussed in Chapter 6, Mn diffusion is the rate-controlling step for coarsening of cementite in the Base steel, therefore, the length step Δx should be larger

than the smallest distance between substitutional positions in BCC crystal ($\frac{\sqrt{3}}{2}$a, a is the lattice parameter), which is chosen as 0.5 nm in the calculation. In addition, the stability equation should be satisfied for the simulation, where the time step is calculated using Equation 7-2.

$$D_b \frac{\Delta t}{\Delta x^2} \leq \frac{1}{2} \qquad \text{Equation 7-2}$$

Here, D_b is the diffusion coefficient of solute atoms along the boundary, Δx is the length step and Δt is the time step.

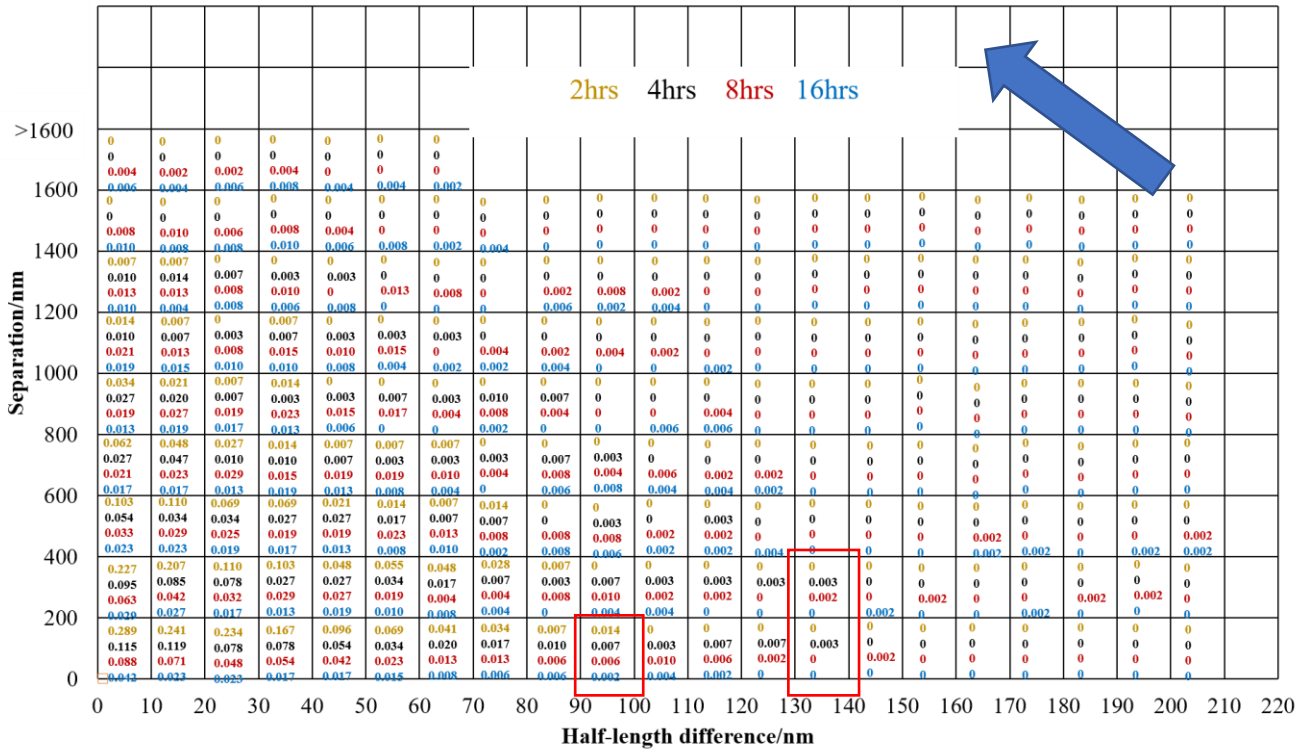

Figure 7-3. Changes of number density for coupled inter-lath cementite with different separations and size (half-length) differences. The bold blue arrow indicates the coarsening direction for inter-lath cementite in the Base steel; the red rectangles point out the particles with largest size differences with smallest separations after tempering for 2 hrs and 4 hrs.

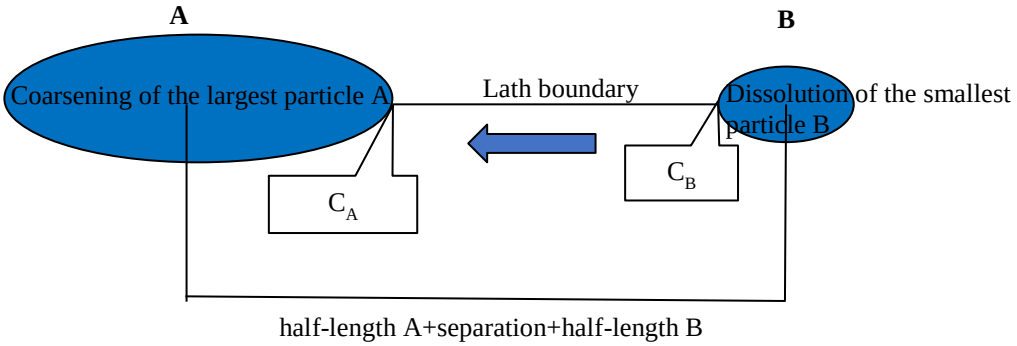

Figure 7-4. Schematic diagram for the coupled inter-lath cementite particles, where the finite difference method is used.

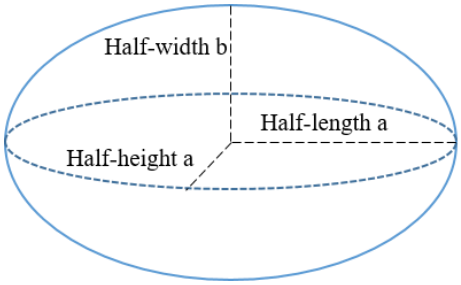

Figure 7-5. Assumed shape of particles along the lath/grain boundary.

Table 7-1. Parameters used in the simulation process for coarsening of inter-lath cementite

Half-length for the coupled inter-lath cementite particles/nm	Smallest separation/nm	Whole distance for simulation/nm
Particle **A** (half-length 135 nm) +Particle **B** (half-length 40 nm) (from 2 hrs to 4 hrs)	100	275
Particle **A** (half-length 135 nm) + Particle **B** (half-length 50 nm) (from 2 hrs to 4 hrs)	100	285
Particle **A** (half-length 195 nm) + Particle **B** (half-length 60 nm) (from 4 hrs to 16 hrs)	200	455

7.2 Assumptions for the mathematical model

1. **Rate-controlling step**: As discussed in Chapters 5 and 6, the equilibrium volume fraction and composition for cementite have been established after tempering for 2 hrs in the Base steel, following which coarsening of inter-lath cementite occurs independently from that of intra-lath cementite. The coupled inter-lath cementite particles with largest size differences and smallest separations have been selected in the model, where the smallest separation between the two particles is less than 200 nm. Due to the small separation between particles, the dissolution of the smaller particle driven by diffusion is assumed to be the rate-controlling step.

2. **Particle aspect ratio change**: The inter-lath cementite aspect ratio - half-length distribution is shown in Figure 7-6. The aspect ratio for inter-lath cementite increases approximately linearly with the increasing half-length in the 40 - 100 nm range, but it slightly fluctuates in the 100 - 140 nm range after tempering for 2 hrs due to the lower number density of larger particles present, Figure 7-2. In addition, the aspect ratios remain similar for tempering from 4 hrs to 16 hrs in the small size range (50 - 140 nm), at values that are slightly lower than those for the same size band after tempering for 2 hrs. This is taken to indicate that some spheroidisation occurs with sufficiently rapid solute atom diffusion around particles for tempering from 2 hrs to 4 hrs. Spheroidisation proceeds very gently with time, Figure 7-6, whereas the dissolution of smaller particles and coarsening of larger ones take place more obviously in the first 2 hours tempering (from 2 hrs to 4 hrs), hence, the predominant solute diffusion still occurs between the smaller and larger particles during tempering from 2 hrs to 4 hrs. The aspect ratio increases approximately linearly with increasing

half-length in the 50 - 140 nm range after tempering for 4 hrs, but it is more variable in the larger size range (140 - >260 nm). Thus, in order to obtain more reasonable aspect ratio values in the full-size range during tempering from 2 hrs to 16 hrs, a fitting line based on the experimental trend in small size range is used to extrapolate the appropriate aspect ratio for particles in the full-size range, Figure 7-6, where the equations are:

$y=0.0462x+1.5182 \qquad x=(\text{half-length}-45)/10+1$ Equation 7-3

(after tempering for 2 hrs)

$y=0.0492x+1.3822 \qquad x=(\text{half-length}-55)/10+1$ Equation 7-4

(for tempering from 4 hrs to16 hrs)

Where y is the fitted aspect ratio.

Based on the fitted aspect ratio trendlines in Figure 7-6, the aspect ratio declines linearly with decrease of particle half-length. Hence, every time when the interface for the smaller or larger particle with the matrix in the coupled inter-lath cementite system moves by a Δx increment, the aspect ratio for that particle is changed linearly (in line with Equation 7-3 and 7-4) for the whole simulation process. The change of aspect ratio results in modifications to the solute concentrations in the interface elements, which influences the amount of solute diffusing between the two particles and finally changes the interface motion for both particles along the lath boundary.

The aspect ratio for the coupled inter-lath cementite particles varies based on different fitting lines in different simulation stages:

(1) First simulation stage from 2 hrs to 4 hrs: The initial aspect ratio (simulation time t=0 hr) for both particles is calculated based on the 2 hrs fitting line. When $0 < t < 2$ hrs, the aspect ratio is assumed to be the average value of the 2 hrs and 4 hrs fitting data for each of the particles. When the simulation time achieves 2 hours, the final aspect ratio for both particles is obtained based on the 4 hrs fitting line.

(2) Second simulation stage from 4 hrs to 16 hrs: The aspect ratio for the coupled inter-lath cementite particles remains following the 4 hrs fitting line (Equation 7-4).

Furthermore, as discussed in assumption 3, the matrix concentration is calculated based on the particle average curvature that is associated with the average aspect ratio. The average aspect ratio can be obtained from the experimental data (average length and width, Figure 5-14), which approximately remains constant as 1.67 during tempering from 2 hrs to 16 hrs, as listed in Table 7-2.

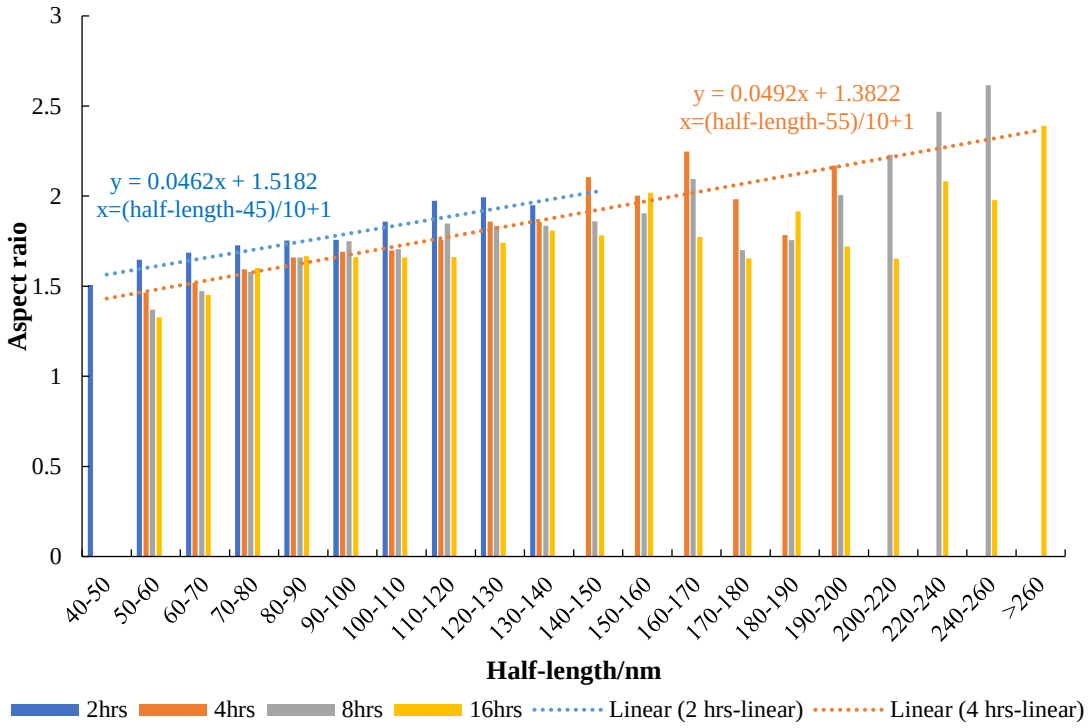

Figure 7-6. The aspect ratio - half-length distribution for cementite on the lath boundary during tempering from 2 hrs to 16 hrs. The blue dotted line is the fitted aspect ratio after tempering for 2 hrs; the orange dotted line is the fitted aspect ratio after tempering for 4 hrs.

Table 7-2. Average aspect ratio based on the experimental length and width measurements

Tempering time/ hrs	Aspect ratio
2	1.67
4	1.67
8	1.67
16	1.66

3. **Manganese concentrations and changes**: As discussed in section 6.1, Mn enriches cementite particles at a level that remains constant for tempering from 2 hrs to 16 hrs. Hence, diffusion of Mn between the smaller and larger particles in the coupled inter-lath cementite system must take place and, as Mn is substitutional, this is likely to be the rate-controlling step. As the interfaces between cementite and ferrite are curved, there should be additional interfacial energy influencing the equilibrium Mn concentration profile in the ferrite matrix.

   The Mn concentration profile in cementite and the ferrite matrix is shown schematically in Figure 7-7. The interface between the smaller cementite particle B and the ferrite matrix has the smaller radius of curvature, leading to a higher Mn concentration C(B) with higher Gibbs free energy addition at the interface element in the matrix, as in the schematic diagram, Figure 7-8. The interface between the larger cementite particle A and the ferrite matrix maintains the greater radius of curvature, resulting in a smaller Mn concentration C(A) at the interface element in the matrix. The Mn content in ferrite with no interfacial energy addition from Thermo-Calc calculation is [Mn]=0.860 wt % ($C_{BCC}(Mn)=1.229\times10^{-24}$ mol/nm^3) at 600 °C. Therefore, the Mn content in the interface elements for both sides can be acquired with different radius of curvatures (associated with different half-length and aspect ratio) based on the Gibbs-Thomson equation, Equation 3-1 [120, 121]. Where $C_0=C_{BCC}(Mn)=1.229\times10^{-24}$ mol/nm^3; λ was the cementite/matrix interfacial energy, taken as 0.5 J/m^2 for inter-lath cementite [178]; V_m was the cementite molar volume 0.6×10^{-5} m^3/mol (Thermo-Calc calculation); R was the ideal gas constant, 8.32 J mol^{-1} K^{-1}; T was the absolute temperature, 600 °C; ρ was the radius of curvature for

particles, m. The Mn contents in the interface elements for the particle A and particle B after tempering for 2 hrs and 4 hrs are listed in Table 7-3. In the simulation process, the Mn concentrations in the two interface elements (C(A) and C(B)) are defined to change when the interface for particles A / B moves by each Δx increment respectively; otherwise, they remain constant at the value of the previous time steps.

Except for the two interface elements, the Mn concentration in other matrix elements remains constant at C(average), Figure 7-7, which is based on the average radius of curvature for inter-lath cementite (related with average half-length and average aspect ratio (1.67) for inter-lath cementite and defined in Equation 7-1). C(average) is decreasing with time during tempering, as shown in Figure 7-9, where two fitted linear lines are used to approximate its variation with time (from 2 hrs to 4 hrs and from 4 hrs to 16 hrs separately). Here, C(average) is defined to decrease once the interface for either particle in the coupled inter-lath particle system moves by a Δx increment during the whole calculation process; otherwise, it remains constant at the value of the previous time steps

The curvature effect is very small for Mn concentration inside cementite, therefore, the Mn content inside cementite is assumed to be constant as [Mn]=14.815 wt % ($C_{cem}(Mn)=2.058\times10^{-23}$ mol/nm^3) obtained from the Thermo-Calc calculation during the whole simulation process and consistent with the measured results from Michel Perez [183].

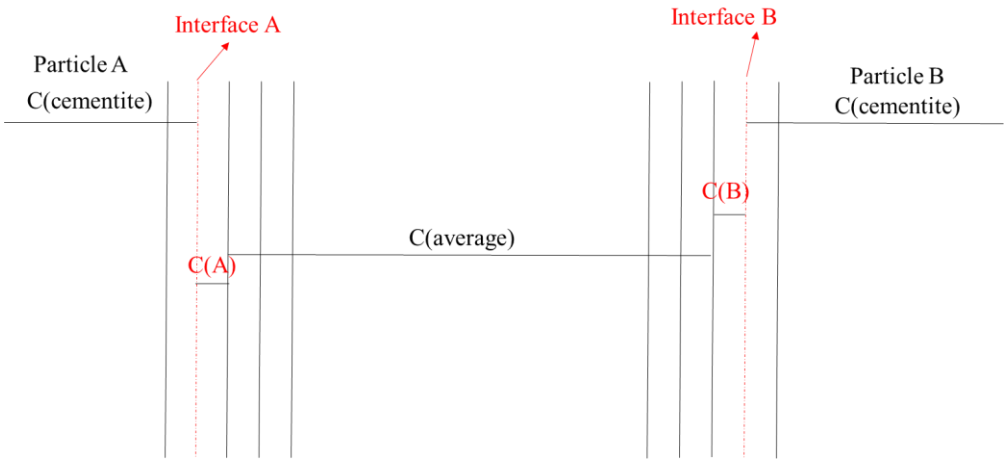

Figure 7-7. Schematic diagram showing the Mn concentration profile in the matrix and cementite.

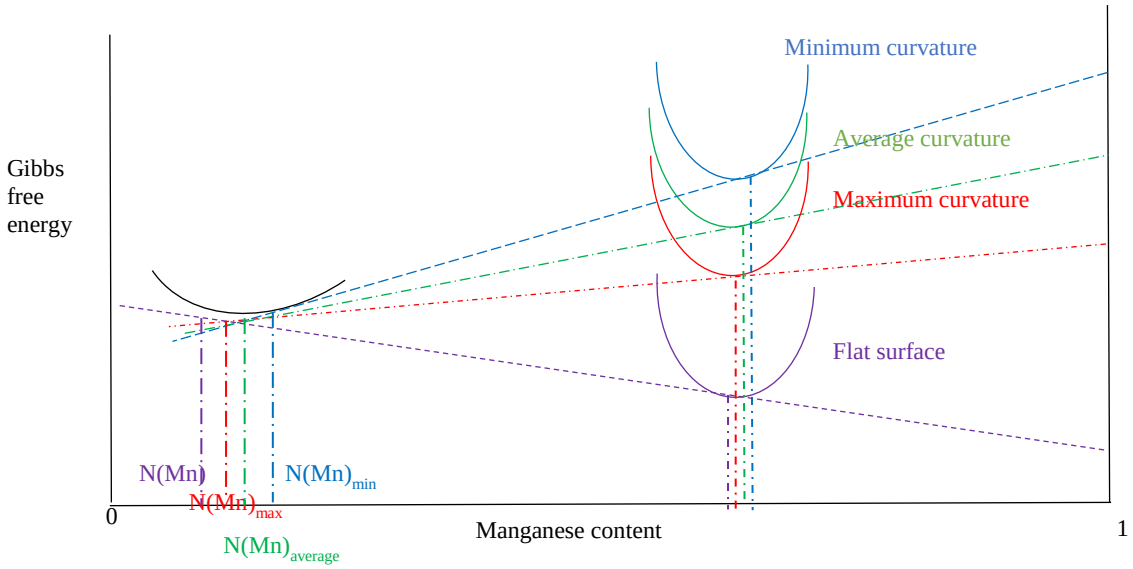

Figure 7-8. Schematic diagram showing the Gibbs free energy and interface Mn concentration changes due to the different particle curvatures.

Table 7-3. Mn concentrations in the interface elements with interfacial energy 0.5 J/m^2 after tempering for 2 hrs and 4 hrs

		Mn concentration/ mol/nm^3
After tempering for 2 hrs	Interface element between the particle B with half-length 40 nm and matrix C(B)	1.289×10^{-24}
	Interface element between the particle B with half-length 50 nm and matrix C(B)	1.280×10^{-24}
	Interface element between the particle A with half-length 135 nm and matrix C(A)	1.258×10^{-24}
After tempering for 4 hrs	Interface element between the particle B with half-length 60 nm and matrix C(B)	1.265×10^{-24}
	Interface element between the particle A with half-length 195 nm and matrix C(A)	1.252×10^{-24}

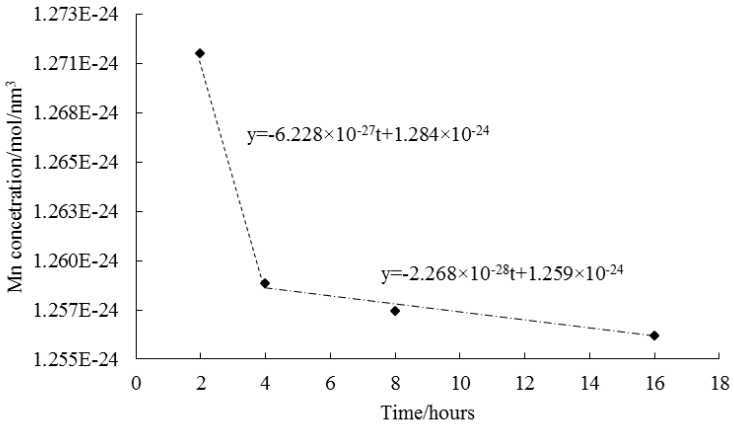

Figure 7-9. C(average) for other boundary elements (except for the interface elements) tempered for different times where the fitted linear lines are used to extrapolate the variation of C(average) with time for interfacial energy 0.5 J/m^2.

4. **Manganese lath boundary diffusivity**: As shown in Figure 7-5, the inter-lath cementite is circular from top view (in the boundary plane) where the half-length is equal to half-height. Based on the qualitative growth law $r=Kt^n$ where r is the particle radius in the boundary plane (r=half-length a), the coarsening exponent for inter-lath cementite is 0.205, Figure 7-10 ($L=126.97t^{0.205}$), consistent with sub-grain (e.g. lath) boundary diffusion-controlled coarsening [145] (summarised in section 3.3). The shape of the power law curve does not fit the data trend particularly well, probably due to the change of the diffusion field around the particles, as the particles are not shape-preserving during coarsening (the aspect ratio changes in different size categories, Figure 7-6). Mn lath boundary diffusivity in the tempered low carbon alloyed martensitic steel is used in the calculation as Mn diffusion is the rate-controlling step for dissolution and coarsening of coupled inter-lath cementite. However, no available data for Mn lath boundary diffusivity in ferrite have been found in the literature, therefore, the diffusivity value is estimated based on the associated literature [74, 184-188].

   As Mn in the periodic table is next to Fe, hence, the Mn diffusivity along lath boundaries should be similar to the self-diffusivity of Fe along lath boundaries in ferrite. Based on Gust's evaluations and correlations of grain boundary self-diffusivities proposed in BCC metals (including in α-Fe) [187], Figure 7-11, the self-diffusivity of Fe along high-angle grain boundaries in α-Fe is

$$\delta D_{Gb}=9.2\times10^{-14}\exp\left(-\frac{10.4T_m}{T}\right) \qquad \text{Equation 7-5}$$

where δ is the boundary thickness, 0.5 nm; T_m is the low carbon steel melting point, approximately 1464 °C [189]; T is the tempering temperature, 600 °C. The grain boundary self-diffusivity of Fe in ferrite is estimated as 1.75×10^{-15} m^2/s at 600 °C, which is much larger than the reported self-diffusivity of Fe in the ferritic matrix ((1 - 2)$\times10^{-21}$ m^2/s [184-186]) at the same temperature. The self-diffusivity of Fe along low-angle grain (lath) boundaries in ferrite is assumed to be 2 orders of magnitude lower than that along high-angle grain boundaries and 4 orders of magnitude higher than that in the lattice [74, 188, 190]. Therefore, Mn lath boundary diffusivity in α-Fe, which is approximately equal to the self-diffusivity of Fe along lath boundaries, is estimated to be 1×10^{-17} m^2/s, agreeing well with $D_{HAGB}>D_{LAGB}>D_V$. Here, $D_{LAGB}(Mn)=1\times10^{-17}$ m^2/s is used in this simulation.

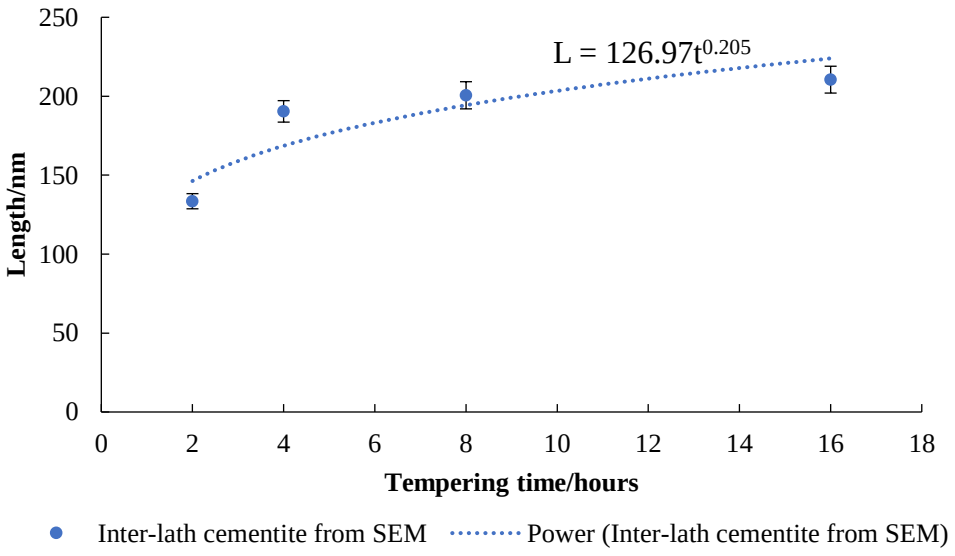

Figure 7-10. The coarsening of inter-lath cementite in the Base steel tempered at 600 °C from 2 hrs to 16 hrs.

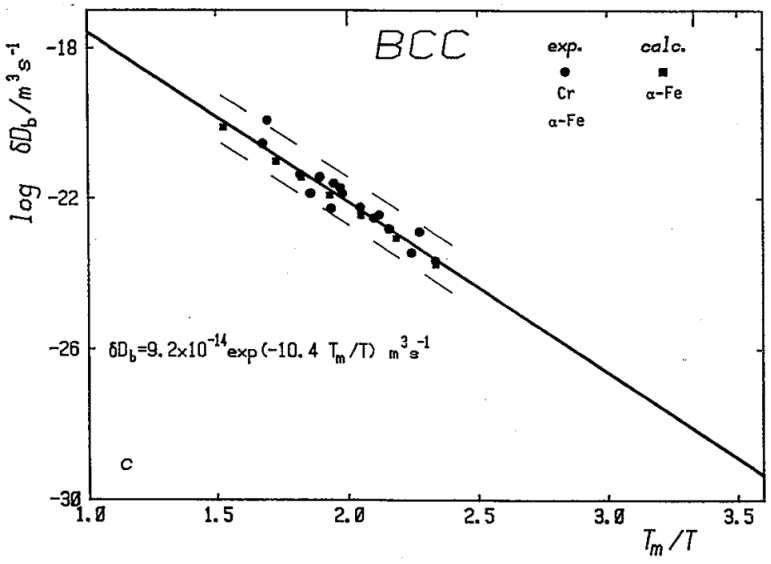

Figure 7-11. Arrhenius plot of the self-diffusivities within the confidence limits (≥ 95%) using a reduced reciprocal temperature scale in BCC metals (including α-Fe) [187].

7.3 Calculation process for the mathematical model

As discussed in assumption 1, the rate-controlling step for the coupled inter-lath cementite system is the dissolution of the smaller particle B to provide manganese to grow the adjacent larger particle A under equilibrium particle composition / volume fraction conditions. This results in manganese diffusion occurring between the interface (cementite/matrix) elements and the adjacent elements in the matrix. As the thickness of the boundary is fixed (normally 0.5 nm [10]), the diffusion process can be simplified to a 1D problem. The minimum flux between two particles is calculated from 1D geometry, whereas the mass balance between two particles is determined from 3D geometry. Therefore, the overall approach contained more than 1D geometry. In addition, a 2D diffusion model for coarsening and dissolution of coupled inter-lath cementite particles could also be considered where the thickness of the boundary, related to the thickness of the lath (or grain) boundary and assumed to be constant, should be included. Therefore, the thickness of boundary elements was not a variable, and hence the 2D problem can be simplified to 1D model. However, a full 3D model for the diffusion of Mn should consider the depth of the boundary, which was a variable and unknown value from experimental observations. Different depths of the boundary can lead to a change of solute diffusion path; even for the two-particle couple, the Mn diffusion path along the boundary can vary from the shortest length to other directions, making the diffusion problem very complex and unsolvable.

As shown in Figure 7-12, when the interface between particle B and the matrix moves from element m to m-1 along the line linking the two particles, the modelling process can be divided into three steps, which are further iterated until particle B dissolves fully.

Step 1 (at the first time step j=0). The manganese concentration profile at the initial time step is shown in Figure 7-12. There is a manganese concentration difference between the interface element m (C(m,j)) and its adjacent element m+1 (C(average,j)) for particle B; thus, manganese diffuses from the interface element m to its adjacent element m+1, which induces the dissolution of particle B to supply manganese to compensate the reduced manganese content in element m. Similarly, there is also a flux of manganese from element m+n-1 to the interface element m+n for particle A, leading to the coarsening of particle A, as indicated by the red rectangular box in Figure 7-12. The flux, based on Fick's first law, for both particle / matrix interfaces can be obtained as:

$$Min(m,j)=Mout(m,j)=-D\frac{C(m+1,j)-C(m,j)}{\Delta x}\Delta t \qquad \text{Equation 7-6}$$

$$Mout(m+n,j)=Min(m+n,j)=-D\frac{C(m+n,j)-C(m+n-1,j)}{\Delta x}\Delta t \qquad \text{Equation 7-7}$$

Where Δx is the length step, 0.5 nm; Δt is the time step, 1×10^{-5} s, obtained from stability equation Equation 7-2; C(m+1,j)=C(m+n-1,j)=C(average,j); and D is the Mn lath boundary diffusivity. In Equation 7-6 and Equation 7-7, the solute flux diffusing in / out of the interface elements satisfies the relationship Min=Mout, where the composition and length of the interface element remain the same. Therefore, no extra solute is accumulated in the interface elements for either particle to ensure that their composition is taken to be the interface curvature-modified equilibrium composition. The minimum amount of manganese diffusional flux Mmin(j) is chosen to maintain Mn diffusion between particles A and B, which is the smaller value between Min(m,j) and Mout(m+n,j). Hence, the movement of interface B at time step j+1 is defined as:

$$\Delta d_B(j+1)=\frac{Mmin(j)}{C(cementite)-C(average,j)} \quad \text{Equation 7-8}$$

The mass balance between the two particles due to the minimum amount of manganese diffusion is $S_A \times \Delta d_A \times C(cementite)=S_B \times \Delta d_B \times C(cementite)$. Therefore, the movement of interface A at time step j+1 can be defined as

$$\Delta d_A(j+1)= \Delta d_B(j+1)\times\frac{S_B(j)}{S_A(j)} \quad \text{Equation 7-9}$$

Where S(B,j) and S(A,j) are the surface areas for particles B and A at time step j.

The diffusion of manganese only takes place between interface elements (m or m+n) and the adjacent elements (m+1 or m+n-1), hence, there is no flux in other elements from m+2 to m+n-2 (Min=Mout=0). Furthermore, there is no flux and Mn concentration change for the elements inside cementite particles A and B.

Step 2 (at time step j=p when the interfaces for both particles have not passed a Δx distance, as shown in Figure 7-13). Based on assumption 3, at time step j=p, the manganese concentrations in the interface elements m and m+n remain constant as C(m, p)=C(m,p-1) and C(m+n, p)=C(m+n,p-1); meanwhile, C(average,p)=C(average,p-1). As the interfaces move with time, the interface elements (m or m+n) and adjacent elements (m+1 or m+n-1) shift as well, but the length of these elements remains Δx, as indicated by the blue lines in Figure 7-13. However, the boundary for elements m+2 and m+n-2 should keep still with time, although the length for m+2 increases (>Δx) and for m+n-2 decreases (<Δx), pointed by the red arrows in Figure 7-13. The stationary boundaries for

elements m+2 and m+n-2 do not influence the modelling process as there is no flux in boundary elements from m+2 to m+n-2 (Min=Mout=0). The interface motion for particle B at this time step j=p ($\Delta d_B(p+1)$) can be obtained using Equation 7-8 due to the minimum Mn diffusional flux between particles A and B. Based on the mass balance between the two particles from the minimum Mn diffusional flux, the interface motion for particle A ($\Delta d_A(p+1)$) is acquired in Equation 7-9.

Step 3 (at time step j=q when the particle B/ matrix interface moves by a total increment of Δx to coincide with the boundary between elements m-1 and m-2, as shown in Figure 7-14). As interface B coincides with the boundary between elements m-1 and m-2, the interface element shifts from element m to m-1 at this time step. Therefore, based on assumption 2, the aspect ratio for particle B changes at this time step. Meanwhile, the interface composition C(m-1,q) for particle B is obtained based on the newly-changed half-length and aspect ratio at this time step from Equation 7-1 and the Gibbs-Thomson Equation 3-1, which is larger than the previous interface composition C(m,q-1) for particle B. Hence, extra manganese from particle B is needed to increase the manganese concentration in element m-1, indicated by the yellow rectangular filled box in element m-1 in Figure 7-14, which is defined as $\Delta M_B(q)$ in Equation 7-10. The Mn concentration in matrix elements (except for the interface elements) C(average,q) at this time step decreases compared to that at previous time steps, based on assumption 3 that C(average) decreases when the interface motion for either particle A or B achieves an increment of Δx. The decreased amount of manganese from the other matrix elements ΔM(average,q), defined in Equation 7-11, is redistributed to contribute to coarsening of particle A,

indicated by the green filled box in Figure 7-14, i.e. back diffusion is assumed not to take place. In addition, C(m,q) is equal to C(average,q) at this time step.

$$\Delta M_B(q)=(C(m-1,q)-C(m,q-1))\times\Delta x \qquad \text{Equation 7-10}$$

$$\Delta M(average,q)=\Delta C(average,q)\times(d(separation+\sum\Delta d_B-\sum\Delta d_A-2\Delta x) \qquad \text{Equation 7-11}$$

The flux from interface B occurs between elements m-1 and m as:

$$Min(m-1,j)=Mout(m-1,j)=-D\frac{C(m,j)-C(m-1,j)}{\Delta x}\Delta t \qquad \text{Equation 7-12}$$

There are two possible situations for the interface of particle A. One situation is that interface A has moved by an increment < Δx in length, as shown in Figure 7-14 (a); the manganese concentration C(m+n,q) in the interface element for particle A remains constant at the value used for previous time steps, and the flux Mout(m+n,q) for interface A is acquired using from Equation 7-7.

Hence, the interface motion for particle B at time step j=q+1 are composed of two parts: one is due to the minimum amount of Mn diffusional flux ($\Delta d_{B1}(q+1)$); the other is due to the solute redistribution in element m-1 ($\Delta d_{B2}(q+1)$), as defined in Equation 7-13. The interface movement for both particles is continuous (seen in steps 1 and 2) based on the minimum Mn flux and only differs when non-continuous composition variation for the interface elements and other matrix elements occurs.

$$\Delta d_B(q+1)=\Delta d_{B1}(q+1)+\Delta d_{B2}(q+1) \qquad \text{Equation 7-13}$$

$$\Delta d_{B1}(q+1)=\frac{Mmin(q)}{C(cementite)-C(average,q)}$$

$$\Delta d_{B2}(q+1)=\frac{\Delta M_B(q)}{C(cementite)-C(average,q)}$$

The interface motion for particle A at the time step j=q+1 also consists of two parts: the first part is due to the mass balance between the two particles (minimum Mn flux induced) $\Delta d_{A1}(q+1)$, which keeps consistent with steps 1 and 2; the second part is based on the solute redistribution in matrix elements from m to m+n-1 (except for the interface elements), which is defined as:

$$\Delta d_A(q+1)=\Delta d_{A1}(q+1)+\Delta d_{A2}(q+1)$$

$$\Delta d_{A1}(q+1)=\Delta d_{B1}(q+1)\times\frac{S_B(q)}{S_A(q)} \qquad \text{Equation 7-14}$$

$$\Delta d_{A2}(q+1)=\frac{\Delta M(average,q)}{C(cementite)-C(m+n,q)}$$

The other situation is that the interface for particle A moves by an increment of Δx to coincide with the boundary between elements m+n-1 and m+n-2, as shown in Figure 7-14 (b). The aspect ratio for particle A changes based on assumption 2. Meanwhile, the Mn concentration in the interface element m+n-1 C(m+n-1,q) for particle A decreases with the newly-changed half-length and aspect ratio. Hence, there is some manganese redistributed from the interface element m+n-1, contributing to the coarsening of particle A, as indicated by the purple filled box in element m+n-1 in Figure 7-14 (b), which is defined as $\Delta M_A(q)$.

$$\Delta M_A(q)=(C(m+n,q-1)-C(m+n-1,q))\times\Delta x \qquad \text{Equation 7-15}$$

The flux from interface A occurs between m+n-1 and m+n-2 is

$$Mout(m+n-1,j)=Min(m+n-1,j)=-D\frac{C(m+n-1,j)-C(m+n-2,j)}{\Delta x}\Delta t \qquad \text{Equation 7-16}$$

At j=q time step, C(m+n-2,q)=C(average,q).

Here Mmin(q) is selected between Min(m-1,q) and Mout(m+n-1,q). The interface motion for particle B at time step j=q+1 is acquired from Equation 7-13.

The interface motion for particle A originated from the mass balance is the same as $\Delta d_{A1}(q+1)$ in Equation 7-14, However, $\Delta d_{A2}(q+1)$ is slightly different in this situation comparing to Equation 7-14 due to the addition of solute redistribution in the interface element m+n-1. Here $\Delta d_{A2}(q+1)$ is defined as:

$$\Delta d_{A2}(q+1)=\frac{\Delta M_A(q)+\Delta M(average,q)}{C(cementite)-C(m+n-1,q)} \qquad \text{Equation 7-17}$$

Then the interface motion for particle A is the sum of $\Delta d_{A1}(q+1)$ and $\Delta d_{A2}(q+1)$.

The above steps are iterated as interfaces for particles A and B move with increasing time until the total interface motion for particle B is equal to the half-length of particle B.

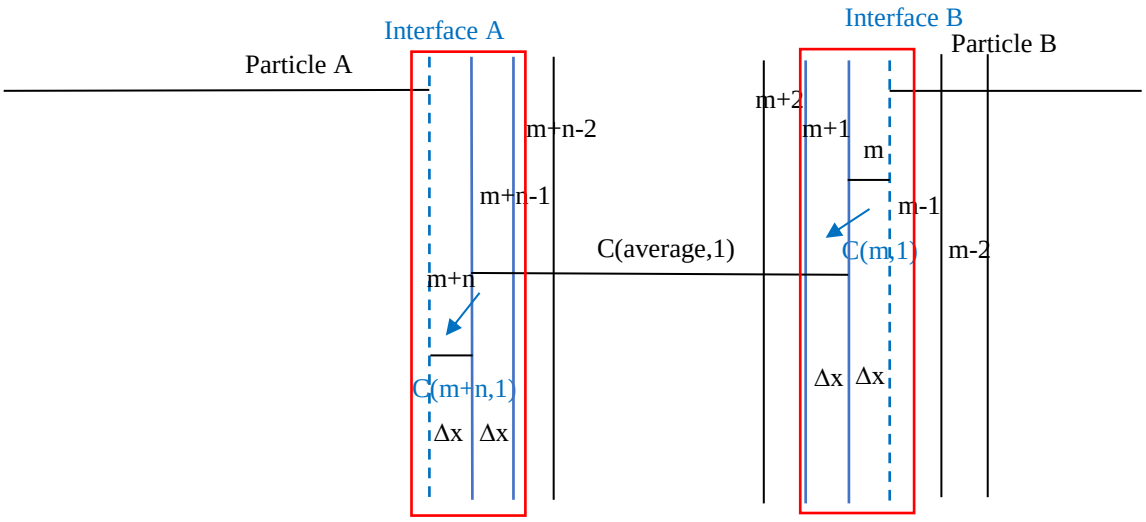

Figure 7-12. Schematic diagram showing manganese concentration profile at the first time step j=0. The blue dashed lines represent the interface positions for both particles. The red rectangles enclose the interface elements and their adjacent elements.

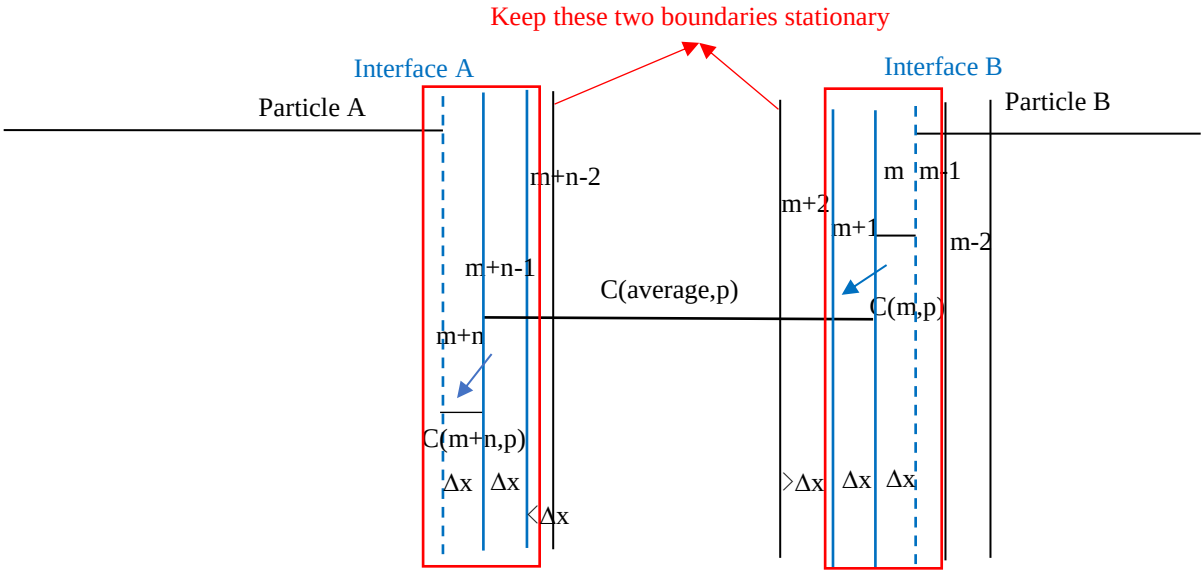

Figure 7-13. Schematic diagram showing manganese concentration profile at time step j=p when the interfaces for both particles have not gone over a Δx distance. The blue dashed lines represent the interface positions for both particles at the time step j=p. The red rectangles enclose the interface elements and their adjacent elements.

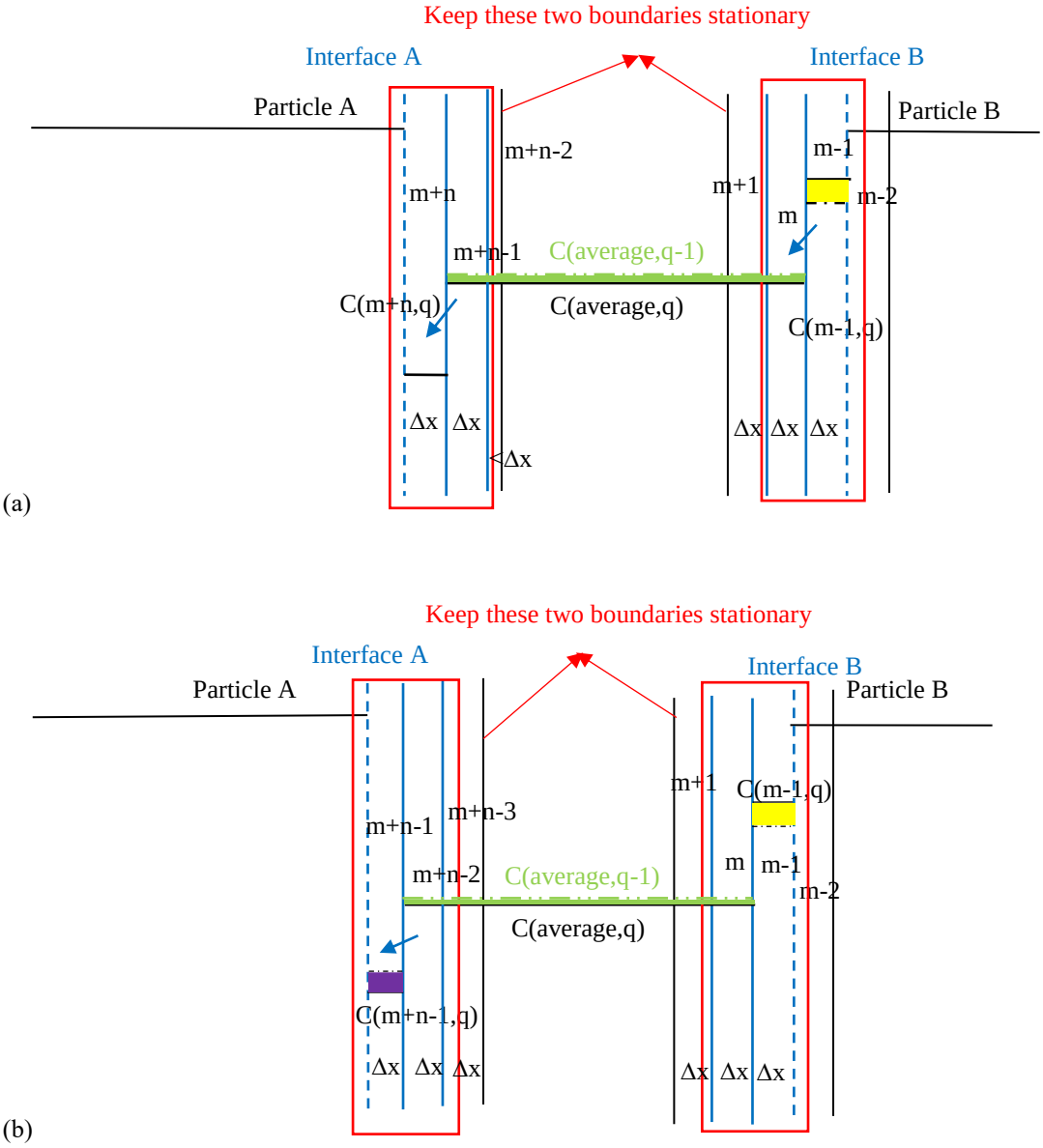

Figure 7-14. Schematic diagram showing manganese concentration profile at time step j=q when the particle B / matrix interface moves a Δx distance to coincide with the boundary between elements m-1 and m-2: (a) the interface for the particle A has not moved over a Δx distance; (b) the interface for the particle A moves by Δx increment to coincide with the boundary between elements m+n-1 and m+n-2. The blue dashed lines represent the interface positions for both particles at time step j=q. The green dashed line refers to Mn concentration C(average, q-1) in other matrix elements (except for the interface elements) at time step j=q-1. The yellow filled box is the amount of solute redistribution in element m-1 due to the interface composition variation for particle B. The green filled box is the amount of solute redistribution

due to the decrease of C(average) contributing to coarsening of particle A. The purple filled box in (b) is the amount of solute redistribution in element m+n-1 due to the interface composition variation for particle A. The red rectangles enclose the interface elements and their adjacent elements.

7.4 Simulation results and discussion for the model

7.4.1 From 2 hrs to 4 hrs

7.4.1.1 Simulation results

The simulated interface motions for the larger particle A with half-length 135 nm and the smaller particle B with half-length 40 nm in 2 hours at 600 °C (from 2 hrs to 4 hrs total tempering time) are shown in Figure 7-15. From this, the predicted time for dissolution of particle B with interfacial energy 0.5 J/m^2 is approximately 54 mins (less than 2 hours) which is consistent with the experimental observation in Figure 7-2, where particles with half-length < 50 nm are all dissolved on tempering from 2 hrs to 4 hrs. However, the interface motion for the larger particle A is about 1.4 nm at the expense of a single particle B during this calculation.

In addition, the predicted dissolution time for the smaller particle B with half-length 50 nm is about 91 mins for the coupled inter-lath cementite system (particle A with half-length 135 nm and particle B with half-length 50 nm) with interfacial energy λ=0.5 J/m^2, Figure 7-16 (a). The interface for particle A moves around 2.6 nm due to dissolution of a single particle B with half-length 50 nm, Figure 7-16 (b). The predicted dissolution times for smaller particles with half-length 40 / 50 nm are in rough agreement with experimental data. However, the calculated coarsening of the larger particle A cannot achieve the experimentally observed largest size with a single smaller particle consumed.

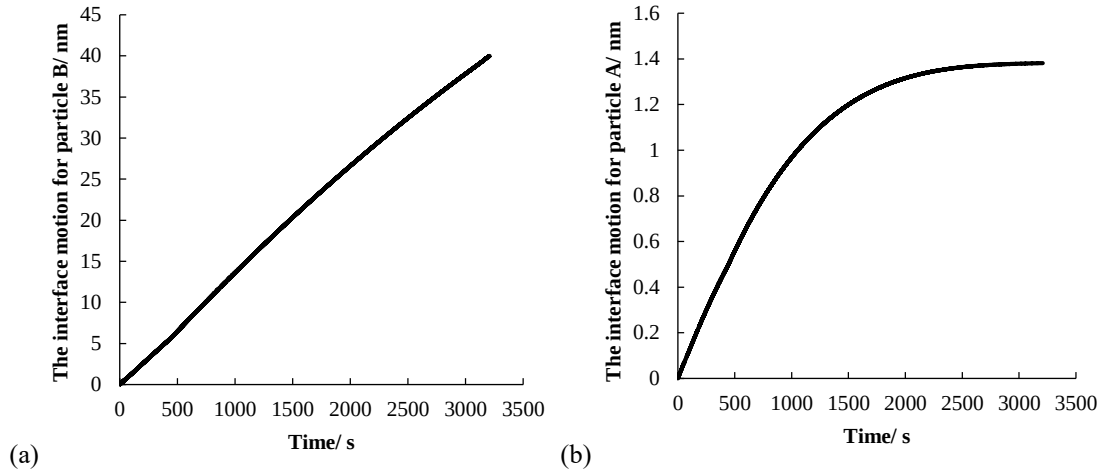

Figure 7-15. The simulated interface motions for the smaller particle B with half-length 40 nm (a) and the larger particle A with half-length 135 nm (b) with separation 100 nm with interfacial energy λ=0.5 J/m^2 during tempering from 2 hrs to 4 hrs at 600 °C.

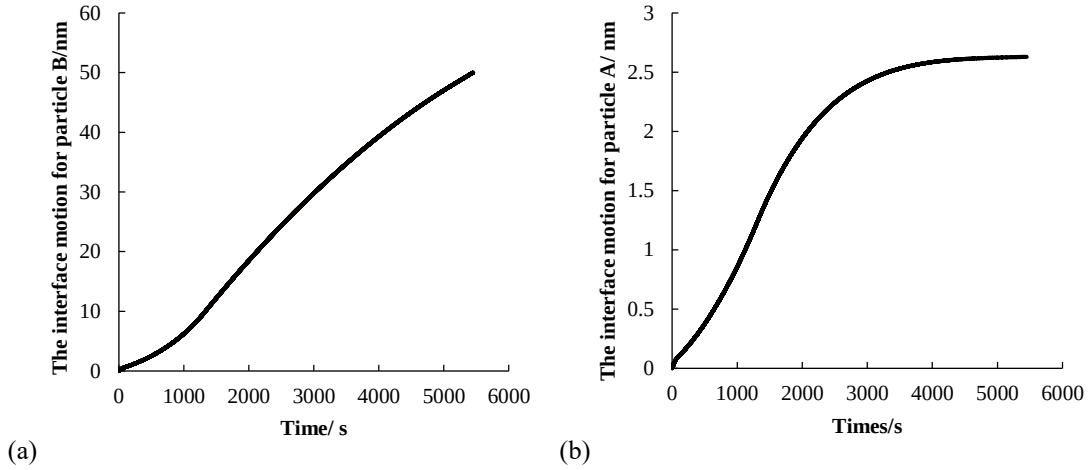

Figure 7-16. The simulated interface motions for the smaller particle B with half-length 50 nm (a) and the larger particle A with half-length 135 nm (b) with separation 100 nm with interfacial energy λ=0.5 J/m^2 during tempering from 2 hrs to 4 hrs at 600 °C.

7.4.1.2 Validation of the simulation based on the experimental data

The larger particle A cannot coarsen to the observed largest size in 2 hours time with only one smaller particle consumed. There is a significant number density decrease for particles with half-length in 40 - 60 nm range tempered from 2 hrs to 4 hrs, Figure 7-2, hence, there should be enough smaller particles dissolving to supply manganese to constitute the largest particle coarsening from half-length 135 nm to half-length 195 nm. The amount of Mn released from the dissolution of smaller particles with half-length in 40 - 60 nm range is about 1.03×10^{-17} mol, which is much larger than the required amount of Mn (3.29×10^{-18} mol) for the largest particles with half-length increasing from 135 nm to 195 nm. Figure 7-17 shows the number density variation with different separations and size differences for coupled inter-lath cementite particles with half-length for one particle ranging in 40 - 60 nm after tempering for 2 hrs. The comparatively larger number densities located in the size difference range 0 - 20 nm with a separation of 0 - 400 nm mean that particles with half-length 40 - 60 nm have the maximum probability to be next to particles with similar sizes, hence, there should be little manganese diffusion between these similarly-sized particles. The number density ratio between coupled particles in the size difference 0 - 20 nm with separation 0 - 400 nm region and coupled particles in the size difference 80 - 100 nm with separation 0 - 400 nm region is about 27.4. Therefore, it is assumed that the smaller particle B with half-length 50 nm is surrounded by another 28 similarly-sized particles in the 2D lath boundary plane, which are all around the larger particle A with half-length 135 nm, as shown in Figure 7-18 (a). In this condition, these similarly-sized particles with half-length 50 nm are supposed to dissolve fully to supply Mn (the released Mn amount=1.97×10^{-16} mol) for the larger particle A to coarsen from

half-length 135 nm to half-length 195 nm (the required Mn amount=1.94×10^{-16} mol). Based on the simulation results in Figure 7-16 (b), the interface motion for the larger particle A with half-length 135 nm is around 76 nm in total after consuming 29 particles with half-length 50 nm, which is roughly consistent with the observed largest particle size in Figure 7-2.

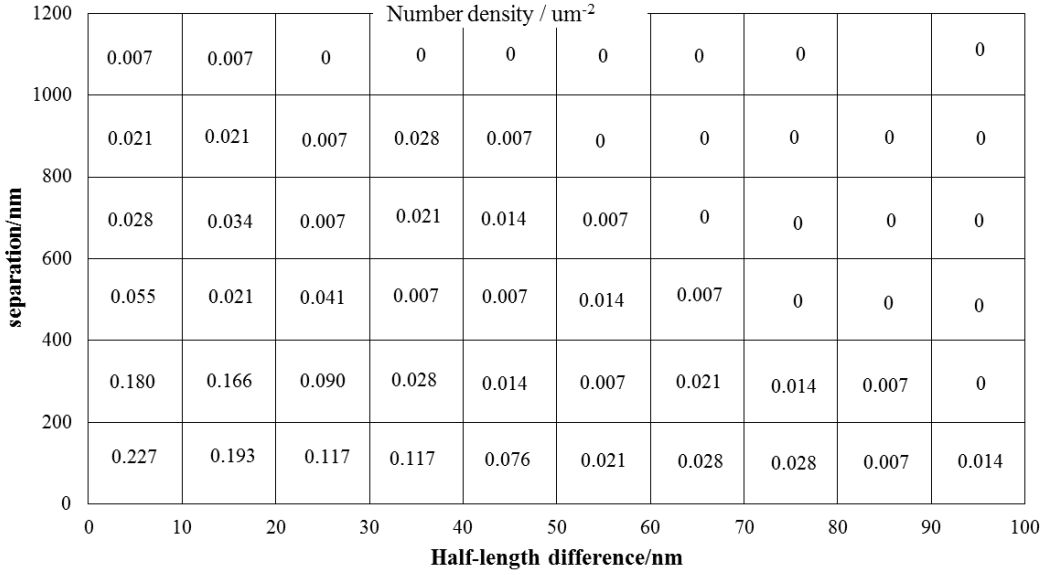

Figure 7-17. The number density variation with different separations and size differences for coupled inter-lath cementite particles with half-length for one particle in 40 - 60 nm range after tempering for 2 hrs at 600 °C.

For the assumed particle arrangement in the lath boundary plane (2D plane) in Figure 7-18 (a), the larger particle A with half-length 135 nm is only adjacent to the smaller particles with half-length 50 nm where the number of the smaller particles varies from 1 to 6 along the lath boundary, Figure 7-18 (b). Lines 1 - 6 in Figure 7-18 (a) correspond to situations 1 - 6 in Figure 7-18 (b) from side view. These assumed situations do appear in the SEM image in the Base steel after tempering for 2 hrs at 600 °C, i.e. in Figure 7-19 indicated by the red rectangular boxes. However, other situations with multi-sized

particles around the largest particle are also observed, indicated by the green rectangular boxes in Figure 7-19, where solute diffusion occurs in the reserved directions along the lath boundary (1D line). As the coarsening of inter-lath cementite occurs independently from that of intra-lath cementite in this steel (discussed in section 5.2), diffusion would occur along lath boundaries into or out of the plane of the SEM image, which is still 1D diffusion between particles along the boundary. The established coupled inter-lath cementite model at least predicts the shortest dissolution time of the smaller particles, which is the basis for a multi-sized inter-lath cementite particle coarsening model (future work).

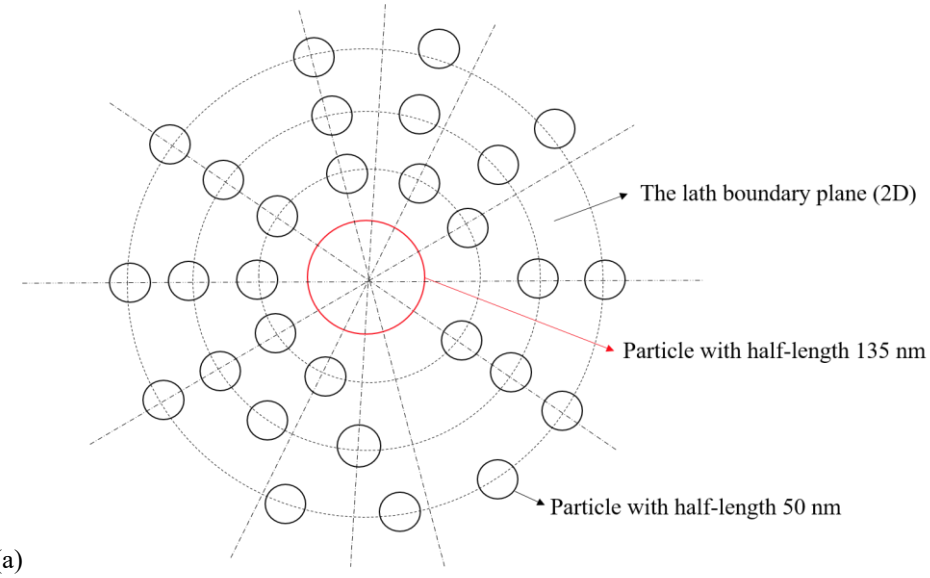

(a)

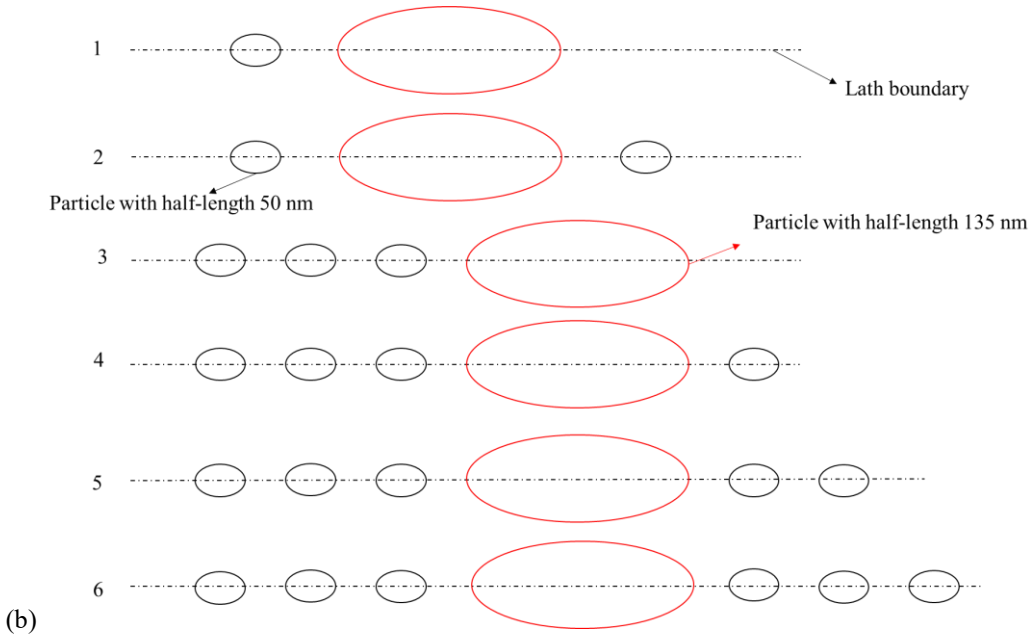

(b)

Figure 7-18. (a) The assumed particle arrangement for the larger particle A with half-length 135 nm surrounded by 29 particles with half-length 50 nm in the 2D lath boundary plane; (b) Based on the assumed particle arrangement in the 2D lath boundary (a), the arrangements between the larger particle with half-length 135 nm and the smaller particles with half-length 50 nm along the lath boundary (1D line).

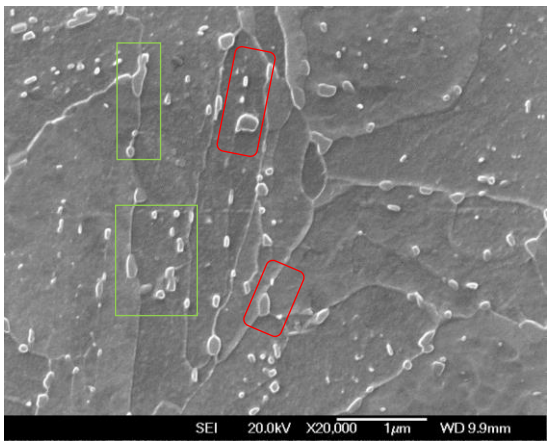

Figure 7-19. The observed particle arrangement around larger particles along the lath boundary (1D line) after tempering for 2 hrs at 600 °C in the Base steel. The red rectangles indicate the largest - smallest particle arrangement and the green rectangles indicate the arrangement of multi-particles in different size ranges.

7.4.2 From 4 hrs to 16 hrs

7.4.2.1 Simulation results

The simulated interface motions for the larger particle A of half-length 195 nm and the smaller particle B of half-length 60 nm with interfacial energy 0.5 J/m^2 are shown in Figure 7-20, where the dissolution time for particle B is about 159 mins, which is much less than 12 hours. The interface for particle A moves 2.3 nm due to dissolution of a single particle B, which is much less than the observed half-length increase for the largest particle from half-length 195 nm to half-length 270 nm.

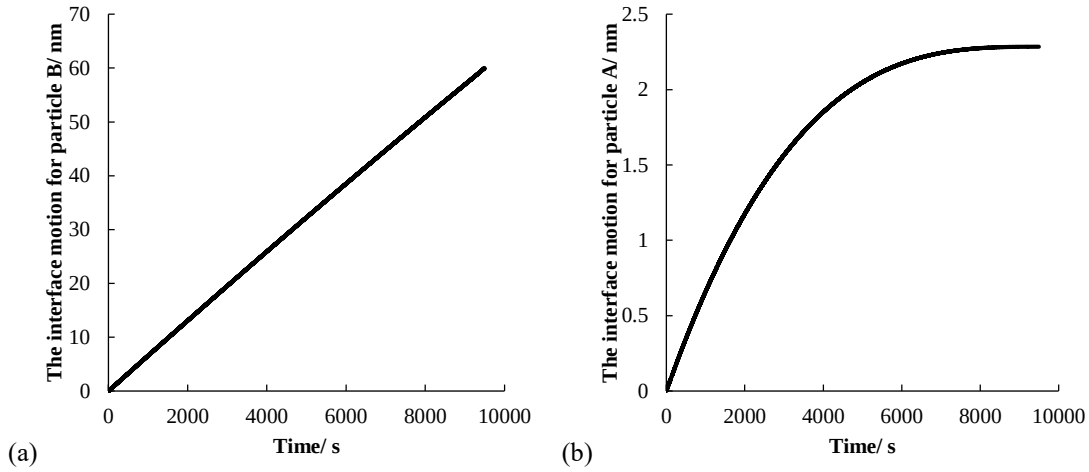

Figure 7-20. The simulated interface motions for the smaller particle B with half-length 60 nm (a) and the larger particle A with half-length 195 nm (b) with separation 200 nm with interfacial energy λ=0.5 J/m^2 during tempering from 4 hrs to 16 hrs at 600 °C.

7.4.2.2 Validation of the simulation based on the experimental data

The above simulation gives the shortest dissolution time for particle B of half-length 60 nm in the coupled inter-lath cementite system, which is much quicker than the experimental observation in Figure 7-2. Actually, a relatively large number density

decrease exists for particles with half-length in 50 - 60 nm range, hence, it is necessary to analyse the number density variation for coupled inter-lath cementite particles with half-length for one particle ranging in 50 - 60 nm after tempering for 4 hrs to select the possible particle arrangements. As shown in Figure 7-21, there are two dominant size categories of particles surrounding the smaller particles with half-length 60 nm: similarly-sized particles with half-length 60 nm (region of size difference approximately in 0 - 30 nm with separation 0 - 400 nm) and comparatively larger particles with half-length around 100 nm (region of size difference in 30 - 50 nm with separation 0 - 400 nm). There should be little manganese diffusion between similarly-sized particles, as the manganese concentration difference between these particles is very small. However, manganese diffusion is expected to occur between particles of half-length 60 nm and particles of half-length 100 nm due to the relatively larger size difference. The number density ratio between coupled particles in the size difference 0 - 30 nm with separation 0 - 400 nm region and coupled particles in the size difference 130 - 140 nm with separation 0 - 400 nm region is about 19. The number density ratio between coupled particles in the size difference 30 - 50 nm with separation 0 - 400 nm region and coupled particles in the size difference 130 - 140 nm with separation 0 - 400 nm region is around 5. Therefore, it is assumed that the larger particle A with half-length 195 nm is surrounded by 20 particles with half-length 60 nm and 5 particles with half-length 100 nm with different separations in the 2D lath boundary plane, Figure 7-22 (a). From these, the total amount of Mn released from particles with half-length 60 nm and 100 nm (5.17×10^{-16} mol) is much larger than the required amount of Mn (3.80×10^{-16} mol) for coarsening of a single particle A with half-length increasing from 195 nm to 270 nm.

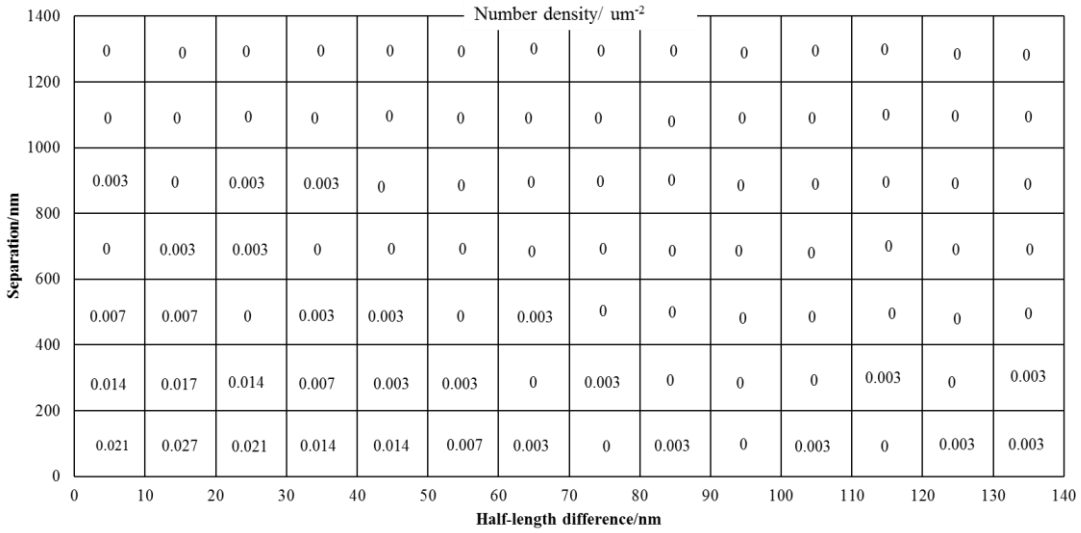

Figure 7-21. The number density variation with different separations and size differences for coupled inter-lath cementite particles with half-length for one particle in 50 - 60 nm range after tempering for 4 hrs at 600 °C.

Due to the assumed particle arrangement in the 2D lath boundary plane in Figure 7-22 (a), several possible particle arrangements along the lath boundary (1D line) can be considered: the largest particle is next to either the smaller ones with half-length 60 nm or particles with half-length 100 nm in Figure 7-22 (b). Lines 1 - 5 in Figure 7-22 (a) are related with situations 1 - 5 in Figure 7-22 (b) along the lath boundary (similar method used as in section 7.4.1.2). Among these situations, there is only one condition (2) for which the largest particle is surrounded by the smallest ones where the dissolution time for these smallest particles is shortest, which is also observed in the SEM image after tempering for 4 hrs (indicated by the red rectangle) in Figure 7-23. Under this situation (2), the interface motion for particle A with half-length 195 nm is about 46 nm due to the dissolution of 20 particles with half-length 60 nm based on the simulation results in Figure 7-20 (b), which is less than the observed half-length increase (about 75 nm) for the largest particle on tempering from 4 hrs to 16 hrs. Hence, multi-particles in different

size ranges (e.g. more than two particles with half-length 60/ 100/ 195 nm, Figure 7-22 (b) (situations 1/ 3/ 4/ 5)) should be considered in the future to achieve the experimental size increase for the largest particles during tempering, where solute diffusion reverses along the lath boundary (arrowed in Figure 7-22 (b)). These situations are also observed in SEM images after tempering for 4 hrs (indicated by the green rectangles) in Figure 7-23. Therefore, as stated in section 7.4.1.2, a multi-sized inter-lath cementite particle coarsening model is also needed here in the future.

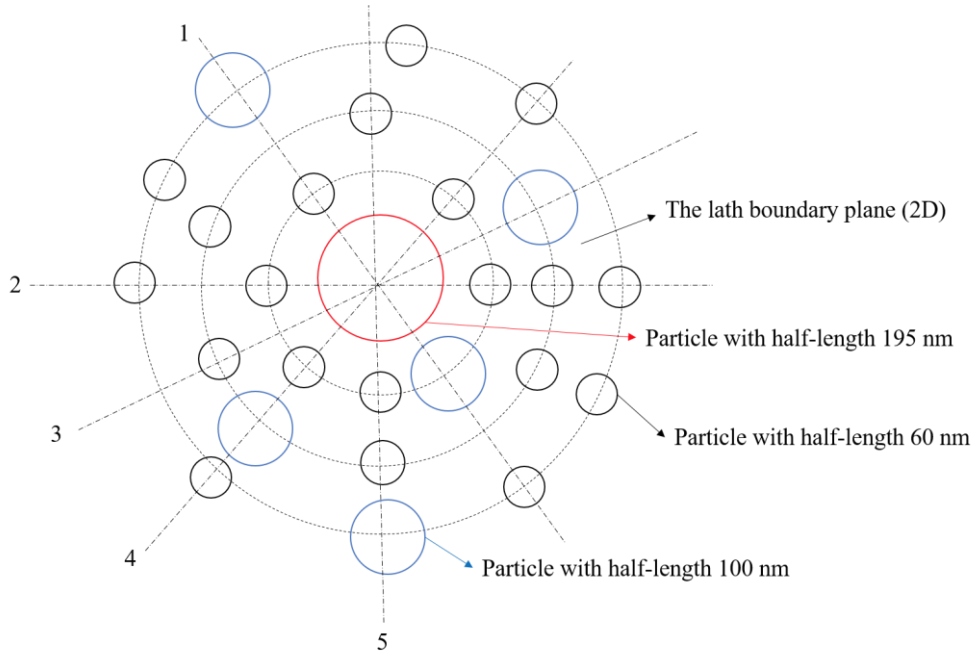

(a)

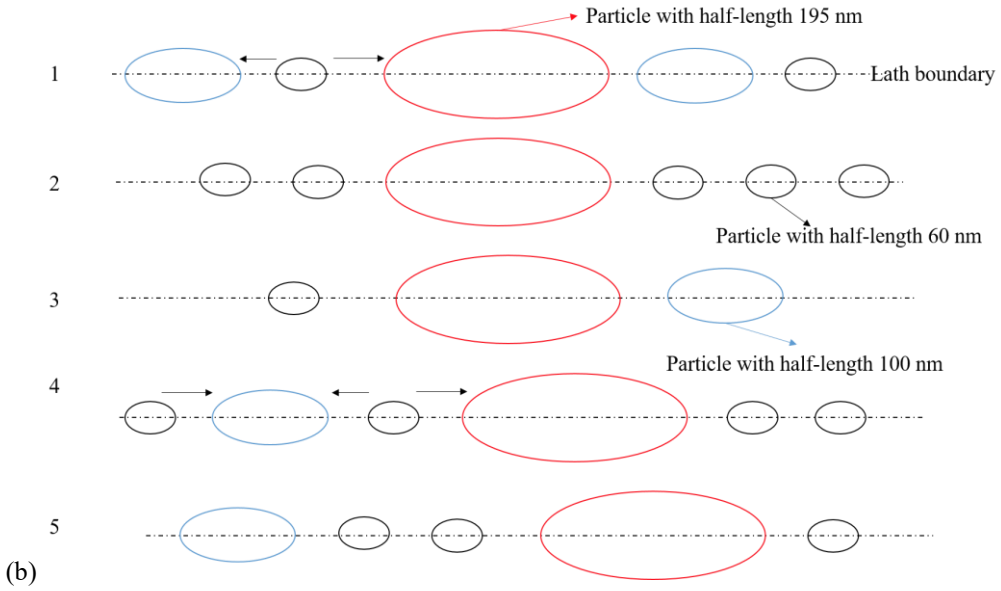

Figure 7-22. (a) The assumed particle arrangement for the larger particle A with half-length 195 nm surrounded by 20 particles with half-length 60 nm and 5 particles with half-length 100 nm in the 2D lath boundary plane; (b) Based on the assumed particle arrangement in (a), five possible situations around particle A with half-length 195 nm along the lath boundary (1D line).

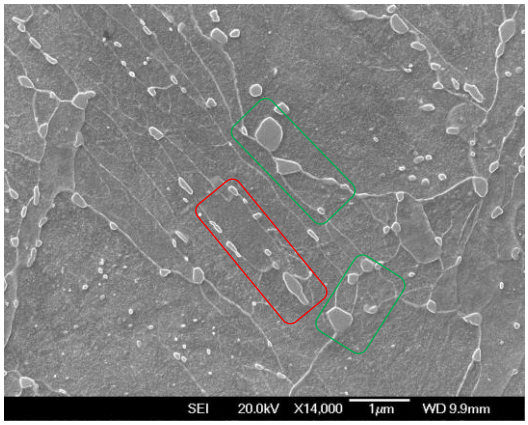

Figure 7-23. The observed particle arrangements around larger particles along the lath boundary after tempering for 4 hrs at 600 °C in the Base steel. The red rectangles indicate the largest - smallest particle arrangement and the green rectangles indicate the arrangement of multi-particles in different size ranges.

Recently, two kinds of mean field models have been reported to simulate the coarsening of particles on the grain/sub-grain boundaries: theoretical models [141-145] and

DICTRA coarsening model [158], which all treat particle coarsening independently. However, there is no reported model treating dissolution of smaller particles and coarsening of larger ones as a continuous and simultaneous process. Comparing the reported models from literature with the newly-established mathematical model, differences between simulation process and results arise from two main aspects:

(1) Simulation process: The reported theoretical models [141-145] and DICTRA model [158] are all mean field models, using the average-sized particle to represent the whole system under equilibrium conditions. The precipitate volume fraction is ignored in these models. However, the particle coarsening rate increases with an increase of particle volume fraction, even at very samll values [130], due to the occurrence of diffusional interaction between particles, which changes the diffusion field around particles. A continuity equation has normally been used to derive the particle distribution in the theoretical models. As discussed in section 5.2, the coarsening of inter-lath cementite takes place independently from that of intra-lath cementite, therefore, mean field approaches will not work in this situation. In the mathematical model, the larger and smaller inter-lath particles that have the maximum possibility to coarsen and dissolve respectively are selected based on the experimental inter-lath carbide size distribution, where dissolution of the smaller particle and coarsening of the larger one is treated as a simultaneous process. The rate-controlling step for the coupled inter-lath cementite system is dissolution of the smaller particle driven by diffusion; therefore, the concentration gradients only exist between the interface elements and adjacent elements to ensure no extra solute added in the system.

(2) Simulation results: The theoretical models [141, 142, 145] give a qualitative relationship between particle radius and time as $r=Kt^{1/4}$ or $Kt^{1/5}$ for precipitates on the

grain/sub-grain boundaries, which has been used in some steels [59, 72, 148] to determine the coarsening kinetics for carbides where the rate constant K is unknown. The quantitative predictions are given by the DICTRA model for coarsening of carbides along the grain boundary in different steels, which disagree with experimental observations [149, 151, 157, 159]. A DICTRA 1D coarsening model has already been checked in details for the coarsening of inter-lath cementite in Chapter 6, and found to be inappropriate to give a reasonable prediction. However, the mathematical model finally predicts the shortest dissolution time for smaller particles with the maximum possibility to dissolve in the coupled inter-lath cementite particle systems, and indicates how the larger particle coarsens with only one smaller particle consumed.

7.5 Conclusions

1. The mathematical model for the coupled inter-lath cementite system has been established based on the experimental analysis, where the largest and smallest particles with the smallest separation have been selected in the model. The dissolution of the smaller particle and coarsening of the larger one have been treated as a continuous and simultaneous process.

2. The diffusion process is simplified as a 1D diffusion process. As the rate-controlling step for the model is the dissolution of the smaller particle driven by diffusion of Mn due to the very short separation, the Mn diffusion process occurs just between the interface elements and the adjacent elements, which is the basis for the whole calculation process. Finite difference method has been used in the model, and the calculation has been carried out and iterated in different boundary elements.

3. The mathematical model predicts the shortest dissolution times for selected smaller particles in different coupled inter-lath particle systems. However, the size increase for the larger particle has been predicted to be much less at the expense of a single smaller particle in the model compared with the observed size increase.

4. The rationalisation of the simulation has been carried out. Different particle arrangements have been proposed compared with the observed SEM images. The simulated simplest particle arrangement between the largest and smallest particles does appear in the SEM images, and the simulation is in rough agreement with the observed results. However, multi-particles in different size ranges along the lath boundary are also observed, where solute diffusion reverses along the lath boundary. Therefore, a multi-

sized inter-lath cementite model is needed in the future based on the established mathematical model for the coupled inter-lath particle system in terms of fully simulating the coarsening of larger particles and dissolution of smaller particles concurrently.

5. Two predominant differences, simulation process and simulation results, have been reviewed between the newly-established mathematical model and the reported models for the coarsening and dissolution of particles along the grain/sub-grain boundary.

Chapter 8 Conclusions and suggestions for future work

8.1 Conclusions

The following conclusions have been obtained based on the characterisation and kinetic modelling of carbide coarsening in the S690-based steels during the early stages of tempering at 600 °C:

Characterisation of precipitation and carbide coarsening during the early stages of tempering at 600 °C:

1. Auto-tempering occurs in the three investigated Q&T steels (Base/ Base-Mo-V/ Base-Cr-Mo-V-Si) during water quenching, where ε'-carbides and cementite have both been identified using trace analysis. Cementite is the predominant carbide in the Base and Base-Mo-V steels. However, with an increase in Si content, the transformation from ε'-carbide to cementite is delayed, meaning that ε'-carbide constitutes a larger number percentage in the Base-Cr-Mo-V-Si steel.

2. The precipitation sequences for the three steels are slightly different during the early stages of tempering due to the different alloying elements present:
   a. Base steel: cementite + ε'-carbide → cementite (predicted equilibrium carbide in this steel) → independent coarsening of inter- and intra-lath cementite (elliptical in shape).
   b. Base-Mo-V and Base-Cr-Mo-V-Si steels: cementite + ε'-carbide → cementite → cementite + secondary carbide (Mo-V-rich M_2C carbide) → independent coarsening of inter- and intra-lath cementite with a slower coarsening rate than the

Base steel. Comparatively large elliptical cementite (in the laths and on the lath/grain boundaries) and fine needle-shaped cementite (within the laths) are both present during tempering. In addition, finer elliptical secondary Mo-V-rich carbides are detected after tempering for 4 hrs.

The coarsening of cementite occurs in the three steels on tempering from 2 hrs to 16 hrs at 600 °C. Substitutional elements, i.e. Mn, Mo, Cr, and V, enrich cementite in the three steels; hence, the rate-controlling step for coarsening of cementite is the diffusion of these substitutional elements. The rate of coarsening of cementite in the three steels ranks as Base> Base-Mo-V> Base-Cr-Mo-V-Si. The coarsening rate of inter-lath cementite is obviously larger than that of intra-lath cementite due to faster solute boundary diffusion.

1. It has been shown that solute diffusion occurs either along the lath/grain boundary resulting in coarsening of inter-lath cementite, or through the bulk leading to coarsening of intra-lath cementite (Base steel) and the formation of secondary Mo-V-rich carbides (Base-Mo-V and Base-Cr-Mo-V-Si steels). Solute diffusion does not occur significantly through the bulk to a boundary during tempering from 2 hrs to 16 hrs.

2. The softening process occurs during tempering consistent with the carbide precipitation and coarsening:

I. In the Base steel, an initial large hardness decrease (approximately 195 HV) is observed during tempering from 0 hr to 2 hrs predominantly due to the retained carbon in solid solution that did not precipitate during auto-tempering diffusing out from solid solution; the coarsening of cementite contributes to the more

gradual hardness decrease on tempering from 2 hrs to 16 hrs (around 40 HV change).

II. The retained carbon contents in the Base and Base-Mo-V steels remain constant after water quenching, resulting in a similar hardness in the as-quenched condition for the two steels (458±12 HV for the Base steel, 454±11 HV for the Base-Mo-V steel). However, a slightly higher retained carbon content as well as alloying contents (such as Cr and Si) are present in the Base-Cr-Mo-V-Si steel, which leads to a little bit higher as-quenched hardness being observed (471±12 HV) in this steel. In the Base-Mo-V and Base-Cr-Mo-V-Si steels, the hardness decreases follow the same trend as the Base steel although the hardness results for the Base-Mo-V and Base-Cr-Mo-V-Si steels are similar and consistently about 100 HV higher than those for the Base steel on tempering from 2 hrs to 16 hrs. Coarsening of cementite also contributes to the softening process in these two steels during tempering. In addition, the observation of fine secondary Mo-V-rich carbides after 4 hours tempering does not appear to result in any secondary hardening peak in the Base-Mo-V and Base-Cr-Mo-V-Si steels.

Kinetic modelling of coarsening of the elliptical inter-lath cementite:

5. **DICTRA coarsening model**: A DICTRA 1D coarsening model was firstly used to model the coarsening of inter-lath cementite in the Base and Base-Mo-V steels, which gave coarsening rates that were too slow compared to the experimental data. The model did take into account the different substitutional elements in the two steels. Uncertainties in the accuracy of the data available in the kinetic database in DICTRA, uncertainties about the interfacial energy effect in related DICTRA governing equations and the

discrepancies between experimental observations and assumptions in the model should all contribute to deviations present between modelling results and experimental observations in the two steels. The deficiencies in the DICTRA model that could not be overcome by modifications to the substitutional element diffusivities or governing equations meant that an alternative modelling approach was considered.

6. **Mathematical model (finite difference model)**: A coupled inter-lath cementite model based on the finite difference method has been established, where the largest and smallest particles with the smallest separation are included in the model based on the experimental analysis. In this model, the dissolution of the smaller particle and coarsening of the larger one are treated as a continuous and simultaneous process.

   a. The diffusion process is simplified as a 1D diffusion process. The rate-controlling step for the model is the dissolution of the smaller particle driven by diffusion of Mn (determined to be the main substitutional element enriching the cementite), hence, the diffusion process occurs just between the interface elements and the adjacent elements, which is the basis for the whole calculation process.
   b. The mathematical model predicts the shortest dissolution times observed for selected smaller particles in the coupled inter-lath particle system. However, the size increase for the larger particle due to dissolution of a single smaller particle has been predicted to be much less than the observed size increase.
   c. The validation for the differences in particle size increases have been considered. Different particle arrangements have been proposed and compared with the observed SEM images. The simulated simplest particle arrangement between the largest and smallest particles does appear in the SEM images, and the simulation

is in rough agreement with the observed results. However, multi-particles in different size ranges on the lath boundary are also observed with solute diffusing in the reserved directions along the lath boundary, hence, a multi-sized inter-lath cementite particle coarsening model is needed in the future.

8.2 Suggestions for future work

1. Carbide precipitation and coarsening on tempering from 0 hr to 16 hrs for three S690-based steels have been investigated in this project, which plays a significant role in the hardness change during tempering. However, other factors such as the change of dislocation density, which also contribute to hardness variation during tempering, have not been quantitatively measured and may be significantly at the early stages of tempering. Hence, it is very valuable to carry out dislocation density measurements in the future to help explain the hardness variation more accurately as many dislocations have been observed in the as-quenched condition for the three steels.

2. The secondary Mo-V-rich carbides are detected by EDS measurements and expected to be M_2C type after tempering for 4 hrs at 600 °C. However, it would be helpful to use the SADP technique to accurately confirm the secondary carbide type. Further analysis of these particles (size, distribution etc) should be carried out to determine if they are having any influence on the hardness of the steels during a longer tempering process. Further consideration of the levels of Mo and V necessary to give the reduced coarsening rate (and hence softening rate) in these steels compared to the Base composition could be considered.

3. In this investigation, a fundamental mathematical model has been established to concurrently simulate the dissolution of a smaller cementite particle and coarsening of a larger one in the coupled inter-lath cementite system during tempering from 2 hrs to 16 hrs in the Base steel. However, multi-particles of different sizes along the lath boundary are also observed; therefore, a multi-sized inter-lath cementite model is needed in the

future based on the established basic coupled inter-lath particle model to fully simulate the coarsening of larger particles and dissolution of smaller particles simultaneously.

4. The coarsening of inter-lath cementite also occurs independently from that of intra-lath cementite in the Base-Mo-V and Base-Cr-Mo-V-Si steels during tempering from 2 hrs to 16 hrs, where the separations between inter-lath cementite particles are even smaller than those in the Base steel. Therefore, it is also worth using the established model from the Base steel to predict the coarsening and dissolution of coupled inter-lath cementite particles in the Base-Mo-V and Base-Cr-Mo-V-Si steels on tempering from 2 hrs to 16 hrs. In these cases the role of diffusion of the other substitutional elements will need to be taken into account.

List of References

[1] Driscoll J. R. An investigation into the microstructure and precipitation characteristics of reheated quenched and tempered 701 Steel (RQT701) quenched from 925 °C in austenite to an autotempered martensitic microstructure, and tempered at 580 °C, 600 °C and 620 °C for between 1 and 100 hours. MRes thesis, University of Birmingham, 2014.

[2] *RQT 701 Quenched and Tempered steel Plate* [Online]. Brown McFarlane. [Accessed].

[3] *RQT technical guide* [Online]. TATA Steel. [Accessed].

[4] *RQT 701 Quenched and Tempered Steel Plate-The remarkable quality of steel* [Online]. GANG Steel. [Accessed].

[5] Bhadeshia H. K. D. H. and Honeycombe R. Steels: microstructure and properties. Butterworth-Heinemann, 2011.

[6] Cohen M. The strengthening of Steel. The Metallurgical Society TMS of AIME, 1962, 224**,** 638-657.

[7] Tamaki K. and Suzuki J. 1982. Precipitation of carbides during tempering of Cr-Mo steels. Research report of the faculty of engineering, Mie University.

[8] Morito S., Huang X., Furuhara T., Maki T. and Hansen N. The morphology and crystallography of lath martensite in alloy steels. Acta Materialia, 2006, 54**,** 5323-5331.

[9] Kaur I., Mishin Y. and Gust W. Fundamentals of grain and interphase boundary diffusion. New York, John Wiley & Sons Inc., 1995.

[10] Fisher J. C. Calculation of diffusion penetration curves for surface and grain boundary diffusion. Journal of Applied Physics, 1951, 22**,** 74-77.

[11] Petty E. R. Martensite: Fundamentals and Technology. London, Longman, 1970.

[12] Wilson E. The γ→ α transformation in low carbon irons. ISIJ international, 1994, 34**,** 615-630.

[13] Krauss G. Martensite in steel: strength and structure. Materials Science and Engineering: A, 1999, 273**,** 40-57.

[14] Marder A. R. and Krauss G. The morphology of martenste in iron-carbon alloys. Transactions of American Society for Metals, 1967, 273-275**,** 40-57.

[15] Thomas G. Retained austenite and tempered martensite embrittlement. Metallurgical Transactions A, 1978, 9**,** 439-450.

[16] Bhadeshia H. K. D. H. and Edmonds D. V. Tempered martensite embrittlement: role of retained austenite and cementite. Metal Science, 1979, 13**,** 325-334.

[17] Maalekian M. 2007. Christian doppler laboratory for early stages of precipitation. The effects of alloying elements on steels (I). Technische Universität Graz Institut für Werkstoffkunde, Schweißtechnik und Spanlose Formgebungsverfahren.

[18] Matsuda H., Mizuno R., Funakawa Y., Seto K., Matsuoka S. and Tanaka Y. Effects of auto-tempering behaviour of martensite on mechanical properties of ultra high strength steel sheets. Journal of Alloys and Compounds, 2013, 577**,** S661-S667.

[19] Kung C. and Rayment J. An examination of the validity of existing empirical formulae for the calculation of Ms temperature. Metallurgical and Materials Transactions A, 1982, 13**,** 328-331.

[20] Andrews K. W. Empirical formulae for the calculation of some transformation temperatures. Journal of the Iron and Steel Institute, 1965, 203**,** 721-727.

[21] Steven W. and Haynes. A. G. The temperature formation of martensite and bainite in low-alloy steels, some effects of chemical composition. Journal of Iron and Steel Institute, 1956, 183**,** 349-359.

[22] Peet M. Predcition of martensite start temperature. Materials Science and Technology, 2015, 31**,** 1370-1375.

[23] Lai G. Y. On the precipitation of epsilon carbide in lower bainite. Metallurgical Transactions A, 1975, 6A**,** 1469-1471.

[24] Parker E. R. Interrelations of compositions, transformation kinetics, morphology, and mechanical properties of alloy steels. Metallurgical Transactions A, 1977, 8**,** 1025-1042.

[25] Padmanabhan R. and Wood W. Precipitation of ϵ carbide in martensite. Materials Science and Engineering, 1984, 65**,** 289-297.

[26] Tan Y. TEM study of six representative low carbon martensitic steels. Acta Metallurgica Sinica, 1985, 21**,** A181-186.

[27] Krauss G. and Thompson S. W. Ferritic microstructures in continuously cooled low- and ultralow-carbon steels. ISIJ International, 1995, 35**,** 937-945.

[28] Ooi S. W., Cho Y. R., Oh J. K. and Bhadeshia H. K. D. H. Carbon enrichment in residual austenite during martensitic transformation. *International Conference on Martensitic Transformations 2009.* Pennsylvania, USA.

[29] Clarke A. J., Miller M. K., Field R. D., Coughlin D. R., Gibbs P. J., Clarke K. D., Alexander D. J., Powers K. A., Papin P. A. and Krauss G. Atomic and nanoscale chemical and structural changes in quenched and tempered 4340 steel. Acta Materialia, 2014, 77**,** 17-27.

[30] Gallego J., Rodrigues A. R., Assis C. L. F. d. and Montanari L. Second phase precipitation in ultrafine-grained ferrite steel. Materials Research, 2014, 17**,** 527-534.

[31] Jack K. H. Structural transformations in the tempering of high-carbon martensitic steels. Journal of Iron and Steel Institute, 1951, 169**,** 26-36.

[32] Taylor K., Olson G., Cohen M. and Vander Sande J. Carbide precipitation during stage I tempering of Fe-Ni-C martensites. Metallurgical Transactions A, 1989, 20**,** 2749-2765.

[33] Shimizu K. i. and Okamoto H. High voltage electron microscopy study of the metastable iron carbide in a eutectoid Fe–C Alloy. Transactions of the Japan Institute of Metals, 1974, 15**,** 193-199.

[34] Tanaka Y. and Shimizu K. i. Carbide formation upon tempering at low temperatures in Fe–Mn–C Alloys. Transactions of the Japan Institute of Metals, 1981, 22**,** 779-788.

[35] Leslie W. C. The quench-ageing of low-carbon iron and iron-manganese alloys an electron transmission study. Acta Metallurgica, 1961, 9**,** 1004-1022.

[36] Wells M. G. H. An electron transmission study of the tempering of martensite in an Fe-Ni-C alloy. Acta Metallurgica, 1964, 12**,** 389-399.

[37] Murphy S. and Whiteman A. The precipitation of epsilon-carbide in twinned martensite. Metallurgical Transactions, 1970, 1**,** 843-848.

[38] Leslie W. and Rauch G. Precipitation of carbides in low-carbon Fe-Al-C alloys. Metallurgical Transactions A, 1978, 9**,** 343-349.

[39] Thompson S. W. Structural characteristics of transition-iron-carbide precipitates formed during the first stage of tempering in 4340 steel. Materials Characterization, 2015, 106**,** 452-462.

[40] Speich G. R. and Leslie W. C. Tempering of steel. Metallurgical Transactions 1972, 3**,** 1043-1055.

[41] Krauss G. Tempering of lath martensite in low and medium carbon steels: assessment and challenges. Steel Research International, 2017.

[42] Ohmori Y. χ-carbide formation and its transformation into cementite during the tempering of martensite. Transactions of the Japan Institute of Metals, 1972, 13**,** 119-127.

[43] Zhang M. X. and Kelly P. M. Crystallography of spheroidite and tempered martensite. Acta Materialia, 1998, 46**,** 4081-4091.

[44] Saleh A. A., Casillas G., Pereloma E. V., Carpenter K. R., Killmore C. R. and Gazder A. A. A transmission Kikuchi diffraction study of cementite in a quenched and tempered steel. Materials Characterization, 2016, 114**,** 146-150.

[45] Bagaryatskii Y. A. Possible mechanism of martensite decomposition. Dokl Acad Nauk SSSR, 1950, 73**,** 1161-1164.

[46] Isaichev I. V. Orientation of cementite in tempered carbon steel. ZhTekhn Fiz, 1947, 17**,** 835-838.

[47] Totten G. E. Steel heat treatment: metallurgy and technologies. Oregon, USA, Taylor and Francis Group, 2007.

[48] Jörgen A., Hans-Olof A., Lars-Erik S. and Henrik J. Microstructure development during tempering of the hot-work tool steel UDDEHOLM QRO 90 Supreme *Tool 09, 8th International Tooling Conference, Tool Steels - Deciding Factor in Worldwide Production 2009*. Aachen: Mainz.

[49] Robert C. S., Averbach B. L. and Cohen M. The mechanism and kinetics of the first stage of tempering. Transactions of American Society for Metals, 1953, 45**,** 576-604.

[50] Lement B. S., Averbach B. L. and Cohen M. Microstructural changes on tempering iron-carbon alloys. Transactions of American Society for Metals, 1954, 46**,** 851.

[51] Ohmori Y. and Tamura I. Epsilon carbide precipitation during tempering of plain carbon martensite. Metallurgical Transactions A, 1992, 23**,** 2737-2751.

[52] Hirotsu Y. and Nagakura S. Crystal structure and morphology of the carbide precipitated from martensitic high carbon steel during the first stage of tempering. Acta Metallurgica, 1972, 20**,** 645-655.

[53] Ahn S. T., Kim D. S. and Nam W. J. Microstructural evolution and mechanical properties of low alloy steel tempered by induction heating. Journal of Materials Processing Technology, 2005, 160**,** 54-58.

[54] Greenwood G. The growth of dispersed precipitates in solutions. Acta metallurgica, 1956, 4**,** 243-248.

[55] Oriani R. Ostwald ripening of precipitates in solid matrices. Acta Metallurgica, 1964, 12**,** 1399-1409.

[56] Caron R. N. and Krauss G. The tempering of Fe-C lath martensite. Metallurgical Transactions, 1972, 3**,** 2381-2389.

[57] Yamasaki S. Modelling Precipitation of Carbides in Martensite Steels. PhD Thesis, University of Cambridge, 2004.

[58] Pešička J., Kužel R., Dronhofer A. and Eggeler G. The evolution of dislocation density during heat treatment and creep of tempered martensite ferritic steels. Acta Materialia, 2003, 51**,** 4847-4862.

[59] Nam W. J. and Bae C. M. Coarsening behavior of cementite particles at a subcritical temperature in a medium carbon steel. Scripta Materialia, 1999, 41**,** 313-318.

[60] Tokizane M., Matsumura N., Tsuzaki K., Maki T. and Tamura I. Recrystallization and formation of austenite in deformed lath martensitic structure of low carbon steels. Metallurgical Transactions A, 1982, 13**,** 1379-1388.

[61] Tua S. J., Weiss R. K., Krauss G. and Thompson S. W.Published. Structual changes induced by high-temperature tempering of martensitic plate steels and a mechanism for the recrystallization of martensite. In*:* Krauss G. and Repas P. E., eds. Fundamentals of aging and tempering in bainitic and martensitic steel products, 1992.Year: Warrendale, PA, 53-66.

[62] Badinier G. Effect of carbon segregation and carbide precipitation on the mechanical response of martensite. PhD Thesis, The University Of British Columbia, 2013.

[63] Deng X., Fu T., Wang Z., Misra R. and Wang G. Epsilon carbide precipitation and wear behaviour of low alloy wear resistant steels. Materials Science and Technology, 2016, 32**,** 320-327.

[64] Kim B., Martin D. S., Chao J. and Rivera-Díaz-Del-Castillo P. E. J. The effect of silicon on the ε→θ transformation in Ultra-strong spring steels. *Materials Science and Technology Conference 2012.* Pittsburgh, Pennsylvania, USA.

[65] Ghosh G. and Olson G. B. Precipitation of paraequilibrium cementite: Experiments, and thermodynamic and kinetic modeling. Acta Materialia, 2002, 50**,** 2099-2119.

[66] Zhu C., Xiong X., Cerezo A., Hardwicke R., Krauss G. and Smith G. Three-dimensional atom probe characterization of alloy element partitioning in cementite during tempering of alloy steel. Ultramicroscopy, 2007, 107**,** 808-812.

[67] Nazemi F., Hamel-Akré J. and Bocher P. Modeling of cementite coarsening during tempering of low-alloyed-medium carbon steel. Journal of Materials Science, 2018, 53**,** 6198-6218.

[68] Miyamoto G., Oh J. C., Hono K., Furuhara T. and Maki T. Effect of partitioning of Mn and Si on the growth kinetics of cementite in tempered Fe–0.6 mass% C martensite. Acta Materialia, 2007, 55**,** 5027-5038.

[69] Deb P. and Chaturvedi M. Coarsening behavior of cementite particles in a ferrite matrix in 10B30 steel. Metallography, 1982, 15**,** 341-354.

[70] Cree A., Faulkner R. and Lyne A. Cementite particle coarsening during spheroidisation of bearing steel SAE 52100. Materials Science and Technology, 1995, 11**,** 566-571.

[71] Foley R. P., Weiss R. K., Thompson S. W. and Krauss. G. Tempering behaviour of martensite plate steels produced by direct quench and reaustenitize- and -quench processing. *In:* Ashahani R. and Tither G. (eds.) *International symposium on low-carbon steels for the 90's, 1993.*

[72] Nam W. J. Effect of initial microstructure on the coarsening behavior of cementite particles. ISIJ international, 1999, 39**,** 1181-1187.

[73] N.A.Gjostein. Diffusion. American society of Metals, 1973**,** 241.

[74] Balluffi R. Grain boundary diffusion mechanisms in metals. Metallurgical transactions B, 1982, 13**,** 527-553.

[75] Janovec J., Svoboda M., Výrostková A. and Kroupa A. Time–temperature–precipitation diagrams of carbide evolution in low alloy steels. Materials Science and Engineering: A, 2005, 402**,** 288-293.

[76] Owen W. S. The effect of Silicon on the kinetic of tempering. Transactions of the ASM, 1954, 46**,** 812-829.

[77] Delagnes D., Lamesle P., Mathon M. H., Mebarki N. and Levaillant C. Influence of silicon content on the precipitation of secondary carbides and fatigue properties of a 5%Cr tempered martensitic steel. Materials Science and Engineering: A, 2005, 394**,** 435-444.

[78] Jang J. H., Kim I. G. and Bhadeshia H. K. D. H. ε-Carbide in alloy steels: first-principles assessment. Scripta Materialia, 2010, 63**,** 121-123.

[79] Bain E. C. 1936. The Alloying Elements in Steel. ASM International.

[80] Zav'yalov A. S. and Senchenko M. I. Effect of alloying elements on the tempering of steel. Metal Science and Heat Treatment of Metals, 1959, 1**,** 3-12.

[81] Chang L. and Smith G. The silicon effect in the tempering of martensite in steels. Journal de Physique Colloques, 1984, 45**,** C9-397-C399-401.

[82] Grange R. A., Hribal C. R. and Porter L. F. Hardness of tempered martensite in carbon and low-alloy steels. Metallurgical Transactions A, 1977, 8**,** 1775-1785.

[83] Llewellyn D. and Hudd R. Steels: metallurgy and applications. Elsevier, 1998.

[84] Mesquita R., Barbosa C., Morales E. and Kestenbach H.-J. Effect of silicon on carbide precipitation after tempering of H11 hot work steels. Metallurgical and Materials Transactions A, 2011, 42**,** 461-472.

[85] Mesquita R. A. and Kestenbach H.-J. Influence of silicon on secondary hardening of 5 wt% Cr steels. Materials Science and Engineering: A, 2012, 556**,** 970-973.

[86] Babu S. S., Hono K. and Sakurai T. Atom probe field ion microscopy study of the partitioning of substitutional elements during tempering of a low-alloy steel martensite. Metallurgical and Materials Transactions A, 1994, 25**,** 499-508.

[87] Pilling J. and Ridley N. Tempering of 2.25 pct Cr-1 pct Mo low carbon steels. Metallurgical Transactions A, 1982, 13**,** 557-563.

[88] Yongtao Z., Lede M., Xiaojun W., Hanqian Z. and Jinfu L. Evolution behavior of carbides in 2.25 Cr-1Mo-0.25 V steel. Materials transactions, 2009, 50**,** 2507-2511.

[89] Taneike M., Sawada K. and Abe F. Effect of carbon concentration on precipitation behavior of M23C6 carbides and MX carbonitrides in martensitic 9Cr steel during heat treatment. Metallurgical and Materials Transactions A, 2004, 35**,** 1255-1262.

[90] Miyata K., Kushida T., Omura T. and Komizo Y. Coarsening kinetics of multicomponent MC-type carbides in high-strength low-alloy steels. Metallurgical and Materials Transactions A, 2003, 34**,** 1565-1573.

[91] Epicier T., Acevedo D. and Perez M. Crystallographic structure of vanadium carbide precipitates in a model Fe–C–V steel. Philosophical Magazine, 2008, 88**,** 31-45.

[92] Liu H., Zhu J., Liu Y. and Lai Z. First-principles study on the mechanical properties of vanadium carbides VC and V4C3. Materials Letters, 2008, 62**,** 3084-3086.

[93] Senior B. A critical review of precipitation behaviour in 1Cr-Mo-V rotor steels. Materials Science and Engineering: A, 1988, 103**,** 263-271.

[94] Janovec J., Vyrostkova A. and Svoboda M. Influence of tempering temperature on stability of carbide phases in 2.6Cr-0.7Mo-0.3V steel with various carbon content. Metallurgical and Materials Transactions A, 1994, 25**,** 267-275.

[95] Výrostková A., Kroupa A., Janovec J. and Svoboda M. Carbide reactions and phase equilibria in low alloy Cr–Mo–V steels tempered at 773–993 K. Part I: Experimental measurements. Acta Materialia, 1998, 46**,** 31-38.

[96] Ustinovshchikov Y. I. Secondary hardening mechanism of alloy steels. Metal science, 1984, 18**,** 337-344.

[97] Serna M. M., Jesus E. R. B., Galego E., Martinez L. G., S.CorrêA H. P. and Rossi J. L. An overview of the microstructures present in high-speed steel - carbides crystallography. Materials Science Forum, 2006, 530-531**,** 48-52.

[98] Baker R. G. and Nutting J. The tempering of a Cr-Mo-V-W and a Mo-V steel. Iron and Steel Institute Special Report, 1959, 64**,** 1-22.

[99] Dunlop G. L. and Honeycombe R. W. K. Ferrite morphologies and carbide precipitation in a Cr-Mo-V creep-resisting steel. Metal Science, 1976, 10:4**,** 124-132.

[100] Kuo K. H. and Jia C. L. Crystallography of $M_{23}C_6$ and M_6C precipitated in a low alloy steel. Acta Metallurgica, 1985, 33**,** 991-996.

[101] Senior B. A critical review of precipitation behaviour in 1Cr- Mo-V rotor steels. Materials Science and Engineering: A, 1988, 103**,** 263-271.

[102] Gingell A. D. B., Bhadeshia H. K. D. H., Jones D. G. and Mawella K. J. A. Carbide precipitation in some secondary hardened steels. Journal of Materials Science, 1997, 32**,** 4815-4820.

[103] Andrews K. W., Hughes H. and Dyson D. J. Constitution diagrams for Cr-Mo-V steels. Journal of the Iron and Steel Institute, 1972, 191**,** 337-350.

[104] Sato T.-o., Nishizawa T. and Tamaki K. Carbides in molybdenum steels. Transactions of the Japan Institute of Metals, 1962, 3**,** 196-202.

[105] Kroupa A., Výrostková A., Svoboda M. and Janovec J. Carbide reactions and phase equilibria in low-alloy Cr–Mo–V steels tempered at 773–993 K. Part II: Theoretical calculations. Acta Materialia, 1998, 46**,** 39-49.

[106] Rong W. and Dunlop G. The crystallography of secondary carbide precipitation in high speed steel. Acta Metallurgica, 1984, 32**,** 1591-1599.

[107] Yamasaki S. and Bhadeshia H. Modelling and characterisation of Mo_2C precipitation and cementite dissolution during tempering of Fe–C–Mo martensitic steel. Materials Science and Technology, 2003, 19**,** 723-731.

[108] Pitsch W. and Schrader A. Die ausscheidungsform des zementits im ferrite 29:485-488. Arch Eisenh, 1958, 29**,** 485-488.

[109] Raynor D., Whiteman J. and Honeycombe R. In-situ transformation of Fe_3C to Mo_2C in iron-molybdenum-carbon alloys. Iron Steel INST J, 1966, 204**,** 1114-1116.

[110] Irvine K. J. and Pickering F. B. The tempering characteristics of low carbon low alloy steels. Journal of the Iron and Steel Institute, 1960, 194**,** 137-153.

[111] Djebaili H., Zedira H., Djelloul A. and Boumaza A. Characterization of precipitates in a 7.9Cr–1.65Mo–1.25Si–1.2V steel during tempering. Materials Characterization, 2009, 60**,** 946-952.

[112] Inoue A., Arakawa S. and Masumoto T. In Situ Transformation of Cementite to M_7C_3 and Internal Defects of M_7C_3 in High Carbon-Chromium Steel by Tempering. Transactions of the Japan Institute of Metals, 1978, 19**,** 11-17.

[113] Inoue A. and Masumoto T. Carbide reactions ($M_3C \rightarrow M_7C_3 \rightarrow M_{23}C_6 \rightarrow M_6C$) during tempering of rapidly solidified high carbon Cr-W and Cr-Mo steels. Metallurgical Transactions A, 1980, 11**,** 739-747.

[114] Thomson R. C. and Bhadeshia H. K. D. H. Carbide precipitation in 12Cr1MoV power plant steel. Metallurgical Transactions A, 1992, 23**,** 1171-1179.

[115] Bain E. C. and Paxton H. W. Alloying elements in steel. ASM, Metals Park, Ohio, USA, 1961.

[116] Baker R. G. and J.Nutting. Precipitation processes in steels. Jounal of the Iron steel Institution, 1959, 192**,** 257.

[117] Pigrova G. D. Effect of long-term operation on carbide phases in Cr – Mo – V steels. Metal Science and Heat Treatment, 2003, 45**,** 84-87.

[118] Russell K. C. and Aaronson H. I. Sequences of precipitate nucleation. Journal of Materials Science, 1975, 10**,** 1991-1999.

[119] Aaron H. B., Fainstein D. and Kotler G. R. Diffusion-limited phase transformations: a comparison and critical evaluation of the mathematical approximations. Journal of applied physics, 1970, 41**,** 4404-4410.

[120] J.W.Martin, R.D.Doherty and B.Cantor. Stability of microstructure in metallic systems. Cambridge, Cambridge University Press 1997.

[121] Baldan A. Review progress in Ostwald ripening theories and their applications to nickel-base superalloys. Part I: Ostwald ripening theories. Journal of Materials Science, 2002, 37**,** 2171-2202.

[122] Lifshitz I. M. and Slyozov V. V. The kinetics of precipitation from supersaturated solid solutions. Journal of Physics and Chemistry of Solids, 1961, 19**,** 35-50.

[123] Wagner C. Theorie der Alterung von Niederschlägen durch Umlösen (Ostwald-Reifung). Zeitschrift für Elektrochemie, Berichte der Bunsengesellschaft für physikalische Chemie, 1961, 65**,** 581-591.

[124] Mullins W. and Vinals J. Self-similarity and growth kinetics driven by surface free energy reduction. Acta Metallurgica, 1989, 37**,** 991-997.

[125] Vedula K. and Heckel R. Spheroidization of binary Fe-C alloys over a range of temperatures. Metallurgical Transactions, 1970, 1**,** 9-18.

[126] Sakuma B. T., Watanabe N. and Nishizawa T. The effect of alloying element on the coaesening behavior of cementite particles in Ferrite. Transactions of the Japan Istitute of Metals, 1980, 21**,** 159-168.

[127] Heckel R. W. and Degregorio R. L. The growth and shrinkage rates of second-phase particles of various size distributions. II Spherodization of a eutectoid steel. Trans Metall Soc AIME, 1965, 233**,** 2001-2011.

[128] Li C.-Y., Blakely J. and Feingold A. Mass transport analysis for Ostwald ripening and related phenomena. Acta Metallurgica, 1966, 14**,** 1397-1402.

[129] Björklund S., Donaghey L. and Hillert M. The effect of alloying elements on the rate of Ostwald ripening of cementite in steel. Acta Metallurgica, 1972, 20**,** 867-874.

[130] Ardell A. The effect of volume fraction on particle coarsening: theoretical considerations. Acta Metallurgica, 1972, 20**,** 61-71.

[131] Chellman D. and Ardell A. The coarsening of γ'precipitates at large volume fractions. Acta Metallurgica, 1974, 22**,** 577-588.

[132] Brailsford A. and Wynblatt P. The dependence of Ostwald ripening kinetics on particle volume fraction. Acta Metallurgica, 1979, 27**,** 489-497.

[133] Tsumuraya K. and Miyata Y. Coarsening models incorporating both diffusion geometry and volume fraction of particles. Acta Metallurgica, 1983, 31**,** 437-452.

[134] Marqusee J. and Ross J. Theory of Ostwald ripening: Competitive growth and its dependence on volume fraction. The Journal of Chemical Physics, 1984, 80**,** 536-543.

[135] Voorhees P. W. and Glicksman M. E. Solution to the multi-particle diffusion problem with applications to Ostwald ripening—II. computer simulations. Acta Metallurgica, 1984, 32**,** 2013-2030.

[136] Lee H. M. and Allen S. M. Coarsening resistance of M_2C carbides in secondary hardening steels: Part III. Comparison of theory and experiment. Metallurgical Transactions A, 1991, 22**,** 2877-2888.

[137] Lee H. M., Allen S. M. and Grujicic M. Coarsening resistance of M_2C carbides in secondary hardening steels: Part I. Theoretical model for multicomponent coarsening kinetics. Metallurgical Transactions A, 1991, 22**,** 2863-2868.

[138] Yamasaki S. and Bhadeshia H. K. D. H. Modelling and characterisation of V_4C_3 precipitation and cementite dissolution during tempering of Fe-C-V martensitic steel. Materials Science and Technology, 2003, 19**,** 1335-1343.

[139] Zener C. Kinetics of the decomposition of austenite. Trans Aime, 1946, 167**,** 550-595.

[140] Zener C. Theory of growth of spherical precipitates from solid solution. Journal of Applied Physics, 1949, 20**,** 950-953.

[141] Speight M. V. Growth kinetics of grain-boundary precipitates. Acta Metallurgica, 1968, 16**,** 133-135.

[142] Kirchner H. O. K. Coarsening of grain-boundary precipitates. Metallurgical Transactions, 1971, 2**,** 2861-2864.

[143] Aaron H. B. and I. Aaronson H. Growth of grain boundary precipitates in Al-4% Cu by interfacial diffusion. Acta Metallurgica, 1968, 16**,** 789-798.

[144] A.D.Brailsford and B.Aaron H. Growth of grain-boundary precipitates. Journal of Applied Physics, 1969, 40**,** 1702-1710.

[145] Ardell A. J. On the coarsening of grain boundary precipitates. Acta Metallurgica, 1972, 20**,** 601-609.

[146] Hoyt J. On the coarsening of precipitates located on grain boundaries and dislocations. Acta metallurgica et materialia, 1991, 39**,** 2091-2098.

[147] Enomoto Y. and Okada A. Many-body effects on the coarsening of grain boundary precipitates. Journal of Physics: Condensed Matter, 1990, 2**,** 6275.

[148] Lindsley B. and Marder A. The morphology and coarsening kinetics of spheroidized Fe-C binary alloys. Acta Materialia, 1997, 46**,** 341-351.

[149] Prat O., Garcia J., Rojas D., Carrasco C. and Inden G. Investigations on the growth kinetics of Laves phase precipitates in 12% Cr creep-resistant steels: experimental and DICTRA calculations. Acta Materialia, 2010, 58**,** 6142-6153.

[150] Agren J. Kinetics of carbide dissolution. Scand J Metall, 1990, 19**,** 2-8.

[151] Bjärbo A. Computer simulation of growth and coarsening of Laves phase in a modified 12% chromium steel. Scandinavian Journal of Metallurgy, 2003, 32**,** 94-99.

[152] Hu X., Li L., Wu X. and Zhang M. Coarsening behavior of $M_{23}C_6$ carbides after ageing or thermal fatigue in AISI H13 steel with niobium. International Journal of Fatigue, 2006, 28**,** 175-182.

[153] Borgenstam A., Höglund L., Ågren J. and Engström A. DICTRA, a tool for simulation of diffusional transformations in alloys. Journal of Phase Equilibria, 2000, 21**,** 269.

[154] Onsager L. Reciprocal relations in irreversible processes. I. Physical Review, 1931, 37**,** 405.

[155] Onsager L. Reciprocal relations in irreversible processes. II. Physical review, 1931, 38**,** 2265.

[156] Andersson J. O. and Ågren J. Models for numerical treatment of multicomponent diffusion in simple phases. Journal of Applied Physics, 1992, 72**,** 1350-1355.

[157] Prat O., Garcia J., Rojas D., Carrasco C. and Kaysser-Pyzalla A. Investigations on coarsening of MX and $M_{23}C_6$ precipitates in 12% Cr creep resistant steels assisted by computational thermodynamics. Materials Science and Engineering: A, 2010, 527**,** 5976-5983.

[158] Diffusion Module (DICTRA) Examples guide Version 2016b. *Foundation of Computational Thermodynamics* [Online].

[159] Gustafson Å. and Hättestrand M. Coarsening of precipitates in an advanced creep resistant 9% chromium steel—quantitative microscopy and simulations. Materials Science and Engineering: A, 2002, 333**,** 279-286.

[160] Sadhan G. Rate-controlling parameters in the coarsening kinetics of cementite in Fe–0.6 C steels during tempering. Scripta Materialia, 2010, 63**,** 273-276.

[161] Ghosh S. Rate-controlling parameters in the coarsening kinetics of cementite in Fe–0.6 C steels during tempering. Scripta Materialia, 2010, 63**,** 273-276.

[162] Bjerregaard L., Geels K., Ottesen B. and Ruckert M. Metalog Guide. Denmark, Copenhagen, 2000.

[163] Rao D. S., Muraleedharan K. and Humphreys C. TEM specimen preparation techniques. Microscopy: Science, Technology, Applications and Education, 2010**,** 1232-1244.

[164] Williams D. B. and Carter C. B. Transmission electron microscopy. Springer, 1996.

[165] Liao Y. 2007. *Practical Electron Microscopy and Database* [Online]. [Accessed].

[166] Zeng R. Precipitation hardening in AZ91 magnesium alloy. PhD Thesis, University of Birmingham, 2013.

[167] Martin J. W. Particle strengthening of metals and alloys. Materials Science and Technology, 1997, 13**,** 705.

[168] Bhadeshia H. K. D. H., David S. A., Vitek J. M. and Reed R. W. Stress induced transformation to bainite in Fe–Cr–Mo–C pressure vessel steel. Materials Science and Technology, 1991, 7**,** 686-698.

[169] Bureau N. 1955. X-ray Powder Data File (cric 539 4 3). *card for alpha-iron.* U.S. Department of commerce.

[170] Génin J.-M. R. On the morphology of the modulated precipitation of extended multiplets and Fe_9C_4 epsilon or eta carbide obtained by aging and tempering in Fe-C martensite. Metallurgical Transactions A, 1988, 19**,** 2901-2909.

[171] Bhadeshia H. K. D. H. *The structure of cementite* [Online]. University of Cambridge. [Accessed].

[172] Goodall A. Effect of initial microstructure on tempering of quenched and tempered steel plates. PhD Thesis, University of Birmingham 2019.

[173] Wert C. A. Diffusion coefficient of C in α-Iron. Physical Review, 1950, 79**,** 601-605.

[174] G.Krauss 1978. Martensitic transformation, structure and properties in hardenable steels. *In:* Doane D. V. and Kirkaldy J. S. (eds.) *Hardenability concepts with applications to steel.* : AIME.

[175] Hirsch P. B. and Humphreys F. J. Physics of strength and plasticity. MIT Press, 1969.

[176] Dieter G. E. Mechanical metallurgy McGraw-Hill Book Company Limited 1988.

[177] Weast R. C. CRC handbook of chemistry and physics. Boca Raton, Florida, CRC Press, 1976.

[178] Martin A. G. and Sellars C. M. Measurement of interfacial energy from extraction replicas of particles on grain boundaries. Metallography, 1970, 3**,** 259-273.

[179] Das S. K., Biswas A. and Ghosh R. N. Volume fraction dependent particle coarsening in plain carbon steel. Acta Materialia, 1993, 41**,** 777-781.

[180] Deb P. and Chaturvedi M. C. Coarsening behavior of cementite particles in a ferrite matrix in 10B30 steel. Metallography, 1982, 15**,** 341-354.

[181] DICTRA User Guide Version 2015b. *Foundation of computational Thermodynamic* [Online].

[182] Liu Z.-K. Introduction of DICTRA. Pennsylvania State University.

[183] Perez M., Ollat M., Mathcvon A., Militzer M., Fabregue D., Massardier V., Buscarlet E., Keovilay F. and Chantrenne P. Models for intercritical austenite formation in a dual-phase steel. *THERMEC'2018 International Conference on Processing & Manufacturing of Advanced Materials Processing, Fabrication, Properties, Applications.* Paris, France.

[184] Hettich G., Mehrer H. and Maier K. Self-diffusion in ferromagnetic a-iron. Scripta Metallurgica, 1977, 11**,** 795-802.

[185] Iijima Y., Kimura K. and Hirano K. Self-diffusion and isotope effect in α-iron. Acta Metallurgica, 1988, 36**,** 2811-2820.

[186] Huang S., Worthington D. L., Asta M., Ozolins V., Ghosh G. and Liaw P. K. Calculation of impurity diffusivities in α-Fe using first-principles methods. Acta Materialia, 2010, 58**,** 1982-1993.

[187] Gust W., Mayer S., Bogel A. and Predel B. Generalized representation of grain boundary self-diffusion data. Journal de Physique Colloques, 1985, 46(C4)**,** 537-544.

[188] Kaur I., Gust W. and Kozma L. Handbook of grain and interphase boundary diffusion data. Ziegler Press, 1989.

[189] 2000. *Metal Melting Temperatures* [Online]. Engineers Edge, LLC. [Accessed].

[190] Shima Y., Ishikawa Y., Nitta H., Yamazaki Y., Mimura K., Isshiki M. and Iijima Y. Self-Diffusion along Dislocations in Ultra High Purity Iron. MATERIALS TRANSACTIONS, 2002, 43**,** 173-177.